



University
of Glasgow

Ritboon, Atirach (2019) *Elements of orbital angular momentum and coherence in quantum optics*. PhD thesis.

<https://theses.gla.ac.uk/74349/>

Copyright and moral rights for this work are retained by the author

A copy can be downloaded for personal non-commercial research or study, without prior permission or charge

This work cannot be reproduced or quoted extensively from without first obtaining permission in writing from the author

The content must not be changed in any way or sold commercially in any format or medium without the formal permission of the author

When referring to this work, full bibliographic details including the author, title, awarding institution and date of the thesis must be given

Enlighten: Theses

<https://theses.gla.ac.uk/>
research-enlighten@glasgow.ac.uk

Elements of Orbital Angular Momentum and Coherence in Quantum Optics

Atirach Ritboon

Supervisors: Stephen M Barnett & Sarah Croke

Submitted in fulfilment of the requirements for the degree of Doctor of Philosophy

School of Physics and Astronomy
College of Science of Engineering
University of Glasgow

August 12, 2019



University
of Glasgow

Declaration

I declare that this thesis has been composed solely by myself and that it has not been submitted, in whole or in part, in any previous application for a degree. Except where otherwise stated, the research presented in this thesis is entirely my own.

Atirach Ritboon

Abstract

It is well established now that light carries both spin and orbital angular momentum which are associated with circular polarisation and helical phase fronts. Orbital angular momentum degrees of freedom recently have been used frequently in quantum information processing as their states are described by vectors in a higher-dimensional Hilbert space which enhances the possibility of realising superior quantum information protocols. On the other hand, quantum coherence, which arises from the superposition principle, is a distinct feature of quantum mechanics that cannot be satisfactorily described by classical physics. Coherence is also identified as essential ingredient for applications of quantum information, computation, and quantum thermodynamics. Three research projects, with their related background information, are presented in this thesis. In the first one, we design a linear optical system to transform the maximally entangled state of a down-converted photon pair into a genuine entangled χ -type state, as this class of genuine entangled states has been showed to have many interesting entanglement properties and can be employed in several quantum information protocols. In the second project, we study the mechanism of angular momentum transfer from light to a dielectric medium when it undergoes total internal reflection. The result shows that the torque associated with angular momentum transfer appears shortly, when the light pulse hits the interface. Finally, we study quantum coherence transfer from a coherence resource initialised in a coherence state to an atomic state by the Jaynes-Cummings model, and we compare it to the coherent operation that uses a resource prepared in a ladder state described by Åberg's model. We found that a resource in a coherent state is more robust against failures.

Acknowledgement

As we all know, studying at PhD level can be difficult, challenging, and enjoyable at the same time. I think to myself that I have a bit of luck because I always have nice and great people around me, and this thesis cannot be done without their support. It is a good opportunity for me to express my gratitude to all of them here.

Firstly, I would like to express my sincere gratitude to my two excellent supervisors Prof. Stephen M. Barnett and Dr. Sarah Croke for their continuous support of my study and research, for their patience, motivation, friendliness, and immense knowledge. These three years I spent in this research group under your guidance is one of the most enjoyable times in my life.

Of course, I also would like to thank all people who are the members and the ex-members of the Quantum Theory Group of the University of Glasgow: Kieran Flatt, Anette Messinger, Frances Crimin, Sijia Gao, Neel Mackinnon, Thomas Brougham, Fiona Speirits, Jim Cresser, Graeme Weir, Jörg Götte, Robert Cameron, Vaclav Potocek, Matthias Sonnleitner, and Gergely Ferenczi for the stimulating discussions and all the fun we have had together in the last three year.

Thanks to all my Thai friends in Thailand and Glasgow for a period of fun and relaxation we had together.

Importantly, I sincerely acknowledge the Institute for Promotion of Teaching Science and Technology (IPST) for giving me a scholarship under the Development and Promotion of Science and Technology Talents Project (DPST) since 2006.

Last but not the least, I would like to thank my father and mother, Mr. Chit and Mrs. Rayong Ritboon, for being supportive all the time in my life. Miss Sasikarn Seetasang, my girlfriend, thank you for always being by my side through good and bad times.

Atirach Ritboon

Publications

- A. Ritboon, S. Croke, and S. M. Barnett, Proposed optical realisation of a two photon, four-qubit entangled state, *J. Opt.* **19** 075201 (2017) [1].
- A. Ritboon, S. Croke, and S. M. Barnett, Optical angular momentum transfer on total internal reflection, *J. Opt. Soc. Am. B* **36** 482 (2019) [2].
- A. Messinger, A. Ritboon, F. Crimin, S. Croke, and S. M. Barnett, Coherence and catalysis in the Jaynes-Cummings model, *Manuscript in preparation* [3].

Overview

We provide this overview chapter in order to give the reader the guideline of the information mentioned in each chapter. The reader who already has some background in the field then can skip some introduction chapters. The original work that I have done with Stephen M. Barnett and Sarah Croke, my supervisors, and Annette Messinger and Frances Crimin, my colleagues, is given in chapters 4, 6 and 7. The other chapters are dedicated to give some background information to help the reader understand the original work.

In chapter 1, we provide an introduction to optical angular momentum and show that even though neither spin or orbital angular momentum is a true angular momentum, both of them are measurable and meaningful. We then review several methods that are popularly used in laboratories to generate and measure orbital angular momentum. At the end of the chapter, we review the correlation of orbital angular momentum of the two down-converted photons.

In chapter 2, we show examples of quantum information protocols that employ orbital angular momentum states. Orbital angular momentum which is realised as a higher-dimensional quantum system can be used to improve the performance of some qubit protocols.

In chapter 3, we introduce the χ -type states and review some of their rich entanglement properties and novel applications in quantum communication. This set of the states has been proven to be a new class of genuine multipartite entangled states.

In chapter 4, we give the transformation that changes the two-photon maximally entangled state, obtained from a spontaneous parametric down-conversion process, into any χ -type state. We then demonstrate our proposed linear optical system as the implementation of the transformation. The effect of each optical element used in the optical system on a composite state of a photon is reviewed and discussed. The work given in this chapter is an original contribution and was published in *J. Opt.* [1].

In chapter 5, we introduce background theories for studying the mechanism of angular momentum transfer, presented in chapter 6. We review Maxwell's equations and the boundary conditions. Optical force and torque on dielectric media are discussed in detail. We end this chapter by reviewing electromagnetic field quantisation and the quantisation of paraxial light.

In chapter 6, we study the mechanism of angular momentum transfer from light to a dielectric medium when it undergoes total internal reflection with the dipole-based forms of optical force and torque given in chapter 5. By applying the physical boundary conditions, we show that the Lorentz force gives us a manifestation of Newton's third law of motion. We then use the form of optical torque to study the angular momentum transfer from a single-photon pulse to an M-shaped Dove

prism. The research given in this chapter was published in *J. Opt. Soc. Am. B* [2].

We begin chapter 7 by reviewing Åberg's scheme and show that it can be used to perform a coherent operation. The problem is that in this scheme a coherence resource in a ladder state is very fragile. A single failure of a coherent operation gives rise the *complete destruction* of the coherence resource. We then study the Jaynes-Cummings model with a resource in a coherent state and use it to perform a coherent operation. We analyse the reason why a resource in a coherent state is more robust to a single error than one in a ladder state. The time evolution of the resource is discussed. The manuscript of this work is in preparation [3].

Contents

1	Optical Angular Momentum	1
1.1	Introduction	1
1.2	Orbital angular momentum of light	2
1.3	Validity of the separation between orbital and spin angular momentum	4
1.4	Optical vortex generation	6
1.4.1	Spiral phaseplates	7
1.4.2	Computer generated hologram	8
1.4.3	Mode converter	10
1.5	Measurement of orbital angular momentum	10
1.5.1	Computer generated hologram	11
1.5.2	Interferometric mode sorter	12
1.6	Orbital angular momentum and spontaneous parametric down conversion	13
2	OAM in quantum communication and processing	17
2.1	Introduction	17
2.2	Information security and cryptography	18
2.3	Quantum key distribution with 3-state systems	21
2.4	Quantum key distribution with entangled qutrits	22
2.5	Quantum Coin Tossing	23
3	The χ states	27
3.1	Introduction	27
3.2	Entanglement properties of χ states	29
3.2.1	How much entanglement do the χ -type states have?	29
3.2.2	Nonlocality of the χ states	31
3.2.3	Robustness of mutual information against a particle loss	33
3.3	Examples of quantum information protocols	35
3.3.1	Faithful quantum teleportation of two-qubit states	35
3.3.2	Quantum dense coding	38
3.3.3	Quantum-information splitting	39
3.3.4	Deterministic secure quantum communication	41

4	Two-photon, four-qubit χ state realisation	44
4.1	Transformation of two entangled photons	44
4.2	Optical realisation	47
4.2.1	Polarisation gates	47
4.2.2	OAM gates	49
4.3	Proposed optical system	51
4.4	Further transformation	53
4.5	Conclusion	53
5	Electromagnetics	55
5.1	Maxwell equations and plane-wave solutions	56
5.2	Boundary conditions	57
5.3	Reflection and refraction of plane electromagnetic waves	59
5.4	Optical force and torque	61
5.4.1	Microscopic scale	63
5.4.2	Macroscopic scale	64
5.4.3	Macroscopic fields	64
5.4.4	Optical torque	65
5.5	Field quantisation	66
5.5.1	Electromagnetic scalar and vector potentials	66
5.5.2	Free field quantisation	68
5.6	Paraxial approximation	73
5.7	Quantisation of paraxial light	74
6	Angular momentum transfer	78
6.1	Angular spectrum representation of a Laguerre-Gaussian beam	79
6.2	Reflected beam	81
6.3	Quantisation of the incident and reflected fields	85
6.4	Optical force and torque	86
6.5	Effective torque and angular momentum transfer	92
6.6	Beam shift analysis	95
6.7	M-shaped Dove prism	97
6.8	Paradox of conservation of angular momentum	101
6.9	Conclusion	106
7	Coherent operation with the Jaynes-Cummings model	107
7.1	Is coherence catalytic?	108
7.1.1	Åberg's scheme	108
7.1.2	Quantum correlations	110
7.2	Jaynes-Cummings model	111
7.3	Two qubits	113
7.4	Robustness analysis	115

7.5	The state of the cavity field	117
7.6	Multiple uses	120
7.7	Quasiprobability distribution	123
7.8	Coherent squeezed states	125
7.9	Conclusion	126

Bibliography		129
---------------------	--	------------

Chapter 1

Optical Angular Momentum

1.1 Introduction

The suggestion that light can have mechanical properties has been noticed or at least suspected in the science community since Kepler tried to explain the observation that the tails of comets always point away from the sun because of the radiation pressure from the sun. These mechanical properties become clear later when Maxwell unified the theory of electricity and magnetism [4]. Even though it was Maxwell who suggested how to quantify the radiation pressure, it was Poynting who quantified the momentum of an electromagnetic field [5]. The momentum density of an electromagnetic wave in vacuum is given by

$$\mathbf{p} = \varepsilon_0 \mathbf{E} \times \mathbf{B}. \quad (1.1)$$

where \mathbf{E} and \mathbf{B} are the electric field and magnetic flux density respectively. The angular momentum density is straightforwardly the vector product of the position and the momentum density

$$\mathbf{j} = \mathbf{r} \times (\varepsilon_0 \mathbf{E} \times \mathbf{B}). \quad (1.2)$$

By using the analogy of the rotating cylindrical shaft, Poynting suggested that circularly polarised light should carry angular momentum of $E\lambda/2\pi$ passing through a plane per unit time, per unit area when E and λ denote the energy density and wavelength of the light [6].

The term photon is nowadays well established to be an elementary particle associated with the quantum of an electromagnetic field so that a photon carries energy $\hbar\omega$ when ω is the frequency of the electromagnetic wave. Therefore, right and left circularly polarised photons must carry \hbar and $-\hbar$ angular momentum respectively. This idea was confirmed experimentally when Beth measured the torque exerted by photons on a single quarter-wave plate which was enhanced by using a mirror for double reflection [7]. This type of angular momentum is now recognised as spin angular momentum \mathbf{S} .

Polarisation cannot cover all the angular momentum that light can carry. After the invention of lasers, it was proved that light can have orbital angular momentum as well. A Laguerre-Gaussian laser mode which contains the azimuthal phase dependent term $\exp(il\phi)$ is now known to carry $\hbar l$ orbital angular momentum per photon [8], where l is an arbitrary integer, which is called the

topological charge of the beam. The identification of the orbital angular momentum is suggested by the analogy of paraxial optics and the time-dependent Schrödinger's equation [9]. The angular momentum in the propagation direction can then be represented by the operator $L_z = -i\hbar\partial/\partial\phi$, and obviously, a function with the term $\exp(il\phi)$ is an eigenfunction of the operator with the eigenvalue $l\hbar$.

This chapter is organised as follows. In the following section, section 1.2, we discuss the analogy between the forms of the local energy flux of an electromagnetic wave and the momentum density of a superfluid as it explicitly suggests the form of light that can carry orbital angular momentum. Then, we show that an optical beam in a Laguerre-Gaussian mode carries an orbital angular momentum of $\hbar l$ for each photon where l is the topological charge of the beam. We then discuss the validity of the separation between spin and optical angular momentum in section 1.3. Section 1.4 gives some examples of technologies that are currently used to generate a laser beam with orbital angular momentum. Then, we discuss ways to measure the orbital angular momentum. Lastly, we review Ref. [10], which shows that the correlation between the orbital angular momentum and the conservation of orbital angular momentum of the idler and signal photons in a spontaneous parametric down-conversion process is the result of the phase-matching condition.

1.2 Orbital angular momentum of light

Let us consider the local energy flux of a monochromatic optical scalar wave with a complex amplitude function u , in the eikonal approximation, given by the Poynting vector, which is [11]

$$\mathbf{g} \propto \text{Im}(u^*\nabla u). \quad (1.3)$$

This means that in the eikonal approximation the direction of the local energy flux is perpendicular to the local phase front. This form of the local energy flux is reminiscent of the momentum density of a superfluid [12, 13]. The orbital angular momentum density of the superfluid along the propagation direction, the z -component, in the cylindrical coordinate is in the form [14]

$$L_z(\mathbf{r}) = \hbar \text{Im} \left(\psi^*(\mathbf{r}) \frac{\partial}{\partial \phi} \psi(\mathbf{r}) \right), \quad (1.4)$$

where ψ is the superfluid wave function and ϕ is the azimuthal coordinate. It is apparent that if the wave function has the phase dependence term $\exp(il\phi)$ then it implies that each quantum of the superfluid will have an orbital angular momentum of $\hbar l$. This analogy between the form of the approximated Poynting vector and the momentum density of a superfluid leads to the idea that if the complex amplitude function u of the electromagnetic wave has the azimuthal dependence $\exp(il\phi)$ that each photon should have an orbital angular momentum of $\hbar l$ in the direction of propagation as well. Nowadays, optical fields in Laguerre-Gaussian modes with the desired azimuthal dependence can be prepared, and the motivation that photons in these spatial modes carry orbital angular momentum originates from the explained analogy.

Reconsidering Eqs.(1.2) and (1.3), we can see that transverse plane waves cannot have angular momentum in the direction of propagation because the direction of the Poynting vector is in the

direction of the wave propagation and the angular momentum density $\mathbf{r} \times (\varepsilon_0 \mathbf{E} \times \mathbf{B})$ then definitely is in the direction perpendicular to the direction of propagation. However, this is not the case for optical beams as they actually have components of their Poynting vectors perpendicular to the propagation direction. The representation of a monochromatic polarised paraxial laser beam propagating in the z -direction is conventionally obtained by the vector potential [8],

$$\mathbf{A}(\mathbf{r}, t) = u(r, \phi, z) e^{i(kz - \omega t)} \tilde{\mathbf{e}}, \quad (1.5)$$

where $\tilde{\mathbf{e}}$ represents the complex polarisation, ω is the angular frequency which relates to the wavenumber by $\omega = kc$, and $u(r, \phi, z)$ is a complex function which satisfies the paraxial wave equation and is slowly varying in the z -direction. The complex amplitude u in a normalised Laguerre-Gaussian mode is given by [8]

$$\begin{aligned} u_{l,p}(r, \phi, z) = & \sqrt{\frac{2p!}{\pi(p+|l|)!}} \frac{1}{w(z)} \left(\frac{r\sqrt{2}}{w(z)} \right)^{|l|} \\ & \times \exp \left[- \left(\frac{1}{w(z)^2} - \frac{ikz}{2(z_R^2 + z^2)} \right) r^2 \right] L_p^{|l|} \left(\frac{2r^2}{w(z)^2} \right) e^{il\phi} \\ & \times \exp(-i(2p + |l| + 1) \tan^{-1}(z/z_R)), \end{aligned} \quad (1.6)$$

where w_0 is the beamwidth at the focus point, $z_R = kw_0^2/2$ is the Rayleigh range, $w(z) = w_0 \sqrt{1 + z^2/z_R^2}$ is the beamwidth at the positions $\pm z$ from the focus point, and $L_p^{|l|}$ is an associated Laguerre polynomial. The radial index number p indicates that there are $p + 1$ nodes in the radial intensity distribution of the beam. The topological charge of the beam is given by the azimuthal index l .

By considering the form of Eq.(1.6) together with Eq.(1.3), we then can notice that the azimuthal component g_ϕ of the Poynting vector is nonzero. With the vector potential \mathbf{A} , we can determine the complex electric and magnetic fields via the Lorenz gauge:

$$\mathbf{E} = i\omega \left(\mathbf{A} + \frac{1}{k^2} \nabla(\nabla \cdot \mathbf{A}) \right), \quad (1.7a)$$

$$\mathbf{B} = \nabla \times \mathbf{A}, \quad (1.7b)$$

where the space and time dependence is omitted for brevity. In the paraxial regime, the Poynting vector of a linearly polarised beam is directly given by [8]

$$\mathbf{g} = \text{Re}(\mathbf{E}^* \times \mathbf{B}) = \omega \text{Im}(u^* \nabla u). \quad (1.8)$$

Substituting the complex functions u from Eq.(1.6), the azimuthal component of the Poynting vector is

$$g_\phi = \frac{\omega l}{kr} |u|^2. \quad (1.9)$$

We can notice that once we multiply this momentum density by the distance from the z -axis we obtain the angular momentum density in the propagation of direction, which has been set to be the z -axis. The integration over the beam then gives non-zero total angular momentum. The ratio between the angular momentum and energy of the beam then turns out to be l/ω . On the other

hand, we can include the spin angular momentum by considering the Poynting vector of a circularly polarised beam:

$$\mathbf{g} = \omega \text{Im}(u^* \nabla u) - \frac{\omega \sigma_z}{2} \frac{\partial |u|^2}{\partial r} \hat{\phi} \quad (1.10)$$

where $\sigma_z = \pm 1$ for the right-handed or left-handed circular polarisation and $\hat{\phi}$ is the unit vector in the azimuthal direction. The component of angular momentum density per unit power in the z -axis is straightforwardly obtained:

$$M_z = \frac{l}{\omega} |u|^2 - \frac{\sigma_z r}{2\omega} \frac{\partial |u|^2}{\partial r}. \quad (1.11)$$

After integration over the beam, the ratio of angular momentum in the z -direction and the energy becomes $(l + \sigma_z)/\omega$. The ratio between angular momentum and energy of the optical beams suggests that each photon in a Laguerre-Gaussian mode carries orbital angular momentum $\hbar l$ and its spin part which originates from the polarisation state [8].

1.3 Validity of the separation between orbital and spin angular momentum

We know that in the case of electrons, which are described by Dirac's equation, we can separate the angular momentum of the free electrons into two different parts, orbital and spin parts. As we found that paraxial light can carry both orbital and spin angular momentum as discussed, it seems that angular momentum of light can also be separated. Darwin proposed the separation of angular momentum of light into spin and orbital parts [15]. If the electric and magnetic fields fall off rapidly at a large distance so that they can be contained within a large finite volume and there is no field at the surface of the volume, the integration over the volume of Eq.(1.2), with the fact that $\mathbf{B} = \nabla \times \mathbf{A}$, gives

$$\mathbf{J} = \int \left(\sum_j E_j (\mathbf{r} \times \nabla) A_j + \mathbf{E} \times \mathbf{A} \right) dV, \quad (1.12)$$

where the integration by parts has been applied. It seems to be apparent from the form of the equation that the angular momentum \mathbf{J} can be separated and the orbital and spin parts are of the forms:

$$\mathbf{L} = \int \sum_j E_j (\mathbf{r} \times \nabla) A_j dV, \quad (1.13a)$$

$$\mathbf{S} = \int \mathbf{E} \times \mathbf{A} dV. \quad (1.13b)$$

However, there are some problems with the validity of the separation and we will discuss these problems in depth below.

First of all, let us consider the gauge transformation: $\mathbf{A} \rightarrow \mathbf{A}' = \mathbf{A} - \nabla \lambda$ where λ represents a complex scalar potential. Replacing the new vector potential into the forms of the previously assigned orbital and spin angular momentum in the previous equations, we obtain

$$\mathbf{L} = \int \sum_j E_j (\mathbf{r} \times \nabla) A_j dV + \int \dot{\mathbf{B}} \lambda dV, \quad (1.14a)$$

$$\mathbf{S} = \int \mathbf{E} \times \mathbf{A} dV - \int \dot{\mathbf{B}} \lambda dV. \quad (1.14b)$$

This indicates automatically that both quantities \mathbf{L} and \mathbf{S} are not gauge invariant. If we use different gauge conditions, they will give different quantities. Only the total angular momentum, $\mathbf{J} = \mathbf{L} + \mathbf{S}$, is the gauge-independent quantity. With this result and the fact that there is no rest frame for photons, the validity of the separation is questionable. As the Helmholtz decomposition states that a smooth vector field, which is twice continuously differentiable and bounded, can be decomposed into a curl-free component and a divergence-free component [16,17], our vector potential can also be decomposed in this way: $\mathbf{A} = \mathbf{A}^\perp + \mathbf{A}^\parallel$, where \mathbf{A}^\perp and \mathbf{A}^\parallel represent the divergence-free and curl-free parts respectively, such that $\nabla \cdot \mathbf{A}^\perp = \mathbf{0}$ and $\nabla \times \mathbf{A}^\parallel = \mathbf{0}$. Further, we know that the divergence-free part of the vector potential \mathbf{A}^\perp is gauge invariant [18]. Replacing the vector potential in Eqs.(1.13a) and (1.13b) with its divergenceless component, we can then obtain the new assigned orbital and spin angular momentum that are independent of the choice of gauge:

$$\mathbf{L} = \int \sum_j E_j (\mathbf{r} \times \nabla) A_j^\perp dV, \quad (1.15a)$$

$$\mathbf{S} = \int \mathbf{E} \times \mathbf{A}^\perp dV. \quad (1.15b)$$

Applying this form of orbital and spin angular momentum to the beam in the Laguerre-Gaussian modes, we obtain the orbital and spin angular momenta of $\hbar l$ and $\hbar \sigma_z$ respectively.

The gauge dependence is not the only question for the validity of the separation. The angular momentum operators of matter obey the commutation relations

$$[\hat{S}_i, \hat{S}_j] = \sum_k i\hbar \epsilon_{ijk} \hat{S}_k, \quad (1.16a)$$

$$[\hat{L}_i, \hat{L}_j] = \sum_k i\hbar \epsilon_{ijk} \hat{L}_k, \quad (1.16b)$$

$$[\hat{J}_i, \hat{J}_j] = \sum_k i\hbar \epsilon_{ijk} \hat{J}_k, \quad (1.16c)$$

where \hat{S}_i , \hat{L}_i and \hat{J}_i are the i th components of spin, orbital and total angular momentum operators respectively. After quantisation of the divergence-free part of the vector potential \mathbf{A}^\perp , van Enk and Nienhuis found that the components of the assigned spin angular momentum mutually commute [19],

$$[\hat{S}_i, \hat{S}_j] = 0. \quad (1.17)$$

This is also the case for the components of the operator $\hat{\mathbf{L}}$. This implies directly that neither the operators $\hat{\mathbf{S}}$ or $\hat{\mathbf{L}}$ can be interpreted as a true angular momentum. They also show that the operators $\hat{\mathbf{L}}$ and $\hat{\mathbf{S}}$ do not commute to each other, which is unlike the case of orbital and spin angular momentum of matter particles. The total angular momentum $\hat{\mathbf{J}}$ is the sum of $\hat{\mathbf{L}}$ and $\hat{\mathbf{S}}$. However, the components of the operator $\hat{\mathbf{J}}$ obey the commutation relation given in Eq.(1.16c). Therefore, it is only the total angular momentum that is a true angular momentum of light.

Another way to test whether $\hat{\mathbf{L}}$ and $\hat{\mathbf{S}}$ are true angular momenta is to test whether they are rotational generators. The spin angular momentum is expected to be the generator that rotates

the orientations of the fields but does not change the field amplitudes, while the orbital angular momentum rotates the amplitudes but has no effect on the field orientations. By introducing a vector $\boldsymbol{\theta}$, the direction of which is the same as the rotation axis and the magnitude of which is the angle of rotation and assumed to be very small ($|\boldsymbol{\theta}| \ll 1$), if $\hat{\mathbf{L}}$ and $\hat{\mathbf{S}}$ are rotational generators that correspond to orbital and angular momentum operators the transformation of the electric field generated by $\boldsymbol{\theta} \cdot \mathbf{L}$ and $\boldsymbol{\theta} \cdot \mathbf{S}$ are respectively expected to be [20]

$$\mathbf{E} \rightarrow \mathbf{E}' = \mathbf{E} - \boldsymbol{\theta} \cdot (\mathbf{r} \times \nabla)\mathbf{E}, \quad (1.18a)$$

$$\mathbf{E} \rightarrow \mathbf{E}' = \mathbf{E} + \boldsymbol{\theta} \times \mathbf{E}. \quad (1.18b)$$

However, it is straightforward to verify that the transformed electric fields are unphysical by showing that they are not divergence-free:

$$\nabla \cdot (\mathbf{E} - \boldsymbol{\theta} \cdot (\mathbf{r} \times \nabla)\mathbf{E}) = -\boldsymbol{\theta} \cdot \dot{\mathbf{B}}, \quad (1.19a)$$

$$\nabla \cdot (\mathbf{E} + \boldsymbol{\theta} \times \mathbf{E}) = \boldsymbol{\theta} \cdot \dot{\mathbf{B}}. \quad (1.19b)$$

In general, the scalar product $\boldsymbol{\theta} \cdot \dot{\mathbf{B}}$ is not zero, which violates the transverseness of free electromagnetic fields. In the same manner, the transformed magnetic fields violate the second Maxwell equation, $\nabla \cdot \mathbf{B}' \neq 0$. This means it is impossible to only rotate the coordinates without rotating the direction of the electromagnetic field by the same angle or vice versa. In other words, it also indicates that the true rotation generator is the operator $\hat{\mathbf{J}}$. However, this result does not mean that the assigned orbital and spin angular momenta, $\hat{\mathbf{L}}$ and $\hat{\mathbf{S}}$, in Eqs.(1.15), are unphysical as the transformed electric fields they generate are

$$\mathbf{E} \rightarrow \mathbf{E}' = \mathbf{E} - [\boldsymbol{\theta} \cdot (\mathbf{r} \times \nabla)\mathbf{E}]^\perp, \quad (1.20a)$$

$$\mathbf{E} \rightarrow \mathbf{E}' = \mathbf{E} + [\boldsymbol{\theta} \times \mathbf{E}]^\perp, \quad (1.20b)$$

which are physical and satisfy Maxwell equations.

To summarise this section, even though neither assigned orbital \mathbf{L} nor spin \mathbf{S} in Eq.(1.15) is a true angular momentum, they are measurable and meaningful as confirmed by many experiments [21–25]. For example, in optical tweezers, a trapped object is rotated about the optical axis if the focused beam having nonzero orbital angular momentum and also rotated about its own axis if the beam is circularly polarised as depicted in figure 1.1 [24, 25]. They also correspond to two different distinct symmetries for free electromagnetic fields. This indicates that they are separately conserved [14, 26].

1.4 Optical vortex generation

In this section, we will review the technologies that have been used to generate laser beams that carry orbital angular momentum. There are several approaches that have been proposed [27–35], but we will focus on the approaches that are popularly employed in experiments.

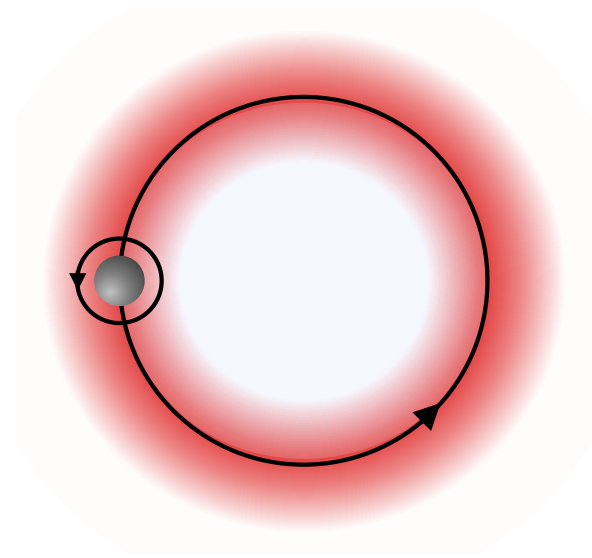


Figure 1.1: An optical tweezer uses a highly focused Laguerre-Gaussian beam to trap an object. The object is rotated about the beam axis due to transfer of orbital angular momentum (OAM), while the spin angular momentum transfer causes the rotation about its own axis.

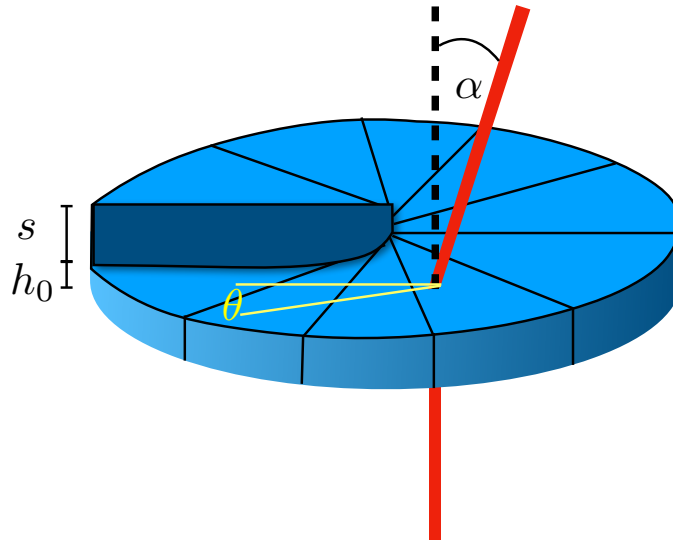


Figure 1.2: The figure shows the spiral phaseplate. At the radius r , the local slope is θ , and it deflects an incident light ray at this radius by an angle α .

1.4.1 Spiral phaseplates

A spiral phaseplate is an optical element that adds an azimuthal term $\exp(il\phi)$ to the transmitted beam of an incident Gaussian beam [27,28]. The structure of spiral phaseplates is given in figure 1.2. Its thickness depends on the azimuthal position ϕ so that their relation can be written as

$$\text{Thickness} = h_0 + \frac{s\phi}{2\pi}, \quad (1.21)$$

where the step height is given by $s = l\lambda/(n-1)$ when λ is the wavelength of the incident beam and l is the desired topological charge of the transmitted beam. With simple geometrical optics analysis, we can straightforwardly show that the phase plate can give us the transmitted photons with an orbital angular momentum of $\hbar l$ per photon as follows. Considering the ring of radius r , as depicted in the figure, the local slope of the spiral surface of the phase plate given by $\theta \approx (s\delta\phi/2\pi)/(r\delta\phi) = s/(2\pi r)$, where θ is small. We can then use Snell's law for small angles to calculate the deflected angle α of the incident ray at the distance r from the optical axis, which is

$$(\theta + \alpha) \approx n\theta, \quad (1.22)$$

where n represents the refractive index of the phaseplate. The deflected angle of the transmitted light ray at the distance r is approximately $\alpha \approx (n-1)s/2\pi r$. This result indicates that if the incident beam has a linear momentum of $p = h/\lambda$ per photon, after refraction, the linear momentum is then deflected to the azimuthal direction by $p_\phi \approx h\alpha/\lambda$. This means the orbital angular momentum of the transmitted beam per photon is

$$L = rp_\phi \approx \hbar \frac{s(n-1)}{\lambda} = l\hbar. \quad (1.23)$$

With the structure of the spiral phase plate, we can see that the optical path length of each incident ray increases with the azimuthal position. Therefore, the path difference introduces the phase difference, and the transmitted beam has the helical wavefront with the phase structure $\exp(il\phi)$.

1.4.2 Computer generated hologram

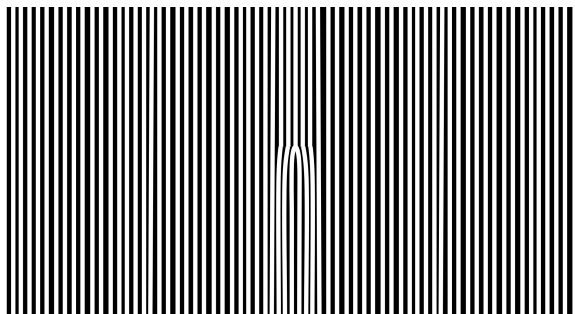


Figure 1.3: The pattern of a binary hologram for generating a light beam with $l = \pm 1$ from a Gaussian beam.

The other familiar method to produce a light beam possessing orbital angular momentum is to use a computer generated hologram. The main idea of this method is simple as demonstrated below. The hologram is the recording of the interference pattern between the field of interest and a simple reference field such as the interference pattern of a Laguerre-Gaussian beam and a plane electromagnetic wave [29]. A Laguerre-Gaussian mode, from Eqs.(1.5) and (1.6), when p index is set to be zero, traveling along the z axis, can be approximately expressed as

$$E_{0l} = E_0(r/w(z))^n \exp[-r^2/w(z)^2] e^{il\phi} e^{ikzr^2/2R} e^{i(kz+\Phi)}. \quad (1.24)$$

where $R = (z_R^2 + z^2)$ and $\Phi = (2p + |l| + 1) \tan^{-1}(z/z_R)$. Then, we suppose that the reference field is a plane wave with its wave vector lying in the xz -plane

$$E_{\text{ref}} = R_0 e^{ik_x x + ik_z z}, \quad (1.25)$$

and we let these two fields interfere on a screen in the xy -plane. The intensity profile on the screen at $z = 0$ becomes

$$\begin{aligned} I &= \left| R_0 e^{ik_x x} + E_0 (r/w_0)^n \exp[-r^2/w_0^2] e^{il\phi} \right|^2 \\ &= R_0^2 + E_0 (r/w_0)^{2n} e^{-2r^2/w_0^2} + 2R_0 E_0 (r/w_0)^n e^{-r^2/w_0^2} \cos(k_x x - l\phi). \end{aligned} \quad (1.26)$$

The last term exhibits the interference pattern on the screen. Then, a hologram that records this pattern can reconstruct the original beam and its complex conjugate when illuminated by a plane wave or a Gaussian beam. To show how this works, we simplify the pattern by neglecting the variation of the amplitudes of these fields but still keep the feature of the interference pattern. The hologram then has the spatially varying transmissivity described by

$$T = \frac{1}{2} (1 - \cos(k_x x - l\phi)). \quad (1.27)$$

If a Gaussian beam propagating along the z -axis illuminates the hologram, the transmitted field will be

$$E_T = T A_0 e^{-r^2/\Omega_0^2}, \quad (1.28)$$

where A_0 is the central amplitude of the beam and Ω_0 is the size of the spot on the screen. The transmissivity in Eq.(1.27) then gives

$$E_T = (A_0/2) e^{-r^2/\Omega_0^2} - (A_0/4) e^{-r^2/\Omega_0^2} e^{i(k_x x - l\phi)} - (A_0/4) e^{-r^2/\Omega_0^2} e^{-i(k_x x - l\phi)}. \quad (1.29)$$

This means we will obtain a field with the azimuthal phase dependent term $\exp(il\phi)$ and its complex conjugate at the first order diffraction angles $\theta = \pm \sin^{-1}(k_x/k)$, when k is the amplitude of the wave vector of the incident beam that illuminates the hologram. This indicates that the beams at the first order of diffraction possess orbital angular momentum of $\pm \hbar l$ per photon. The problem is that it is not practical to create a hologram with a sinusoidal pattern of the transmissivity. A binary hologram with square-wave variation of transmissivity, however, can still produce the transmitted beams which have the azimuthal phase dependent terms. The transmissivity function of the binary hologram can be expressed as

$$T = \frac{1}{2} - \sum_{n=1}^{\infty} \text{sinc}(n\pi/2) \cos[n(k_x x - l\phi)]. \quad (1.30)$$

The appearance of the hologram is similar to a grating with a defect in the shape of a fork as illustrated in figure 1.3. This type of binary holograms sometimes is called a fork hologram. The transmissivity function implies that the output field will contain terms of the following form

$$E_n = (A_0/4) \text{sinc}(n\pi/2) e^{-r^2/\Omega_0^2} e^{in(k_x x - l\phi)}, \quad (1.31)$$

and their complex conjugates. Each n th term corresponds to the n th-order diffracted beam which has orbital angular momentum of $n\hbar l$ per photon.

1.4.3 Mode converter

Normal laser light usually has the transverse amplitude distribution described by a product of Hermite polynomials $H_n(x)H_m(y)$, which implies that a conventional laser is normally in Hermite-Gaussian modes instead of Laguerre-Gaussian ones [8]. The mode converter scheme is used to convert a Hermite-Gaussian mode into a Laguerre-Gaussian mode by using the strong relation between these two modes. A Laguerre-Gaussian can be decomposed into a superposition of a set of Hermite-Gaussian modes of the same order as [8, 30]

$$u_{nm}^{\text{LG}}(x, y, z) = \sum_{k=0}^N i^k b(n, m, k) u_{N-k, k}^{\text{HG}}(x, y, z). \quad (1.32)$$

with

$$b(n, m, k) = \left(\frac{(N-k)!k!}{2^N n!m!} \right)^{1/2} \frac{1}{k!} \frac{d^k}{dt^k} [(1-t)^n (1+t)^m] \Big|_{t=0},$$

where the radial index p and the topological charge l of a Laguerre polynomial L_p^l is obtained by $p = \min(n, m)$ and $l = m - n$. On the other hand, a Hermite-Gaussian mode whose principal axes are rotated by $\pi/4$ with respect to the (x, y) axes can be decomposed in the same way as

$$u_{nm}^{\text{HG}} \left(\frac{x+y}{\sqrt{2}}, \frac{x-y}{\sqrt{2}}, z \right) = \sum_{k=0}^N b(n, m, k) u_{N-k, k}^{\text{HG}}(x, y, z). \quad (1.33)$$

For example, we find

$$\begin{aligned} u_{01}^{\text{LG}}(x, y, z) &= \frac{u_{10}^{\text{HG}} + i u_{01}^{\text{HG}}}{\sqrt{2}}, \\ u_{01}^{\text{HG}} \left(\frac{x+y}{\sqrt{2}}, \frac{x-y}{\sqrt{2}}, z \right) &= \frac{u_{10}^{\text{HG}} + u_{01}^{\text{HG}}}{\sqrt{2}}. \end{aligned} \quad (1.34)$$

These two decompositions have exactly the same coefficients $b(n, m, k)$ but different internal phases. To convert them from one to the other, we need to rephase the terms in the decomposition, which could be done using the fact that the Gouy phase, $\psi(z) = \tan^{-1}(z/z_R)$, of each Hermite-Gaussian mode in the decomposition changes differently when the beam is focused. This means there is a way to arrange cylindrical lenses to achieve this goal. With the calculation given in [30], two cylindrical lenses separated by $f\sqrt{2}$, where f is the focal length of the two lenses, as shown in figure 1.4, will add a relative phase difference between two components of the diagonal Hermite-Gaussian or Laguerre-Gaussian mode of $\pi/2$. Therefore, the diagonal HG mode will be converted into the LG mode when it goes through the two cylindrical lenses. As the orbital angular momentum of the beam changes, the mode converter should feel a torque acting on it when the photons pass through so that the total angular momentum of the light and the converter is conserved.

1.5 Measurement of orbital angular momentum

As mentioned, the orbital angular momentum of light is measurable, and there are several schemes to do so [36–42]. However, we will focus on two commonly employed schemes whose underlying ideas are clear and simple to understand as follows.

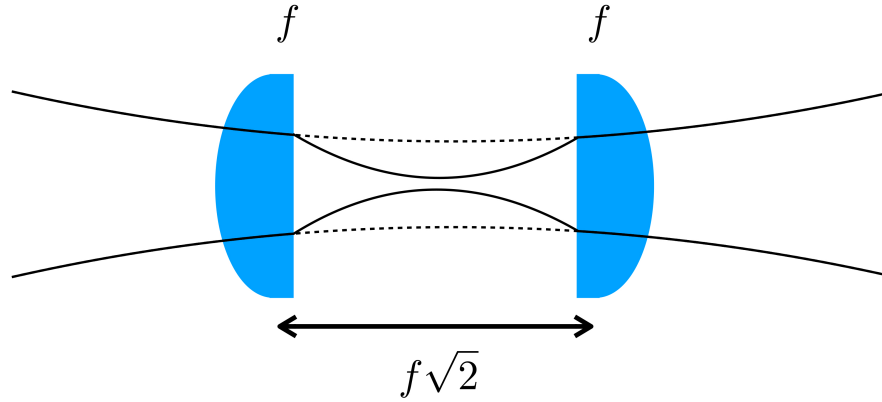


Figure 1.4: This arrangement of two cylindrical lenses can be used to convert a diagonal HG beam into an LG beam or vice versa. The dashed line represents the propagation of the beam in the other transverse direction.

1.5.1 Computer generated hologram

The generated hologram we discussed previously can be used not only to generate an optical beam with orbital angular momentum but also to measure it. The idea is simple and straightforward. Let us consider again Eq.(1.27). When we illuminate the hologram with a beam with a topological charge l' , the transmitted field will be

$$\begin{aligned}
 E_T &= \frac{1}{2}(1 - \cos(k_x x - l\phi))A_0 e^{-r^2/\Omega_0^2} e^{il'\phi} \\
 &= (A_0/2)e^{-r^2/\Omega_0^2} e^{il'\phi} - (A_0/4)e^{-r^2/\Omega_0^2} e^{i(k_x x - (l-l')\phi)} \\
 &\quad - (A_0/4)e^{-r^2/\Omega_0^2} e^{i(k_x x - (l+l')\phi)}.
 \end{aligned} \tag{1.35}$$

This means by picking up the right hologram such that $l = l'$ we will observe the fundamental Gaussian beam at the first order diffraction. We note that it is only the fundamental Gaussian mode that can be coupled with a mono mode optical fibre [36]. We can see that even though the hologram can be used to measure orbital angular momentum of individual photons it can only test whether the beam is in a particular Laguerre-Gaussian mode or not [36, 37].

Moreover, a hologram can also be used to measure a superposition of orbital angular momentum states between $l = 0$ and l an arbitrary integer. The idea actually begins from the fact that we can use a hologram to create such a state as well. Recall that in the previous discussion, we can use a hologram to generate a beam with orbital angular momentum from a Gaussian beam if we illuminate the hologram in the way that the dislocation of the hologram is at the center of the beam waist. Vaziri and colleagues found that by displacing the dislocation of the hologram from the center of the beam a superposition state is created [43]. The reverse process is also realisable and practical. The displaced hologram can also be used to measure a superposition state in that it converts the superposition state into a Gaussian beam, which can be coupled with an optical fibre and detected.

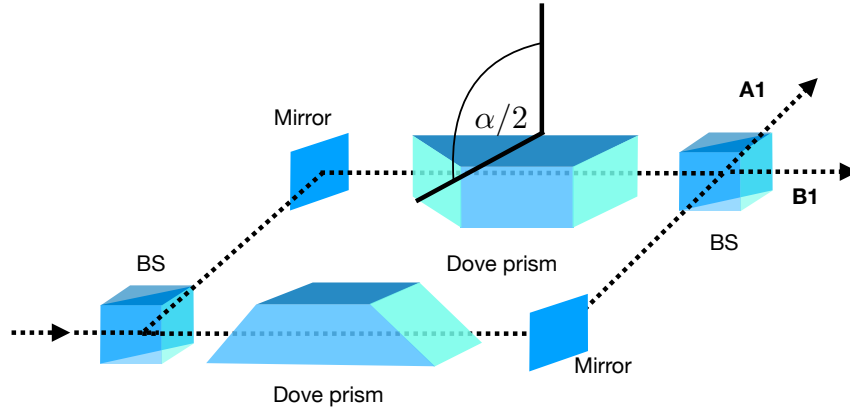


Figure 1.5: The Mach-Zehnder interferometer with a Dove prism in each arm, such that one Dove prism is rotated with respect to the other. Optical beams with odd and even topological charge are sorted to emit into different ports.

1.5.2 Interferometric mode sorter

The main idea relies on the phase shift of a Laguerre-Gaussian mode when a beam is rotated so that the beam with azimuthal term $e^{il\phi}$ will be changed to be $e^{il(\phi+\alpha)}$ when it is rotated by α [44]. While a non-rotated Dove prism gives a non-rotated, reflected image, a Dove prism rotated by an angle of $\alpha/2$ gives an α -rotated, reflected image. This means we can use rotated Dove prisms to rotate our outgoing beam. With this fact, we use a Mach-Zehnder interferometer such that there is a Dove prism in each arm of the interferometer, and one of the Dove prisms is rotated by an angle of $\alpha/2$ with respect to the other. The relative phase difference of the beams in these two arms becomes $\Delta\psi = l\alpha$. This means $\Delta\psi = l\pi$ when the Dove prism in one arm is rotated by an angle $\alpha/2 = \pi/2$ with respect to the other arm. By correctly adjusting the path length of the interferometer, the beams with odd and even values of the topological charge l go to different ports [38]. As shown in figure 1.5, if the input beam has even (odd) l it will go to the port A1 (B1). After the port A1, we add another interferometer in which the angle between the Dove prisms is $\alpha/2 = \pi/4$ so that the relative phase difference between each arm in the second stage is $\Delta\psi = l\pi/2$. Thus, the photons in with $l = 4n$ and $l = 4n + 2$, where n is an integer, go into the port A2 and B2 respectively. On the other hand, after the port B1, we introduce a hologram to increase the topological charge of the odd- l photons by 1 and add the second stage interferometer with the angle $\alpha/2 = \pi/4$ so that we can sort the odd- l photons in the same way as the even- l photons. With cascading Mach-Zehnder interferometers with different relative rotation angles of the Dove prisms, as shown in figure 1.6, we can measure the angular momentum of a given beam.

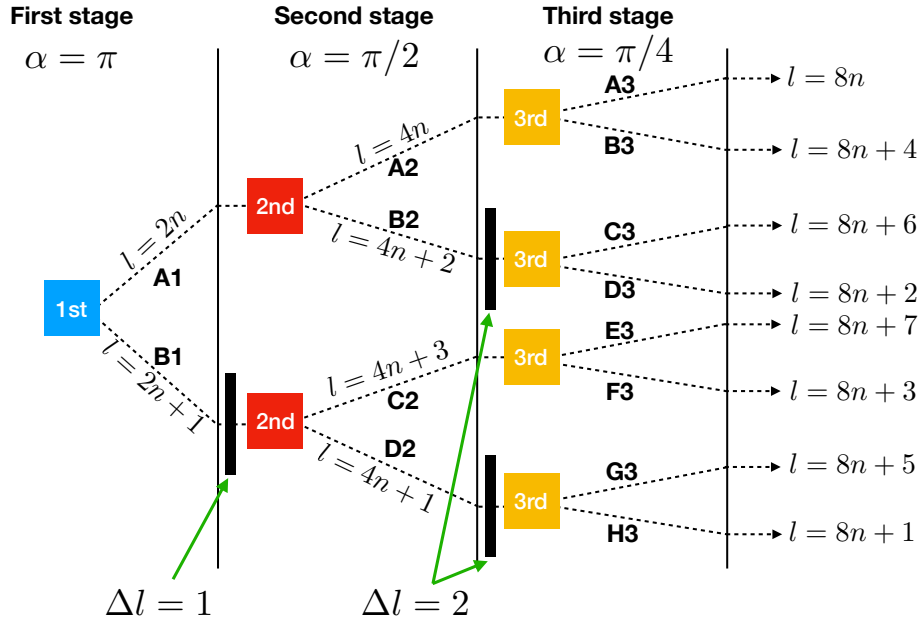


Figure 1.6: A cascade of interferometers can be used to measure the orbital angular momentum of a given beam. The boxes with different colours represent the interferometers of the form shown in figure 1.5 with different relative angles between the Dove prisms. In the first stage, we use the phase shift of $\alpha = \pi$ in order to sort the beams with even l s into port A1 and odd l s into port B1. The odd- l photons then travel through a $\Delta l = 1$ hologram, and this makes their topological charges increase by 1 to become even- l photons. In the second stage, we introduce a phase shift of $\alpha = \pi/2$, in order that it sorts even photons into even and odd multiples of 2. The $\Delta l = 2$ holograms are introduced before the third stage in order to sort the photons further. In this figure we use the solid black lines to represent generated holograms. We also show the paths that the photons with different l s take. For example, for the beam with $l = 8n$, where n is an integer, is sorted into port A3.

1.6 Orbital angular momentum and spontaneous parametric down conversion

Entanglement is one of the most important properties of quantum theory as it cannot be described classically. For example, the experimental tests of Bell's inequality prove that nature is fundamentally quantum and does not obey local realism. There are still many aspects of entanglement that we do not yet understand. It also plays an important role in several applications of quantum information and quantum imaging, such as quantum cryptography, teleportation, and ghost imaging [45–54].

Spontaneous parametric down-conversion (SPDC) is a nonlinear interaction between light and matter that converts one photon with higher energy into a pair of photons with lower energy in accordance with energy and momentum conservation. The output photons are spatially separated and are usually called the signal and idler. They are entangled in their transverse positions, time of arrival at the respective detector, and polarisation states [55–59]. There are several experiments

showing that they are also entangled in their orbital angular momentum [36, 60, 61]. We will review Ref. [10] which theoretically shows that the correlation of orbital angular momentum of a photon pair and the conservation of the orbital angular momentum in an SPDC process arise from phase matching in the nonlinear crystal.

Let $\Phi_{0,1,2}(\mathbf{x})$ be normalised transverse mode functions where \mathbf{x} is a transverse position vector. The subscripts 0, 1 and 2 indicate quantities and operators of the pump, signal and idler photons respectively. The two-photon states of the signal and idler are created by applying the creation operators $\hat{a}_1^\dagger(\mathbf{k}_1)\hat{a}_2^\dagger(\mathbf{k}_2)$ to the vacuum state $|0\rangle$. The transverse components of the wave vector of the signal, idler, and pump photons are denoted by \mathbf{k}_1 , \mathbf{k}_2 , and \mathbf{k}_0 respectively. The polarisations of the signal and idler photons are determined by the nonlinear electric susceptibility of the crystal. In the case of type I down-conversion, the polarisations of the signal and idler photons will be identical, where their direction is determined by the polarisation of the pump. For type II down-conversion, the polarisations of the two down-converted photons are perpendicular to each other. With specific setups, this can give polarisation entanglement in each pair of signal and idler photons. Assuming that the polarisation states satisfy the condition indicated by the nonlinear susceptibility of the nonlinear crystal, the phase matching between the pump and the emitted photons is described by a sinc function of the transverse wave vectors $\prod_{j=x,y} \text{sinc}[(\mathbf{k}_0 - \mathbf{k}_1 - \mathbf{k}_2)L_j/2]$, where L_j is the length of the crystal in the transverse direction of propagation. Supposing that the transverse dimension of the crystal is sufficiently large, much larger than the photon wavelengths, the phase-matching condition then can be approximated by a two-dimensional delta function $\delta^2(\mathbf{k}_0 - \mathbf{k}_1 - \mathbf{k}_2)$. Moreover, the absolute difference of the transverse wave vectors of the signal and idler photons, $|\mathbf{k}_1 - \mathbf{k}_2|$, cannot be arbitrarily large. This is because a large value of $|\mathbf{k}_1 - \mathbf{k}_2|$ results from large values of \mathbf{k}_1 and/or \mathbf{k}_2 which are proportional to the signal and idler frequencies, ω_1 and ω_2 . These two frequencies are constrained by conservation of energy $\omega_0 \simeq \omega_1 + \omega_2$. This means the constraint of the absolute difference of the transverse wave vectors is $|\mathbf{k}_1 - \mathbf{k}_2| \leq 2\pi/\lambda$, where λ is the wavelength of the pump photon. We can then define $\Delta(\mathbf{k}_1 - \mathbf{k}_2)$ as a geometric function such that it is normalised, $\int d\mathbf{k}\Delta(\mathbf{k}) = 1$, and vanishes for large values of its argument so that it is in agreement with the energy conservation.

The two-photon state of the signal and idler then can be expressed as

$$|\Psi\rangle = \int d\mathbf{k}_0 \int d\mathbf{k}_1 \int d\mathbf{k}_2 \Phi_0(\mathbf{k}_0) \hat{a}_1^\dagger(\mathbf{k}_1) \hat{a}_2^\dagger(\mathbf{k}_2) \times \Delta(\mathbf{k}_1 - \mathbf{k}_2) \delta^2(\mathbf{k}_0 - \mathbf{k}_1 - \mathbf{k}_2) |0\rangle. \quad (1.36)$$

We omit the polarisation states of the two down-converted photons in order to focus only on their transverse modes. As the polarisation states are omitted and this equation describe the phase-matching condition, this equation holds for both type I and type II down-conversions. With Fourier transformation, the two-photon state in the position representation is

$$|\Psi\rangle = \int d\mathbf{x}_1 \int d\mathbf{x}_2 \Phi_0\left(\frac{\mathbf{x}_1 + \mathbf{x}_2}{2}\right) \Delta(\mathbf{x}_1 - \mathbf{x}_2) \hat{a}_1^\dagger(\mathbf{x}_1) \hat{a}_2^\dagger(\mathbf{x}_2) |0\rangle. \quad (1.37)$$

The normalised photon states of the signal and idler, in modes Φ_1 and Φ_2 are given by

$$|\Psi_{1,2}\rangle = \int d\mathbf{x}_{1,2} \Phi_{1,2}(\mathbf{x}_{1,2}) \hat{a}_{1,2}^\dagger(\mathbf{x}_{1,2}) |0\rangle. \quad (1.38)$$

In each photon pair, the probability of detecting the signal photon in the mode Φ_1 and the idler photon in the mode Φ_2 is

$$\begin{aligned} P(\Phi_1, \Phi_2) &= |\langle \Psi_1, \Psi_2 | \Psi \rangle|^2 \\ &= \left| \int d\mathbf{x}_1 \int d\mathbf{x}_2 \Phi_1^*(\mathbf{x}_1) \Phi_2^*(\mathbf{x}_2) \Phi_0 \left(\frac{\mathbf{x}_1 + \mathbf{x}_2}{2} \right) \Delta(\mathbf{x}_1 - \mathbf{x}_2) \right|^2. \end{aligned} \quad (1.39)$$

By averaging this expression over all possible signal modes, the probability that the idler photon is in the mode Φ_2 is given by

$$\begin{aligned} P(\Phi_2) &= |\langle \Psi_2 | \Psi \rangle|^2 \\ &= \int d\mathbf{x}_1 \int d\mathbf{x}_2 \int d\mathbf{x}'_2 \Phi_2(\mathbf{x}'_2) \Phi_2^*(\mathbf{x}_2) \Phi_0^* \left(\frac{\mathbf{x}_1 + \mathbf{x}'_2}{2} \right) \\ &\quad \times \Phi_0 \left(\frac{\mathbf{x}_1 + \mathbf{x}_2}{2} \right) \Delta^*(\mathbf{x}_1 - \mathbf{x}'_2) \Delta(\mathbf{x}_1 - \mathbf{x}_2), \end{aligned} \quad (1.40)$$

A similar expression for the probability to find the signal photon in the mode Φ_1 is obtained in the same way.

The function $\Delta(\mathbf{k})$ is a very broad and it follows that the function $\Delta(\mathbf{x})$ is very narrow as it is the Fourier transform of $\Delta(\mathbf{k})$. Therefore, the mode functions in Eqs.(1.39) and (1.40) vary very little in the region that the function $\Delta(\mathbf{x})$ does not vanish. We can then approximate Eqs.(1.39) and (1.40) as

$$P(\Phi_1, \Phi_2) = \left| \int d\mathbf{y} \Delta(\mathbf{y}) \right|^2 \left| \int d\mathbf{x} \Phi_1^*(\mathbf{x}) \Phi_2^*(\mathbf{x}) \Phi_0(\mathbf{x}) \right|^2 \quad (1.41)$$

$$P(\Phi_2) = \left| \int d\mathbf{y} \Delta(\mathbf{y}) \right|^2 \int d\mathbf{x} |\Phi_2^*(\mathbf{x}) \Phi_0(\mathbf{x})|^2 \quad (1.42)$$

The state of the idler photon in the mode Φ_2 for a given pump mode Φ_0 and detected signal mode Φ_1 is

$$\begin{aligned} |\Psi_2\rangle &= \langle \Psi_1 | \Psi \rangle \\ &= \int d\mathbf{y} \Delta(\mathbf{y}) \int d\mathbf{x}_2 \Phi_1^*(\mathbf{x}_2) \Phi_0(\mathbf{x}_2) \hat{a}_2^\dagger(\mathbf{x}_2) |0\rangle, \end{aligned} \quad (1.43)$$

where we use $|\Psi\rangle$ and $|\Psi_1\rangle$ from Eqs.(1.36) and (1.37) and the fact that the function $\Delta(\mathbf{x})$ is very narrow. Comparing Eqs.(1.38) and (1.43), we find that the mode function of the idler photon can be expressed as the product of the pump mode and the signal mode:

$$\Phi_2 = \left(\int d\mathbf{y} \Delta(\mathbf{y}) \right) \Phi_0 \Phi_1^*. \quad (1.44)$$

We substitute the mode functions $\Phi_{0,1,2}$ in the form of Laguerre-Gaussian modes given in Eq.(1.6) and compare the azimuthal phase dependent terms. We find that

$$l_0 = l_1 + l_2, \quad (1.45)$$

where l_i are the topological charges of the beams. This automatically indicates the correlation of the orbital angular momentum of the signal and idler photons and ensures the conservation of angular momentum. The coincidence probability is found to be proportional to a sinc function

$$P(\Phi_1, \Phi_2) \propto \text{sinc}^2 [(l_1 + l_2 - l_0)\pi], \quad (1.46)$$

which arises from the integration of the product of the transverse Laguerre-Gaussian modes, which are substituted as $\Phi_{0,1,2}$ in Eq.(1.41), over the azimuthal phase ϕ . The probability $P(\Phi_1, \Phi_2)$ is then maximal when the orbital angular momentum is conserved and vanishes when $(l_1 + l_2 - l_0)$ is a nonzero integer. We note that there exist optical beams with fractional values of l . However, they are not structurally stable and cannot maintain their amplitude distributions while they are propagating. The relation of the orbital angular momentum of the pump, signal and idler photon, which is shown in Eq.(1.45), is solely obtained by the phase-matching condition for the Laguerre-Gaussian modes.

Chapter 2

Orbital angular momentum in quantum communication and processing

2.1 Introduction

Light has been used for communication for a long time. For example, signal lamps are visual signalling devices to produce the Morse code, and photophones (radiophones) encode the sound of the speakers with light beams and transmitted to the receivers' phone. Nowadays, we use optical fibres to transmit information from one to another distant place. In quantum information, light is used as an information carrier between quantum communication systems [49, 62]. Its polarisation state can be encoded as one bit of information. For example, horizontal and vertical polarisations traditionally represent 0 and 1 of digital information respectively. The polarisation of light does not need to be horizontal or vertical only. It can be left or right circular polarisation or a superposition of any two orthogonal polarisation states. This means a polarisation state also serves as a qubit in quantum communication. There are various alternative competing physical systems that nowadays have been used as qubits, such as superconducting Josephson junctions [63], quantum dots [64], and trapped cold ions [65], which provide many feasible quantum information applications. However, the generation, manipulation and detection of polarisation states are simple and inexpensive compared to the other physical system. A well-known quantum communication protocol that used polarised light as the information carrier is BB84 which is a quantum key distribution scheme proposed by Bennett and Brassard [62].

As discussed in the previous chapter, orbital angular momentum (OAM) of light is the component of angular momentum depending on the beam profile which is characterised by the azimuthal phase dependence $\exp(il\phi)$. This phase dependence is founded in Laguerre-Gaussian or Bessel modes of optical beams, and each of these mode families is an infinite and orthogonal basis set. Therefore, OAMs can be realised as higher-dimensional quantum systems: so-called qunits or qudits. Higher-

dimensional systems can provide some applications of quantum information that are superior to two-dimensionals such as an increase of coding density and higher security margin [66]. With higher dimensions, more information can be encoded in each system. For example, for binary systems, we need 8 bits of information to encode the standard ASCII characters, while we only use 5.048 trits to do so in trinary systems. In this chapter, we continue from the previous chapter by showing some examples of quantum information protocols that employ OAM degrees of freedom.

The structure of this chapter is given as follows. In section 2.2, we give a brief discussion on a secret key algorithm in cryptography. Then, we review three quantum information protocols in sections 2.3-2.5.

2.2 Information security and cryptography

The main purpose of cryptography is to prevent unpermitted parties to access secret information. Secure communication is very important in recent days. A leaking trade secret, for example, may lead to the collapse of a big company. In wartime, this could decide the results of battles or even the future of a kingdom. Even in our everyday life, cryptography is used to protect our money in the banks, to shop online and to protect our data in social media. While information is more important nowadays, in the modern computer age, the classical algorithm-based cryptography could be broken more easily than ever. It is probably a matter of time before we need to employ a new scheme to protect our precious information.

The simplest cipher that one might think of is the transposition, the so-called Caesarean cipher, where all letters are shifted by a known (but secret) number of places in the alphabet [49]. For example, if we decide the shift to be 1, then the letter A will be replaced by B, B→C, C→D,..., Z→A in the message. With this cipher, the word PHYSICS is then replaced by a nonsense word QIZTJET. However, it is fairly easy to decipher if the receivers know the amount and direction of the shift as they just need to shift the letters back to the original. This cipher is really weak and can be cracked by trying all 25 possible shifts until obtaining a readable and sensible message, but it is the simplest cipher that uses a private-key cryptography system, a cryptographic algorithm being used today. Its idea is as shown below. Alice wants to send a plaintext message (the secret information) \mathcal{P} to Bob. Both of them need to share a secret key \mathcal{K} which is known to Alice and Bob only. Alice then is able to use this key to generate a ciphertext \mathcal{C} and sends it to Bob, and he can use the same key to decipher the ciphertext into the original plaintext \mathcal{P} . In this way, we can think of the ciphertext \mathcal{C} as a function of the plaintext and the key,

$$\mathcal{C} = \mathcal{C}(\mathcal{P}, \mathcal{K}), \quad (2.1)$$

and the plaintext as the function of the ciphertext and the key,

$$\mathcal{P} = \mathcal{P}(\mathcal{C}, \mathcal{K}). \quad (2.2)$$

In the transposition cipher that we have reviewed the key is the number of the shift. One can improve this cipher by using a substitution cipher when a letter is randomly replaced by another letter so that the secret key is rather difficult to find out as it has $26! \approx 4 \times 10^{26}$ possible keys. However, it

A	8.2%	J	0.1%	S	6.3%
B	1.5%	K	0.8%	T	9.0%
C	2.8%	L	4.0%	U	2.8%
D	4.2%	M	2.4%	V	1.0%
E	12.7%	N	6.7%	W	2.4%
F	2.2%	O	7.5%	X	0.1%
G	2.0%	P	1.9%	Y	2.0%
H	6.1%	Q	0.1%	Z	0.1%
I	7.0%	R	6.0%		

Table 2.1: The approximate relative frequencies of the letter in English-language messages [49].

is still not sufficiently secure as each letter in the English language normally appears in a text with different frequencies and some of them often come together such as "LL", "SS". The approximate relative frequencies of English letters in the majority of messages are shown in table 2.1. This means by checking the frequency of the letters appearing in the ciphertext together with the knowledge of the English language, part of the secret message can be read.

As we are now living in the digital age, in which all the messages written in our computers or digital gadgets are represented by strings of binary digits. The message may be encoded in a string of bits by using the American Standard Code for Information Interchange, the so-called ASCII code.

Let us assume that the plaintext which Alice wants to send to Bob is encoded by the following string of binary digits:

$$\mathcal{P} = 1001110010110, \quad (2.3)$$

and the secret key that Alice and Bob possess is

$$\mathcal{K} = 1101001001110. \quad (2.4)$$

Alice can then produce the ciphertext by modulo 2 addition and performing this addition bit by bit between the given plaintext and the key as

$$\begin{aligned} \mathcal{P} &= 1001110010110, \\ \mathcal{K} &= 1101001001110, \\ \mathcal{C} &= \mathcal{P} \oplus \mathcal{K} = 0100111011000. \end{aligned} \quad (2.5)$$

She then can send this binary string to Bob. As Bob already has the secret key \mathcal{K} , he can retrieve Alice's message perfectly by performing the modulo 2 addition between the obtained ciphertext and the secret key as

$$\begin{aligned} \mathcal{C} &= 0100111011000, \\ \mathcal{K} &= 1101001001110, \\ \mathcal{P} &= \mathcal{C} \oplus \mathcal{K} = 1001110010110. \end{aligned} \quad (2.6)$$

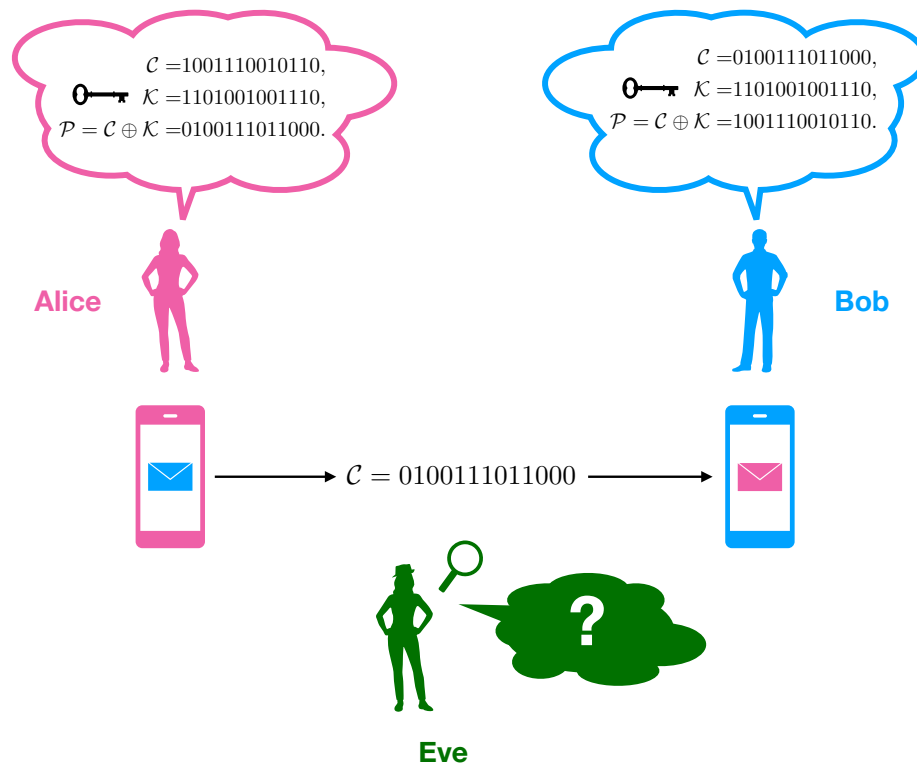


Figure 2.1: The figure shows how Alice and Bob communicate securely by sharing a secret key, which is a random binary string. In the figure, Alice sends a ciphertext to Bob with a mobile phone, and Bob retrieves the original message with the secret key. Eve, on the other hand, cannot gain any information from the sent message, if she does not have any information about the secret key.

In this way, Alice can send the message \mathcal{P} to Bob securely by sending the ciphertext via a classical communication channel as long as Eve, an eavesdropper, on the network does not have the secret key \mathcal{K} . This is because even if Eve is able to access the ciphertext \mathcal{C} , she still cannot retrieve any sensible information of the plaintext \mathcal{P} without the key. The secret key \mathcal{K} should be a random binary string in the way that the digits 0 and 1 randomly appear in the string with the probability of 0.5. In this case, the ciphertext \mathcal{C} will directly inherit the randomness of the secret key, and, therefore, contain no information about the plaintext unless the listener has the secret key \mathcal{K} . This means to send the messages securely, Alice and Bob need to be only two persons who have the key. The problem is now changed from how to send a message securely to how to send the secret key securely or how to produce the key that can only be accessed by the authorised parties and how we can employ the laws of nature to do so. In the next sections, we will review some work that employs quantum mechanics of OAMs to send or produce the secret key between two parties securely.

2.3 Quantum key distribution with 3-state systems

This protocol is an extension to BB84 for three dimensional systems proposed by Bechmann-Pasquinucci and Peres [67]. They introduced four mutually unbiased bases as follows. The first basis is a set of three orthogonal unit vectors: $|\alpha\rangle$, $|\beta\rangle$ and $|\gamma\rangle$. The second basis is a discrete Fourier transform of the first basis,

$$|\alpha_2\rangle = (|\alpha\rangle + |\beta\rangle + |\gamma\rangle)/\sqrt{3}, \quad (2.7)$$

$$|\beta_2\rangle = (|\alpha\rangle + e^{2\pi i/3}|\beta\rangle + e^{-2\pi i/3}|\gamma\rangle)/\sqrt{3}, \quad (2.8)$$

$$|\gamma_2\rangle = (|\alpha\rangle + e^{-2\pi i/3}|\beta\rangle + e^{2\pi i/3}|\gamma\rangle)/\sqrt{3} \quad (2.9)$$

Two remaining bases are of the forms

$$|\alpha_3\rangle = (e^{2\pi i/3}|\alpha\rangle + |\beta\rangle + |\gamma\rangle)/\sqrt{3}, \quad (2.10)$$

$$|\beta_3\rangle = (|\alpha\rangle + e^{2\pi i/3}|\beta\rangle + |\gamma\rangle)/\sqrt{3}, \quad (2.11)$$

$$|\gamma_3\rangle = (|\alpha\rangle + |\beta\rangle + e^{2\pi i/3}|\gamma\rangle)/\sqrt{3}, \quad (2.12)$$

and

$$|\alpha_4\rangle = (e^{-2\pi i/3}|\alpha\rangle + |\beta\rangle + |\gamma\rangle)/\sqrt{3}, \quad (2.13)$$

$$|\beta_4\rangle = (|\alpha\rangle + e^{-2\pi i/3}|\beta\rangle + |\gamma\rangle)/\sqrt{3}, \quad (2.14)$$

$$|\gamma_4\rangle = (|\alpha\rangle + |\beta\rangle + e^{-2\pi i/3}|\gamma\rangle)/\sqrt{3}. \quad (2.15)$$

This means if unit vectors $|e_j\rangle$ and $|e_\mu\rangle$ belong to different bases the modulus of their inner product satisfies $|\langle e_j | e_\mu \rangle|^2 = 1/3$.

Similar to BB84, this protocol is given as follows. Alice randomly prepares one of these 12 states and sends the quantum state to Bob. Bob then randomly picks one of the four bases to measure the state. After that, Bob announces the basis he used, but not the result he obtained. Alice then reveals whether the choice of bases that he used is correct or not. If Bob used the right basis, then they share one trit of information: the information that is encoded by ternary digits (or trits) 0, 1 and 2. They discard the transmitted result if Bob chose an incorrect basis. The process is repeated until Alice and Bob share long enough key. Then, they can sacrifice some of their shared trits to check the security of their protocol. If the error rate is lower than the security threshold they can keep the remaining key for their communication, otherwise they discard all the key and postpone the protocol.

In the intercept/resend attack, Eve intercepts Alice's particle, measures its state and resends it to Bob. The probability that she picks the correct basis and does not disturb the state of the particle is only 1/4, while she is more likely to pick the wrong basis and causes the maximal disturbance to the transmission with the probability of 3/4. This disturbance produces Bob's error rate of 2/3 (the probability that Bob chooses the correct basis but obtains wrong outcomes) in the identification stage. This means, with 3-state systems, Eve obtains less information and produces a higher error rate. Thus, it is easier for Alice and Bob to detect the existence of Eve.

The three orthogonal states, $|\alpha\rangle$, $|\beta\rangle$ and $|\gamma\rangle$ can be realised by the OAM states with different orbital angular momentum such as $l = 0$, $l = 1$ and $l = -1$.

2.4 Quantum key distribution with entangled qutrits

In this section, we review the work of Gröblacher *et al.* [68]. They use three OAM states of photons with the radial index $p = 0$ to encode qutrits. The maximally entangled state of down-converted photons is used as the entangled resource of the protocol,

$$|\Psi\rangle = \frac{1}{\sqrt{3}}(|0\rangle|0\rangle + |1\rangle|2\rangle + |2\rangle|1\rangle), \quad (2.16)$$

where $|0\rangle$, $|1\rangle$ and $|2\rangle$ represent the states of the down-converted photons in the Laguerre-Gaussian modes with $l = 0$, $l = 1$ and $l = -1$ respectively. This maximally entangled state can violate the following three-dimensional Bell inequality [69, 70],

$$\begin{aligned} S_3 = & P(A_1 = B_1) + P(A_2 = B_1 - 1) + P(A_2 = B_2) + P(A_1 = B_2) \\ & - P(A_1 = B_1 - 1) - P(A_2 = B_1) - P(A_2 = B_2 - 1) \\ & - P(A_1 = B_2 + 1) \leq 2, \end{aligned} \quad (2.17)$$

with

$$P(A_a = B_b + k) = \sum_{j=1}^3 P(A_a = j, B_b = (j + k) \pmod{3}) \quad (2.18)$$

being the probabilities that the measurement results A_a and B_b of two different observers Alice (A) and Bob (B) are different by $k \pmod{3}$. The observables A_1 and A_2 (B_1 and B_2) represent two different measurements of the observer A (B). Different measurements can be realised by displacing the centres of holograms differently to measure different superpositions of OAM states. The maximal violation for the maximally entangled state $|\Psi\rangle$ is $4/(6\sqrt{3} - 9) \approx 2.873$.

The scheme of the protocol is as follows. Alice and Bob perform their measurements randomly and independently so that A_1 , A_2 , B_1 and B_2 are the settings that maximise the violation of the given inequality whereas A_3 and B_3 are the settings used to produce the secret key from the perfect correlations. After obtaining a sufficiently long string of outcomes, Alice and Bob compare their hologram settings. A part of the obtained data is used to check the violation of the Bell inequality to examine the existence of Eve, an eavesdropper. Bob then announces his data publicly for the Bell inequality check, and A determines the value of S_3 . In the case that $S_3 > 2$, the key is secure enough as an eavesdropper does not have enough useful information, and they can use a part of the remaining data as the secret key. The experimental set up of the protocol is given in figure 2.2.

In the experiment, they used step motors to displace the individual holograms to measure superpositions of the three OAM states. Their result shows that the Bell parameter $S_3 = 2.688 \pm 0.171$, which is significantly larger than two. This implies the violation of local realism. The data of 150 trits were produced as the secret key with 14 trits as errors which correspond to the quantum trit error rate of 9.3%. This indicates the possibility to have secure communication between two distant parties. It is worthwhile to note that the state they used as the entanglement resource of the protocol is not even maximally entangled.

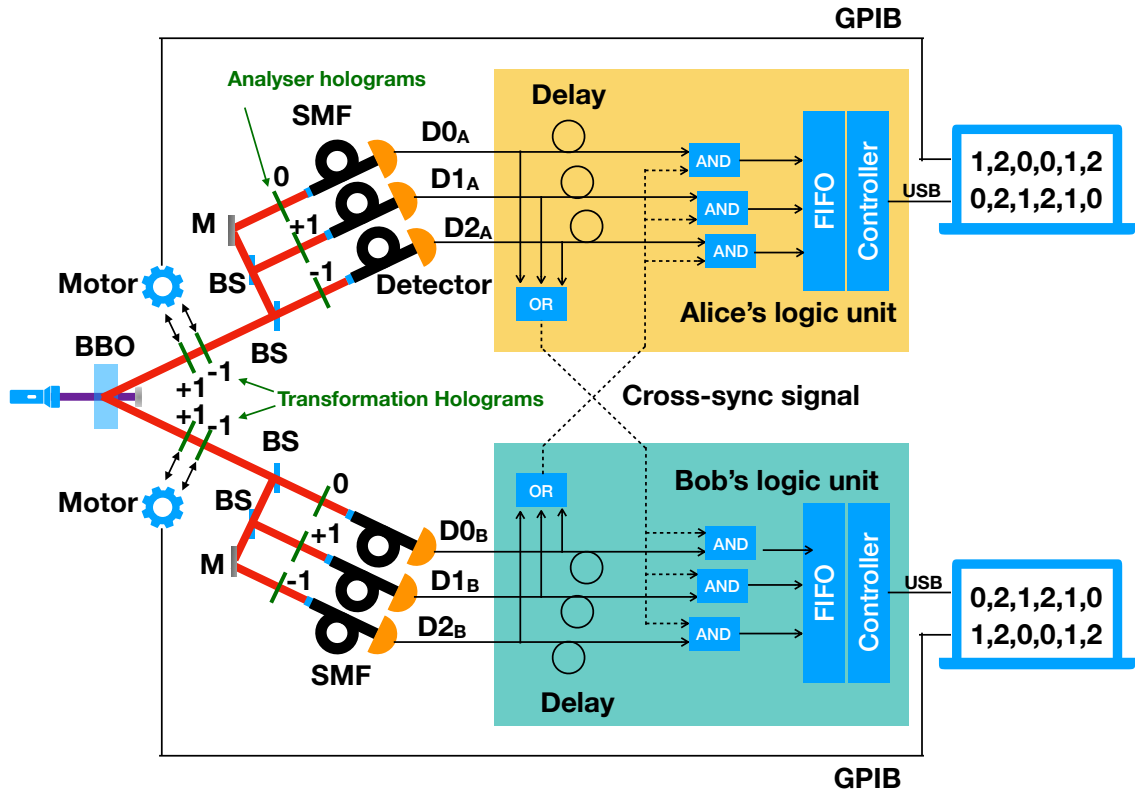


Figure 2.2: The diagram represents the experimental set up of the key-distribution protocol of Gröblacher and colleagues [68]. An Ar⁺ laser pumps a BBO crystal in order to produce down converted photons in the state given in Eq.(2.16). Two phase holograms in each down-conversion path, mounted on step motors controlled by Alice's and Bob's computers, are used to transform the maximally entangled qutrit state. After that, the photons then travel to the probabilistic mode analyser consisting of beam splitters (BSs), analyser holograms, represented by green lines, single mode fibres (SMFs) which are coupled with photon detectors (Ds). The probabilistic mode analysers can distinguish among the three different OAM states. The detection signals are processed in two logic units belonging to Bob and Alice. The cross-sync signals are used to identify the coincidences. The processed value, being either 0, 1 or 2, is passed to the logics first-in-first-out buffer (FIFO) before being read out by a computer.

2.5 Quantum Coin Tossing

The motivation for this protocol is that Alice and Bob have divorced, and they do not want to meet each other. However, they need to make a decision on who can keep the dog, but they do not trust each other and any third party to interfere. Thus, they decided to toss a coin and used telephones to communicate the result. If the result is heads then Alice can keep the dog, otherwise, it will belong to Bob. The problem is that how can Bob trust Alice's result of tossing as Alice can always say that the result is heads to win the game and he cannot even check that Alice says the truth.

The coin tossing protocol is one of the novel cryptographic challenges where the problem is not detecting or ruling out an eavesdropper but to communicate with a distant partner that cannot be trusted. The applications of this protocol, for example, are mail certification, remote contract signing, mental poker, etc. The classical version of this protocol is that Alice tosses a coin and then locks it in a suitcase and sends it to Bob. After he receives the suitcase, he can somehow prove that the coin has been tossed without seeing it and makes his bet. Alice then sends the key to Bob to unlock the suitcase and check the result. In fact, however, there is no such classical protocol that is secure against unrestricted cheating schemes if one of them is dishonest [71].

However, with the help of quantum mechanics in a three-dimensional Hilbert space, this type of protocol is possible and has some security. Even though the following protocol is still not perfectly secure, it limits the possibility that the cheater can win the game for certain without any risk of being detected.

In the quantum coin tossing scheme [71,72], the classical suitcase is replaced by a three-dimensional state. For Alice and Bob, the result of coin tossing is replaced by the random choice of one of two orthogonal bases where each element of one basis is nonorthogonal to any state from the other. Alice randomly selects a state from these two bases and send it to Bob. Once Bob receives the state, he then makes his bet. At this stage, Bob can cheat by measuring the state. However, the measurement result cannot tell him which state he possesses for sure. Once Alice announces her result and Bob has not cheated, he can then check Alice's honesty by measuring the state. Alice can lie, but there is a reliable possibility that her cheat can be detected. This protocol has been proposed by Ambainis [72] and implemented by Molina-Terriza *et al* [71]. Two sets of the four states that Alice can only randomly pick up and send to Bob are given in table 2.2. Each set represents a different coin tossing result. A state vector in one set is nonorthogonal to a state vector in the other set. This provides the security against Bob's dishonesty as, even he performs a measurement on the state he obtains, his outcome cannot help him to decide which set that the state belongs to. On the other hand, each of Bob's bases comprises of three orthogonal states. The additional states in these bases are required so that Bob can be able to detect Alice's dishonesty with a reliable amount of probability.

The realisation of this protocol is given as follows. Alice produces a three-dimensional maximally entangled state by a parametric down conversion process as given in Eq.(2.16). With different encoding, the state is given by

$$|\Psi\rangle = \frac{1}{\sqrt{3}}(|0\rangle_A|0\rangle_B + |1\rangle_A|1\rangle_B + |2\rangle_A|2\rangle_B), \quad (2.19)$$

where, in this case, the states $|1\rangle_A$ and $|1\rangle_B$ represent the Laguerre-Gaussian beams with $l = 1$ and $l = -1$ respectively. On the other hand, the states $|2\rangle_A$ and $|2\rangle_B$ are the Laguerre-Gaussians with $l = -1$ and $l = 1$. The subscripts A and B identify the states of two entangled photons: the former is kept by Alice and the latter is sent to Bob. Alice then makes a projection measurement on her photon state. With the entanglement of the photon pair, she non-locally projects Bob's state into a particular state. She contacts Bob with a classical communication channel so that he can make a bet. Alice then announces which state is the result of her measurement. Bob can measure his state to verify her honesty. The coincidence measurement of the electronic signals from Alice and Bob is required to check that they are working on the same pair of photons.

Set	Label	Alice's states	Coin	Bob's bases	Label
1	A11	$(0\rangle + 1\rangle)/\sqrt{2}$	Heads	$(0\rangle + 1\rangle)/\sqrt{2}$	B11
	A12	$(0\rangle - 1\rangle)/\sqrt{2}$		$(0\rangle - 1\rangle)/\sqrt{2}$	B12
			Heads	$ 2\rangle$	B13
2	A21	$(0\rangle + 2\rangle)/\sqrt{2}$	Tails	$(0\rangle + 2\rangle)/\sqrt{2}$	B21
	A22	$(0\rangle - 2\rangle)/\sqrt{2}$		$(0\rangle - 2\rangle)/\sqrt{2}$	B22
			Tails	$ 1\rangle$	B23

Table 2.2: The table shows Alice's four possible states, and one of them is randomly chosen and sent to Bob. These states are divided into two different sets, called 1 and 2. Each set represents a different coin tossing result. Bob's two bases of measurement for checking Alice honesty are shown.

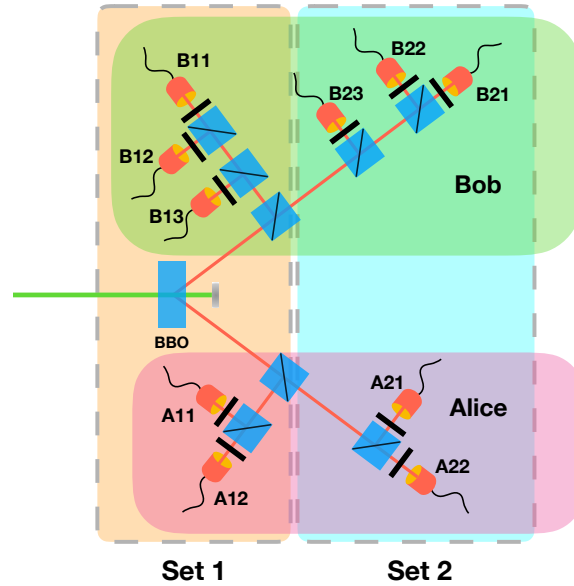


Figure 2.3: The experimental realisation of the coin tossing protocol given in [71]. In front of all detectors, there are displaced holograms that are used to measure the OAM states of the down-converted photons in the bases given in table 2.2.

The experimental set up of this protocol is shown in figure 2.3. The experiment reports that Bob wins in half of the throws. The failures are only around 6% of the throws due to misalignments. With this 6% noise, the protocol is proved to be more secure than qubit protocols, even if they are noiseless [71, 73], where the level of security is quantified by the trace distance D and the fidelity F

between the density matrices of the heads and tails states: $D + F^2$.

If Alice just lies, for example, she knows that the state $(|0\rangle + |2\rangle)/\sqrt{2}$ is sent and Bob bet on tail, which is correct answer, but she still insists that it is head with the state $(|0\rangle + |1\rangle)/\sqrt{2}$, then the probability that Bob can detect Alice's lie is 75%. The possible way that Alice can cheat with a higher probability of not being detected is as follows. She prepares a classical mixture between the states $(|0\rangle - |1\rangle)/\sqrt{2}$ and $(|0\rangle + |2\rangle)/\sqrt{2}$ which represent the classical mixture of head and tail and sends it to Bob. Once Bob makes his bet, she can always say that it is the opposite. For example, if Bob says it is head, she may say that the answer is tail $(|0\rangle + |2\rangle)/\sqrt{2}$. Bob then checks in the tail basis. The probability that her dishonesty is not be detected is 62.5%. However, it is really difficult for her to win without being detected in a row. As we can see, the protocol is not perfectly secure, but it limits the ability of the two involved parties to cheat.

Chapter 3

The χ states

3.1 Introduction

As we know, entanglement is one of the fundamental features that distinguish between classical and quantum theories. It is also the main resource of various quantum computation and quantum information processing tasks including quantum dense coding, quantum cryptography and quantum teleportation [45–52]. The bipartite entanglement is the obvious example used to demonstrate the nonclassical effects and simple quantum information protocols as it is simple and well understood. However, for multipartite entanglement, there are many aspects that are still unclear as there is no trivial way to extend our understanding of the bipartite case to this case directly [74–77]. It is still one of the active areas of research in the field. Even though we do not understand it well yet, there is a lot of research proposing quantum information protocols that employ the entanglement properties of such states, such as universal error correction [78], quantum secret sharing [79], telecloning [80], and deterministic secure quantum communication [81].

Assume that there are two N -qubit states $|\psi\rangle$ and $|\phi\rangle$ shared among N parties, and each party can only access one qubit. A local protocol can be defined as a series of rounds of local operations and communication such that, in each round, an involved party can locally manipulate its local subsystem and classically communicate the result of its operation, if the operation includes a measurement, to the rest of the parties. The decision about the operations in the subsequent rounds depends on the previous announced results. This means the protocol splits into several branches. We then say the states $|\psi\rangle$ and $|\phi\rangle$ are equivalent under stochastic local operations and classical communication (SLOCC) if and only if there exists a local protocol that least one of its branches can convert one of these states into another [82]. Any two entangled states are different classes, if they cannot be converted from one to the other via SLOCC protocols or we can say that they are SLOCC inequivalent.

There are two classes of well-known genuine multipartite entangled states: the Greenberger-Horne-Zeilinger (GHZ) state

$$|\text{GHZ}\rangle_N = \frac{1}{\sqrt{2}} (|0\rangle^{\otimes N} + |1\rangle^{\otimes N}), \quad (3.1)$$

and the Werner (W) state

$$|W\rangle_N = \frac{1}{\sqrt{N}} \sum_{i=1}^N |0\rangle^{\otimes(i-1)} |1\rangle |0\rangle^{\otimes(N-i)}, \quad (3.2)$$

where we use the short hand of the tensor product, for example $|0\rangle^{\otimes 3} = |000\rangle = |0\rangle \otimes |0\rangle \otimes |0\rangle$ [49]. In the case of four-qubit states, these two states can be written explicitly as

$$|\text{GHZ}\rangle = \frac{1}{\sqrt{2}} (|0000\rangle + |1111\rangle)_{abcd}, \quad (3.3)$$

and

$$|W\rangle = \frac{1}{2} (|0001\rangle + |0010\rangle + |0100\rangle + |1000\rangle)_{abcd}. \quad (3.4)$$

As the GHZ and W states are SLOCC inequivalent [77, 82], it means they undoubtedly have different entanglement properties. For example, the Bell-type inequality is maximally violated if the system is in the GHZ state [83, 84]. A. Karlsson and M. Bourennane proposed the open-destination-teleportation protocol by using the GHZ state as the entanglement resource [85]. On the other hand, the entanglement of the W state is robust against a particle loss as its reduced state is not separable and this property is not valid for the GHZ state [86].

A new type of four-qubit entangled states has been introduced by Yeo and Chua in 2006 [87]. It is called χ -type states which have the following forms:

$$|\chi^{00}\rangle = \frac{1}{\sqrt{2}} (|\zeta^0\rangle + |\zeta^1\rangle)_{abcd}, \quad (3.5)$$

$$|\chi^{ij}\rangle = \sigma^i \otimes \sigma^j \otimes I \otimes I |\chi^{00}\rangle, \quad (3.6)$$

where

$$|\zeta^0\rangle \equiv \frac{1}{2} (|0000\rangle - |0011\rangle - |0101\rangle + |0110\rangle), \quad (3.7)$$

$$|\zeta^1\rangle \equiv \frac{1}{2} (|1001\rangle + |1010\rangle + |1100\rangle + |1111\rangle). \quad (3.8)$$

We use σ^j to represent the Pauli matrices such that $\sigma^1 = \sigma^x$, $\sigma^2 = \sigma^y$, and $\sigma^3 = \sigma^z$. The two-dimensional identity operator is denoted by $I = \sigma^0$. These states cannot be transformed into the GHZ and W states or the other classes of four-qubit genuine entangled states via SLOCC. However, to the best of our knowledge, these states have been first introduced publicly in 2002 by Lee *et al.* [88], but at that time they did not report that these states are a new type of genuine entangled states. In the work of Lee *et al.*, they show that these states can be obtained by a nonlocal transformation of the tensor product of the EPR states: $|\Phi^+\rangle_{a'b'} \otimes |\Phi^+\rangle_{c'd'}$, where $|\Phi^+\rangle = (|00\rangle + |11\rangle)/\sqrt{2}$, and can be used as a teleportation channel. The properties of this type of states and its application will be discussed in the following sections.

We summarise this introduction as follows. The χ -type states are proved to be a new class of four-qubit genuine entangled states. Their entanglement properties are distinct from that of the GHZ and W states as discussed in the following section.

The structure of this chapter is as follows. We discuss the entanglement properties of the χ -type states compared to that of the GHZ and W states in section 3.2. We evaluate the von Neumann

mutual information between two pairs of particles in the states and then demonstrate the violation of Bell inequalities. The entanglement robustness against a particle loss is discussed at the end of section 3.2. In section 3.3, we give some examples of quantum information protocols that employ the χ -type states: faithful quantum teleportation of two-qubit states, quantum dense coding, quantum-information splitting, and deterministic secure quantum communication.

3.2 Entanglement properties of χ states

This section is devoted to discussions about the entanglement properties of the χ states when comparing this class of states with the other well-known four-qubit genuine entangled states. Some properties that have been briefly discussed in the introduction are shown explicitly in this section.

3.2.1 How much entanglement do the χ -type states have?

As mentioned, the entanglement measure of multipartite states is not trivial as the knowledge that we have for the case of bipartite entanglement cannot be applied directly to the multipartite case. One of the standard ways to measure the entanglement of a multipartite system is to bisect the particles in the state into two subsystems and using the entanglement measure to quantify the entanglement between these two subsystems [75, 89]. In the case of a four-qubit system, there are three different ways to equally bisect the involved particles. We use the von Neumann mutual information to quantify the entanglement between each pair of particles with von Neumann entropy [49]:

$$I(X : Y) = E_A + E_B - E_{AB}, \quad (3.9)$$

where E_A , E_B and E_{AB} are the entropy of the subsystems A and B and the total entropy of the system, and the von Neumann entropy is of the form

$$E = -\text{Tr}(\rho \log_2 \rho). \quad (3.10)$$

For example, the two-qubit reduced states of the four-qubit GHZ state, given in Eq.(3.3), are

$$\rho_{xy} = \frac{1}{2}(|00\rangle\langle 00| + |11\rangle\langle 11|), \quad (3.11)$$

where the subscripts x and y represent all possible pairs of particles in the state. As the state is pure, the last term in Eq.(3.9) does not contribute. Therefore, the mutual information of each pair in the GHZ state is given by

$$I(ab : cd) = I(ac : bd) = I(ad : bc) = E_{ab} + E_{cd} = \log_2 2 + \log_2 2 = 2. \quad (3.12)$$

In the case of the W state, the two-qubit reduced states are of the form

$$\rho_{xy} = \frac{1}{4}(|10\rangle + |01\rangle)(\langle 10| + \langle 01|) + \frac{1}{2}|00\rangle\langle 00|. \quad (3.13)$$

This form of the density matrices is diagonal in the following orthonormal basis:

$$\mathcal{D}_W \in \left\{ |00\rangle, (|10\rangle + |01\rangle)/\sqrt{2}, (|10\rangle - |01\rangle)/\sqrt{2}, |11\rangle \right\}. \quad (3.14)$$

The two nonzero diagonal elements of the density matrices in this basis are equal with the value of $1/2$. The mutual information of each pair in the W state is then exactly the same as the case of the GHZ state as

$$I(\text{ab} : \text{cd}) = I(\text{ac} : \text{bd}) = I(\text{ad} : \text{bc}) = E_{\text{ab}} + E_{\text{cd}} = \log_2 2 + \log_2 2 = 2. \quad (3.15)$$

In the case of the χ -type states, the reduced states of the state $|\chi^{00}\rangle$ are

$$\rho_{\text{ab}} = \rho_{\text{cd}} = \rho_{\text{ac}} = \rho_{\text{bd}} = \frac{1}{4}I, \quad (3.16)$$

and

$$\rho_{\text{ad}} = \frac{1}{2}|\Phi^+\rangle\langle\Phi^+| + \frac{1}{2}|\Psi^-\rangle\langle\Psi^-|, \quad (3.17)$$

$$\rho_{\text{bc}} = \frac{1}{2}|\Phi^+\rangle\langle\Phi^+| + \frac{1}{2}|\Psi^+\rangle\langle\Psi^+|, \quad (3.18)$$

where $|\Phi^+\rangle = (|00\rangle + |11\rangle)/\sqrt{2}$, $|\Psi^+\rangle = (|01\rangle + |10\rangle)/\sqrt{2}$ and $|\Psi^-\rangle = (|01\rangle - |10\rangle)/\sqrt{2}$ are the states in the Bell's basis. The entanglement of each pair of the particles in this state then given by

$$I(\text{ab} : \text{cd}) = I(\text{ac} : \text{bd}) = E_{\text{ab}} + E_{\text{cd}} = \log_2 4 + \log_2 4 = 4, \quad (3.19)$$

and

$$I(\text{ad} : \text{bc}) = E_{\text{ad}} + E_{\text{bc}} = \log_2 2 + \log_2 2 = 2. \quad (3.20)$$

The mutual information of each pair in the other states of the χ -type states is the same as the result given above as the von Neumann entropy is invariant under local unitary transformation. Unlike the case of the W and GHZ states, we can notice from the forms of the χ -type states given in Eqs.(3.5), (3.6), (3.7), (3.8) that there is no entanglement between any one particle in the state and any other. The information obtained by measuring the state of a particle in these χ states cannot be used to refer to the state of another particle. With the result of entanglement measure given above, this means the entanglement of this class of genuine entangled states purely originates from the entanglement between pairs of particles in the states so that the pairs (a,b) and (c,d), and (a,c) and (b,d) are maximally entangled while there is some entanglement between the pairs (a,d) and (b,c) as shown in the above equations.

With the mutual information given above, we can see that the value of the summation of the mutual information over all possible pairs in the case of the χ -type states is higher than that of the GHZ and W states. This then raises the further questions of whether there is any state in which all possible pairs are maximally entangled, and in the case that the answer is no, then what is the state that can give the highest value of the summation of mutual information. The answer to the first question is given in the work of Higuchi and Sudbery where they give a proof that there is no such state in theorem 1 of their paper [75]. The paper shows that it is impossible to express any four-qubit state in terms of rank four Schmidt decomposition for all possible pairs by using the method of proof by contradiction. The answer to the second problem is still unclear, even though it has been suggested that the states of the forms [75, 90]

$$|M_4\rangle = \frac{1}{\sqrt{6}} (|0011\rangle + |1100\rangle + \omega(|1010\rangle + |0101\rangle) + \omega^2(|1001\rangle + |0110\rangle)), \quad (3.21)$$

where $\omega = e^{2\pi i/3}$, or the complex conjugate of this forms, $|\overline{M}_4\rangle$, give the *local* maximal entropy, but to the best of my knowledge, there is still no mathematical proof that this state can give the *global* maximal entropy. The reduced states of the state $|M_4\rangle$ are given as

$$\rho_{ab} = \rho_{ac} = \rho_{ad} = \frac{1}{6} (|00\rangle\langle 00| + |11\rangle\langle 11| + |\Psi^+\rangle\langle \Psi^+|) + \frac{1}{2} |\Psi^-\rangle\langle \Psi^-|. \quad (3.22)$$

The entanglement entropies then are

$$E_{ab} = E_{ac} = E_{ad} = 1 + \frac{1}{2} \log_2 3. \quad (3.23)$$

We note that in Eqs.(3.22) and (3.23) we do not show the reduced states and the entropy of the pairs (c,d), (b,d) and (b,c) because complementary pairs have equal entropy: $E_{ab} = E_{cd}$, $E_{ac} = E_{bd}$ and $E_{ad} = E_{bc}$. The value of the summation of the mutual information of this state is higher than the one obtained from the χ -type states. Like in the case of the χ states, we notice that the entanglement of this class of states also originates from the entanglement between pairs of particles in the states, and there is no entanglement between any particle and any others. However, because there is no pair of particles in these states that is maximally entangled with the other, we found that it is difficult to find a quantum information protocol that uses the entanglement of these states.

3.2.2 Nonlocality of the χ states

This subsection is devoted to giving a brief review of the nonlocality properties of the χ -type states. First, we begin with the entanglement filters which Yeo and Chua used to identify that the χ -type states are SLOCC independent to the GHZ and W states. Osterloh and Siewert have introduced the third-, fourth-, and sixth-order four-qubit filters, which are denoted by $\mathcal{F}_1^{(4)}$, $\mathcal{F}_2^{(4)}$, and $\mathcal{F}_3^{(4)}$ respectively, to study the classes of entangled states [91]. In the case of the χ -type states, these filters give the following expectation values [92]:

$$\langle \chi | \mathcal{F}_1^{(4)} | \chi \rangle \equiv \sum_{\alpha, \beta, \gamma=0}^3 \delta_{\alpha_1 \beta_1} \delta_{\alpha_2 \gamma_1} \delta_{\beta_2 \gamma_2} E_{\alpha_1 \alpha_2} E_{\beta_2}^{\beta_1} E^{\gamma_1 \gamma_2} = 0, \quad (3.24)$$

$$\langle \chi | \mathcal{F}_2^{(4)} | \chi \rangle \equiv \sum_{\alpha, \beta, \lambda, \epsilon=0}^3 \delta_{\alpha_1 \beta_1} \delta_{\alpha_2 \lambda_1} \delta_{\beta_2 \epsilon_1} \delta_{\lambda_2 \epsilon_2} E_{\alpha_1 \alpha_2} E_{\beta_2}^{\beta_1} E_{\lambda_2}^{\lambda_1} E^{\epsilon_1 \epsilon_2} = 1, \quad (3.25)$$

$$\langle \chi | \mathcal{F}_3^{(4)} | \chi \rangle \equiv \frac{1}{2} \sum_{\alpha, \beta, \gamma=0}^3 E^{\alpha_1 \alpha_2} E_{\alpha_1 \alpha_2} E^{\beta_1 \beta_2} E_{\beta_1 \beta_2} E^{\gamma_1 \gamma_2} E_{\gamma_1 \gamma_2} = 1, \quad (3.26)$$

with

$$E^{\alpha_1 \alpha_2} \equiv \langle \chi | \sigma^{\alpha_1} \otimes \sigma^{\alpha_2} \otimes \sigma^2 \otimes \sigma^2 | \chi \rangle, \quad (3.27)$$

$$E^{\beta_1 \beta_2} \equiv \langle \chi | \sigma^{\beta_1} \otimes \sigma^2 \otimes \sigma^{\beta_2} \otimes \sigma^2 | \chi \rangle, \quad (3.28)$$

$$E^{\gamma_1 \gamma_2} \equiv \langle \chi | \sigma^2 \otimes \sigma^{\gamma_1} \otimes \sigma^{\gamma_2} \otimes \sigma^2 | \chi \rangle, \quad (3.29)$$

$$E^{\lambda_1 \lambda_2} \equiv \langle \chi | \sigma^2 \otimes \sigma^{\lambda_1} \otimes \sigma^2 \otimes \sigma^{\lambda_2} | \chi \rangle, \quad (3.30)$$

$$E^{\epsilon_1 \epsilon_2} \equiv \langle \chi | \sigma^2 \otimes \sigma^2 \otimes \sigma^{\epsilon_1} \otimes \sigma^{\epsilon_2} | \chi \rangle. \quad (3.31)$$

The tensor components satisfy the index lowering with the matrix tensor $g_{\mu\nu} = \text{diag}\{-1, 1, 0, 1\}$ as

$$E_{\kappa\lambda} = g_{\kappa\mu}g_{\lambda\nu}E^{\mu\nu}, \quad (3.32)$$

where the Einstein summation convention is used such that the indices that appear twice represent the summation over four components of the involved tensors. The expectation values of these filters for the GHZ states are $\mathcal{F}_1^{(4)} = 1$, $\mathcal{F}_2^{(4)} = 1$ and $\mathcal{F}_3^{(4)} = 1/2$, and, for the case of the W state, these expectation values are identically zero [92]. A state with a finite expectation value for one of the above filters cannot be transformed into a state with zero expectation value for the same filter by SLOCC transformations [92]. This identifies that the χ -type states are SLOCC inequivalent to the GHZ and W states and become a new type of genuine entangled states as mentioned.

Next, Mermin, Ardehali, Belinskii, and Klyshko have reported the first Bell inequality for four-qubit states [83, 93, 94]. We then call this inequality the MABK inequality. We consider four observers, Alice (A), Bob (B), Charles (C) and Diana (D). Each of them possesses one qubit. In the MABK inequality, every observer can choose between two dichotomic observables. The outcomes of the four observers are denoted by X_i ($X=A, B, C, D$) where the subscripts $i = 1, 2$ indicate the observables that the observers choose. The correlation of the outcomes of the four observers can be represented by the product of the outcomes: $A_i B_j C_k D_l$ where $i, j, k, l = 1, 2$. The expectation value of the product is given as

$$Q(A_i B_j C_k D_l) = \langle A_i B_j C_k D_l \rangle. \quad (3.33)$$

In local realism, the MABK inequality is [83, 92–94]

$$\begin{aligned} Q_{1111} - Q_{1112} - Q_{1121} - Q_{1211} - Q_{2111} - Q_{1122} - Q_{1212} - Q_{2112} - Q_{1221} - Q_{2121} \\ - Q_{2211} + Q_{2222} + Q_{2221} + Q_{2212} + Q_{2122} + Q_{1222} \leq 4, \end{aligned} \quad (3.34)$$

where we use Q_{ijkl} as the short forms of $Q(A_i B_j C_k D_l)$. We suppose that the two possible observables are the measurement of the spin of qubit X in the \hat{n}_1^X or \hat{n}_2^X directions. For the χ -type states the correlation functions then are given by

$$Q(A_i B_j C_k D_l) = \langle \chi | \hat{n}_i^A \cdot \boldsymbol{\sigma} \otimes \hat{n}_j^B \cdot \boldsymbol{\sigma} \otimes \hat{n}_k^C \cdot \boldsymbol{\sigma} \otimes \hat{n}_l^D \cdot \boldsymbol{\sigma} | \chi \rangle, \quad (3.35)$$

where $\boldsymbol{\sigma} = \sigma^x \hat{x} + \sigma^y \hat{y} + \sigma^z \hat{z}$ and σ^i are the Pauli matrices. With the experimental settings that $\hat{n}_1^A = \hat{x}$, $\hat{n}_2^A = \hat{z}$; $\hat{n}_1^B = \hat{y}$, $\hat{n}_2^B = \hat{z}$; $\hat{n}_1^C = \hat{y}$, $\hat{n}_2^C = \hat{z}$; and $\hat{n}_1^D = (\hat{z} - \hat{x})/\sqrt{2}$, $\hat{n}_2^D = (\hat{z} + \hat{x})/\sqrt{2}$, the value of the left-hand side of Eq.(3.34) is $4\sqrt{2}$. This means the χ -type states violate the MABK inequality. However, it is still not the optimal violation for the inequality.

C. Wu and *et al.* introduced a new Bell inequality as follows [92]. Instead of the four observers freely picking one of the two possible dichotomic observables, Alice is allowed to measure the spin of her qubit only in a single direction \hat{n}_1^A . The other observers can still freely pick one of the two dichotomic observables as in the previous case. We then find that

$$Q(A_1 B_1 C_1 D_1) + Q(B_1 C_2 D_2) + Q(B_2 C_1 D_2) - Q(A_1 B_2 C_2 D_1) \leq 2. \quad (3.36)$$

We call this new Bell inequality the WYKO inequality to honour the people who introduced it. With the following measurement settings,

$$\begin{aligned}\hat{n}_1^A &= \hat{x} \\ \hat{n}_1^B &= \hat{z}, \hat{n}_2^B = \hat{y}, \\ \hat{n}_1^C &= \hat{z}, \hat{n}_2^C = \hat{y}, \\ \hat{n}_1^D &= \hat{x}, \hat{n}_2^D = \hat{y},\end{aligned}\tag{3.37}$$

the left-hand side of the WYKO inequality in Eq.(3.36) is 4. The correlation functions $Q(A_1 B_j C_k D_l)$ and $Q(B_j C_k D_l)$ can be either +1 or -1. Therefore, the maximum possible value of the inequality is 4. This inequality is optimally violated by the χ -type states. On the other hand, the inequality is not violated by the GHZ state as

$$Q^{\text{GHZ}}(B_j C_k D_l) = \langle \text{GHZ} | I^A \otimes \hat{n}_j^B \cdot \boldsymbol{\sigma} \otimes \hat{n}_k^C \cdot \boldsymbol{\sigma} \otimes \hat{n}_l^D \cdot \boldsymbol{\sigma} | \text{GHZ} \rangle = 0,\tag{3.38}$$

and $Q^{\text{GHZ}}(A_1 B_j C_k D_l)$ can only be ± 1 which makes the left-hand side of the inequality never greater than 2.

3.2.3 Robustness of mutual information against a particle loss

Let us compare the robustness of mutual information against a particle loss of the GHZ, W and the χ -type states. Let us start with the GHZ state. Four particles a, b, c and d are entangled and their state is described by the four-qubit GHZ state. The reduced three-qubit state of the state is

$$\sigma_{\text{GHZ}} = \frac{1}{2}(|000\rangle\langle 000| + |111\rangle\langle 111|)_{\text{bcd}}.\tag{3.39}$$

The von Nuemann entropy of this reduced state is $S(\sigma_{\text{GHZ}}) = \log_2 2 = 1$. Notice that the reduced state is now in the form of a convex combination of two three-qubit separable states. The reduced state then becomes separable. We can study the correlation between a particle and the other two particles in this state by determining the mutual information. It is straightforward that the state of a particle in this reduced state is maximally mixed: $\rho_b = (|0\rangle\langle 0| + |1\rangle\langle 1|)_b/2$ while the state of the other two is $\rho_{\text{cd}} = (|00\rangle\langle 00| + |11\rangle\langle 11|)_{\text{cd}}/2$. The mutual information between a particle and the other two is given as

$$I(b : \text{cd}) = S(\rho_b) + S(\rho_{\text{cd}}) - S(\sigma_{\text{GHZ}}) = \log_2 2 + \log_2 2 - \log_2 2 = 1.\tag{3.40}$$

Note that we begin by assuming that particle *a* is lost and study the entanglement of its reduced state. However, as the GHZ state is invariant under qubit permutations, the mutual informations for any other case of a particle loss for the GHZ state are identical to $I(b : \text{cd})$, or in other words $I(i : jk) = 1$ where $i, j, k \in \{a, b, c, d\}$. Similarly, the W state is also invariant under qubit permutations. This means the same holds for the case of W state as well: the mutual informations for all one-particle-loss cases are identical. The reduced state of the W state is given by

$$\sigma_{\text{W}} = \frac{3}{4}|\text{W}_3\rangle\langle \text{W}_3|_{\text{bcd}} + \frac{1}{4}|000\rangle\langle 000|_{\text{bcd}},\tag{3.41}$$

where $|W_3\rangle = (|001\rangle + |010\rangle + |100\rangle)/\sqrt{3}$ is the three-qubit W state. As the states $|W_3\rangle$ and $|000\rangle$ are orthonormal to each other, these two vectors together with additional two mutual orthogonal vectors can form a basis and in this basis the reduced W state is diagonal. This means the entropy of the reduced state is

$$S(\sigma_W) = -\frac{3}{4} \log_2 \frac{3}{4} - \frac{1}{4} \log_2 \frac{1}{4} = 0.811. \quad (3.42)$$

The entropy is lower than the case of the GHZ state. Notice that unlike the case of the GHZ state the reduced state of the W state is not a separable state. The state of particle b is given by

$$\rho_b = \frac{3}{4}|0\rangle\langle 0| + \frac{1}{4}|1\rangle\langle 1|, \quad (3.43)$$

which is not a maximally mixed state. The state of the other two particles is

$$\rho_{cd} = \frac{1}{2} \left(\frac{|01\rangle + |10\rangle}{\sqrt{2}} \right) \left(\frac{\langle 01| + \langle 10|}{\sqrt{2}} \right) + \frac{1}{2}|00\rangle\langle 00|. \quad (3.44)$$

The mutual information between particle b and the other two particles in the reduced state straightforwardly is

$$I(b : cd) = S(\rho_b) + S(\rho_{cd}) - S(\sigma_W) = 0.811 + 1 - 0.811 = 1. \quad (3.45)$$

For the case of the χ states, it is slightly different. As the states of this type are not invariant under qubit permutations, the three-qubit reduced state after particle a is lost is not the same as the reduced states for any other particle is lost instead. However, by studying this case we can still see some physics underly it. The reduced state of the $|\chi^{00}\rangle$ state is

$$\sigma_{\chi^{00}} = \frac{1}{2}|\eta_0\rangle\langle \eta_0|_{bcd} + \frac{1}{2}|\eta_1\rangle\langle \eta_1|_{bcd}, \quad (3.46)$$

where $|\eta_0\rangle = (|000\rangle - |011\rangle - |101\rangle + |110\rangle)/2$ and $|\eta_1\rangle = (|001\rangle + |010\rangle + |100\rangle + |111\rangle)/2$. As the states $|\eta_0\rangle$ and $|\eta_1\rangle$ are orthonormal to each other, these two state vectors are eigenvectors of the reduced state. The entropy of the reduced state in this case is then the same as the case of the GHZ state as

$$S(\sigma_{\chi^{00}}) = 1. \quad (3.47)$$

However, the reduced state of the χ -type states is not separable, even though the origin of the entanglement of these states comes from the entanglement between pair of particles rather than the entanglement between a particle and any other particle in the states. In this case, the state of particle b, ρ_b , and the state of the other two particles, c and d, are maximally mixed:

$$\rho_b = \frac{1}{2}|0\rangle\langle 0| + \frac{1}{2}|1\rangle\langle 1|, \quad (3.48)$$

$$\rho_{cd} = \frac{1}{4}|\Phi^+\rangle\langle \Phi^+| + \frac{1}{4}|\Psi^+\rangle\langle \Psi^+| + \frac{1}{4}|\Phi^-\rangle\langle \Phi^-| + \frac{1}{4}|\Psi^-\rangle\langle \Psi^-|. \quad (3.49)$$

The entanglement between particle b and the other two particles is given by the mutual information:

$$I(b : cd) = S(\rho_b) + S(\rho_{cd}) - S(\sigma_{\chi^{00}}) = 1 + 2 - 1 = 2. \quad (3.50)$$

The other cases of mutual information between one particle and the other two particles are given as

$$I(c : bd) = 2, \quad (3.51)$$

$$I(d : bc) = 1. \quad (3.52)$$

This means even though one particle in the state is lost, one particle in the reduced state is still entangled with the remaining pair of particles. Notice that the mutual information $I(d : bc)$ is lower than the other two. This is because pairs (a,d) and (b,c) are the only particle pairs that are not maximally entangled, and the entanglement between pairs of particles passes to the entanglement between one particle and the remaining pair in the scenario of a particle loss.

3.3 Examples of quantum information protocols

In this section, we review several quantum information protocols that use the χ -type states as the entanglement resource. We start with the faithful teleportation and quantum dense coding protocol given by Yeo and Chua that makes this group of states known as a new type of genuine entangled states [87]. Then, a number of other distinct protocols are discussed to demonstrate how we can employ the entanglement of these states.

3.3.1 Faithful quantum teleportation of two-qubit states

The χ -type states have been noticed to be a set of genuine entangled states that can give faithful teleportation of an arbitrary two qubits [87]. Let us first review the principles of quantum teleportation. The main idea of quantum teleportation is that we use an entangled state as a quantum channel together with a classical communication channel to teleport an arbitrary quantum state from one place to another distant place [52]. The well-known example of quantum teleportation is given as follows. We suppose that two parties, Alice and Bob, share a pair of particles that are maximally entangled, in one of the EPR states: $|\Psi_{\text{EPR}}^0\rangle_{AB}$. Alice also possesses a particle in an unknown state, $|\phi\rangle_a$, and she wants to send this state to Bob. At the moment, the state of these three particles is given as

$$|\phi\rangle_a \langle\phi| \otimes |\Psi_{\text{EPR}}^0\rangle_{AB} \langle\Psi_{\text{EPR}}^0|. \quad (3.53)$$

Then, Alice can send the quantum part of the information about her $|\phi\rangle_a$ state with the quantum channel by performing the von Neumann measurement in the well-known Bell basis (or EPR basis),

$$|\Psi_{\text{EPR}}^i\rangle_{aA} = (\sigma_a^i \otimes \sigma_A^0) |\Psi_{\text{EPR}}^0\rangle_{aA}, \quad (3.54)$$

where σ^i are Pauli matrices and σ^0 is the identity as previously denoted, on both of her particles, a and A . Notice that this equation shows that other maximally entangled EPR states can be obtained by performing two dimensional local Pauli rotations on an EPR state. The state of Bob's particle

after Alice performing her measurement is given by

$$\begin{aligned}
\frac{1}{p_i} \text{Tr}_{aA} [(|\phi\rangle_a \langle\phi| \otimes |\Psi_{\text{EPR}}^0\rangle_{AB} \langle\Psi_{\text{EPR}}^0|) (|\Psi_{\text{EPR}}^i\rangle_{aA} \langle\Psi_{\text{EPR}}^i| \otimes I_B)] \\
&= \frac{1}{p_i} {}_{aA} \langle\Psi_{\text{EPR}}^0| (\sigma_a^i |\phi\rangle_a \otimes |\Psi_{AB}^0\rangle) ({}_a \langle\phi| \sigma_a^i \otimes {}_{AB} \langle\Psi_{\text{EPR}}^0|) |\Psi_{\text{EPR}}^0\rangle_{aA} \\
&= \frac{1}{4p_i} \sigma_B^i |\phi\rangle_B \langle\phi| \sigma_B^i,
\end{aligned} \tag{3.55}$$

where the factor $p_i = \text{Tr}[(|\phi\rangle_a \langle\phi| \otimes |\Psi_{\text{EPR}}^0\rangle_{AB} \langle\Psi_{\text{EPR}}^0|) (|\Psi_{\text{EPR}}^i\rangle_{aA} \langle\Psi_{\text{EPR}}^i| \otimes I_B)] = 1/4$, is the normalisation factor of the post-measurement state. Notice that, in the second line of the equation, there is the following term which, after expanding it, we can recognise as the so-called *transfer operator*:

$$\begin{aligned}
{}_{aA} \langle\Psi_{\text{EPR}}^0| \Psi_{\text{EPR}}^0\rangle_{AB} &= \frac{1}{2} \sum_{i,j=0}^1 ({}_a \langle i| \otimes {}_A \langle i|) (|j\rangle_A \otimes |j\rangle_B) \\
&= \frac{1}{2} \sum_{i=0}^1 |i\rangle_B \otimes {}_a \langle i|.
\end{aligned} \tag{3.56}$$

As a result, this operator transfers an arbitrary state in vector space a to vector space B and that is the reason why the last line of Eq.(3.55) is obtained. Notice that the result of Eq.(3.55) is already in the form of the state $|\phi\rangle$, so after he obtains the two bits of information about Alice's measurement result Bob can operate the specific Pauli rotation on his particle to obtain the $|\phi\rangle_B$ state.

Now, we move to the teleportation of an arbitrary two-qubit state: $|\psi\rangle_{a_1 a_2} = \sum_{i,j=0}^1 a_{ij} |ij\rangle_{a_1 a_2}$. In 2005, Rigolin showed that the tensor product of two EPR states can be used as the quantum channel for teleportation of such a state [95]. Similar to the previous example of quantum transportation, he defined the basis of 16 G states: $|G^{ij}\rangle_{A_1 B_1 A_2 B_2} = [(\sigma_{A_1}^i \otimes \sigma_{B_1}^0) \otimes (\sigma_{A_2}^j \otimes \sigma_{B_2}^0)] |G^{00}\rangle_{A_1 B_1 A_2 B_2}$, where

$$|G^{00}\rangle_{A_1 B_1 A_2 B_2} = |\Psi_{\text{EPR}}^0\rangle_{A_1 B_1} \otimes |\Psi_{\text{EPR}}^0\rangle_{A_2 B_2}, \tag{3.57}$$

as the basis for Alice's measurement. Therefore, we can see that the transfer operator in this case is

$$\begin{aligned}
{}_{a_1 A_1 a_2 A_2} \langle G^{00} | G^{00} \rangle_{A_1 B_1 A_2 B_2} &= \sum_{i,j,k,l=0}^1 [({}_{a_1} \langle i| \otimes {}_{A_1} \langle i|) \otimes ({}_{a_2} \langle j| \otimes {}_{A_2} \langle j|)] \\
&\quad \times [(|k\rangle_{A_1} \otimes |k\rangle_{B_1}) \otimes (|l\rangle_{A_2} \otimes |l\rangle_{B_2})] \\
&= \sum_{i,j=0}^1 |ij\rangle_{B_1 B_2} \otimes {}_{a_1 a_2} \langle ij|,
\end{aligned} \tag{3.58}$$

which is the operator that transfers a two arbitrary qubit state in $a_1 \otimes a_2$ space to $B_1 \otimes B_2$. This means by analogy with the teleportation of a qubit state the state $|G^{00}\rangle$ can be used as the quantum channel for teleporting an arbitrary two-qubit state.

In the case of the χ -type states, we can easily verify that these states can be used as a quantum channel to teleport an arbitrary two-qubit state by examining whether these states can form the transfer operators. As the forms of the states in the χ basis given in Eqs.(3.5), (3.6), (3.7) and (3.8), the protocol that we use to teleport a two-qubit state is as follows. Alice and Bob share a χ -type entangled state. For simplicity, we suppose that they share the $|\chi^{00}\rangle_{A_1 A_2 B_1 B_2}$ state. Alice can send a state $|\psi\rangle_{a_1 a_2} = \sum_{i,j=0}^1 a_{ij} |ij\rangle_{a_1 a_2}$ to Bob by performing a measurement on her qubits in the χ basis.

Then, she sends four bits of information corresponding to her measurement result to Bob so that Bob can retrieve Alice's state by performing a local unitary transformation. We note that the state $|\chi^{00}\rangle_{A_1 A_2 B_1 B_2}$ can be rewritten in the following form:

$$\begin{aligned}
|\chi^{00}\rangle_{A_1 A_2 B_1 B_2} &= \frac{1}{2} \left(|00\rangle \left(\frac{|00\rangle - |11\rangle}{\sqrt{2}} \right) + |01\rangle \left(\frac{|10\rangle - |01\rangle}{\sqrt{2}} \right) + |10\rangle \left(\frac{|10\rangle + |01\rangle}{\sqrt{2}} \right) \right. \\
&\quad \left. + |11\rangle \left(\frac{|00\rangle + |11\rangle}{\sqrt{2}} \right) \right)_{A_1 A_2 B_1 B_2} \\
&= \frac{1}{2} (|00\rangle_{A_1 A_2} |\Phi^-\rangle_{B_1 B_2} - |01\rangle_{A_1 A_2} |\Psi^-\rangle_{B_1 B_2} + |10\rangle_{A_1 A_2} |\Psi^+\rangle_{B_1 B_2} \\
&\quad + |11\rangle_{A_1 A_2} |\Phi^+\rangle_{B_1 B_2}) \\
&= \frac{1}{2} (|00\rangle_{A_1 A_2} |J_0\rangle_{B_1 B_2} + |01\rangle_{A_1 A_2} |J_1\rangle_{B_1 B_2} + |10\rangle_{A_1 A_2} |J_2\rangle_{B_1 B_2} \\
&\quad + |11\rangle_{A_1 A_2} |J_3\rangle_{B_1 B_2}), \tag{3.59}
\end{aligned}$$

where we define

$$|J_0\rangle \equiv |\Phi^-\rangle, \tag{3.60}$$

$$|J_1\rangle \equiv -|\Psi^-\rangle, \tag{3.61}$$

$$|J_2\rangle \equiv |\Psi^+\rangle, \tag{3.62}$$

$$|J_3\rangle \equiv |\Phi^+\rangle. \tag{3.63}$$

This set of Bell states forms an orthogonal basis for two dimensional Hilbert space. We can also rewrite the state in another form as

$$\begin{aligned}
|\chi^{00}\rangle &= \frac{1}{2} \left(\left(\frac{|00\rangle + |11\rangle}{\sqrt{2}} \right) |00\rangle - \left(\frac{|00\rangle - |11\rangle}{\sqrt{2}} \right) |11\rangle + \left(\frac{|10\rangle - |01\rangle}{\sqrt{2}} \right) |01\rangle \right. \\
&\quad \left. + \left(\frac{|10\rangle + |01\rangle}{\sqrt{2}} \right) |10\rangle \right) \\
&= \frac{1}{2} (|\Phi^+\rangle|00\rangle - |\Psi^-\rangle|01\rangle + |\Psi^+\rangle|10\rangle - |\Phi^-\rangle|11\rangle) \\
&= \frac{1}{2} (|J'_0\rangle|00\rangle + |J'_1\rangle|01\rangle + |J'_2\rangle|10\rangle + |J'_3\rangle|11\rangle), \tag{3.64}
\end{aligned}$$

where

$$|J'_0\rangle \equiv |\Phi^+\rangle, \tag{3.65}$$

$$|J'_1\rangle \equiv -|\Psi^-\rangle, \tag{3.66}$$

$$|J'_2\rangle \equiv |\Psi^+\rangle, \tag{3.67}$$

$$|J'_3\rangle \equiv -|\Phi^-\rangle. \tag{3.68}$$

This set of states is also an orthogonal basis for two dimensional Hilbert space. By using two forms of the state $|\chi^{00}\rangle$ given above, the transfer operator for this case is then given as

$${}_{a_1 a_2 A_1 A_2} \langle \chi^{00} | \chi^{00} \rangle_{A_1 A_2 B_1 B_2} = \frac{1}{4} \sum_{i=0}^3 |J_i\rangle_{B_1 B_2} \otimes {}_{a_1 a_2} \langle J'_i|. \tag{3.69}$$

Two bits of information	Alice's transformation	Bob's obtained state
00	$I_A \otimes I_B \Psi^-\rangle_{AB} = \Psi^-\rangle_{AB}$	$ \Psi^-\rangle_{AB}$
01	$\sigma_A^x \otimes I_B \Psi^-\rangle_{AB} = - \Phi^-\rangle_{AB}$	$- \Phi^-\rangle_{AB}$
10	$\sigma_A^y \otimes I_B \Psi^-\rangle_{AB} = i \Phi^+\rangle_{AB}$	$i \Phi^+\rangle_{AB}$
11	$\sigma_A^z \otimes I_B \Psi^-\rangle_{AB} = \Psi^+\rangle_{AB}$	$ \Psi^+\rangle_{AB}$

Table 3.1: The table shows the encoding scheme for Alice and Bob. The first column shows the two-bit string of information that Alice wants to send to Bob. The middle column shows the local unitary operators that Alice uses to perform her encoding. The last column gives the possible states that Bob will possess after receiving Alice's qubit. By performing a measurement in the Bell basis he then perceives the information that Alice intends to send.

This means this type of entangled states can be used as a quantum channel for faithful teleportation of an arbitrary two-qubit state. However, only the pairs that are maximally entangled that can be used as a faithful teleportation channel. In the case of (a, d) and (b, c) pairs in the Eqs.(3.5) and (3.6) which are not maximally entangled, we can still form an orthonormal basis for an eight-dimensional subspace as,

$$\{(I_a \otimes I_b \otimes I_c \otimes \sigma_d^i) |\chi^{00}\rangle_{abcd}, (\sigma_a^3 \otimes I_b \otimes I_c \otimes \sigma_d^i) |\chi^{00}\rangle_{abcd}\}. \quad (3.70)$$

Using the non-maximally entangled pairs as the quantum channel with the same protocol given above, the transfer operator is in the form of

$${}_{a_1 a_2 A_1 B_2} \langle \chi^{00} | \chi^{00} \rangle_{A_1 A_2 B_1 B_2} = \frac{1}{4} (|J_3\rangle_{A_2 B_1} \otimes_{a_1 a_2} (\langle J'_0| + \langle J'_3|) + |J_2\rangle_{A_2 B_1} \otimes_{a_1 a_2} (-\langle J'_1| + \langle J'_2|)). \quad (3.71)$$

This means by using the non-maximally entangled pairs, we can see that the protocol cannot be used to teleport an arbitrary two-qubit state but can still faithfully teleport some forms of states, for example, the state that is in the following form: $|\phi\rangle = \alpha_1 |\Phi^+\rangle + \alpha_2 |\Psi^+\rangle$, where α_1 and α_2 are arbitrary complex numbers that satisfy the normalisation condition $|\alpha_1|^2 + |\alpha_2|^2 = 1$.

3.3.2 Quantum dense coding

The χ -type states can also be used as the entanglement resource for the quantum dense coding protocol as mentioned in [87]. Before demonstrating this fact explicitly, we will first review the basics of the protocol with the well-known and simplest example. The idea of quantum dense coding was first mentioned by Bennett and Wiesner [50]. The scenario is that Alice and Bob share an entangled state, and for this simple example case, we suppose that the state is $|\Psi^-\rangle_{AB}$. Alice and Bob want to communicate two bits of information securely, so they make an agreement about their encoding scheme as shown in table 3.1. Alice then applies a local unitary transformation to her qubit that corresponding to the information she wants to send. Then, she sends her qubit to Bob. In order that Bob can receive the message from Alice, he needs to perform the Bell measurement

on both qubits. The result of his measurement reflects the unitary transformation that Alice has applied to her qubit and he then can know the message.

Suppose Eve, an eavesdropper, attacks this protocol by intercepting the particle that Alice is sending to Bob. She can perform the measurement on the stolen qubit and gain one bit of information. However, she also destroys the entanglement between the intercepted qubit and Bob's qubit. This means that, before performing the protocol, Alice and Bob can verify the existence of Eve by running some irrelevant messages and checking whether Bob obtains the correct information. After that, they can perform the usual protocol. We can notice easily that from the above protocol, we can also send four bits of information by using two Bell states as well. In the case that there are two message receivers, Bob (B_1) and Blair (B_2), Alice can also use two Bell states to send her two-bit message to each of them independently. There is no requirement that Bob and Blair need to cooperate to read the message.

If she wants Bob and Blair to read the message together, she needs to use a new entanglement resource, and the χ -type states can help her to do so as follows. Suppose that Alice, Bob and Blair share the state $|\chi^{00}\rangle_{A_1A_2B_1B_2}$. Alice possesses two particles which are denoted by A_1 and A_2 , while Bob and Blair have particles B_1 and B_2 respectively. With Eq.(3.6), Alice can transform the state $|\chi^{00}\rangle_{A_1A_2B_1B_2}$ to be one of the other χ -type states by performing a local unitary transformation on her particles. With all possible local transformations given in Eq.(3.6), she can encode her four-bit message to the shared state. Then, she sends each of her particles to Bob and Blair respectively. Bob and Blair can read the message by performing a measurement in the χ basis. Bob or Blair alone cannot read the message without help from the other. This means by using this type of states as the resource, Alice can make sure that Bob and Blair can only read her message when they read the message together.

3.3.3 Quantum-information splitting

This is another example of quantum information protocols demonstrating the utility of the entanglement of the χ -type states. The protocol has been proposed by X-W Wang *et al.* [96]. The situation is that Alice (A) wants to send her unknown qubit $|\xi\rangle_a$ to a group of people including Bob (B), Charles (C) and Diana (D) so that one of them can retrieve the secret state with help from the other two, or at least one of them. Alice then can use the χ -type state to perform the following protocol. We suppose that Alice, Bob, Charles, and Diana share four entangled particles in the state $|\chi^{00}\rangle_{ABCD}$. The state can be rewritten as

$$|\chi^{00}\rangle_{ABCD} = \frac{1}{\sqrt{2}} (|0\rangle_A |\varphi^0\rangle_{BCD} + |1\rangle_A |\varphi^1\rangle_{BCD}), \quad (3.72)$$

with

$$|\varphi^0\rangle_{BCD} = \frac{1}{2} (|000\rangle - |011\rangle - |101\rangle + |110\rangle)_{BCD}, \quad (3.73)$$

$$|\varphi^1\rangle_{BCD} = \frac{1}{2} (|001\rangle + |010\rangle + |100\rangle + |111\rangle)_{BCD}. \quad (3.74)$$

We suppose that Alice's unknown qubit is of the form

$$|\xi\rangle_a = \frac{1}{\sqrt{1+|\lambda|^2}} (|0\rangle + \lambda|1\rangle)_a, \quad (3.75)$$

where λ is an arbitrary complex number. The total state of all particle, including the one that Alice wants to send, is

$$\begin{aligned} |\xi\rangle_a |\chi^{00}\rangle_{ABCD} &= \frac{1}{\sqrt{2(1+|\lambda|^2)}} (|00\rangle_{aA} |\varphi^0\rangle_{BCD} + |01\rangle_{aA} |\varphi^1\rangle_{BCD}) \\ &+ \frac{\lambda}{\sqrt{2(1+|\lambda|^2)}} (|10\rangle_{aA} |\varphi^0\rangle_{BCD} + |11\rangle_{aA} |\varphi^1\rangle_{BCD}). \end{aligned} \quad (3.76)$$

Alice then performs a joint measurement on her two particles a and A in the Bell basis $\{|\Phi^\pm\rangle, |\Psi^\pm\rangle\}$. Each of Alice's four possible outcomes causes the state of particles held by Bob, Charles, and Diana to collapse as follows,

$$|\Phi^\pm\rangle = \frac{1}{\sqrt{2}} (|00\rangle \pm |11\rangle)_{aA} \rightarrow |\phi^\pm\rangle_{BCD} = \frac{1}{\sqrt{1+|\lambda|^2}} (|\varphi^0\rangle \pm \lambda|\varphi^1\rangle)_{BCD}, \quad (3.77)$$

$$|\Psi^\pm\rangle = \frac{1}{\sqrt{2}} (|01\rangle \pm |10\rangle)_{aA} \rightarrow |\psi^\pm\rangle_{BCD} = \frac{1}{\sqrt{1+|\lambda|^2}} (|\varphi^1\rangle \pm \lambda|\varphi^0\rangle)_{BCD}. \quad (3.78)$$

As the no-cloning theorem states that it is impossible to clone an unknown state, this means only one of the receivers can have the secret state, not all of them, and in order to do so, they need to cooperate with each other. The single-particle states of particles held by Bob, Charles, and Diana after Alice's measurement are

$$\rho_{B(C)} = \frac{1}{2} (|0\rangle\langle 0| + |1\rangle\langle 1|)_{B(C)}, \quad (3.79)$$

$$\rho_D^\pm = \frac{1}{2} (|0\rangle\langle 0| + |1\rangle\langle 1|)_D \pm i \frac{\text{Im}(\lambda)}{(1+|\lambda|^2)} (|1\rangle\langle 0| - |0\rangle\langle 1|)_D. \quad (3.80)$$

Diana's particle state will be either ρ_D^+ , when Alice's measurement outcome is $|\Phi^+\rangle$ or $|\Psi^+\rangle$, or ρ_D^- , when the outcome is $|\Phi^-\rangle$ or $|\Psi^-\rangle$. We can see that with the form of the single-particle states Bob and Charles have been sealed perfectly from the secret qubit if they do not cooperate with the others. However, Diana has the potential to gain some information on the secret state, but she cannot retrieve the state perfectly without help from Bob or Charles. This means Alice has distributed her quantum secret asymmetrically. We can show that Diana can retrieve the state perfectly with help from one of the others. Bob and Charles, on the other hand, need to cooperate with both of the other two in order to retrieve the state.

We first consider the case that the three partners agree to let Diana possess the secret state. The shared entangled state of these three after Alice's measurement can be written as

$$|\phi^\pm\rangle_{BCD} = \frac{1}{\sqrt{2(1+|\lambda|^2)}} [|++\rangle_{BC} (|-\rangle \pm \lambda|+\rangle)_D + |--\rangle_{BC} (|+\rangle \mp \lambda|-\rangle)_D], \quad (3.81)$$

$$|\psi^\pm\rangle_{BCD} = \frac{1}{\sqrt{2(1+|\lambda|^2)}} [|++\rangle_{BC} (|+\rangle \pm \lambda|-\rangle)_D - |--\rangle_{BC} (|-\rangle \mp \lambda|+\rangle)_D], \quad (3.82)$$

where $|\pm\rangle = (|0\rangle \pm |1\rangle)/\sqrt{2}$. The above equations show explicitly the following. If Bob and Charles measure their qubits in the basis $\{|+\rangle, |-\rangle\}$, then their measurement results are perfectly correlated and only one of Bob's or Charles's result, together with the outcome of Alice's measurement, is enough for Diana to retrieve the secret state. For example, if Alice's result is announced to be $|\Phi^+\rangle$ and Bob's (Charles's) outcome is $|+\rangle$ and being told to Diana, Diana then know that her state is

$$|\xi'\rangle_D = \frac{1}{\sqrt{(1+|\lambda|^2)}} (|-\rangle + \lambda|+\rangle). \quad (3.83)$$

The secret state can be retrieved if she performs the unitary operation $\sigma^x \hat{H}$ on her qubit, where \hat{H} is the Hadamard transformation. On the other hand, if Bob wants to retrieve the secret state he needs the assistance from both Charles and Diana. The shared entangled state of the three partners after Alice's measurement can also be written as

$$|\phi^\pm\rangle_{BCD} = \frac{1}{2\sqrt{1+|\lambda|^2}} [(|0\rangle \pm \lambda|1\rangle)_B |00\rangle_{CD} - (|1\rangle \mp \lambda|0\rangle)_B |01\rangle_{CD} + (|1\rangle \pm \lambda|0\rangle)_B |10\rangle_{CD} - (|0\rangle \mp \lambda|1\rangle)_B |11\rangle_{CD}], \quad (3.84)$$

$$|\psi^\pm\rangle_{BCD} = \frac{1}{2\sqrt{1+|\lambda|^2}} [(|1\rangle \pm \lambda|0\rangle)_B |00\rangle_{CD} + (|0\rangle \mp \lambda|1\rangle)_B |01\rangle_{CD} + (|0\rangle \pm \lambda|1\rangle)_B |10\rangle_{CD} + (|1\rangle \mp \lambda|0\rangle)_B |11\rangle_{CD}]. \quad (3.85)$$

This means, if Charles and Diana measure their states in the logical basis $\{|0\rangle, |1\rangle\}$, Bob can reconstruct the secret state $|\xi\rangle$ only if he uses the information of the measurement results from Alice, Charles, and Diana. After he has known the results of the other parties, he can then just apply a local unitary transformation to recover the secret state $|\xi\rangle$.

3.3.4 Deterministic secure quantum communication

This protocol, proposed by X-M Xiu and *et al*, uses the idea of entanglement swapping to perform a deterministic secure communication [81]. Let us start by reviewing the basic idea of entanglement swapping. The original concept of entanglement swapping is given in [97]. The first experimental realisation has been done by Pan and his colleagues [98]. Suppose that Alice and Bob share two pairs of EPR states: $|\Phi^+\rangle_{A_1 B_1} \otimes |\Phi^+\rangle_{A_2 B_2}$. Alice owns particles A_1 and A_2 , while particles B_1 and B_2 are Bob's. The state of these particles is rewritten as

$$|\Phi^+\rangle_{A_1 B_1} \otimes |\Phi^+\rangle_{A_2 B_2} = \frac{1}{2} (|\Phi^+\rangle_{A_1 A_2} |\Phi^+\rangle_{B_1 B_2} + |\Phi^-\rangle_{A_1 A_2} |\Phi^-\rangle_{B_1 B_2} + |\Psi^+\rangle_{A_1 A_2} |\Psi^+\rangle_{B_1 B_2} + |\Psi^-\rangle_{A_1 A_2} |\Psi^-\rangle_{B_1 B_2}), \quad (3.86)$$

where the definition of these EPR states is as given previously. From this equation, we can see that if Alice performs a Bell-basis measurement on her own particles, this measurement will project Bob's particles into one of the EPR states. This means the two particles owned by Bob are not entangled in the first place, but the entanglement of these two particles is created after Alice's measurement even though they have never interacted with each other. This is what we call entanglement swapping.

The protocol that we can use the χ -type states as the entanglement resource for secure communication is given as follows. Alice prepares a group of four particles that are in the entangled state:

$$|\bar{\chi}^{00}\rangle_{A_1 A_2 B_1 B_2} = I_{A_1} \otimes I_{A_2} \otimes CZ_{B_1 B_2} |\chi^{00}\rangle_{A_1 A_2 B_1 B_2} \quad (3.87)$$

where $|\chi^{00}\rangle$ is as given in Eq (3.5). The two-dimensional identity and the controlled Z gate are denoted by I and CZ respectively. Other fifteen states that orthogonal to this state are given straightforwardly as,

$$|\bar{\chi}^{ij}\rangle_{A_1 A_2 B_1 B_2} = I_{A_1} \otimes I_{A_2} \otimes CZ_{B_1 B_2} |\chi^{ij}\rangle_{A_1 A_2 B_1 B_2} \quad (3.88)$$

After that, she sends two particles, B_1 and B_2 , to Bob. After he received the particles, he then tells Alice via a classical communication channel that the particles have arrived. To test the existence of an eavesdropper (Eve), Bob decides to sacrifice a sufficiently large group of particles he possesses and uses the remaining particles as the communication channel. Bob then performs measurements on the test particles in the two-qubit computational basis $\{|00\rangle, |01\rangle, |10\rangle, |11\rangle\}$, and the Bell-basis $\{|\Phi^\pm\rangle, |\Psi^\pm\rangle\}$. He then tells Alice which particles are selected as the test group together with his measurement bases and outcomes. With the form of Eq.(3.87) together with Eqs.(3.59) and (3.64), we find [81]

$$\begin{aligned} |\bar{\chi}^{00}\rangle &= \frac{1}{2}(|\Phi^+\rangle|00\rangle + |\Phi^-\rangle|11\rangle - |\Psi^-\rangle|01\rangle + |\Psi^+\rangle|10\rangle) \\ &\quad \frac{1}{2}(|00\rangle|\Phi^+\rangle + |11\rangle|\Phi^-\rangle - |01\rangle|\Psi^-\rangle + |10\rangle|\Psi^+\rangle) \end{aligned}$$

we can see that once Alice knows Bob's bases of measurement and his results she then can deduce her two-qubit state. To check the existence of Eve, she measures her state in the opposite bases from Bob. Therefore, if Eve does gain some information, it will be most likely that she destroys the entanglement between the particles and can be detected. We will discuss the security against this and other attacks later.

We can rewrite the tensor product of the two $|\bar{\chi}^{00}\rangle_{A_1 A_2 B_1 B_2}$ states prepared by Alice as follows,

$$\begin{aligned} |\xi\rangle &= |\bar{\chi}^{00}\rangle_{A_1 A_2 B_1 B_2} |\bar{\chi}^{00}\rangle_{A_3 A_4 B_3 B_4} \\ &\quad \frac{1}{4} \left(|\bar{\chi}^{00}\rangle_{A_1 A_2 A_3 A_4} |\bar{\chi}^{00}\rangle_{B_1 B_2 B_3 B_4} + |\bar{\chi}^{01}\rangle_{A_1 A_2 A_3 A_4} |\bar{\chi}^{12}\rangle_{B_1 B_2 B_3 B_4} \right. \\ &\quad + |\bar{\chi}^{02}\rangle_{A_1 A_2 A_3 A_4} |\bar{\chi}^{11}\rangle_{B_1 B_2 B_3 B_4} + |\bar{\chi}^{03}\rangle_{A_1 A_2 A_3 A_4} |\bar{\chi}^{03}\rangle_{B_1 B_2 B_3 B_4} \\ &\quad + |\bar{\chi}^{10}\rangle_{A_1 A_2 A_3 A_4} |\bar{\chi}^{10}\rangle_{B_1 B_2 B_3 B_4} + |\bar{\chi}^{11}\rangle_{A_1 A_2 A_3 A_4} |\bar{\chi}^{02}\rangle_{B_1 B_2 B_3 B_4} \\ &\quad + |\bar{\chi}^{12}\rangle_{A_1 A_2 A_3 A_4} |\bar{\chi}^{01}\rangle_{B_1 B_2 B_3 B_4} + |\bar{\chi}^{13}\rangle_{A_1 A_2 A_3 A_4} |\bar{\chi}^{13}\rangle_{B_1 B_2 B_3 B_4} \\ &\quad + |\bar{\chi}^{20}\rangle_{A_1 A_2 A_3 A_4} |\bar{\chi}^{33}\rangle_{B_1 B_2 B_3 B_4} + |\bar{\chi}^{21}\rangle_{A_1 A_2 A_3 A_4} |\bar{\chi}^{21}\rangle_{B_1 B_2 B_3 B_4} \\ &\quad + |\bar{\chi}^{22}\rangle_{A_1 A_2 A_3 A_4} |\bar{\chi}^{22}\rangle_{B_1 B_2 B_3 B_4} + |\bar{\chi}^{23}\rangle_{A_1 A_2 A_3 A_4} |\bar{\chi}^{30}\rangle_{B_1 B_2 B_3 B_4} \\ &\quad + |\bar{\chi}^{30}\rangle_{A_1 A_2 A_3 A_4} |\bar{\chi}^{23}\rangle_{B_1 B_2 B_3 B_4} + |\bar{\chi}^{31}\rangle_{A_1 A_2 A_3 A_4} |\bar{\chi}^{31}\rangle_{B_1 B_2 B_3 B_4} \\ &\quad \left. + |\bar{\chi}^{32}\rangle_{A_1 A_2 A_3 A_4} |\bar{\chi}^{32}\rangle_{B_1 B_2 B_3 B_4} + |\bar{\chi}^{33}\rangle_{A_1 A_2 A_3 A_4} |\bar{\chi}^{20}\rangle_{B_1 B_2 B_3 B_4} \right) \quad (3.89) \end{aligned}$$

Particles B_i are sent to Bob. Alice has agreed with Bob to encode two bits of classical information with the superscripts so that $00 \rightarrow 0$, $01 \rightarrow 1$, $10 \rightarrow 2$ and $11 \rightarrow 3$. Alice makes a measurement in

the $\bar{\chi}$ basis, $\{|\bar{\chi}^{ij}\rangle\}$. She can create a public message by binary addition between the secret message and her measurement result. For example, if her measurement result is $|\bar{\chi}^{11}\rangle$ which corresponds to the binary information 0101 and her secret message is 1010, the message she sends to Bob then becomes 0101+1010=1111. After Bob has obtained the classical information from Alice, he then makes a measurement in the same basis. His result then tells him that what is Alice's key. He then can reverse the operation and obtain the secret message. With the form of Eq.(3.89), we can see that Bob can also use this quantum channel to send his secret message to Alice as well.

The *measure-resend attack*: Eve intercepts particles B_i that Alice sends to Bob. She then performs the $\bar{\chi}$ basis measurement on these particles and sends it to Bob. Eve can deduce the secret message if Alice announces her ciphered message publicly as the measurement results that she has obtained are correlated with Alice's. However, in the check process, as there is no entanglement between Alice's and Bob's particles after Eve measurement, this attack can be detected with the probability 75% [81].

The *intercept-resend attack*: Eve prepares particles in $|\bar{\chi}^{00}\rangle_{E_1 E_2 B'_1 B'_2}$. She then intercepts the particles that Alice sends to Bob and sends particles B'_1 and B'_2 that she has prepared to Bob. As the intercepted particles are entangled with Alice's particles she can then deduce the secret information when Alice announce the public message to Bob via a classical channel. However, as particles B'_1 and B'_2 that Eve has sent are not entangled with Alice's particles this attack will create errors that can be detected with 75% [81].

The *entangle-measure attack*: Eve intercepts the particles in transmission and then performs a unitary operation on both the intercepted particles and her auxiliary particles. She thus sends the intercepted particles to Bob. Her auxiliary particles are then entangled with Alice and Bob particles as [81]

$$\begin{aligned}
|\xi'\rangle = & \frac{1}{2\sqrt{2}} [|\Phi^+\rangle_A (|00\rangle_B \alpha_1 |\varepsilon_{\Phi+00}\rangle + |01\rangle_B \beta_1 |\varepsilon_{\Phi+01}\rangle + |10\rangle_B \gamma_1 |\varepsilon_{\Phi+10}\rangle + |11\rangle_B \delta_1 |\varepsilon_{\Phi+11}\rangle) \\
& + |\Phi^-\rangle_A (|00\rangle_B \alpha_2 |\varepsilon_{\Phi-00}\rangle + |01\rangle_B \beta_2 |\varepsilon_{\Phi-01}\rangle + |10\rangle_B \gamma_2 |\varepsilon_{\Phi-10}\rangle + |11\rangle_B \delta_2 |\varepsilon_{\Phi-11}\rangle) \\
& - |\Psi^-\rangle_A (|00\rangle_B \alpha_3 |\varepsilon_{\Psi-00}\rangle + |01\rangle_B \beta_3 |\varepsilon_{\Psi-01}\rangle + |10\rangle_B \gamma_3 |\varepsilon_{\Psi-10}\rangle + |11\rangle_B \delta_3 |\varepsilon_{\Psi-11}\rangle) \\
& + |\Psi^+\rangle_A (|00\rangle_B \alpha_4 |\varepsilon_{\Psi+00}\rangle + |01\rangle_B \beta_4 |\varepsilon_{\Psi+01}\rangle + |10\rangle_B \gamma_4 |\varepsilon_{\Psi+10}\rangle + |11\rangle_B \delta_4 |\varepsilon_{\Psi+11}\rangle)] , \quad (3.90)
\end{aligned}$$

where Eve's auxiliary state is represented by $|\varepsilon_i\rangle$. The complex numbers α_i , β_i , γ_i and δ_i satisfy the normalization condition: $|\alpha_i|^2 + |\beta_i|^2 + |\gamma_i|^2 + |\delta_i|^2 = 1$. From this form of the equation, we can see that this attacking strategy will induce the error rate of

$$\epsilon = 1 - |\alpha_1|^2 = 1 - |\delta_2|^2 = 1 - |\beta_3|^2 = 1 - |\gamma_4|^2. \quad (3.91)$$

This means that the more information she gains from this attack the higher probability her existence will be detected.

Chapter 4

Two-photon, four-qubit χ state realisation

As discussed in the previous chapter, the so-called χ -type entangled states have interesting entanglement properties and can be used as an entanglement resource for several novel quantum information protocols [81,87,92,96,99–101]. This gives rise to an interest, in the field of quantum information and quantum cryptography, in how we can prepare these states effectively. There are several schemes proposed to generate these states [102–108]. For example, Liu and Kuang proposed a scheme to prepare these states by utilising the interaction between light and four atoms in four separate optical cavities [106].

In this chapter, we show an alternative scheme to prepare these states, $|\chi^{ij}\rangle$. The overview of our proposed scheme is given as follows. Two hyper-entangled photons, which are maximally entangled in both polarisation and orbital angular momentum degrees of freedom, can be obtained by spontaneous parametric down-conversion (SPDC). We present a linear optical system that can then transform the initial state of these two photons into the state $|\chi^{00}\rangle$. The further transformations required in order to obtain the other χ -type states from $|\chi^{00}\rangle$ may also be achieved through linear optical elements and are also given. This work given in this chapter is an original contribution and was published in *J. Opt.* [1].

The structure of this chapter is given as follows. In section 4.1, we will briefly review the experiment in [109] which gives hyper-entangled photons and the quantum circuit that can transform the initial state of the photon pairs into the desired state. Section 4.2 reviews the effects of some particular optical elements and interferometers on the photon state. The proposed optical system is then given and explained in the following section. In the last section, we discuss the further transformation that transforms the state $|\chi^{00}\rangle$ into any other states of this class.

4.1 Transformation of two entangled photons

From [109], photon pairs which are maximally entangled in their polarisation and orbital angular momentum can be produced as follows. Barreiro and colleagues used a 351 nm Argon ion laser with

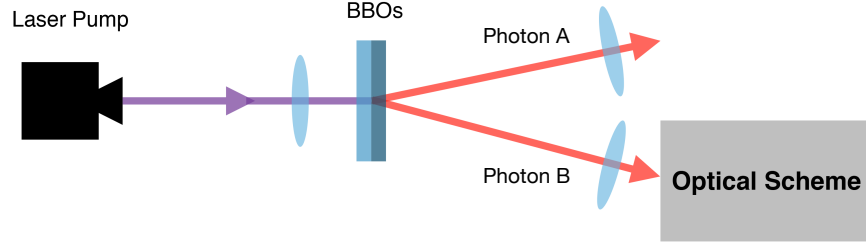


Figure 4.1: The signal and idler photons which are maximally entangled in their polarisation and orbital angular momentum are obtained by coherent sequential spontaneous parametric down-conversion. The two connected BBO crystals are pumped by the argon ion laser. One of the down-converted photons, photon B, is sent to our designed optical system given in figure 4.5.

120 mW power pumping into two connected β -barium borate (BBO) crystals, as shown in figure 4.1. The optical axes of these two BBO crystals are set to be perpendicular to each other. If the pumping photons interact with the first crystal, the two generated photons, signal and idler, will be either horizontally or vertically polarised. In the case that interaction takes place in the second crystal, on the other hand, the vertically polarised photons are produced. As the crystals are in close proximity, we cannot distinguish the interaction place of the generated photon pairs. Hence, the unnormalised states of the emitted photon pairs can be written as

$$(|\text{HH}\rangle + |\text{VV}\rangle)_{\text{AB}}^p \otimes (|\text{RL}\rangle + \alpha|\text{GG}\rangle + |\text{LR}\rangle)_{\text{AB}}^o, \quad (4.1)$$

where H and V represent horizontal and vertical polarisation states. We use R, L and G to denote the orbital angular momentum modes of $+\hbar$, $-\hbar$ and 0 respectively for each photon. We note that there is also a possibility that the emitted photons have higher orbital angular momentum, but the relative sizes of the probability amplitudes can be controlled [110, 111]. The state given in this equation obeys the conservation of OAM [10] as reviewed in chapter 1. The superscripts p and o indicate the polarisation and orbital angular momentum states respectively, while the subscripts A and B are used to indicate whether it is the state of photon A or B. The complex amplitude α is determined by mode-matching conditions [10, 112]. As mentioned previously, the photon pairs are also entangled in their emission times and frequencies, but in this work, it is only important in the way that the arrival time of one entangled photon at a detector can be used to determine that of its

partner at the other separated detector. At this point, we can see that the state of the photon pairs will be maximally entangled if we omit the state $|GG\rangle$ in the superposition. This can be done by spatial filtering to remove the beam centre or using a mode-sorter [38], which is discussed previously, to select only the odd values of the orbital angular momentum. The normalised state of the two photons then becomes

$$\begin{aligned} |\Phi^+\rangle_{AB}^P \otimes |\Psi^+\rangle_{AB}^O &= \frac{1}{2}(|HH\rangle + |VV\rangle)_{AB}^P \otimes (|RL\rangle + |LR\rangle)_{AB}^O \\ &= \frac{1}{2}(|00\rangle + |11\rangle)_{AB}^P \otimes (|01\rangle + |10\rangle)_{AB}^O. \end{aligned} \quad (4.2)$$

In the second line of Eq.(4.2), we identify the horizontal and vertical polarisation states, $|H\rangle^P$ and $|V\rangle^P$, with the computational states $|0\rangle^P$ and $|1\rangle^P$ respectively. Similarly, the OAM states $|R\rangle^O$ and $|L\rangle^O$ are encoded with the states $|0\rangle^O$ and $|1\rangle^O$. We can then rewrite the state as a superposition of computational basis states of photon A and B as

$$|X\rangle_{AB} = \frac{1}{2}(|00\rangle_A |01\rangle_B + |01\rangle_A |00\rangle_B + |10\rangle_A |11\rangle_B + |11\rangle_A |10\rangle_B), \quad (4.3)$$

where the first qubits of photons A and B are the polarisation states of the photons while the second qubits represent the OAM states. For example, the state $|00\rangle_A$ of photon A in the first term of the superposition represents the composite state $|H\rangle^P |R\rangle^O$.

At this point, we find that the state $|\chi^{00}\rangle$ is obtained if we can transform the initial state of photon B as

$$\begin{aligned} |00\rangle_B &\rightarrow \frac{1}{\sqrt{2}}(|10\rangle - |01\rangle)_B, \\ |01\rangle_B &\rightarrow \frac{1}{\sqrt{2}}(|00\rangle - |11\rangle)_B, \\ |10\rangle_B &\rightarrow \frac{1}{\sqrt{2}}(|00\rangle + |11\rangle)_B, \\ |11\rangle_B &\rightarrow \frac{1}{\sqrt{2}}(|10\rangle + |01\rangle)_B. \end{aligned} \quad (4.4)$$

As the states of photons A and B in Eq.(4.3) are identical, this task can alternatively be achieved by applying this transformation to the state of photon A. The transformation is described by the quantum circuit given in figure 4.2. The first operation in the circuit is the controlled NOT (CNOT) gate which applies the Pauli X gate to the target qubit if the associated control qubit is in the state $|0\rangle$ or does nothing if the control qubit is $|1\rangle$. The second CNOT gate, on the other hand, does the opposite: It applies the Pauli X gate to the target qubit if the control qubit is $|1\rangle$ or leaves the target qubit unchanged if the control qubit is $|0\rangle$ instead. We denote by H and Z in the quantum circuit the Hadamard and Pauli Z gates respectively. The two-photon state after this transformation can be expressed as

$$|X\rangle_{AB} \rightarrow |\chi^{00}\rangle_{AB} = \frac{1}{\sqrt{2}} (|\zeta^0\rangle + |\zeta^1\rangle)_{AB} \quad (4.5)$$

with

$$|\zeta^0\rangle \equiv \frac{1}{2}(|0000\rangle - |0011\rangle - |0101\rangle + |0110\rangle), \quad (4.6)$$

$$|\zeta^1\rangle \equiv \frac{1}{2}(|1001\rangle + |1010\rangle + |1100\rangle + |1111\rangle). \quad (4.7)$$

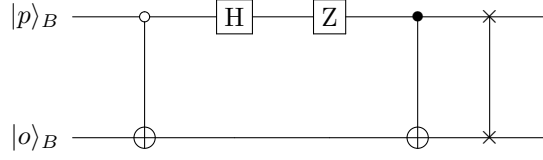


Figure 4.2: The quantum circuit to achieve the transformation given in Eq.(4.4), where $|p\rangle_B$ and $|o\rangle_B$ are the polarisation and OAM parts of the composite state of photon B.

The swap gate at the end of the quantum circuit can be realised easily as the OAM state of photon B is recognised as the third qubit while its polarisation becomes the last qubit. We note that without the swap gate, the state of the photon pair becomes the entangled state $|\chi_{Lee}^{00}\rangle$,

$$|\chi_{Lee}^{00}\rangle = \frac{1}{\sqrt{2}}(|\lambda^0\rangle + |\lambda^1\rangle)_{AB}, \quad (4.8)$$

with

$$|\lambda^0\rangle \equiv \frac{1}{2}(|0000\rangle - |0011\rangle - |0110\rangle + |0101\rangle), \quad (4.9)$$

$$|\lambda^1\rangle \equiv \frac{1}{2}(|1001\rangle + |1010\rangle + |1100\rangle + |1111\rangle) = |\zeta^1\rangle, \quad (4.10)$$

proposed by Lee *et al* to be a quantum channel for teleportation [88].

4.2 Optical realisation

4.2.1 Polarisation gates

In this section, we discuss how each optical element included in our proposed optical system affects and alters the composite state of the incident photon. First, we start with birefringent waveplates. Their effects on the polarisation states of the input photons are well-known. In quantum optics, they are usually utilised as single-qubit gates for polarisation qubits of photons as the following demonstrates. The function of birefringent waveplates is to realise a different optical path length and therefore phase delay for polarisation components perpendicular to or parallel to their optical axis differently. There are two well-known birefringent waveplates: half- and quarter- wave plates. A half-wave plate delays the phase of the polarisation component that is parallel to its optical axes by π with respect to the perpendicular component. A quarter-wave plate, on the other hand, introduces a relative phase between these two components of $\pi/2$. These effects of half- and quarter- wave plates with their fast axes horizontal can be described by the following Jones matrices [113, 114]:

$$J_h = \begin{pmatrix} 1 & 0 \\ 0 & -1 \end{pmatrix}, \quad (4.11)$$

and

$$J_q = \begin{pmatrix} 1 & 0 \\ 0 & i \end{pmatrix}, \quad (4.12)$$

respectively, where we denote

$$\vec{p}_\perp = \begin{pmatrix} 1 \\ 0 \end{pmatrix} \quad \text{and} \quad \vec{p}_\parallel = \begin{pmatrix} 0 \\ 1 \end{pmatrix}, \quad (4.13)$$

as unit vectors that are perpendicular and parallel to the optical axis, respectively. In the case that the optical axis is aligned vertically, this automatically implies that

$$|H\rangle = \vec{p}_\perp \quad \text{and} \quad |V\rangle = \vec{p}_\parallel. \quad (4.14)$$

For example, with this set up, if the incoming photon is right-circularly polarised, described by the state $(|H\rangle + i|V\rangle)/2$, the polarisation state of the outgoing photon will be left-circular polarisation, $(|H\rangle - i|V\rangle)/2$, if it passes through a half-wave plate, or linear polarisation, $(|H\rangle - |V\rangle)/2$, if the waveplate is a quarter-wave plate instead.

The effects of half- and quarter- wave plates on the horizontal and vertical polarisation are, of course, changed if they are rotated. The Jones matrices of half- and quarter- wave plates which are rotated by an angle θ with respect to the horizontal axis are [115]

$$\begin{aligned} J_h(\theta) &= \begin{pmatrix} \cos \theta & -\sin \theta \\ \sin \theta & \cos \theta \end{pmatrix} \begin{pmatrix} 1 & 0 \\ 0 & -1 \end{pmatrix} \begin{pmatrix} \cos \theta & \sin \theta \\ -\sin \theta & \cos \theta \end{pmatrix} \\ &= \begin{pmatrix} \cos 2\theta & \sin 2\theta \\ \sin 2\theta & -\cos 2\theta \end{pmatrix}. \end{aligned} \quad (4.15)$$

$$\begin{aligned} J_q(\theta) &= \begin{pmatrix} \cos \theta & -\sin \theta \\ \sin \theta & \cos \theta \end{pmatrix} \begin{pmatrix} 1 & 0 \\ 0 & i \end{pmatrix} \begin{pmatrix} \cos \theta & \sin \theta \\ -\sin \theta & \cos \theta \end{pmatrix} \\ &= \begin{pmatrix} \cos^2 \theta + i \sin^2 \theta & (1-i) \sin \theta \cos \theta \\ (1-i) \sin \theta \cos \theta & \sin^2 \theta + i \cos^2 \theta \end{pmatrix}, \end{aligned} \quad (4.16)$$

respectively. These two types of birefringent waveplates affect only the polarisation state of the input photon but do not change the amplitude profile. The OAM state of the input photon is not altered after it passes the waveplates. The total effect of these waveplates on the composite state is given by

$$|p', o'\rangle = J_i \otimes I |p, o\rangle \quad \text{with} \quad i = h, q, \quad (4.17)$$

where we denote by $|p', o'\rangle$ and $|p, o\rangle$ the composite states before and after the photon passes through the waveplate.

According to the Jones matrix of oriented half-wave plates given in Eq.(4.15), many single-qubit gates for polarisation qubits can be realised by appropriately oriented half-wave plates. For example, the Pauli Z- and X- gates can be realised as half-wave plates with their fast axes parallel to and rotated by an angle $\pi/4$ with respect to the horizontal plane: $J_h(\theta = 0) = \sigma^z$ and $J_h(\theta = \pi/4) = \sigma^x$. As $\sigma^z \sigma^x = i\sigma^y$, the realisation of the Pauli Y-gate for polarisation qubits is obtained by using two half-wave plates with different orientations. On the other hand, if we rotate a half-wave plate such that its fast axis is at an angle $\pi/8$ with respect to the horizontal plane, the Jones matrix of the

rotated half-wave plate then becomes,

$$J_h(\theta = \pi/8) = \begin{pmatrix} \frac{1}{\sqrt{2}} & \frac{1}{\sqrt{2}} \\ \frac{1}{\sqrt{2}} & -\frac{1}{\sqrt{2}} \end{pmatrix}. \quad (4.18)$$

This is the matrix representation of the Hadamard transformation. A $\pi/8$ -oriented half-wave plate thus is the realisation of the Hadamard gate.

4.2.2 OAM gates

A Dove prism is an optical element frequently employed for changing the sign of the orbital angular momentum of the incoming photon in various OAM experiments [38, 44, 116–118]. For our case, a Dove prism converts the topological charge of the photon from $l = 1$ to $l = -1$ or vice versa. In other words, with our encoding, it changes the state $|0\rangle^o$ into the state $|1\rangle^o$ or the other way round. Therefore, Dove prisms act as the Pauli X gates for OAM qubits. In general, when a light beam passes through the Dove prism it encounters at least one total internal reflection, as it was originally invented to invert the input image. This means a Dove prism, in whatever shape it is, changes both the polarisation and OAM states of the input photons. The effect on polarisation qubits is determined by the shape of the Dove prism as its shape determines how the light beam refracts and reflects within it. In our case, for simplicity, we will consider M-shaped Dove prisms, as illustrated in figure 4.4, as their Jones matrix is simpler than that of a trapezoid Dove prism. M-shaped Dove prisms were originally invented to be quarter-wave retarders [119]. The effect on polarisation is thus the same as a quarter-wave plate. The total effect on the composite state is then given by

$$|p', o'\rangle = J_D \otimes \sigma^x |p, o\rangle, \quad (4.19)$$

where

$$J_D = \begin{pmatrix} 1 & 0 \\ 0 & i \end{pmatrix}. \quad (4.20)$$

Next, let us consider the interferometer depicted in figure 4.3. The incoming beam that enters this interferometer is split into two different paths at the first polarising beam splitter. In this work, we appoint all polarising beam splitters to transmit horizontally and reflect vertically polarised beams. Therefore, this interferometer allows us to apply different transformations to the OAM qubit, conditioned on the polarisation state of the incoming photon. In this way, the controlled gates in which the control and target qubits are the polarisation and OAM states respectively are realisable. For example, for the interferometer given in figure 4.3, a vertically polarised beam is reflected from the polarising beam splitter and travels in path 2 in which an M-shaped Dove prism and a $\pi/2$ rotated quarter-wave plate are introduced. The OAM state of the vertically polarised beam in this path is flipped by the Dove prism and the polarisation effect from the Dove prism is cancelled by the rotated quarter-wave plate. On the other hand, the horizontally polarised part travels along path 1 where there is no optical element that changes its polarisation or OAM states in this path. These two beams with different polarisations are then recombined at the second polarising beam splitter. Alternatively, without the quarter-wave plate, the same physical result can be obtained by carefully

adjusting the internal paths of the interferometer such that the relative phase shift between two different polarisations becomes a global phase shift of the outgoing photons. We can then summarise the total effect of this interferometer on the composite state of the incident photons as follows. The interferometer flips the OAM state if the incoming photon is vertically polarised or does nothing if it is horizontally polarised. As we encode the horizontal and vertical polarisation states to be $|0\rangle^P$ and $|1\rangle^P$ respectively, this interferometer is then realised as the second CNOT gate in the quantum circuit, in figure 4.2, and the control and target qubits are polarisation and OAM states respectively. On the other hand, the first CNOT gate of the quantum circuit (the one that changes the target qubit when the control qubit is in the state $|0\rangle$) can also be realised by introducing an M-shaped Dove prism and a $\pi/2$ -rotated quarter-wave plate in path 1 of the interferometer instead of path 2. Then, the OAM state is flipped when the incoming beam is horizontally polarised, which is encoded by $|0\rangle^P$, and left unchanged if the beam is vertically polarised, $|1\rangle^P$. We note that an interferometer built on this principle (sending differently polarised light into different paths) have been used successfully to measure both spin and OAM states of light at the single photon level [38, 120, 121].

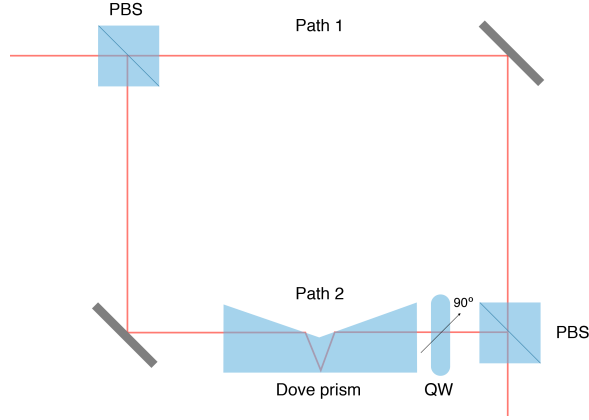


Figure 4.3: The interferometer which is realised as the second CNOT gate of the quantum circuit in figure 4.2. An M-shaped Dove prism and a quarter-wave plate (QW) with its fast axis at angle $\pi/2$ with respect to the horizontal plane are introduced to path 2.

Recall that the complex amplitude of a beam in a Laguerre-Gaussian mode contains an azimuthal phase dependence $\exp(il\phi)$, where l is the topological charge or orbital angular momentum quantum number of the beam [8]. If the beam is rotated by an angle α the azimuthal term then becomes $\exp(il(\phi + \alpha))$ [38, 44]. In other words, this rotation of the Laguerre-Gaussian beam contributes to a phase shift of $\Delta\psi = l\alpha$. We can rotate an optical beam by using suitably oriented Dove prisms as follows. A non-rotated Dove prisms gives a non-rotated, reflected image, while a Dove prism which is oriented by an angle β gives an image that is rotated by an angle 2β . As discussed previously, non-rotated Dove prisms are realised as the Pauli X-gate for OAM qubits as it changes the OAM state of the input beam from $|l\rangle$ to $|-l\rangle$ or vice versa. The Pauli Y- and Z- gates for OAM qubits can be implemented by rotated M-shaped Dove prisms as described in the following detail. An M-shaped

Dove prism which is rotated by $\pi/4$ with respect to the vertical plane transforms an OAM qubit as

$$|0\rangle^o \rightarrow e^{-i\pi/2}|1\rangle^o, \quad (4.21)$$

$$|1\rangle^o \rightarrow e^{i\pi/2}|0\rangle^o, \quad (4.22)$$

for the case that $l = \pm 1$. This is the transformation when we apply the Pauli-Y gate on a qubit. At this point, we can implement both the X- and Y- gates for OAM qubits. As $\sigma^x \sigma^y = i\sigma^z$, the Pauli Z-gate can be implemented by using two Dove prisms where the first one is oriented by $\pi/4$ with respect to the vertical plane and the second is non-oriented. As mentioned earlier, M-shaped Dove prisms also have an effect on the polarisation of photons. The total effect of a rotated Dove prism at an angle θ on a composite state can be summed up as

$$|p', o'\rangle = J_q(\theta) \otimes \begin{pmatrix} 0 & e^{2i\theta} \\ e^{-2i\theta} & 0 \end{pmatrix} |p, o\rangle. \quad (4.23)$$

We summarise the effect of all optical elements discussed above on a composite state in table 4.1.

Table 4.1: Summary of the effects of optical elements on composite qubits

Optical Elements	Effects on composite qubits
Quarter-wave plate fast axis at angle θ	$U_q(\theta) = J_q(\theta) \otimes I$
Half-wave plate with fast axis at angle θ	$U_h(\theta) = J_h(\theta) \otimes I$
Rotated M-shaped Dove prism at angle θ	$U_D(\theta) = J_q(\theta) \otimes \begin{pmatrix} 0 & e^{2i\theta} \\ e^{-2i\theta} & 0 \end{pmatrix}$

4.3 Proposed optical system

In this section, we use the information given in the previous section to design an optical system that can transform the composite state of photon B so that the two-photon state is in any one of the χ -type states. This can be done by considering the quantum circuit in figure 4.2 and implementing each quantum gate that appears in the circuit.

We start with the two CNOT gates of the quantum circuit. Some detail has been given in the previous section, but in this section, we give the complete picture of its use in the optical network implementing the circuit. The first CNOT gate, as mentioned, transforms the target qubit by applying the Pauli X-gate to it if the control qubit is in the state $|0\rangle^p$ or does nothing if the control qubit is $|1\rangle^p$. Recall that we identify the horizontal and vertical polarisation states, $|H\rangle^p$ and $|V\rangle^p$, with the computational qubit states $|0\rangle^p$ and $|1\rangle^p$ respectively. This CNOT gate then can be implemented by an interferometer similar to the one given in figure 4.4, but in which the Dove prism and the quarter-wave plate are in path 1. The implementation of the first CNOT gate is illustrated by the first interferometer in figure 4.5. If the incoming beam is horizontally polarised, it then goes

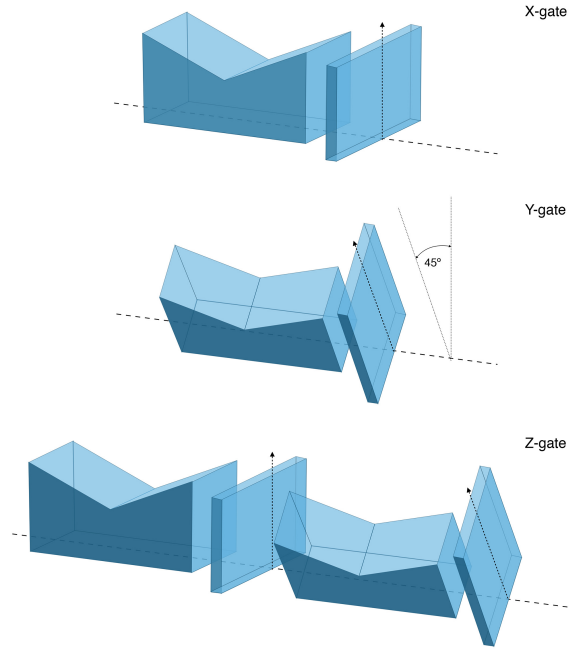


Figure 4.4: The particular alignments of M-shaped Dove prisms with quarter-wave plates, in order to compensate the polarisation effect of the Dove prisms, provide us with the physical realisations of the Pauli gates for OAM qubits when $l = \pm 1$.

to path 1 and passes through the Dove prism. The OAM state of the horizontally polarised beam is then flipped. On the other hand, the vertically polarised light goes to path 2 and its composite state is left unchanged. The effect of the first interferometer on the composite state can be written as

$$\begin{aligned} |0\rangle^P \otimes |s\rangle^O &\rightarrow |0\rangle^P \otimes \sigma^x |s\rangle^O, \\ |1\rangle^P \otimes |s\rangle^O &\rightarrow |1\rangle^P \otimes |s\rangle^O. \end{aligned} \quad (4.24)$$

The second CNOT gate is different to the first one as it changes the target qubit when the control qubit is in the state $|1\rangle^P$ and leaves the target qubit untouched if the control qubit is $|0\rangle^P$. The realisation of this gate is exactly as the interferometer in figure 4.3 and the second interferometer in figure 4.5. The interferometer forces the horizontally polarised component to travel along internal path 1 where there is no optical element that can change the composite state of the beam. On the other hand, the vertically polarised component goes to the other internal path and encounters both the M-shaped Dove prism and the rotated quarter-wave plate. Its OAM state is changed to the opposite sign. The effect on the composite state of the second interferometer can then be expressed explicitly as

$$\begin{aligned} |0\rangle^P \otimes |s\rangle^O &\rightarrow |0\rangle^P \otimes |s\rangle^O, \\ |1\rangle^P \otimes |s\rangle^O &\rightarrow |1\rangle^P \otimes \sigma^x |s\rangle^O. \end{aligned} \quad (4.25)$$

For the single-qubit gates in the quantum circuit, the Hadamard and Z- gates of the polarisation state in the quantum circuit can be realised by two half-wave plates with different orientation. The

half-wave plate with its fast axis at an angle $\pi/8$ with respect to the horizontal plane is the realisation of the Hadamard gate. The other with its fast axis is aligned horizontally is the realisation of the Z-gate. These two half-wave plates are placed between the first and the second interferometers as suggested in the quantum circuit and are depicted in figure 4.5. The swap gate at the end of the quantum circuit, as mentioned, can be achieved easily by relabelling the composite state of photon B. With the proposed optical system given in figure 4.5, we can transform the state of two entangled photons obtained from SPDC into the state $|\chi^{00}\rangle$.

4.4 Further transformation

Once the state $|\chi^{00}\rangle$ is obtained, any other χ -type state can also be obtained by applying local Pauli operations to the state $|\chi^{00}\rangle$ as

$$|\chi^{ij}\rangle_{AB} = \sigma^i \otimes \sigma^j \otimes I \otimes I |\chi^{00}\rangle_{AB}. \quad (4.26)$$

To achieve this task, we need to implement the Pauli gates for both polarisation and OAM states. As mentioned previously, the Pauli gates for polarisation can be realised by oriented half-wave plate. For the OAM states, these gates are implemented by oriented Dove prisms, together with quarter-wave plates to compensate the polarisation effect of the Dove prisms as discussed. For example, in order to realise the product of the Pauli X and Y operators for polarisation and OAM qubits, $\sigma_p^x \otimes \sigma_o^y$, we use a half-wave plate with its fast axis at an angle $\pi/4$ to the horizontal plane and an M-shaped Dove prism together with a quarter-wave plate that are rotated by $\pi/4$ with respect to the vertical plane.

To summarise this section, an arbitrary χ -type state, $|\chi^{ij}\rangle$ can be achieved by applying birefringent wave plate and M-shaped Dove prisms with specific orientations after the optical network of figure 4.5.

4.5 Conclusion

We have presented the transformation required to convert the maximally-entangled state of a down-converted photon pair to the state $|\chi^{00}\rangle$, a state in the χ state basis, in terms of a quantum circuit. The effects of each optical element on the composite state have been given, and the optical system which is a realisation of the quantum circuit has been proposed. The other χ -type states can be obtained by further transformations which are realised by birefringent wave plates and M-shaped Dove prisms.

All optical elements in the proposed optical system are linear optical components that are readily available in optical laboratories. As a result, preparation of the desired states is practically achievable with current technology. In contrast to some previous work, our proposed operation does not have any post selection process which means the efficiency of successful transformation does not depend on the efficiency of photon detectors. We expect that the proposed scheme may be realised experimentally to produce this class of multipartite genuine entangled states so that we can gain a better insight of their entanglement, and enable the demonstration of novel quantum information protocols.

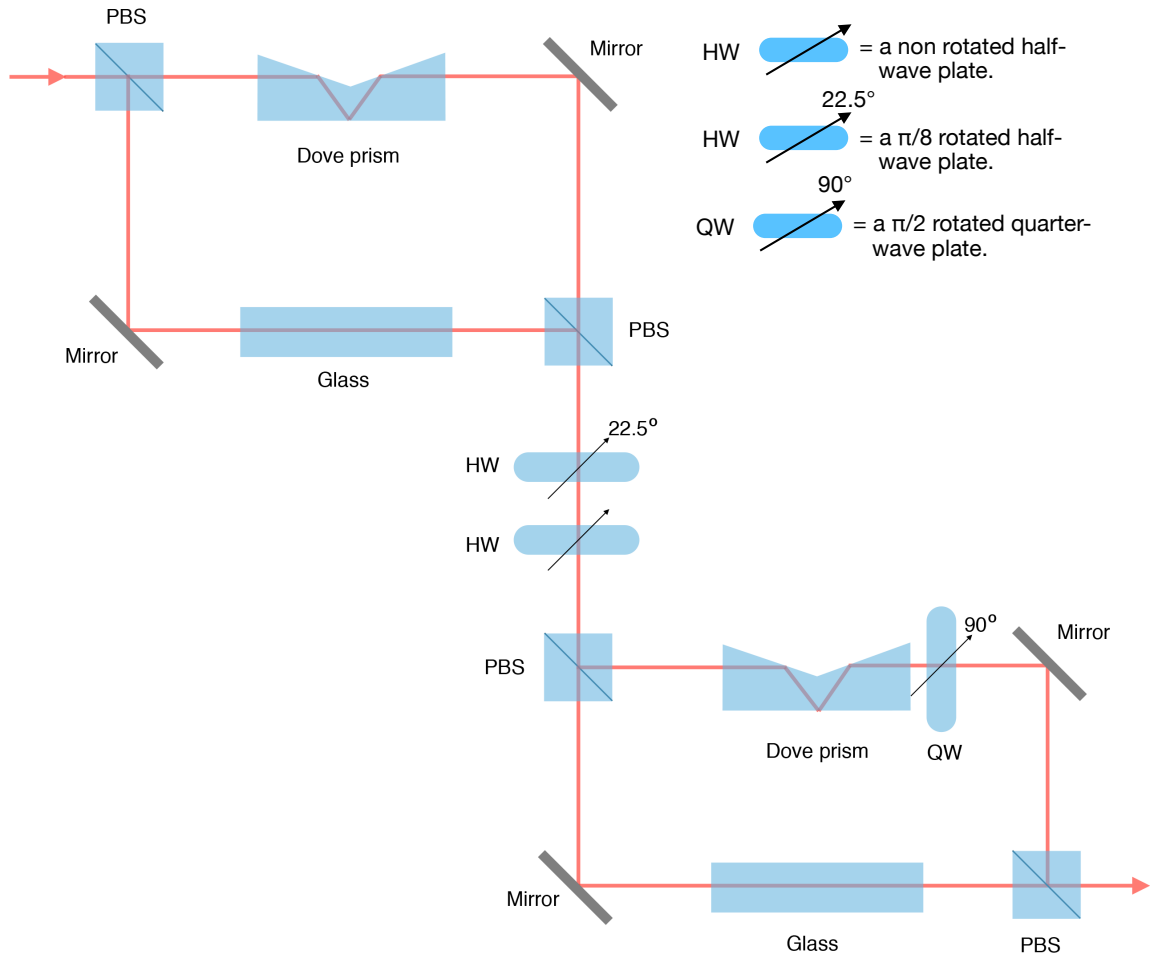


Figure 4.5: The proposed optical system which transforms the composite qubits as the quantum circuit given in figure 4.2. We introduce the pieces of glass in the two interferometers in order to compensate for the delay associated with propagation through the Dove prism and quarter wave plate in the other internal paths. The two interferometers in the figure are the implementations of the two CNOT gates of the quantum circuit. The two half-wave plates are introduced between the two interferometers. The first half-wave plate is rotated by $\pi/8$ or 22.5 degrees, while the second is nonrotated. These two half-wave plates are the implementations of the Hadamard and Pauli Z gates of the quantum circuit. The quarter-wave plate in the second interferometer is rotated by $\pi/2$ or 90 degrees in order to compensate the polarisation effect of the Dove prism.

Chapter 5

Electromagnetics

We do not know for sure when humanity's interest in light began. One of the first studies of light was done by Euclid when he wrote the law of reflection mathematically in his *Optica* in about 300 BC [122]. Isaac Newton presented in his book, *Opticks*, that white light could be disassembled into different colours of light by using a prism [123]. The idea that light is an electromagnetic wave was first suggested by Maxwell in his *Dynamical Theory of the Electromagnetic Field* published in 1865 [124], and experimentally confirmed by Hertz by designing an electromagnetic wave receptor to prove Maxwell's hypothesis of the existence of electromagnetic wave [125]. Like the other waves, light carries its energy along its propagation direction. However, in contrast to many types of waves, light does not need a medium to propagate from one point to another, and it can propagate in vacuum with a constant speed c , a universal physical constant. In relativity, the speed of light is the same for all observers.

In modern days, light has been used in many different ways. For example, we use radio waves to broadcast TV shows. We use it as an information carrier in communications. As discussed in the previous chapters, the quantum states of light can also be used for quantum information and computation. Despite a long history of studies, there are also many aspects that we do not yet fully understand, and of course the more we understand light, the better we may make use of it.

This chapter is organised as follows. We begin this chapter by reviewing Maxwell's equations and the plane wave solutions in the case when there is no free charge and current. We then use Maxwell's equations to derive the boundary conditions of electromagnetic fields in section 5.2. The laws of reflection and refraction of plane electromagnetic waves are presented in section 5.3. In section 5.4, the two competing forms of the Lorentz force density, which have been shown to give identical total force and torque, are reviewed. Section 5.5 demonstrates the quantisation process of electromagnetic fields. The paraxial approximation and quantisation of paraxial light are given in sections 5.6 and 5.7 respectively.

5.1 Maxwell equations and plane-wave solutions

Before giving a discussion of the boundary conditions, let us review Maxwell equations for electromagnetic fields in nonconducting media. Electromagnetic fields are perfectly described by Maxwell's equations for observers in any inertial reference frame. The derivative forms of Maxwell's equations are given as [18]

$$\nabla \cdot \mathbf{D} = \rho_{\text{free}}, \quad (5.1)$$

$$\nabla \cdot \mathbf{B} = 0, \quad (5.2)$$

$$\nabla \times \mathbf{E} = -\frac{\partial \mathbf{B}}{\partial t}, \quad (5.3)$$

$$\nabla \times \mathbf{H} = \mathbf{J}_{\text{free}} + \frac{\partial \mathbf{D}}{\partial t}, \quad (5.4)$$

where \mathbf{D} , \mathbf{B} , \mathbf{E} and \mathbf{H} are the electric displacement, magnetic and electric fields, and the magnetic field strength respectively. The sources of electric and magnetic fields, the free charge and current densities, are denoted by ρ_{free} and \mathbf{J}_{free} . The relation between electric displacement \mathbf{D} and electric field \mathbf{E} is $\mathbf{D} = \varepsilon_0 \mathbf{E} + \mathbf{P}$, where \mathbf{P} is a polarisation field. On the other hand, the magnetic field and the magnetic field strength are related by $\mathbf{B} = \mu_0 \mathbf{H} + \mathbf{M}$, where \mathbf{M} is the magnetisation field.

In the source free case, the two of these equations that contain the source terms are simply reduced to

$$\nabla \cdot \mathbf{D} = 0, \quad (5.5)$$

$$\nabla \times \mathbf{H} = \frac{\partial \mathbf{D}}{\partial t}. \quad (5.6)$$

This implicitly implies the existence of travelling electromagnetic waves. As we know, an electromagnetic wave represents the transfer of electromagnetic energy from one point to another. The wave solutions can be obtained straightforwardly as follows. Assuming that these fields have harmonic time dependence $\exp(-i\omega t)$ with the frequency ω , the two equations that contain the time derivative become

$$\nabla \times \mathbf{E} = i\omega \mathbf{B}, \quad (5.7)$$

$$\nabla \times \mathbf{H} = -i\omega \mathbf{D}. \quad (5.8)$$

For a uniform isotropic linear medium, the polarisation and the magnetisation of the medium are proportional to the electric field and magnetic field respectively. We, therefore, can express the electric displacement and the magnetic field strength in terms of the electric and magnetic fields as $\mathbf{D} = \varepsilon \mathbf{E}$ and $\mathbf{B} = \mu \mathbf{H}$, where the permittivity ε and the permeability μ are in general complex functions of the frequency ω . In the case of a lossless medium, where both ε and μ are real numbers, the equations for the electric and magnetic fields are

$$\nabla \times \mathbf{E} = i\omega \mathbf{B}, \quad (5.9)$$

$$\nabla \times \mathbf{B} = -i\omega \mu \varepsilon \mathbf{E}. \quad (5.10)$$

The combination of the above equations gives the so-called Helmholtz equation [18]:

$$(\nabla^2 + \mu\epsilon\omega^2) \begin{bmatrix} \mathbf{E} \\ \mathbf{B} \end{bmatrix} = \mathbf{0}. \quad (5.11)$$

The divergence-free equations, Eqs.(5.2) and (5.5), indicate that the electromagnetic wave must be transverse. The simplest solution of Eq.(5.11) is the plane-wave solution, which gives the electric and magnetic fields in the following forms,

$$\mathbf{E}(\mathbf{r}, t) = \mathbf{E}_0 e^{i(\mathbf{k}\cdot\mathbf{r} \pm \omega t)}, \quad (5.12)$$

$$\mathbf{B}(\mathbf{r}, t) = \mathbf{B}_0 e^{i(\mathbf{k}\cdot\mathbf{r} \pm \omega t)}, \quad (5.13)$$

where \mathbf{E}_0 and \mathbf{B}_0 are constant vectors representing the initial electric and magnetic fields at the origin of the coordinate system. The wave vector \mathbf{k} indicates the propagation direction of the travelling wave. From Eq.(5.11), its magnitude is related to the frequency ω as $|\mathbf{k}| = k = \sqrt{\mu\epsilon}\omega$. The relative sign of the terms in the exponential indicates whether the wave propagates in the same direction as the wave vector \mathbf{k} or in the opposite direction. Conventionally, if the relative sign is negative, then the wave travels in the same direction as \mathbf{k} [18].

5.2 Boundary conditions

In the presence of a boundary between two different nonconducting media, the fields are in general neither smooth nor continuous if there exist free charge and current at the interface. However, they still obey Maxwell's equations. Let us consider a closed cylindrical volume, as illustrated in figure 5.1. The volume integration over the closed volume of the first Maxwell equation, Eq.(5.1), gives

$$\int_V \nabla \cdot \mathbf{D} dV = \oint_S \mathbf{D} \cdot d\mathbf{S} = \int_V \rho_{\text{free}} dV, \quad (5.14)$$

where the divergence theorem has been used to make a volume integral V into a surface integral. The height δh of the cylindrical volume is assumed to be small, and the electromagnetic fields vary slowly across the surface δA . Then, the left-hand side of the equation becomes

$$\mathbf{D}_1 \cdot \mathbf{n} \delta A - \mathbf{D}_2 \cdot \mathbf{n} \delta A + \text{flux through the side surface} = \int_V \rho_{\text{free}} dV, \quad (5.15)$$

where the subscripts identify the fields near the interface in each medium and \mathbf{n} is a unit vector normal to the interface. In the case that the height δh approaches zero, the terms that are associated with the flux through the side surface then vanish. We then have

$$(\mathbf{D}_1 - \mathbf{D}_2) \cdot \mathbf{n} = \rho_{\text{free}} \delta h. \quad (5.16)$$

On the other hand, with the same derivation, a divergence-free magnetic field gives rise to the following boundary condition,

$$(\mathbf{B}_1 - \mathbf{B}_2) \cdot \mathbf{n} = 0. \quad (5.17)$$

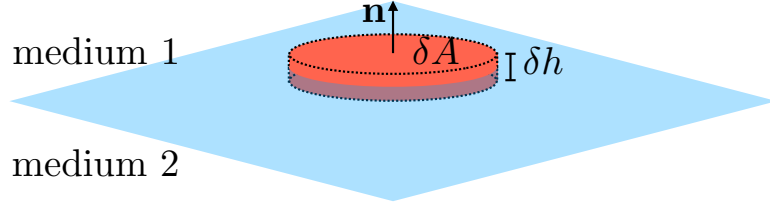


Figure 5.1: The integration volume of Eq.(5.14) is the closed cylindrical box on the interface of the two media.

The above two equations describe how the normal components of these fields on one side of the interface are related to that of the fields on the other side. In the case of no free electric charge on the interface, we can write these boundary conditions as

$$D_1^\perp = D_2^\perp, \quad (5.18)$$

$$B_1^\perp = B_2^\perp. \quad (5.19)$$

Next, let us consider the last Maxwell equation. Integrating both sides of the equation over surface $abcd$, shown in figure 5.2, gives

$$\int_{abcd} (\nabla \times \mathbf{H}) \cdot \mathbf{b} dS = \int_{abcd} \left[\mathbf{J}_{\text{free}} + \frac{\partial \mathbf{D}}{\partial t} \right] \cdot \mathbf{b} dS. \quad (5.20)$$

According to Stokes' theorem, the left hand side of the equation becomes a closed line integral as

$$\begin{aligned} \int_{abcd} (\nabla \times \mathbf{H}) \cdot \mathbf{b} dS &= \oint_{abcd} \mathbf{H} \cdot d\mathbf{r}, \\ &= -\mathbf{H}_1 \cdot \mathbf{t}L + \mathbf{H}_2 \cdot \mathbf{t}L + \text{contributions from } ac \text{ and } bd \text{ lines}, \end{aligned} \quad (5.21)$$

where \mathbf{t} is a unit vector parallel to both the interface and surface $abcd$ as depicted in the figure. The unit vector \mathbf{b} is parallel to the interface but normal to the plane $abcd$, and the lengths of lines ab and cd are L . As the lengths of the lines ac and bd approach zero, the contributions from these lines are suppressed and become negligible. Only the first two terms of the above equation remain. Once the lengths of the short sides approach zero, the magnetic flux through the plane $abcd$ vanishes. However, the right-hand side of Eq.(5.20) does not all disappear if there is free surface current density \mathbf{K} flowing exactly on the interface. Under the circumstances, we then have,

$$(\mathbf{H}_2 - \mathbf{H}_1) \cdot \mathbf{t} = \mathbf{K}. \quad (5.22)$$

With the same idea, Eq.(5.3) gives the following boundary condition

$$(\mathbf{E}_2 - \mathbf{E}_1) \cdot \mathbf{t} = 0. \quad (5.23)$$

In the case that there is no free current density and the media have low magnetic susceptibilities such that $\mu = \mu_0$, the magnetic field and magnetic field strength are related as $\mu_0 \mathbf{H} = \mathbf{B}$. In this

case, the boundary conditions for the fields can be summarised as follows,

$$D_1^\perp = D_2^\perp, \quad (5.24)$$

$$E_1^\parallel = E_2^\parallel, \quad (5.25)$$

$$\mathbf{B}_1 = \mathbf{B}_2, \quad (5.26)$$

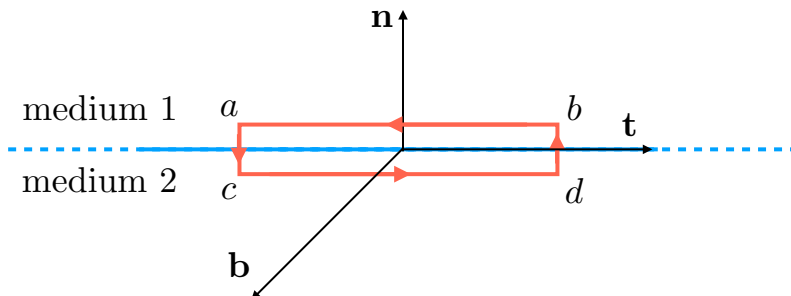


Figure 5.2: The surface is bounded by the closed line $abcd$ at the interface between the two media.

5.3 Reflection and refraction of plane electromagnetic waves

With the boundary conditions given in the previous section, for a given incident plane wave, the reflected and transmitted wave can be determined straightforwardly as follows. Let us consider the following situation. A generic incident plane wave with the wave vector \mathbf{k} whose electric and magnetic fields are written as [18]

$$\mathbf{E} = \mathbf{E}_0 e^{i(\mathbf{k} \cdot \mathbf{r} - \omega t)}, \quad (5.27)$$

$$\mathbf{B} = \sqrt{\mu_1 \varepsilon_1} \frac{\mathbf{k} \times \mathbf{E}}{k}, \quad (5.28)$$

is travelling from one dielectric medium toward another as depicted in figure 5.3. The permeabilities and permittivities of these media are μ_1, ε_1 and μ_2, ε_2 respectively. The transmitted and reflected fields then are of the forms

$$\mathbf{E}^t = \mathbf{E}_0^t e^{i(\mathbf{k}^t \cdot \mathbf{r} - \omega t)}, \quad (5.29)$$

$$\mathbf{B}^t = \sqrt{\mu_2 \varepsilon_2} \frac{\mathbf{k}^t \times \mathbf{E}^t}{k^t}, \quad (5.30)$$

and

$$\mathbf{E}^r = \mathbf{E}_0^r e^{i(\mathbf{k}^r \cdot \mathbf{r} - \omega t)}, \quad (5.31)$$

$$\mathbf{B}^r = \sqrt{\mu_1 \varepsilon_1} \frac{\mathbf{k}^r \times \mathbf{E}^r}{k}, \quad (5.32)$$

respectively. The wave number magnitudes satisfy

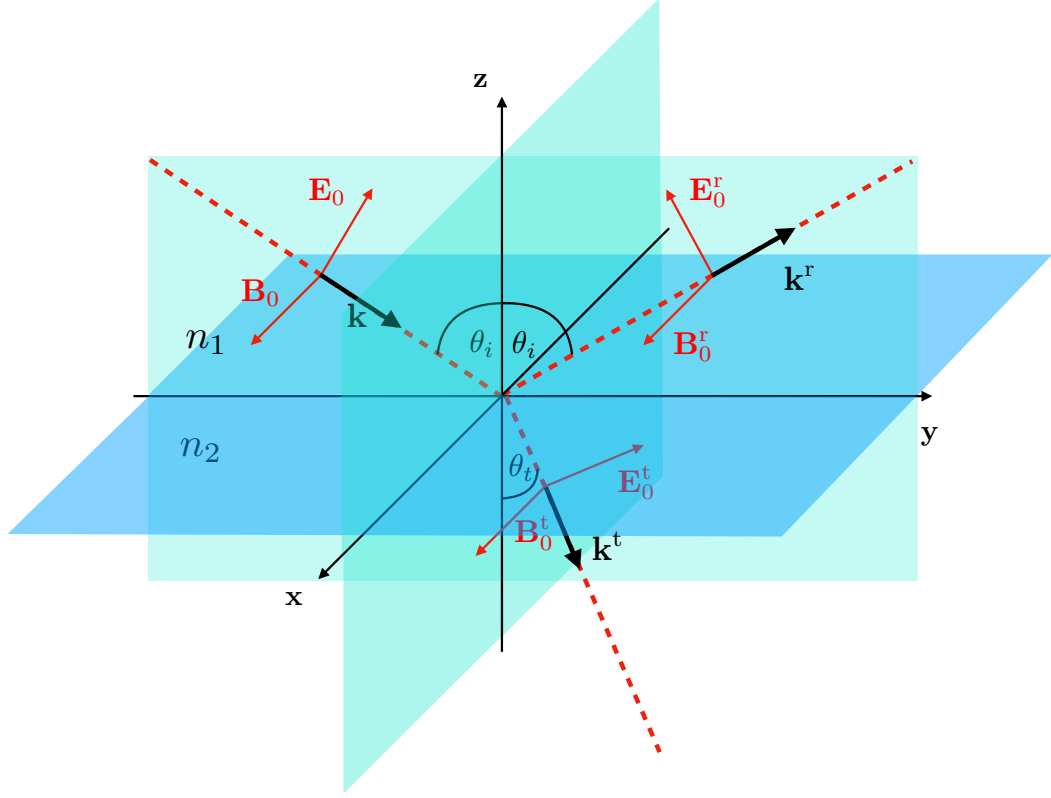


Figure 5.3: The initial plane wave travelling in the direction of propagation \mathbf{k}/k from medium 1 with refractive index n_1 toward medium 2 with refractive index n_2 . The plane wave is then transmitted and reflected as shown.

$$|\mathbf{k}| = |\mathbf{k}^r| = k = \omega\sqrt{\mu_1\varepsilon_1}, \quad (5.33)$$

$$|\mathbf{k}^t| = k^t = \omega\sqrt{\mu_2\varepsilon_2}. \quad (5.34)$$

The refractive indices of medium 1 and medium 2 are defined as $n_1 = \sqrt{\mu_1\varepsilon_1/\mu_0\varepsilon_0}$ and $n_2 = \sqrt{\mu_2\varepsilon_2/\mu_0\varepsilon_0}$ respectively. We assume that the interface is at the plane $z = 0$. As these three plane waves meet at the interface, the boundary conditions enforce a phase matching condition such that the spatial variation of all fields must have the same phase at the interface, $z = 0$:

$$\mathbf{k} \cdot \mathbf{r}|_{z=0} = \mathbf{k}^r \cdot \mathbf{r}|_{z=0} = \mathbf{k}^t \cdot \mathbf{r}|_{z=0}. \quad (5.35)$$

In other words, it means the components of the incident, reflected and transmitted wave vectors parallel to the interfaces are identical. This phase matching condition gives rise to the so-called Snell's law [18] as

$$k \sin \theta_i = k^t \sin \theta_t = k^r \sin \theta_r, \quad (5.36)$$

which determines the propagation directions of the reflected and transmitted plane waves. Applying the boundary conditions discussed previously, the electric and magnetic fields of these plane waves

at the plane $z = 0$ satisfy

$$\varepsilon_1 (\mathbf{E}_0 + \mathbf{E}_0^r) \cdot \mathbf{n} = \varepsilon_2 \mathbf{E}_0^t \cdot \mathbf{n}, \quad (5.37)$$

$$(\mathbf{k} \times \mathbf{E}_0 + \mathbf{k}^r \times \mathbf{E}_0^r) \cdot \mathbf{n} = (\mathbf{k}^t \times \mathbf{E}_0^t) \cdot \mathbf{n}, \quad (5.38)$$

$$(\mathbf{E}_0 + \mathbf{E}_0^r) \cdot \mathbf{t} = \mathbf{E}_0^t \cdot \mathbf{t}, \quad (5.39)$$

$$\frac{1}{\mu_1} (\mathbf{k} \times \mathbf{E}_0 + \mathbf{k}^r \times \mathbf{E}_0^r) \cdot \mathbf{t} = \frac{1}{\mu_2} (\mathbf{k}^t \times \mathbf{E}_0^t) \cdot \mathbf{t}. \quad (5.40)$$

By decomposing the electric fields to be in the directions perpendicular and parallel to the plane of incidence respectively, we then find the Fresnel coefficients as [18]

$$t^s = \frac{\mathbf{E}_0^t \cdot \mathbf{e}^s}{\mathbf{E}_0 \cdot \mathbf{e}^s} = \frac{2\mathbf{k} \cdot \mathbf{n}}{\mathbf{k} \cdot \mathbf{n} + \frac{\mu_1}{\mu_2} \mathbf{k}^t \cdot \mathbf{n}}, \quad (5.41)$$

$$r^s = \frac{\mathbf{E}_0^r \cdot \mathbf{e}^s}{\mathbf{E}_0 \cdot \mathbf{e}^s} = \frac{\mathbf{k} \cdot \mathbf{n} - \frac{\mu_1}{\mu_2} \mathbf{k}^t \cdot \mathbf{n}}{\mathbf{k} \cdot \mathbf{n} + \frac{\mu_1}{\mu_2} \mathbf{k}^t \cdot \mathbf{n}}, \quad (5.42)$$

$$t^p = \frac{\mathbf{E}_0^t \cdot \mathbf{e}^p(\mathbf{k}^t)}{\mathbf{E}_0 \cdot \mathbf{e}^p(\mathbf{k})} = \frac{2n\mathbf{k} \cdot \mathbf{n}}{\frac{\mu_1}{\mu_2} \mathbf{k} \cdot \mathbf{n} + n^2 \mathbf{k}^t \cdot \mathbf{n}}, \quad (5.43)$$

$$r^p = \frac{\mathbf{E}_0^r \cdot \mathbf{e}^p(\mathbf{k}^r)}{\mathbf{E}_0 \cdot \mathbf{e}^p(\mathbf{k})} = \frac{\frac{\mu_1}{\mu_2} \mathbf{k} \cdot \mathbf{n} - n^2 \mathbf{k}^t \cdot \mathbf{n}}{\frac{\mu_1}{\mu_2} \mathbf{k} \cdot \mathbf{n} + n^2 \mathbf{k}^t \cdot \mathbf{n}}, \quad (5.44)$$

where we denote by \mathbf{e}^s and $\mathbf{e}^p(\mathbf{k})$ the unit vectors perpendicular and parallel to the plane of incidence, given by

$$\mathbf{e}^s = \frac{\mathbf{n} \times \mathbf{k}}{k}, \quad (5.45)$$

$$\mathbf{e}^p(\mathbf{k}^j) = \frac{\mathbf{e}^s \times \mathbf{k}^j}{k^j}; \quad j = r, t \quad (5.46)$$

We note that for each given plane of incidence the unit vector \mathbf{e}^s is a constant vector while the direction of $\mathbf{e}^p(\mathbf{k}_j)$ depends on the propagation direction of the wave of interest. We also denote the relative index of refraction with $n \equiv n_1/n_2$. Since the directions of propagation of the reflected and transmitted fields are determined by Snell's law, and their amplitudes are given by Fresnel coefficients, for a given incident plane wave, the reflected and transmitted electric and magnetic fields given from Eq.(5.29) to Eq.(5.32) are obtained.

5.4 Optical force and torque

Optical force and torque have been studied for a long time to understand the physical interaction between light and media. They were first mentioned by Kepler who tried to explain the reason why a comet's tail always points away from the sun. There are several experimental and theoretical studies of this topic in the literature, which over time, successively clarified the picture [126–137]. However, there remain aspects to be explored. Additionally, the study of radiation pressure not only gives us a physical understanding of light-matter interaction but also guides us to its noble applications especially in optical tweezers, which play a vital part of various biological studies in recent years, including studies of bacterial flagella, DNA structure and mechanical properties of macromolecules [138].

Recall that light is a propagating wave of an electromagnetic field that carries its energy along the propagation direction. The optical force acting on a medium is described by the Lorentz force. The Lorentz force tells us how charged particles, or indeed neutral composite particles made up of charged particles, react to external electric and magnetic fields. Interestingly, in the case of dielectric media, there are actually two distinct competing forms of the Lorentz force density [131, 132]. Each of them originates from different microscopic models of the medium. If we think of the medium as formed from individual charges, the optical force density then will have the form [130]

$$\mathbf{f}^c = -(\nabla \cdot \mathbf{P})\mathbf{E} + \dot{\mathbf{P}} \times \mathbf{B}, \quad (5.47)$$

where we use the dot sign above vector fields to represent their time derivative. On the other hand, in the case that the medium is thought of as being formed by individual electric dipoles, its form then becomes [129]

$$\mathbf{f}^d = (\mathbf{P} \cdot \nabla)\mathbf{E} + \dot{\mathbf{P}} \times \mathbf{B}. \quad (5.48)$$

Only the first terms of these two forms are different. In the charge-based form, the idea of the first term is that when an external field is present, the points in the medium where the polarisation is not divergenceless corresponding to the locations of bound charges. These bound charges then are pushed or pulled by the external electric field. In the second form, the first term is the result of the net force that the external electric field exerts on each individual charge of the electric dipoles.

It has been proved that these two forms give rise to an equivalent total optical force and torque [131]. We will review the derivation of each form in detail and show that they actually give the same total force and torque. Let us begin with the Lorentz force density. The force per unit volume of electric and magnetic fields acting on charged particles is given by

$$\mathbf{f}^L = \rho\mathbf{E} + \mathbf{J} \times \mathbf{B}. \quad (5.49)$$

From the first Maxwell equation, Eq.(5.1), as the dielectric medium is electrically neutral, there is no free charge, only bound charges, and the electric displacement is thus divergenceless. Recall that in free space, the first Maxwell equation is $\nabla \cdot \mathbf{E} = \rho$, when ρ is the total charge density including both free and bound charge densities so that $\rho = \rho_{\text{free}} + \rho_{\text{bound}}$. The relation between the electric displacement and the polarisation fields is given by $\mathbf{D} = \epsilon_0\mathbf{E} + \mathbf{P}$, as previously mentioned, and in neutral media such as dielectrics, we have $\nabla \cdot \mathbf{D} = \rho_{\text{free}} = 0$. The divergenceless electric displacement therefore gives rise to the following relation between the polarisation field and the bound charge density:

$$\nabla \cdot \mathbf{P} = -\rho_{\text{bound}}. \quad (5.50)$$

Applying the time derivative on both sides of the equation and the continuity equation, we find

$$\nabla \cdot \dot{\mathbf{P}} = -\dot{\rho}_{\text{bound}} = \nabla \cdot \mathbf{J}^P. \quad (5.51)$$

The movement of bound charges creates the current density \mathbf{J}^P . This equation, however, gives us the relation between the longitudinal parts of the polarisation field and the current density. Without loss of generality, we can define the current \mathbf{J}^P in such a way that it is the result of the change in the polarisation field per unit time so that

$$\dot{\mathbf{P}} = \mathbf{J}^P. \quad (5.52)$$

Substituting these results back to the Lorentz force density, we then obtain the charge-based form of the force density.

Let us consider the case of the second form of the force density. The total Lorentz force acting on a single point dipole is given by

$$\mathbf{F}^{\text{spd}} = (\mathbf{d} \cdot \nabla)\mathbf{E} + \dot{\mathbf{d}} \times \mathbf{B}, \quad (5.53)$$

Consequently, the force density is

$$\mathbf{f}^{\text{spd}} = ((\mathbf{d} \cdot \nabla)\mathbf{E}(\mathbf{r}) + \dot{\mathbf{d}} \times \mathbf{B}(\mathbf{r}))\delta(\mathbf{r} - \mathbf{R}), \quad (5.54)$$

where \mathbf{R} is the location of the dipole. The integration over a volume including the dipole then gives back the total force on the dipole. Recall that the polarisation is the dipole density,

$$\mathbf{P} = \sum_i \mathbf{d}_i \delta(\mathbf{r} - \mathbf{R}_i). \quad (5.55)$$

where the sum runs over all dipoles in a unit volume. Then, the total force on the unit volume becomes the second form of the force density, \mathbf{f}^{d} .

5.4.1 Microscopic scale

At the microscopic scale, we consider a single point dipole at position \mathbf{R} . We then can show that the total forces acting on the dipole obtained from both forms are identical as follows. The polarisation field of the dipole is given by

$$\mathbf{P}(\mathbf{r}) = \mathbf{d}\delta(\mathbf{r} - \mathbf{R}). \quad (5.56)$$

Substituting this into the two force density forms, we then have

$$\begin{aligned} \mathbf{f}^{\text{c}} &= -(\mathbf{d} \cdot \nabla\delta(\mathbf{r} - \mathbf{R}))\mathbf{E} + \dot{\mathbf{d}} \times \mathbf{B}\delta(\mathbf{r} - \mathbf{R}), \\ \mathbf{f}^{\text{d}} &= ((\mathbf{d} \cdot \nabla)\mathbf{E} + \dot{\mathbf{d}} \times \mathbf{B})\delta(\mathbf{r} - \mathbf{R}). \end{aligned} \quad (5.57)$$

Integration over a volume containing the dipole gives us the total force acting on the dipole from these two forms, and we find

$$\begin{aligned} \mathbf{F}^{\text{d}} &= \int \mathbf{f}^{\text{d}} dV = (\mathbf{d} \cdot \nabla)\mathbf{E} + \dot{\mathbf{d}} \times \mathbf{B}, \\ \mathbf{F}^{\text{c}} &= \int \mathbf{f}^{\text{c}} dV = - \int \mathbf{E}(\mathbf{d} \cdot \nabla\delta(\mathbf{r} - \mathbf{R}))dV + \dot{\mathbf{d}} \times \mathbf{B} \\ &= (\mathbf{d} \cdot \nabla)\mathbf{E} + \dot{\mathbf{d}} \times \mathbf{B} \\ &= \mathbf{F}^{\text{d}}, \end{aligned} \quad (5.58)$$

where we have used integration by parts to evaluate the term containing the derivatives of the delta function. As we can see that both force densities give the same total force, both forms of force density are equivalent at the microscopic scale.

5.4.2 Macroscopic scale

In this case, we consider the electromagnetic force acting on a macroscopic medium. In order to calculate the total force on the medium by volume integration, we need to choose the integration volume carefully. The integration volume V , which is bounded by the surface S , must contain the entire medium and a thin layer of vacuum inside it so that the dielectric-vacuum surface is fully contained inside the volume. Since there is no polarisation field in vacuum, there is no force density in the vacuum region. The volume integral of the difference between these two forms is

$$\begin{aligned} F_i^{\text{d}} - F_i^{\text{c}} &= \int_V (P_j \nabla_j + (\nabla_j P_j)) E_i dV, \\ &= \int_V \nabla_j (P_j E_i) dV, \end{aligned} \quad (5.59)$$

where the subscripts identify the i th components of these vector fields in a Cartesian coordinate system. The Einstein summation convention has been used such that each index appearing twice implies a summation over the three values of the Cartesian components. With Gauss's theorem, the volume integration can be reexpressed as a surface integral,

$$F_i^{\text{d}} - F_i^{\text{c}} = \int_S P_j E_i dS_j = 0, \quad (5.60)$$

as there is no polarisation field at the surface of the volume. Therefore, the two distinct forms of the force density still give the same prediction at the macroscopic scale. We note that even though we are working at the macroscopic scale, the electromagnetic fields involved are the microscopic versions. The equivalence of these two forms implies that there is no difference between the net force obtained by the summation of the forces acting on each charge directly, \mathbf{F}^{c} , and that obtained by the summation of the net force acting on each dipole, \mathbf{F}^{d} .

5.4.3 Macroscopic fields

As discussed in the preceding subsection, the two force density forms give identical predictions if the fields are microscopic. However, working with microscopic fields is not practical. In this section, we calculate the Lorentz force with macroscopic fields and observe the form of the force density. Let us consider the electric part of the Lorentz force acting on a volume v containing charged particles with charge density $\rho(\mathbf{r})$:

$$\mathbf{F}_{\text{E}}^{\text{L}} = \int_v \rho(\mathbf{r}) \mathbf{E}(\mathbf{r}) dV. \quad (5.61)$$

The electric field arising from the sources within the volume v cannot contribute to the net force as they cancel each other in accordance with Newton's third law of motion. Only the external electric fields can affect the motion of the centre of mass. We assume that the volume v is small and the electric field does not change much over the dimension of the volume v . The microscopic electric field then can be replaced by the local macroscopic field $\bar{\mathbf{E}}$ [131]. Supposing \mathbf{r}_0 is a position vector inside the volume v , the electric field at any point inside the volume can then be approximated by using the Taylor expansion

$$\mathbf{E}(\mathbf{r}) \approx \bar{\mathbf{E}}(\mathbf{r}_0) + ((\mathbf{r} - \mathbf{r}_0) \cdot \nabla) \bar{\mathbf{E}}(\mathbf{r}_0), \quad (5.62)$$

where $\nabla\bar{\mathbf{E}}(\mathbf{r}_0)$ represents the derivative of the local average field $\bar{\mathbf{E}}(\mathbf{r})$ evaluated at the position \mathbf{r}_0 . Substituting back into the electric force, we then have

$$\mathbf{F}_E^L \approx \left(\int_v \rho(\mathbf{r}) dV \right) \bar{\mathbf{E}}(\mathbf{r}_0) + \int_v \rho(\mathbf{r}) (\mathbf{r} - \mathbf{r}_0) dV \cdot \nabla \bar{\mathbf{E}}(\mathbf{r}_0). \quad (5.63)$$

As we are considering the case of dielectric media which are electrically neutral, the first term vanishes,

$$\int_v \rho(\mathbf{r}) dV = 0. \quad (5.64)$$

The second integration term reminds us of the form of the macroscopic polarisation field,

$$\bar{\mathbf{P}}(\mathbf{r}_0) = \frac{1}{v} \int_v \rho(\mathbf{r}) (\mathbf{r} - \mathbf{r}_0) dV. \quad (5.65)$$

The electric force acting on this small volume v then becomes

$$\mathbf{F}_E^L = v (\bar{\mathbf{P}}(\mathbf{r}_0) \cdot \nabla) \bar{\mathbf{E}}(\mathbf{r}_0) \quad (5.66)$$

Therefore, by dividing this with the volume v , the macroscopic force density acting on the dielectric at a general point \mathbf{r} in the medium is

$$\mathbf{f}_E^L = (\bar{\mathbf{P}}(\mathbf{r}) \cdot \nabla) \bar{\mathbf{E}}(\mathbf{r}). \quad (5.67)$$

This form of force density is the same as the form of the dipole-based force density. This means in the case of macroscopic fields the dipole-based form is preferable to the charge-based one. The problem for the charge-based form when using macroscopic fields comes from the fact that the average of the field derivatives is not the same as the derivatives of the average of the fields [131],

$$\overline{\nabla \cdot \mathbf{P}} \neq \nabla \cdot \bar{\mathbf{P}}. \quad (5.68)$$

This is because, in general, averaging and differentiation do not commute. If the boundary of the volume v is in the region of that the polarisation field \mathbf{P} is non-zero, the boundary term then is not necessarily zero. This fact can be shown explicitly as [139]

$$\overline{\nabla \cdot \mathbf{P}(\mathbf{r})} = \nabla \cdot \bar{\mathbf{P}}(\mathbf{r}) + \int_s d\mathbf{S}' \cdot \mathbf{P}(\mathbf{r}') w(\mathbf{r} - \mathbf{r}'), \quad (5.69)$$

where $w(\mathbf{r})$ is the averaging kernel, which is a real, non-negative and continuous function normalised to unity: $\int_v dV w(\mathbf{r}) = 1$, and we have defined s to be the surface of the volume v . The last term then represents the average of the polarisation field \mathbf{P} over the surface s .

5.4.4 Optical torque

An electromagnetic field can also exert torque on a dielectric medium, and indeed it is this torque that is used to prove the existence of optical spin and orbital angular momentum [140]. For example, in optical tweezer experiments, dielectric objects rotate around the optical axis if they are illuminated by a light beam with orbital angular momentum [23–25]. Another example is Beth's experiment where the spin angular momentum transferred from circularly polarised light to a birefringent wave plate was observed [7].

Recall that the dipole-based force density is obtained from the summation of all forces acting on the centres of mass of electric dipoles in a unit volume. To obtain the complete torque density, the internal torque $\mathbf{P} \times \mathbf{E}$ which acts to align the electric dipole parallel to the external electric field must be added. The form of the dipole-based torque density then becomes

$$\mathbf{t}^d = \mathbf{r} \times \mathbf{f}^d + \mathbf{P} \times \mathbf{E}. \quad (5.70)$$

On the other hand, since the charge-based force density originates from the electromagnetic force acting on each individual charge in a unit volume, the form of the charge-based torque density can be obtained directly as

$$\mathbf{t}^c = \mathbf{r} \times \mathbf{f}^c. \quad (5.71)$$

In order to calculate the total torque on the medium, we perform the volume integration of these forms of the torque density. The volume of integration once again must contain the entire medium and a thin layer of vacuum within it, and there is no polarisation field at its surface S . We then find

$$\begin{aligned} \mathbf{T}^d &= \int_V dV \left(\mathbf{r} \times ((\mathbf{P} \cdot \nabla)\mathbf{E} + \dot{\mathbf{P}} \times \mathbf{B}) + \mathbf{P} \times \mathbf{E} \right), \\ \mathbf{T}^c &= \int_V dV \left(\mathbf{r} \times ((-\nabla \cdot \mathbf{P})\mathbf{E} + \dot{\mathbf{P}} \times \mathbf{B}) \right) \\ &= - \int_S (\mathbf{r} \times \mathbf{E})\mathbf{P} \cdot d\mathbf{S} + \int_V dV ((\mathbf{P} \cdot \nabla)(\mathbf{r} \times \mathbf{E}) + \mathbf{r} \times (\dot{\mathbf{P}} \times \mathbf{B})) \\ &= \int_V dV \left(\mathbf{r} \times ((\mathbf{P} \cdot \nabla)\mathbf{E} + \dot{\mathbf{P}} \times \mathbf{B}) + \mathbf{P} \times \mathbf{E} \right) = \mathbf{T}^d. \end{aligned} \quad (5.72)$$

In the above expression, we have used integration by parts and the fact that there is no polarisation field at the surface of the integration volume. The first term in the last line then disappears. This indicates that both of the forms of torque density give identical total torque.

5.5 Field quantisation

In this section, we review and discuss the processes that are required to quantise electromagnetic fields. The key idea of the field quantisation is that the classical fields are replaced by their corresponding field operators [141]. The equation of motion of these fields must be in the same form as the classical equation of motion, or, in our case, the electromagnetic field operators must still obey Maxwell's equations. It is easier and more straightforward to quantise the classical fields if we write the classical equation in the form of a classical harmonic oscillator. Then, we can replace it with its quantum version.

5.5.1 Electromagnetic scalar and vector potentials

Before demonstrating the quantisation process explicitly, let us review the process to obtain the classical electric and magnetic fields from the scalar and vector potentials: ϕ and \mathbf{A} . For a given scalar potential ϕ and a vector potential \mathbf{A} , we can determine the corresponding electric and magnetic

fields as [18]

$$\mathbf{B} = \nabla \times \mathbf{A}, \quad (5.73)$$

$$\mathbf{E} = -\nabla\phi - \frac{\partial\mathbf{A}}{\partial t}. \quad (5.74)$$

In free space, Maxwell's equations are reduced to

$$\nabla \cdot \mathbf{E} = \rho, \quad (5.75)$$

$$\nabla \cdot \mathbf{B} = 0, \quad (5.76)$$

$$\nabla \times \mathbf{E} = -\frac{\partial\mathbf{B}}{\partial t}, \quad (5.77)$$

$$\nabla \times \mathbf{B} = \varepsilon_0\mu_0 \frac{\partial\mathbf{E}}{\partial t} + \mathbf{J}. \quad (5.78)$$

These four equations can be represented in terms of the scalar and vector potentials and may be rewritten as two coupled differential equations:

$$\nabla(\nabla \cdot \mathbf{A}) - \nabla^2\mathbf{A} + \frac{1}{c^2} \frac{\partial}{\partial t} \nabla\phi + \frac{1}{c^2} \frac{\partial^2\mathbf{A}}{\partial t^2} = \mu_0\mathbf{J}, \quad (5.79)$$

and

$$-\varepsilon_0\nabla^2\phi - \varepsilon_0\nabla \cdot \frac{\partial\mathbf{A}}{\partial t} = \rho, \quad (5.80)$$

where we have used the following vector identity

$$\nabla \times \nabla \times \mathbf{A} = \nabla(\nabla \cdot \mathbf{A}) - \nabla^2\mathbf{A}. \quad (5.81)$$

The current and charge densities, \mathbf{J} and ρ , are the source terms of these two coupled differential equations, which can be used to determine the fields. As we know, for given electric and magnetic fields, there are multiple choices of pairs of the corresponding vector and scalar potentials. Two pairs of potentials, (ϕ, \mathbf{A}) and (ϕ', \mathbf{A}') , that give the same electromagnetic fields are related by a gauge transformation [18, 141]:

$$\mathbf{A}' = \mathbf{A} + \nabla\lambda, \quad (5.82)$$

$$\phi' = \phi - \frac{\partial\lambda}{\partial t}. \quad (5.83)$$

A gauge in electromagnetics then means a specific relation between the vector and scalar potentials. Generally, to simplify the problem, the Coulomb gauge is used:

$$\nabla \cdot \mathbf{A} = 0. \quad (5.84)$$

In this gauge, the vector potential is transverse. One gauge can be transformed to another gauge by using the above gauge transformation. With the Coulomb gauge, the two differential equations then become

$$-\nabla^2\mathbf{A} + \frac{1}{c^2} \frac{\partial}{\partial t} \nabla\phi + \frac{1}{c^2} \frac{\partial^2\mathbf{A}}{\partial t^2} = \mu_0\mathbf{J}, \quad (5.85)$$

$$-\nabla^2\phi = \rho/\varepsilon_0. \quad (5.86)$$

The second equation then is in the form of Poisson's equation of electrostatics whose solution is the Coulomb potential between charged particles. The first equation can be simplified further by using Helmholtz's theorem such that a vector field can be decomposed as a sum of transverse and longitudinal parts of the field [142]:

$$\mathbf{J} = \mathbf{J}_T + \mathbf{J}_L, \quad (5.87)$$

where

$$\nabla \cdot \mathbf{J}_T = 0, \quad (5.88)$$

$$\nabla \times \mathbf{J}_L = \mathbf{0}. \quad (5.89)$$

Eq.(5.85) then can be separated as

$$-\nabla^2 \mathbf{A} + \frac{1}{c^2} \frac{\partial^2 \mathbf{A}}{\partial t^2} = \mu_0 \mathbf{J}_T, \quad (5.90)$$

and

$$\frac{1}{c^2} \frac{\partial}{\partial t} \nabla \phi = \mu_0 \mathbf{J}_L. \quad (5.91)$$

The first equation is the equation of motion of the vector potential in the Coulomb gauge. The second equation together with Eq.(5.86) give the equation of charge conservation:

$$\nabla \cdot \mathbf{J}_L = -\frac{\partial \rho}{\partial t}. \quad (5.92)$$

The electric field can be separated accordingly as

$$\mathbf{E} = \mathbf{E}_T + \mathbf{E}_L, \quad (5.93)$$

where

$$\mathbf{E}_T = -\frac{\partial \mathbf{A}}{\partial t}, \quad (5.94)$$

$$\mathbf{E}_L = -\nabla \phi. \quad (5.95)$$

The benefit of using the Coulomb gauge is that, as we can see, it offers a clean separation of the field equations into two different and independent sets so that the transverse equations describe electromagnetic waves and the longitudinal equations describe the fields given by the charge density [141].

5.5.2 Free field quantisation

In this case, we consider a region in which the transverse current density \mathbf{J}_T vanishes and the equation of motion of the vector potential then becomes

$$-\nabla^2 \mathbf{A} + \frac{1}{c^2} \frac{\partial^2 \mathbf{A}}{\partial t^2} = 0. \quad (5.96)$$

We then consider a cubic cavity of space where the length of each side is L . This is not a real cavity but the quantisation cavity, and the electromagnetic waves contained within are not standing waves

but running waves with periodic boundary conditions [141]. The vector potential in this scenario can consequently be written in terms of a superposition of the allowed modes in the cavity:

$$\mathbf{A}(\mathbf{r}, t) = \sum_{\mathbf{k}} \sum_{\sigma=1,2} \mathbf{e}_{\mathbf{k},\sigma} A_{\mathbf{k},\sigma}(\mathbf{r}, t), \quad (5.97)$$

where

$$A_{\mathbf{k},\sigma}(\mathbf{r}, t) = A_{\mathbf{k},\sigma}(t)e^{i\mathbf{k}\cdot\mathbf{r}} + A_{\mathbf{k},\sigma}^*(t)e^{-i\mathbf{k}\cdot\mathbf{r}}, \quad (5.98)$$

and the components of the wave vectors satisfy

$$k_x = 2\pi\nu_x/L, \quad k_y = 2\pi\nu_y/L, \quad k_z = 2\pi\nu_z/L, \quad (5.99)$$

where ν_x, ν_y, ν_z are arbitrary integers. The wave vector \mathbf{k} and the unit polarisation vectors, $\mathbf{e}_{\mathbf{k},1}$ and $\mathbf{e}_{\mathbf{k},2}$ form a Cartesian coordinate system, as the Coulomb gauge constrains the wave vector to be normal to the polarisation:

$$\mathbf{k} \cdot \mathbf{e}_{\mathbf{k},\sigma} = 0, \quad (5.100)$$

and the polarization vectors can be chosen such that they are orthogonal to each other:

$$\mathbf{e}_{\mathbf{k},\sigma} \cdot \mathbf{e}_{\mathbf{k},\sigma'} = \delta_{\sigma,\sigma'}, \quad (5.101)$$

where the Kronecker delta is unity when its two indices are identical and zero otherwise. This means each mode component $A_{\mathbf{k},\sigma}(t)$ (and its complex conjugate) is independent of other modes. These cavity modes independently satisfy Eq.(5.96),

$$k^2 A_{\mathbf{k},\sigma}(t) + \frac{1}{c^2} \frac{\partial^2 A_{\mathbf{k},\sigma}(t)}{\partial t^2} = 0. \quad (5.102)$$

Noticeably, this equation is already in the form of the equation of motion of a classical simple harmonic oscillator:

$$\frac{\partial^2 A_{\mathbf{k},\sigma}(t)}{\partial t^2} + \omega_k^2 A_{\mathbf{k},\sigma}(t) = 0, \quad (5.103)$$

when the mode angular frequency ω_k is related to the magnitude of the wave vector by $\omega_k = kc$. The solution of a simple harmonic oscillator then gives us the time dependence of the components as

$$A_{\mathbf{k},\sigma}(t) = A_{\mathbf{k},\sigma} e^{-i\omega_k t}. \quad (5.104)$$

Eq.(5.98) then becomes

$$\mathbf{A}_{\mathbf{k},\sigma}(\mathbf{r}, t) = A_{\mathbf{k},\sigma} e^{i(\mathbf{k}\cdot\mathbf{r} - \omega_k t)} + A_{\mathbf{k},\sigma}^* e^{-i(\mathbf{k}\cdot\mathbf{r} - \omega_k t)}. \quad (5.105)$$

From this equation, the transverse electric and magnetic fields are given as,

$$\mathbf{E}_T(\mathbf{r}, t) = \sum_{\mathbf{k}} \sum_{\sigma=1,2} \mathbf{e}_{\mathbf{k},\sigma} E_{\mathbf{k},\sigma}(\mathbf{r}, t), \quad (5.106)$$

where

$$E_{\mathbf{k},\sigma}(\mathbf{r}, t) = i\omega_k \left(A_{\mathbf{k},\sigma} e^{i(\mathbf{k}\cdot\mathbf{r}-\omega_k t)} - A_{\mathbf{k},\sigma}^* e^{-i(\mathbf{k}\cdot\mathbf{r}-\omega_k t)} \right), \quad (5.107)$$

and

$$\mathbf{B}(\mathbf{r}, t) = \sum_{\mathbf{k}} \sum_{\sigma=1,2} \frac{\mathbf{k} \times \mathbf{e}_{\mathbf{k},\sigma}}{k} B_{\mathbf{k},\sigma}(\mathbf{r}, t), \quad (5.108)$$

with

$$B_{\mathbf{k},\sigma}(\mathbf{r}, t) = ik \left(A_{\mathbf{k},\sigma} e^{i(\mathbf{k}\cdot\mathbf{r}-\omega_k t)} - A_{\mathbf{k},\sigma}^* e^{-i(\mathbf{k}\cdot\mathbf{r}-\omega_k t)} \right). \quad (5.109)$$

The ratio of the magnitudes of the electric and magnetic fields is equal to the velocity of light in free space as expected. The total energy of the electromagnetic waves inside the cavity is given by [141]

$$\mathcal{E} = \frac{1}{2} \int_{\text{cavity}} dV \left(\varepsilon_0 \mathbf{E}_T \cdot \mathbf{E}_T + \frac{1}{\mu_0} \mathbf{B} \cdot \mathbf{B} \right). \quad (5.110)$$

With Eq.(5.99), we find

$$\int_{\text{cavity}} dV \exp [\pm i(\mathbf{k} - \mathbf{k}') \cdot \mathbf{r}] = V \delta_{\mathbf{k},\mathbf{k}'}, \quad (5.111)$$

where $V = L^3$ is the volume of the cavity. Substituting the electric and magnetic fields given in Eqs.(5.107) and (5.109) into Eq.(5.110) and using the above spatial integration, the total radiation energy within the cavity can be written as

$$\begin{aligned} \mathcal{E} = & \frac{V}{2} \sum_{\mathbf{k}} \sum_{\sigma,\sigma'} \left\{ (A_{\mathbf{k},\sigma} A_{\mathbf{k},\sigma'}^* + A_{\mathbf{k},\sigma}^* A_{\mathbf{k},\sigma'}) \left(\varepsilon_0 \omega_k^2 \mathbf{e}_{\mathbf{k},\sigma} \cdot \mathbf{e}_{\mathbf{k},\sigma'} + \mu_0^{-1} (\mathbf{k} \times \mathbf{e}_{\mathbf{k},\sigma}) \cdot (\mathbf{k} \times \mathbf{e}_{\mathbf{k},\sigma'}) \right) \right. \\ & \left. - (A_{\mathbf{k},\sigma} A_{-\mathbf{k},\sigma'} e^{-2i\omega_k t} + A_{\mathbf{k},\sigma}^* A_{-\mathbf{k},\sigma'}^* e^{2i\omega_k t}) \left(\varepsilon_0 \omega_k^2 \mathbf{e}_{\mathbf{k},\sigma} \cdot \mathbf{e}_{-\mathbf{k},\sigma'} - \mu_0^{-1} (\mathbf{k} \times \mathbf{e}_{\mathbf{k},\sigma}) \cdot (\mathbf{k} \times \mathbf{e}_{-\mathbf{k},\sigma'}) \right) \right\} \end{aligned} \quad (5.112)$$

We note that $(\mathbf{k} \times \mathbf{e}_{\mathbf{k},\sigma}) \cdot (\mathbf{k} \times \mathbf{e}_{\pm\mathbf{k},\sigma'}) = k^2 \mathbf{e}_{\mathbf{k},\sigma} \cdot \mathbf{e}_{\pm\mathbf{k},\sigma'}$. Therefore, with $\omega = kc$, the second term in the summation, the time dependent term, vanishes. Finally, the total radiative energy in the cavity is then time-independent and can be expressed as

$$\mathcal{E} = \sum_{\mathbf{k}} \sum_{\sigma} \mathcal{E}_{\mathbf{k},\sigma}, \quad (5.113)$$

with

$$\mathcal{E}_{\mathbf{k},\sigma} = \varepsilon_0 V \left(A_{\mathbf{k},\sigma} A_{\mathbf{k},\sigma}^* + A_{\mathbf{k},\sigma}^* A_{\mathbf{k},\sigma} \right). \quad (5.114)$$

Let us briefly review the quantum mechanics of a harmonic oscillator system. The Hamiltonian of a one-dimensional harmonic oscillator is of the form

$$\hat{H} = \frac{\hat{p}^2}{2m} + \frac{1}{2} m \omega^2 \hat{q}^2, \quad (5.115)$$

where the position \hat{q} and momentum \hat{p} operators satisfy the well-known commutation relation

$$[\hat{q}, \hat{p}] = i\hbar. \quad (5.116)$$

On the other hand, one can also express the Hamiltonian in terms of a pair of dimensionless operators as

$$\hat{H} = \frac{1}{2}\hbar\omega (\hat{a}\hat{a}^\dagger + \hat{a}^\dagger\hat{a}), \quad (5.117)$$

where \hat{a} and \hat{a}^\dagger are the annihilation and creation operators which obey the following commutation relation:

$$[\hat{a}, \hat{a}^\dagger] = \hat{a}\hat{a}^\dagger - \hat{a}^\dagger\hat{a} = 1. \quad (5.118)$$

The relations between the annihilation and creation operators and the position and momentum operators are given by

$$\hat{a} = \sqrt{\frac{1}{2m\hbar\omega}}(m\omega\hat{q} + i\hat{p}), \quad (5.119)$$

$$\hat{a}^\dagger = \sqrt{\frac{1}{2m\hbar\omega}}(m\omega\hat{q} - i\hat{p}). \quad (5.120)$$

The effect of the annihilation operator on the eigenstates of the Hamiltonian operator is to shift the energy eigenstate down by one level as

$$\sqrt{n}|n-1\rangle = \hat{a}|n\rangle, \quad (5.121)$$

where we define $|n\rangle$ to be the energy eigenstate associated with the energy eigenvalue $\hbar\omega(n+1/2)$. In the case of the ground state, as the energy of the system cannot be negative and there is no energy level to go down, the result of applying the annihilation operator to the ground state is zero:

$$\hat{a}|0\rangle = 0. \quad (5.122)$$

In contrast, the creation operator causes the energy eigenstate go up by one as

$$\sqrt{n+1}|n+1\rangle = \hat{a}^\dagger|n\rangle. \quad (5.123)$$

To quantise the electromagnetic fields, we treat each mode in the cavity as an independent quantum harmonic oscillator. This may be achieved by promoting the energy of each mode to the corresponding quantum harmonic oscillator Hamiltonian. For example, from Eq.(5.114), for the mode (\mathbf{k}, σ) :

$$\mathcal{E}_{\mathbf{k},\sigma} = \varepsilon_0 V (A_{\mathbf{k},\sigma} A_{\mathbf{k},\sigma}^* + A_{\mathbf{k},\sigma}^* A_{\mathbf{k},\sigma}) \rightarrow \hat{H}_{\mathbf{k},\sigma} = \frac{\hbar\omega_k}{2} (\hat{a}_{\mathbf{k},\sigma} \hat{a}_{\mathbf{k},\sigma}^\dagger + \hat{a}_{\mathbf{k},\sigma}^\dagger \hat{a}_{\mathbf{k},\sigma}), \quad (5.124)$$

The total Hamiltonian then becomes

$$\hat{H} = \sum_{\mathbf{k}} \sum_{\sigma} \hat{H}_{\mathbf{k},\sigma} = \sum_{\mathbf{k}} \sum_{\sigma} \frac{\hbar\omega_k}{2} (\hat{a}_{\mathbf{k},\sigma} \hat{a}_{\mathbf{k},\sigma}^\dagger + \hat{a}_{\mathbf{k},\sigma}^\dagger \hat{a}_{\mathbf{k},\sigma}). \quad (5.125)$$

This means the conversions from the classical amplitudes $A_{\mathbf{k},\sigma}$ of the vector potential to the corresponding quantum mechanical mode operators are

$$A_{\mathbf{k},\sigma} \rightarrow \sqrt{\frac{\hbar}{2\varepsilon_0 V \omega_k}} \hat{a}_{\mathbf{k},\sigma}, \quad (5.126)$$

$$A_{\mathbf{k},\sigma}^* \rightarrow \sqrt{\frac{\hbar}{2\varepsilon_0 V \omega_k}} \hat{a}_{\mathbf{k},\sigma}^\dagger. \quad (5.127)$$

The commutation relation between the creation and annihilation operators becomes

$$\left[\hat{a}_{\mathbf{k},\sigma}, \hat{a}_{\mathbf{k}',\sigma'}^\dagger \right] = \delta_{\mathbf{k},\mathbf{k}'} \delta_{\sigma,\sigma'}. \quad (5.128)$$

Substituting this back into the classical vector potential, the quantum version of the vector potential therefore becomes

$$\hat{\mathbf{A}}(\mathbf{r}, t) = \sum_{\mathbf{k}} \sum_{\sigma} \mathbf{e}_{\mathbf{k},\sigma} \hat{A}_{\mathbf{k},\sigma}(\mathbf{r}, t), \quad (5.129)$$

with

$$\hat{A}_{\mathbf{k},\sigma}(\mathbf{r}, t) = \sqrt{\frac{\hbar}{2\varepsilon_0 V \omega_k}} \left(\hat{a}_{\mathbf{k},\sigma} e^{i(\mathbf{k}\cdot\mathbf{r} - \omega_k t)} + \hat{a}_{\mathbf{k},\sigma}^\dagger e^{-i(\mathbf{k}\cdot\mathbf{r} - \omega_k t)} \right). \quad (5.130)$$

The electric field are replaced by their associated quantum operator accordingly as

$$\hat{\mathbf{E}}_{\mathbf{T}}(\mathbf{r}, t) = \hat{\mathbf{E}}_{\mathbf{T}}^+(\mathbf{r}, t) + \hat{\mathbf{E}}_{\mathbf{T}}^-(\mathbf{r}, t), \quad (5.131)$$

where

$$\hat{\mathbf{E}}_{\mathbf{T}}^+(\mathbf{r}, t) = i \sum_{\mathbf{k}} \sum_{\sigma} \sqrt{\frac{\hbar \omega_k}{2\varepsilon_0 V}} \mathbf{e}_{\mathbf{k},\sigma} \hat{a}_{\mathbf{k},\sigma} e^{i(\mathbf{k}\cdot\mathbf{r} - \omega_k t)}, \quad (5.132)$$

$$\hat{\mathbf{E}}_{\mathbf{T}}^-(\mathbf{r}, t) = -i \sum_{\mathbf{k}} \sum_{\sigma} \sqrt{\frac{\hbar \omega_k}{2\varepsilon_0 V}} \mathbf{e}_{\mathbf{k},\sigma} \hat{a}_{\mathbf{k},\sigma}^\dagger e^{-i(\mathbf{k}\cdot\mathbf{r} - \omega_k t)}. \quad (5.133)$$

These two parts of the electric field operator are known as the positive and negative frequency parts respectively according to the sign of the frequencies in the exponential arguments [141]. On the other hand, the magnetic field operator becomes

$$\hat{\mathbf{B}}(\mathbf{r}, t) = \hat{\mathbf{B}}^+(\mathbf{r}, t) + \hat{\mathbf{B}}^-(\mathbf{r}, t), \quad (5.134)$$

with

$$\hat{\mathbf{B}}^+(\mathbf{r}, t) = i \sum_{\mathbf{k}} \sum_{\sigma} \sqrt{\frac{\hbar}{2\varepsilon_0 V \omega_k}} \mathbf{k} \times \mathbf{e}_{\mathbf{k},\sigma} \hat{a}_{\mathbf{k},\sigma} e^{i(\mathbf{k}\cdot\mathbf{r} - \omega_k t)}, \quad (5.135)$$

$$\hat{\mathbf{B}}^-(\mathbf{r}, t) = -i \sum_{\mathbf{k}} \sum_{\sigma} \sqrt{\frac{\hbar}{2\varepsilon_0 V \omega_k}} \mathbf{k} \times \mathbf{e}_{\mathbf{k},\sigma} \hat{a}_{\mathbf{k},\sigma}^\dagger e^{-i(\mathbf{k}\cdot\mathbf{r} - \omega_k t)}. \quad (5.136)$$

At this point we can define a single photon state in the mode (\mathbf{k}, σ) as the first energy state of the corresponding harmonic oscillator Hamiltonian:

$$|1\rangle_{\mathbf{k},\sigma} = \hat{a}_{\mathbf{k},\sigma}^\dagger |0\rangle_{\mathbf{k},\sigma}. \quad (5.137)$$

In the general case, a single photon state can be a superposition of multiple modes with amplitudes described by $\xi_{\mathbf{k},\sigma}$ as [141]

$$|1\rangle_{\xi} = \sum_{\mathbf{k}} \sum_{\sigma} \xi_{\mathbf{k},\sigma} \hat{a}_{\mathbf{k},\sigma}^\dagger |0\rangle, \quad (5.138)$$

where we represent the ground state or the vacuum state as the tensor product of the ground states of all possible modes [143]

$$|0\rangle = \prod_{\mathbf{k},\sigma} |0\rangle_{\mathbf{k},\sigma}, \quad (5.139)$$

and the probability amplitudes satisfy the normalisation condition:

$$\sum_{\mathbf{k}} \sum_{\sigma} |\xi_{\mathbf{k},\sigma}|^2 = 1. \quad (5.140)$$

The field quantisation inside the cavity can be extended into real free space by taking the limit in which the length of the cavity goes to infinity. In this limit, the discrete set of the allowed wave vectors \mathbf{k} becomes a continuous set as the components of the allowed wave vector k_x , k_y and k_z can be arbitrary. The summation over all possible wave vectors is changed to be a continuous integral as

$$\sum_{\mathbf{k}} \rightarrow \frac{V}{(2\pi)^3} \int d^3\mathbf{k}. \quad (5.141)$$

The commutation relation in Eq.(5.128) becomes [144]

$$[\hat{a}_{\sigma}(\mathbf{k}), \hat{a}_{\sigma'}^{\dagger}(\mathbf{k}')] = \delta^3(\mathbf{k} - \mathbf{k}') \delta_{\sigma,\sigma'}, \quad (5.142)$$

where the Kronecker delta is now replaced by the Dirac delta function. The annihilation operator in the discrete regime does not have the same dimension as its continuous version as they are related by [144]

$$\hat{a}_{\mathbf{k},\sigma} = \sqrt{\frac{(2\pi)^3}{V}} \hat{a}_{\sigma}(\mathbf{k}). \quad (5.143)$$

Therefore, we can use the results of the field quantisation in the cavity so far to obtain the quantisation in free space straightforwardly. In the continuous limit, the positive frequency part of the vector potential in Eq.(5.130) becomes

$$\hat{\mathbf{A}}^+(\mathbf{r}, t) = \sum_{\sigma} \int d^3\mathbf{k} \sqrt{\frac{\hbar}{16\pi^3 \epsilon_0 \omega}} \hat{\mathbf{e}}_{\sigma}(\mathbf{k}) \hat{a}_{\sigma}(\mathbf{k}) e^{i(\mathbf{k}\cdot\mathbf{r} - \omega t)}. \quad (5.144)$$

Using the Coulomb gauge, the electric and magnetic field operators can be obtained directly.

5.6 Paraxial approximation

The paraxial approximation is normally used in Gaussian optics to describe an electromagnetic wave in the form of an optical beam when the rays propagating through lenses only make small angles with the optical axis, and spherical aberration is suppressed [145]. Normally, it is used to describe a laser beam which has finite cross section [146, 147]. In this section, we focus on an optical beam propagating along the positive z -axis. We factorise the vector potential into the product of a complex function $U(\mathbf{r})$ and the solution of a plane wave propagating in the z -direction as follows:

$$\mathbf{A}(\mathbf{r}, t) = U(\mathbf{r}) e^{i(kz - \omega t)} \mathbf{x}, \quad (5.145)$$

where k is the magnitude of the wave vector and \mathbf{x} is the polarisation unit vector. We normally call $U(\mathbf{r})$ the complex envelope as it is the function that describes the shape of the beam [115]. The envelope is a slowly varying function of z compared to the scale of the wavelength λ [115, 147]:

$$\frac{\partial U}{\partial z} \ll \frac{U}{\lambda} \sim kU, \quad (5.146)$$

in other words,

$$\frac{\partial^2 U}{\partial z^2} \ll k \frac{\partial U}{\partial z} \ll k^2 U. \quad (5.147)$$

The exponential term in Eq.(5.145) is then the main part that describes the z dependence of the vector potential. Substituting this form of the vector potential to Eq.(5.96), we have

$$\nabla_{\perp}^2 U - 2ik\partial_z U = 0, \quad (5.148)$$

where we have used the dispersion relation, $\omega = kc$, and ∇_{\perp} is the derivatives with respect to the transverse directions. We have dropped the second derivative with respect to z of the function U as it is much smaller than the remaining terms. The above equation is called the paraxial wave equation [147]. The vector polarisation \mathbf{x} has been omitted as each term in Eq.(5.96) has the same unit vector. We can, therefore, fully concentrate on the components of the vector field. We notice that, in contrast to plane electromagnetic waves, the derivative of a paraxial wave in the transverse direction is nonzero, which indicates that the wavefront of a paraxial wave is different to that of plane waves. The local wave vectors which are normal to the wavefront locally are not necessarily parallel to the propagation direction. However, this does not contradict Maxwell's equations as the corresponding electric and magnetic fields are still divergenceless [146, 148]. The local polarisation of the electric field is perpendicular to the local wave vector and tangential to the local wavefront as depicted in figure 5.4. The modes of light that satisfy the paraxial wave equation are, for example, Laguerre-Gaussian and Hermite-Gaussian *etc* [147].

Paraxial light can be written as a superposition of plane waves that propagate nearly parallel to the z -axis: $k_{\perp} \ll k$, where k_{\perp} is the transverse component of the wave vector [147]. The z component of the waves vector of these plane wave can be approximated as

$$k_z = \sqrt{k^2 - k_x^2 - k_y^2} \approx k - \frac{(k_x^2 + k_y^2)}{2k}. \quad (5.149)$$

The amplitudes of those plane waves for which the wave vector significantly diverges from the z -axis are suppressed.

5.7 Quantisation of paraxial light

In this section, we use information discussed in this chapter so far to derive the form of electric and magnetic field operators for paraxial beams. We start by changing the integration variables in Eq.(5.144) as, with the paraxial approximation,

$$\int d^3\mathbf{k} \approx \frac{1}{c} \int d\omega \int d^2k_{\perp}, \quad (5.150)$$

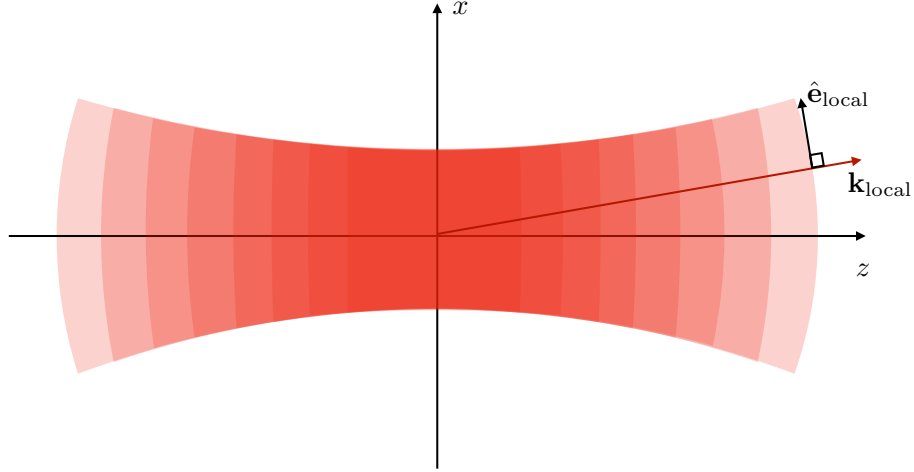


Figure 5.4: The wavefront of the Gaussian beam travelling in the positive z -direction has nonzero curvature. In the figure the local polarisation unit vector $\hat{\mathbf{e}}_{\text{local}}$ is perpendicular and tangential to the local wave vector $\mathbf{k}_{\text{local}}$ and the local wavefront respectively. The direction of the polarisation vector depends on the location in the beam.

because $k_z \approx k = \omega/c$. As we consider a beam propagating in the positive z -direction, we then take the integration from $\omega = 0$ to $\omega = \infty$. Applying Eq.(5.149), the positive electric field operator then becomes

$$\hat{\mathbf{E}}^+(\mathbf{r}, t) = i \int_0^\infty d\omega \int d^2k_\perp \sqrt{\frac{\hbar\omega}{16\pi^3\varepsilon_0 c}} \exp[i(kz - \omega t)] \sum_\sigma \hat{\mathbf{e}}_\sigma(\mathbf{k}_\perp, \omega) \hat{a}_\sigma(\mathbf{k}_\perp, \omega) \times \exp\left[\mathbf{i}\mathbf{k}_\perp \cdot \mathbf{x}_\perp - iz \frac{k_\perp^2}{2k}\right], \quad (5.151)$$

where $\mathbf{x}_\perp = (x, y)$. The annihilation operator $\hat{a}_\sigma(\mathbf{k}_\perp, \omega)$ in Eq.(5.144) has been replaced by the new operator $\sqrt{c}\hat{a}_\sigma(\mathbf{k}_\perp, \omega)$. The commutation relation for this annihilation operator is

$$\left[\hat{a}_\sigma(\mathbf{k}_\perp, \omega), \hat{a}_{\sigma'}^\dagger(\mathbf{k}'_\perp, \omega')\right] = \delta_{\sigma,\sigma'} \delta^2(\mathbf{k}_\perp - \mathbf{k}'_\perp) \delta(\omega - \omega'). \quad (5.152)$$

This electric field is in the form of a superposition of electric field operators of plane waves, propagating nearly parallel to the z -axis, as depicted in figure 5.5. For a plane wave component of the superposition with local wave vector $\mathbf{k}_{\text{local}} = (k_x, k_y, k - k_\perp^2/2k)$, we can set the local polarisation unit vectors to be

$$\hat{\mathbf{e}}_1(\mathbf{k}_\perp, \omega) \approx \hat{\mathbf{x}} - \hat{\mathbf{z}}k_x/k, \quad (5.153)$$

$$\hat{\mathbf{e}}_2(\mathbf{k}_\perp, \omega) \approx \hat{\mathbf{y}} - \hat{\mathbf{z}}k_y/k, \quad (5.154)$$

which are perpendicular to each other and to the local wave vector $\mathbf{k}_{\text{local}}$. We define $\hat{\mathbf{x}}$, $\hat{\mathbf{y}}$ and $\hat{\mathbf{z}}$ to be unit vectors in the x -, y - and z -directions. We find that

$$i\hat{\mathbf{x}}_\sigma \cdot \nabla_\perp \exp(\mathbf{i}\mathbf{k}_\perp \cdot \mathbf{x}_\perp) = -k_{x_\sigma} \exp(\mathbf{i}\mathbf{k}_\perp \cdot \mathbf{x}_\perp), \quad (5.155)$$

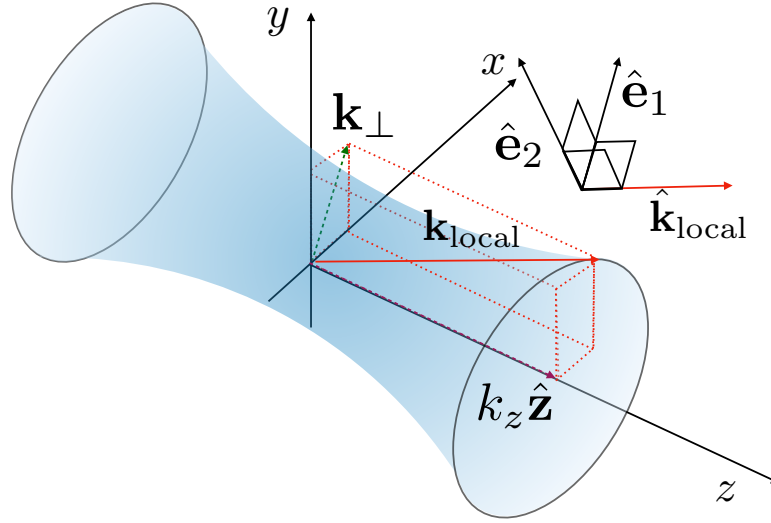


Figure 5.5: The wave vector $\mathbf{k}_{\text{local}}$ of a local plane wave component of the superposition is nearly parallel to the propagation direction. The polarisation unit vectors of the plane wave are illustrated by the arrows $\hat{\mathbf{e}}_1$ and $\hat{\mathbf{e}}_2$.

where $\hat{\mathbf{x}}_\sigma = \hat{\mathbf{x}}, \hat{\mathbf{y}}$. The electric field operator becomes

$$\hat{\mathbf{E}}^+(\mathbf{r}, t) = \frac{i}{c} \int_0^\infty d\omega \int d^2k_\perp \sqrt{\frac{\hbar\omega}{16\pi^3\epsilon_0 c}} \exp[i(kz - \omega t)] \sum_\sigma \hat{a}_\sigma(\mathbf{k}_\perp, \omega) \times \left(\hat{\mathbf{x}}_\sigma + \frac{i}{k} \hat{\mathbf{z}}(\hat{\mathbf{x}}_\sigma \cdot \nabla_\perp) \right) \exp \left[i\mathbf{k}_\perp \cdot \mathbf{x}_\perp - iz \frac{k_\perp^2}{2k} \right], \quad (5.156)$$

We then define a new annihilation operator as

$$\hat{a}_\sigma(\mathbf{x}_\perp, z, \omega) \equiv \frac{1}{2\pi} \int d^2k_\perp \hat{a}_\sigma(\mathbf{k}_\perp, \omega) \exp \left[i\mathbf{k}_\perp \cdot \mathbf{x}_\perp - iz \frac{k_\perp^2}{2k} \right]. \quad (5.157)$$

The commutation relation for the new operators is inherited from the commutation relation in Eq.(5.152) as

$$\left[\hat{a}_\sigma(\mathbf{x}_\perp, z, \omega), \hat{a}_{\sigma'}^\dagger(\mathbf{x}'_\perp, z, \omega') \right] = \delta_{\sigma, \sigma'} \delta(\mathbf{x}_\perp - \mathbf{x}'_\perp) \delta(\omega - \omega'). \quad (5.158)$$

We can use the following relation to evaluate the integration in Eq.(5.157) [149, 150]:

$$\frac{1}{2\pi} \exp \left[i\mathbf{k}_\perp \cdot \mathbf{x}_\perp - iz \frac{k_\perp^2}{2k} \right] = \sum_{n,m} \tilde{\psi}_{nm}^*(\mathbf{k}_\perp, \omega) \psi_{nm}(\mathbf{x}_\perp, z, \omega), \quad (5.159)$$

where $\psi_{nm}(\mathbf{x}_\perp, z, \omega)$ is a complete orthonormal set of functions

$$\int \psi_{nm}^*(\mathbf{x}_\perp, z, \omega) \psi_{n'm'}(\mathbf{x}_\perp, z, \omega) d^2x = \delta_{n,n'} \delta_{m,m'}, \quad (5.160)$$

$$\sum_{n,m} \psi_{nm}^*(\mathbf{x}_\perp, z, \omega) \psi_{nm}(\mathbf{x}'_\perp, z, \omega) = \delta(\mathbf{x} - \mathbf{x}'), \quad (5.161)$$

and n and m are integers. The complex function $\tilde{\psi}_{nm}(\mathbf{k}_\perp, \omega)$ is the two dimensional Fourier transform of the function $\psi_{nm}(\mathbf{x}_\perp, z = 0, \omega)$:

$$\tilde{\psi}_{nm}(\mathbf{k}_\perp, \omega) = \frac{1}{2\pi} \int \psi_{nm}(\mathbf{x}_\perp, z = 0, \omega) \exp(-i\mathbf{x}_\perp \cdot \mathbf{k}_\perp) d^2x. \quad (5.162)$$

The set of the functions $\psi_{nm}(\mathbf{x}_\perp, z, \omega)$ can be either Hermite-Gaussian or Laguerre-Gaussian which are two different sets of the paraxial solutions [149, 150]. The integration of Eq.(5.157) becomes

$$\hat{a}_\sigma(\mathbf{x}_\perp, z, \omega) = \sum_{n,m} \hat{a}_{\sigma nm}(\omega) \psi_{nm}(\mathbf{x}_\perp, z, \omega), \quad (5.163)$$

where we have define the operator $\hat{a}_{\sigma nm}(\omega)$ as

$$\hat{a}_{\sigma nm}(\omega) = \int d^2k_\perp \tilde{\psi}_{nm}^*(\mathbf{k}_\perp, \omega) \hat{a}_\sigma(\mathbf{k}_\perp, \omega). \quad (5.164)$$

The new defined operator $\hat{a}_{\sigma nm}(\omega)$ obeys the following commutation relation:

$$\left[\hat{a}_{\sigma nm}(\omega), \hat{a}_{\sigma' n' m'}^\dagger(\omega') \right] = \delta_{\sigma, \sigma'} \delta_{n, n'} \delta_{m, m'} \delta(\omega - \omega'). \quad (5.165)$$

Therefore, the positive-frequency part of the electric field can be written as

$$\hat{\mathbf{E}}^+(\mathbf{r}, t) = i \int_0^\infty d\omega \sqrt{\frac{\hbar\omega}{4\pi\epsilon_0 c}} \exp[i(kz - \omega t)] \sum_{\sigma, n, m} \hat{a}_{\sigma nm} \left(\hat{\mathbf{x}}_\sigma + \frac{i}{k} \hat{\mathbf{z}}(\hat{\mathbf{x}}_\sigma \cdot \nabla_\perp) \right) \psi_{nm}(\mathbf{x}_\perp, z, \omega). \quad (5.166)$$

The corresponding magnetic field operator can be obtained by the third Maxwell equation. For an optical beam in a particular mode, we can obtain its electric field operator by replacing the superposition over all possible modes in the equation by the desired mode.

We can summarise this chapter as follows. We have reviewed the Maxwell equations and showed how plane wave solutions and boundary conditions are obtained from them. The optical force and torque which are the main ingredient of the next chapter, to describe the mechanism of angular momentum transfer from light to a dielectric medium, have been discussed and carefully explained. The conventional quantisation of free electromagnetic fields have been given, and from that the quantisation of paraxial light is obtained.

Chapter 6

Angular momentum transfer from light to a dielectric medium by total internal reflection

In this chapter, we study the mechanism of angular momentum transfer from light to a lossless dielectric medium when the light undergoes total internal reflection. We use the dipole-based force density \mathbf{f}^d to calculate the total force and torque acting on the dielectric [131]. For definiteness, we consider the light beam to be in a Laguerre-Gaussian mode with a zero radial index, $p = 0$. The incident beam is assumed to be a paraxial single-photon pulse with a narrow-bandwidth spectrum. Every quantity given in this chapter is normalised for one photon. The size of the dielectric is assumed to be very large compared to the pulse length. This assumption allows us to treat reflection and transmission at each interface of the dielectric separately. The central wavelength of the photon pulses is taken to be much smaller than the beam waist. We consider the case that the refractive index, $n(\omega)$, of the medium varies insignificantly in the range of the allowed bandwidth of single-photon pulses. We can, therefore, think of the medium to be nondispersive. The shape of the pulses is constant along its propagation. The physical results given in this chapter may also be obtained equivalently by classical electrodynamics. The quantum picture, however, gives us the key advantage so that we can eliminate the complications arising from the coexistence of reflection and transmission at each interface by conditioning the calculation results on the transmission or reflection of the photon, which helps us simplify the analysis and also give a clear picture of the physical interaction between the dielectric and photons. This work presented in this chapter is an original contribution and was published in *J. Opt. Soc. Am. B* [2].

This chapter consists of 8 sections. We start by introducing the angular spectrum representation of Laguerre-Gaussian beams, which is the main ingredient of the rest of the chapter, in the first section. We then use the angular spectrum representation together with the law of reflection to determine the form of the reflected beams in section 6.2. In section 6.3, we quantise both the incident and reflected beams. The optical force and torque on the dielectric with the presence of

the boundary are analysed in section 6.4, and we identify the torque that contributes to the change of the angular momentum of the dielectric and evaluate its quantity in section 6.5. The beam shift effect is analysed and evaluated in section 6.6 to verify that there is a part of the effective torque associated with the change of the extrinsic angular momentum of the photon pulse. In section 6.7, we use the part of effective torque associated with the change of intrinsic angular momentum of a single photon to analyse the mechanism of the angular momentum transfer between a photon and an M-shaped Dove prism. The paradoxical of expressing optical force and torque densities in terms of polarisation \mathbf{P} and using its conventional form: $\mathbf{P} = \epsilon_0(n^2 - 1)\mathbf{E}$ when the boundary is present, is explicitly demonstrated in section 6.8.

6.1 Angular spectrum representation of a Laguerre-Gaussian beam

We start this chapter by reviewing the angular representation as it is a key material we use in this chapter. A paraxial light beam in a Laguerre-Gaussian mode with a frequency ω traveling along the z -axis in a dielectric with a refractive index $n(\omega)$ has a Lorenz-gauge vector potential that is of the form [8, 134]:

$$\mathbf{A}(\mathbf{r}, t) = A_0(\alpha\mathbf{x} + \beta\mathbf{y})u_{k,l}(x, y, z)e^{-i\omega t + ikz}, \quad (6.1)$$

where A_0 is a complex constant, \mathbf{x} and \mathbf{y} are unit vectors in positive x - and y -directions respectively, $k = n(\omega)\omega/c$ is the wave vector. The complex constants α and β satisfy the normalisation condition: $|\alpha|^2 + |\beta|^2 = 1$ and they determine the polarisation of the beam. As mentioned, we study the case that our medium is lossless, its refractive index is a real number. To simplify the problem, we consider only the case of the radial index $p = 0$. In such a mode, the complex scalar function given in the above equation is given by [8, 134]

$$\begin{aligned} u_{k,l}(x, y, z) &= \sqrt{\frac{2}{\pi |l|! w^2(z)}} \left(\frac{\sqrt{2}(x + \text{sign}(l)iy)}{w(z)} \right)^{|l|} \\ &\quad \times \exp \left[- \left(\frac{1}{w^2(z)} - \frac{ikz}{2(z^2 + z_R^2)} \right) (x^2 + y^2) \right] \\ &\quad \times \exp[-i(|l| + 1) \tan^{-1}(z/z_R)] \\ &\approx \frac{1}{\sqrt{\pi |l|!}} \left(\frac{\sqrt{2}}{w_0} \right)^{|l|+1} (x + i\text{sign}(l)y)^{|l|} \\ &\quad \times \exp \left[- \left(\frac{1}{w_0^2} - \frac{ikz}{2z_R^2} \right) (x^2 + y^2) - i(|l| + 1) \frac{z}{z_R} \right]. \end{aligned} \quad (6.2)$$

This is the complex function given in Eq.(1.6) of chapter 1, but it is expressed in a Cartesian coordinate system. The meaning and definition of each parameter are already given in chapter 1. In this work, we only focus in the region within the Rayleigh range of the beam such that $z \ll z_R$. We can, therefore, approximate the complex function, $u_{k,l}$, as given in the last line of the above

equation. The complex function is normalised so that its integration over the xy -plane is unity:

$$\int_{-\infty}^{\infty} \int_{-\infty}^{\infty} dx dy |u_{k,l}(x, y, z)|^2 = 1, \quad (6.3)$$

where

$$|u_{k,l}(x, y, z)|^2 = \frac{2^{|l|+1}}{\pi |l|! w_0^{2(|l|+1)}} (x^2 + y^2)^{|l|} \exp(-2(x^2 + y^2)/w_0^2). \quad (6.4)$$

As the beam is paraxial light, the wavelength is much smaller than its beam waist, in other words, $kw_0 \gg 1$. The spin angular momentum quantum number is denoted by σ and can be calculated from the polarisation coefficients as [7]

$$\sigma = i(\alpha\beta^* - \alpha^*\beta). \quad (6.5)$$

We can see that $\sigma = \pm 1$ for right- and left-circularly polarised beams respectively and $\sigma = 0$ for linearly polarised beams.

The reason that we need to review the angular spectrum representation is that it is a tool that helps us to determine the reflected beam. According to Fourier optics, an electromagnetic beam is actually a superposition of plane electromagnetic waves whose amplitudes and propagation directions are varied. This means when the beam undergoes total internal reflection each plane wave hits the dielectric interface with a different incident angle and has its own plane of incidence. The physics of reflection is applied to each plane wave component of the superposition to determine its corresponding reflected plane wave. The superposition of the reflected plane waves gives the form of the reflected beam. With the paraxial approximation, we can rewrite the vector potential field in terms of its two dimensional Fourier transform as

$$\begin{aligned} \mathbf{A}(\mathbf{r}, t) &= (\alpha\mathbf{x} + \beta\mathbf{y})e^{-i\omega t + ikz} \frac{A_0}{(2\pi)^2} \\ &\times \int_{-\infty}^{\infty} \int_{-\infty}^{\infty} dk_x dk_y \tilde{u}_l(k_x, k_y) e^{-iz(k_x^2 + k_y^2)/2k} e^{i(k_x x + k_y y)}, \end{aligned} \quad (6.6)$$

where

$$\tilde{u}_l(k_x, k_y) \propto (\text{sign}(l)ik_x - k_y)^{|l|} \exp\left[-\frac{(k_x^2 + k_y^2)w_0^2}{4}\right], \quad (6.7)$$

and we have applied the paraxial approximation $k_z \approx k - (k_x^2 + k_y^2)/2k$. The transverse components, k_x and k_y , of the wave vector are much smaller than the wave vector magnitude: $k_{\perp} \ll k$, where k_{\perp} represents the transverse components. With the Lorenz gauge, the paraxial electric and magnetic fields with the positive frequency ω can be determined by the vector potential \mathbf{A} as [147, 151]

$$\begin{aligned} \mathbf{E}(\mathbf{r}, t) &= -\nabla\phi(\mathbf{r}, t) - \frac{\partial\mathbf{A}(\mathbf{r}, t)}{\partial t}, \\ &= i\frac{c^2}{\omega n^2}\nabla(\nabla \cdot \mathbf{A}(\mathbf{r}, t)) + i\omega\mathbf{A}(\mathbf{r}, t) \\ &= e^{i(kz - \omega t)} \frac{A_0}{(2\pi)^2} \int_{-\infty}^{\infty} \int_{-\infty}^{\infty} dk_x dk_y \tilde{u}_l(k_x, k_y) e^{-iz(k_x^2 + k_y^2)/2k} \\ &\quad \times \left\{ i\omega(\alpha\mathbf{x} + \beta\mathbf{y}) - \frac{ic}{n}(\alpha k_x + \beta k_y)\mathbf{z} \right\} e^{i(k_x x + k_y y)}, \\ &\approx A_0 \left\{ i\omega(\alpha\mathbf{x} + \beta\mathbf{y})u_{k,l} - \frac{c}{n}\mathbf{z} \left(\alpha \frac{\partial u_{k,l}}{\partial x} + \beta \frac{\partial u_{k,l}}{\partial y} \right) \right\} e^{i(kz - \omega t)}, \end{aligned} \quad (6.8)$$

$$\begin{aligned}
\mathbf{B}(\mathbf{r}, t) &= \nabla \times \mathbf{A}(\mathbf{r}, t), \\
&= e^{i(kz - \omega t)} \frac{A_0}{(2\pi)^2} \int_{-\infty}^{\infty} \int_{-\infty}^{\infty} dk_x dk_y \tilde{u}_l(k_x, k_y) e^{-iz(k_x^2 + k_y^2)/2k} \\
&\quad \times \left\{ \frac{-i\omega n}{c} (\beta \mathbf{x} - \alpha \mathbf{y}) + i(\beta k_x - \alpha k_y) \mathbf{z} \right\} e^{i(k_x x + k_y y)}, \\
&\approx A_0 \left\{ -ik(\beta \mathbf{x} - \alpha \mathbf{y}) u_{k,l} + \mathbf{z} \left(\beta \frac{\partial u_{k,l}}{\partial x} - \alpha \frac{\partial u_{k,l}}{\partial y} \right) \right\} e^{i(kz - \omega t)}. \tag{6.9}
\end{aligned}$$

We have omitted the terms that are of order $(k_{\perp})^2/k$ or higher as their contributions are extremely small compared to the remaining terms. We notice that the electric and magnetic fields in the above equations have components in the longitudinal direction which is in contrast to the case of plane waves as we have discussed paraxial quantisation in the previous chapter. These two fields still obey the Maxwell first and second equations for the free-source case as they are divergenceless fields, $\nabla \cdot \mathbf{E} = 0 = \nabla \cdot \mathbf{B}$. Thus, the electric and magnetic fields given above are physical. The longitudinal components of the electric and magnetic fields are much smaller than the transverse components. It is these longitudinal components that make a Laguerre-Gaussian beam have $\hbar l$ orbital angular momentum per photon as the azimuthal part of the Poynting vector is the result of the vector product between the transverse and longitudinal components of the electric and magnetic fields [134, 148, 152].

6.2 Reflected beam

The aim of this section is to demonstrate explicitly how the form of the reflected beam is obtained via angular spectrum representation and the physics of reflection. The incident beam is assigned to be in a Laguerre-Gaussian mode with the radial index $p = 0$ as discussed in the previous section. As mentioned, in the angular spectrum representation, the incident beam is a superposition of plane waves. We treat each component of the superposition as an independent plane wave. The physics of transmission and reflection of a plane wave, which is given in the following detail, is used to determine the transmitted and reflected plane waves of each superposition component. The superposition of these transmitted and reflected plane waves then give us the form of the transmitted and reflected beams as desired.

We define three different coordinate systems: incident, reflection and interface coordinates which are denoted by (x_i, y_i, z_i) , (x_r, y_r, z_r) and (x, y, z) respectively as shown in figure 6.1. We set the xy -plane of the interface coordinates to be at the interface between air and the dielectric medium, so that the dielectric occupies the region $z > 0$. The y -axes of these three coordinates are assigned to point in the same direction: $\mathbf{y}_i = \mathbf{y}_r = \mathbf{y}$. The origins of these coordinate systems are defined to be at the location where the centre of the incident beam hits the interface.

Let us start with the incident beam. As shown in figure 6.1, the incident beam propagates in the direction with the angle of incidence θ . The forms of electric and magnetic fields of the beam are the same as the previous section when they are written in terms of the incident coordinates (x_i, y_i, z_i) . The beam waist is located at the origin of the coordinates. However, in order to apply the laws of reflection and transmission, it is more convenient to do so in the interface coordinates (x, y, z) . The

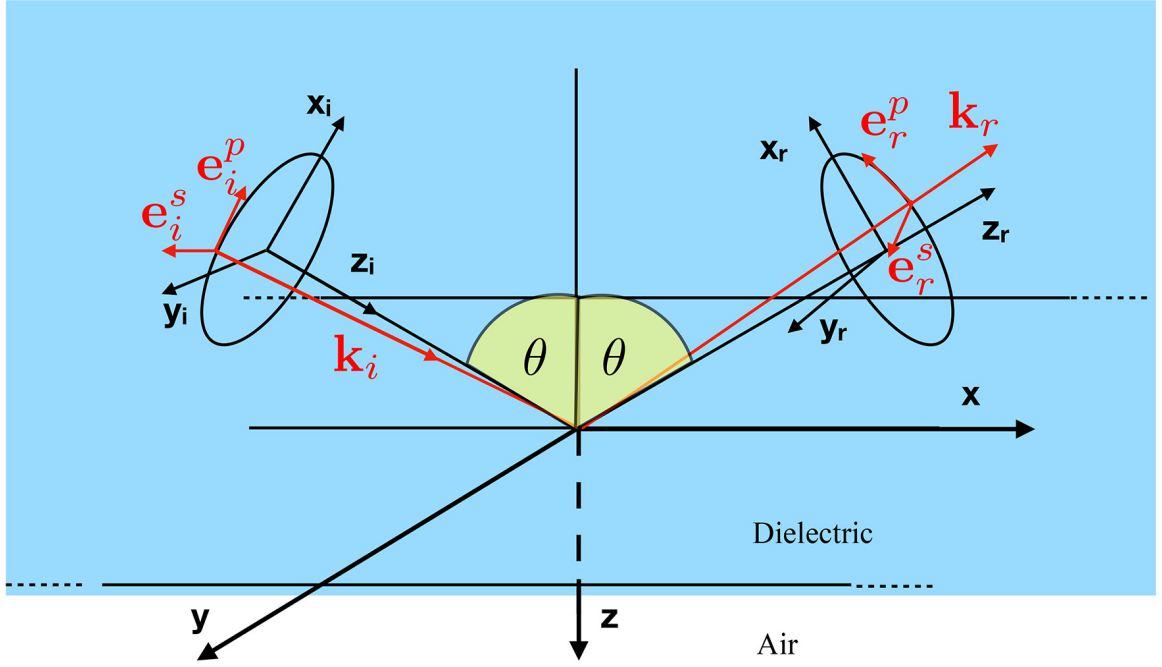


Figure 6.1: The figure shows the geometrical alignment of the incident, reflected and interface coordinate systems. The red line shows the propagation path of a superposition component, a local plane wave, with its incident wave vector \mathbf{k}_i . The local polarisations of the local incident and reflected plane waves are illustrated with the red arrow. The directions of the axes of these three coordinates, (x_i, y_i, z_i) , (x_r, y_r, z_r) and (x, y, z) , are as shown in the figure. The three coordinate systems, however, share the same origin, at the location where the centre of the incident beam hits the interface.

coordinate transformation between the incident and interface coordinates is given by

$$\begin{aligned} x_i &= x \cos \theta - z \sin \theta, \\ y_i &= y, \\ z_i &= z \cos \theta + x \sin \theta. \end{aligned} \quad (6.10)$$

We then apply this coordinate transformation to the angular spectrum representation of the incident electric field. The form of the field in the interface coordinates is expressed as

$$\mathbf{E}_i(x, y, z, t) = \frac{1}{(2\pi)^2} \int_{-\infty}^{\infty} \int_{-\infty}^{\infty} dk_x dk_y \mathbf{E}_i(k_x, k_y, t), \quad (6.11)$$

with

$$\begin{aligned} \mathbf{E}_i(k_x, k_y, t) &\equiv A_0 e^{-i\omega t} \left\{ \left(i\omega\alpha \cos \theta - \frac{ic}{n}(\alpha k_x + \beta k_y) \sin \theta \right) \mathbf{x} + i\omega\beta \mathbf{y} \right. \\ &\quad \left. - \left(i\omega\alpha \sin \theta + \frac{ic}{n}(\alpha k_x + \beta k_y) \cos \theta \right) \mathbf{z} \right\} \tilde{u}_l(k_x, k_y) \\ &\quad \times \exp [i((k - \kappa) \sin \theta + k_x \cos \theta)x + k_y y + ((k - \kappa) \cos \theta - k_x \sin \theta)z], \end{aligned} \quad (6.12)$$

where κ is the shorthand for the term $(k_x^2 + k_y^2)/2k$. We note that $\mathbf{E}_i(k_x, k_y, t)$ is in the form of a plane wave with the propagation direction described by its own wave vector $\mathbf{k}_i = ((k - \kappa) \sin \theta +$

$k_x \cos \theta, k_y, (k - \kappa) \cos \theta - k_x \sin \theta$). The form of the incident beam is now written explicitly as a superposition of plane waves in the interface coordinates. From now on, we call a component of the superposition, $\mathbf{E}_i(k_x, k_y, t)$, an incident local plane wave. We note that, k_x and k_y in the incident coordinates are the transverse component of the local wave vector \mathbf{k}_i in the positive x_i - and y_i -directions respectively. Their physical meanings in the interface coordinates, however, is rather complicated. We thus treat them as transform variables.

At this point, we can treat each of the local plane waves independently. Every local plane wave in the superposition has its own plane of incidence. For the local plane wave $\mathbf{E}_i(k_x, k_y, t)$, its own plane of incidence is defined as a plane in which both its wave vector \mathbf{k}_i and the normal vector \mathbf{n} which is perpendicular to the interface, in our case it is equal to the unit vector \mathbf{z} of the interface coordinates, lie. We can then decompose the vector of the local electric field into the directions perpendicular and parallel to its plane of incidence. As discussed in the previous chapter, we define $\mathbf{e}^s(\mathbf{k}_i)$ and $\mathbf{e}^p(\mathbf{k}_i)$ as unit vectors that are perpendicular and parallel to the plane of incidence for the local plane wave $\mathbf{E}_i(k_x, k_y, t)$ respectively as

$$\mathbf{e}^s(\mathbf{k}_i) = \frac{\mathbf{z} \times \mathbf{k}_i}{|\mathbf{z} \times \mathbf{k}_i|}, \quad (6.13)$$

and

$$\mathbf{e}^p(\mathbf{k}_i) = \frac{\mathbf{e}^s(\mathbf{k}_i) \times \mathbf{k}_i}{k}. \quad (6.14)$$

The local plane wave $\mathbf{E}_i(k_x, k_y, t)$ can thus be expressed in terms of these unit vectors as

$$\mathbf{E}_i(k_x, k_y, t) = \{E_i^s(\mathbf{k}_i)\mathbf{e}^s(\mathbf{k}_i) + E_i^p(\mathbf{k}_i)\mathbf{e}^p(\mathbf{k}_i)\} e^{-i\omega t + i\mathbf{k}_i \cdot \mathbf{r}}, \quad (6.15)$$

where $E_i^s(\mathbf{k}_i) = \mathbf{E}_i(k_x, k_y, t) \cdot \mathbf{e}^s(\mathbf{k}_i)e^{i\omega t - i\mathbf{k}_i \cdot \mathbf{r}}$ and $E_i^p(\mathbf{k}_i) = \mathbf{E}_i(k_x, k_y, t) \cdot \mathbf{e}^p(\mathbf{k}_i)e^{i\omega t - i\mathbf{k}_i \cdot \mathbf{r}}$ and \mathbf{r} is the position vector in the interface coordinates (x, y, z) . The unit vector $\mathbf{e}^s(\mathbf{k}_i)$ and $\mathbf{e}^p(\mathbf{k}_i)$ are also known as the eigenpolarisations of the local plane wave. At this point, we are ready to apply the physics of reflection and transmission discussed in the previous chapter to the local plane wave $\mathbf{E}_i(k_x, k_y, t)$. The directions of propagation of the local transmitted and reflected plane waves are determined by Snell's law given in the Eqs.(5.33), (5.34) and (5.35). On the other hand, the amplitudes of the local transmitted and reflected plane waves in the s - and p -directions can be obtained through the Fresnel coefficients given in Eqs.(5.41)- (5.44). As the local plane waves in the superposition have different propagation directions, their Fresnel coefficients are different. With the conditions given above, the reflected and transmitted beams can be determined straightforwardly.

As our study focuses only on total internal reflection, only the reflected beam is enough to analyse the mechanism of momentum and angular momentum transfer. We will show later that the transmitted evanescent field does not have an influence on the angular momentum exchange. The Taylor expansion of the reflection coefficients around $k_x = k_y = 0$ gives

$$r^s(k_x) \approx \bar{r}^s + \bar{r}'^s k_x = \bar{r}^s(1 + ik_x D^s), \quad (6.16)$$

$$r^p(k_x) \approx \bar{r}^p + \bar{r}'^p k_x = \bar{r}^p(1 + ik_x D^p), \quad (6.17)$$

where \bar{r}^s and \bar{r}^p are the reflection coefficients evaluated at $k_x = k_y = 0$ while \bar{r}'^s and \bar{r}'^p are their first derivatives. The paraxial approximation has been applied. The terms including k_y are negligible as

their contributions are much smaller than the mentioned terms. We have defined \bar{r}^s/\bar{r}^s and \bar{r}^p/\bar{r}^p to be iD^s and iD^p respectively, as we will show later that D^s and D^p correspond to the amount of longitudinal beam shifts. The reflected plane wave of the local plane wave $\mathbf{E}_i(k_x, k_y, t)$ is then given by

$$\mathbf{E}_r(k_x, k_y, t) = \{r^s(k_x)E_1^s(\mathbf{k}_i)\mathbf{e}^s(\mathbf{k}_r) + r^p(k_x)E_1^p(\mathbf{k}_i)\mathbf{e}^p(\mathbf{k}_r)\} e^{-i\omega t + i\mathbf{k}_r \cdot \mathbf{r}}. \quad (6.18)$$

We note that $\mathbf{e}^s(\mathbf{k}_r) = \mathbf{e}^s(\mathbf{k}_i)$ as the local incident and reflected plane waves share the same plane of incidence. The superposition of every reflected plane wave then gives the form of the reflected beam:

$$\mathbf{E}_r(x, y, z, t) = \frac{1}{(2\pi)^2} \int_{-\infty}^{\infty} \int_{-\infty}^{\infty} dk_x dk_y \mathbf{E}_r(k_x, k_y, t), \quad (6.19)$$

with

$$\begin{aligned} \mathbf{E}_r(k_x, k_y, t) = & A_0 e^{-i\omega t} \left\{ \left(-ir^p \omega \alpha \cos \theta + \frac{ir^p c}{n} (\alpha k_x \sin \theta - \beta k_y \cot \theta \cos \theta) - \frac{ir^s c \beta k_y}{n \sin \theta} \right) \mathbf{x} \right. \\ & + \left(ir^s \omega \beta - \frac{ic \alpha k_y \cot \theta}{n} (r^s + r^p) \right) \mathbf{y} \\ & \left. - r^p \left(i\omega \alpha \sin \theta + \frac{ic}{n} (\alpha k_x \cos \theta + \beta k_y \cot \theta \sin \theta) \right) \mathbf{z} \right\} \tilde{u}_l(k_x, k_y) \\ & \times \exp [i((k_x \cos \theta + (k - \kappa) \sin \theta)x + k_y y - ((k - \kappa) \cos \theta - k_x \sin \theta)z)]. \end{aligned} \quad (6.20)$$

The form of the reflected beam is significantly simplified when it is expressed in terms of the reflection coordinates (x_r, y_r, z_r) . The coordinate transformation between the interface and reflection coordinates is given as

$$\begin{aligned} x_r &= -x \cos \theta - z \sin \theta, \\ y_r &= y, \\ z_r &= -z \cos \theta + x \sin \theta. \end{aligned} \quad (6.21)$$

Applying this transformation and performing the integration over k_x and k_y , we obtain

$$\mathbf{E}_r(x_r, y_r, z_r, t) = A_0 \{ \chi_x \mathbf{x}_r + \chi_y \mathbf{y}_r + \chi_z \mathbf{z}_r \} e^{-i\omega(t - nz_r/c)}, \quad (6.22)$$

with

$$\chi_x = i\omega \alpha \bar{r}^p \left(\underline{u}_{k,l} - D^p \frac{\partial \underline{u}_{k,l}}{\partial x_r} \right) + \frac{c}{n} \beta \cot \theta (\bar{r}^p + \bar{r}^s) \frac{\partial \underline{u}_{k,l}}{\partial y_r}, \quad (6.23)$$

$$\chi_y = i\omega \beta \bar{r}^s \left(\underline{u}_{k,l} - D^s \frac{\partial \underline{u}_{k,l}}{\partial x_r} \right) - \frac{c}{n} \alpha \cot \theta (\bar{r}^p + \bar{r}^s) \frac{\partial \underline{u}_{k,l}}{\partial y_r}, \quad (6.24)$$

$$\chi_z = -\frac{c}{n} \left(\alpha \bar{r}^p \frac{\partial \underline{u}_{k,l}}{\partial x_r} + \beta \bar{r}^s \frac{\partial \underline{u}_{k,l}}{\partial y_r} \right). \quad (6.25)$$

We have defined $\underline{u}_{k,l} = u_{k,l}(-x_r, y_r, z_r)$, where $u_{k,l}(x, y, z)$ is the complex function given in Eq.(6.2), where the minus sign in front of x_r indicates that the topological charge of the beam is changed after reflection from l to $-l$. The magnetic field of the reflected beam can be obtained by using the third Maxwell's equation as

$$\begin{aligned} \mathbf{B}_r(x_r, y_r, z_r, t) &= \frac{1}{i\omega} \nabla \times \mathbf{E}_r(x_r, y_r, z_r, t), \\ &= \frac{A_0}{c} \left\{ n \chi_x \mathbf{y}_r - n \chi_y \mathbf{x}_r + c \left(\beta \bar{r}^s \frac{\partial \underline{u}_{k,l}}{\partial x_r} - \alpha \bar{r}^p \frac{\partial \underline{u}_{k,l}}{\partial y_r} \right) \mathbf{z}_r \right\} e^{-i\omega(t - nz_r/c)}. \end{aligned} \quad (6.26)$$

Within the paraxial approximation, the obtained reflected electric and magnetic fields are transverse as $\nabla \cdot \mathbf{E}_r = 0$ and $\nabla \cdot \mathbf{B}_r = 0$. At this point, one might think that we can avoid the mathematical complexity by treating the whole beam as a plane wave with the wave vector \mathbf{k} pointing in the direction of propagation of the incident beam. The approximated amplitudes of the reflected and transmitted beams should be then obtained by multiplication of the Fresnel coefficients and the approximated incident plane wave, while their propagation directions are given by geometrical optics. Even though it is a good approximation, the approximated electric and magnetic fields of the reflected and transmitted beams are not transverse: $\nabla \cdot \mathbf{E}_r \neq 0$ and $\nabla \cdot \mathbf{B}_r \neq 0$. This approximation, therefore, is not good enough for our analysis.

6.3 Quantisation of the incident and reflected fields

With the forms of the incident and reflected electric and magnetic fields given in the previous section, we can obtain their corresponding quantum operators by using the forms of electric and magnetic field operators in the paraxial regime given in the previous chapter. The classical fields in their own frames of reference are promoted to the corresponding field operators as [134]

$$\hat{\mathbf{E}}_i^+(x_i, y_i, z_i, t) = \int_0^\infty d\omega \left(\frac{\hbar}{4\pi\epsilon_0 c n \omega} \right)^{1/2} \hat{a}(\omega) e^{-i\omega(t - n z_i/c)} \times \left\{ i\omega(\alpha \mathbf{x}_i + \beta \mathbf{y}_i) u_{k,l}^i - \frac{c}{n} \left(\alpha \frac{\partial u_{k,l}^i}{\partial x_i} + \beta \frac{\partial u_{k,l}^i}{\partial y_i} \right) \mathbf{z}_i \right\}, \quad (6.27)$$

$$\hat{\mathbf{B}}_i^+(x_i, y_i, z_i, t) = \int_0^\infty d\omega \left(\frac{\hbar}{4\pi\epsilon_0 c^3 n \omega} \right)^{1/2} \hat{a}(\omega) e^{-i\omega(t - n z_i/c)} \times \left\{ -in\omega(\beta \mathbf{x}_i - \alpha \mathbf{y}_i) u_{k,l}^i + c \left(\beta \frac{\partial u_{k,l}^i}{\partial x_i} - \alpha \frac{\partial u_{k,l}^i}{\partial y_i} \right) \mathbf{z}_i \right\}, \quad (6.28)$$

$$\hat{\mathbf{E}}_r^+(x_r, y_r, z_r, t) = \int_0^\infty d\omega \left(\frac{\hbar}{4\pi\epsilon_0 c n \omega} \right)^{1/2} \hat{a}(\omega) e^{-i\omega(t - n z_r/c)} \{ \chi_x \mathbf{x}_r + \chi_y \mathbf{y}_r + \chi_z \mathbf{z}_r \}, \quad (6.29)$$

$$\hat{\mathbf{B}}_r^+(x_r, y_r, z_r, t) = \int_0^\infty d\omega \left(\frac{\hbar}{4\pi\epsilon_0 c^3 n \omega} \right)^{1/2} \hat{a}(\omega) e^{-i\omega(t - n z_r/c)} \times \left\{ n\chi_x \mathbf{y}_r - n\chi_y \mathbf{x}_r + c \left(\beta \bar{r}^s \frac{\partial u_{k,l}}{\partial x_r} - \alpha \bar{r}^p \frac{\partial u_{k,l}}{\partial y_r} \right) \mathbf{z}_r \right\}, \quad (6.30)$$

where we define $u_{k,l}^i \equiv u_{k,l}(x_i, y_i, z_i)$. The annihilation operators $\hat{a}(\omega)$ are the same annihilation operator that defined in Eq.(5.164) in the previous chapter. Their subscripts have been omitted for brevity. The commutation relation of the annihilation and creation operators is as already given. The space and time dependence of the electric and magnetic field operators is exactly the same as their classical version in order to satisfy Maxwell's equations.

We note that in the preceding chapter we used the Coulomb gauge when we quantise an electromagnetic field, and finally the paraxial quantisation is obtained. In this chapter, in contrast, we use the Lorenz gauge to determine the electric and magnetic fields and quantise them accordingly. Both ways of quantisation are correct and sensible, even though the gauge conditions are different. This is because for a given electric field the corresponding vector potential is not unique, and this

nonuniqueness leads to a gauge freedom. We can see that both gauges we have chosen give the same incident electric field. The reason we use the Lorenz gauge in this chapter because it is easier and more straightforward to obtain the paraxial electric field, while in the previous chapter the Coulomb gauge has been reviewed because it is the conventional way to quantise an electromagnetic field.

As we discussed in the previous chapter, the state of a single-photon pulse is given as [141, 153]

$$|1\rangle = \int d\omega \xi(\omega) \hat{a}^\dagger(\omega) |0\rangle, \quad (6.31)$$

where the state $|0\rangle$ is the vacuum state. The function $\xi(\omega)$ describes the distribution of the probability amplitude in the frequency domain. In this case, we take it to be a narrowband Gaussian distribution as [134, 137]

$$\xi(\omega) = \left(\frac{L^2}{2\pi c^2} \right)^{1/4} \exp \left[-\frac{L^2(\omega - \omega_0)^2}{4c^2} \right], \quad (6.32)$$

where L is the spatial length of the pulse and $c/L \ll \omega_0$. The peak of the frequency spectrum is at the central frequency ω_0 and the magnitude of the distribution function $\xi(\omega)$ is very small in the regions far from the peak. The function $\xi(\omega)$ given in the above equation is normalised:

$$\int d\omega |\xi(\omega)|^2 = 1. \quad (6.33)$$

In quantum mechanics, we cannot predict the outcome of a measurement deterministically, but it only gives us the probability distribution which tells us how likely a given outcome is obtained. For a large number of the same measurements on an identical state, the average value of an observable approaches the quantum expectation value. Therefore, we can extract physical quantities by evaluating the expectation values of the given operators.

6.4 Optical force and torque

In this section, we are interested in the interaction between light and the dielectric medium with the presence of the boundary between two dielectric media, air and the dielectric. There is no free charge and current present in our this case. The problem is that when the boundary is included the component of the electric field perpendicular to the boundary is neither smooth nor continuous at the boundary. The magnetic field, on the other hand, is continuous but not smooth. Recall that the vector calculus identities rely on both smoothness and continuity. Without them, the calculus we know is ill-defined. We need to deal with this problem cautiously.

In this work, we use the dipole-based force density to study the interaction between light and the dielectric. Instead of expressing the force density in terms of polarisation $\mathbf{P}(\mathbf{r})$, we replaced it with the dielectric displacement and the electric field: $\mathbf{P} = \mathbf{D} - \varepsilon_0 \mathbf{E}$. Unlike the electric and polarisation fields, the component of the electric displacement perpendicular to the interface is continuous over the boundary. We then can use Maxwell's equations to transform the form of the dipole-based force density into [131]

$$\mathbf{f} = (\mathbf{D} \cdot \nabla) \mathbf{E} - \varepsilon_0 (\mathbf{E} \cdot \nabla) \mathbf{E} - \varepsilon_0 \mathbf{E} \times (\nabla \times \mathbf{E}) - \mathbf{B} \times \left(\nabla \times \frac{\mathbf{B}}{\mu_0} \right) - \frac{\partial}{\partial t} (\varepsilon_0 \mathbf{E} \times \mathbf{B}). \quad (6.34)$$

The space and time dependence of these fields is omitted for brevity. There are two terms that lack continuity across an interface: the first and second. In physics, we generally introduce a distribution function to deal with discontinuity. The distribution function for a function with a jump is normally expressed in terms of the Heaviside function [154]:

$$H(z) = \begin{cases} 0 & z < 0 \\ 1 & z > 0 \end{cases}, \quad (6.35)$$

Recall that we suppose that the dielectric occupies in the region $z > 0$ and the boundary is at $z = 0$. We exclude $z = 0$ in our definition of the Heaviside function as the fields in Eq.(6.34) are not well-defined in the boundary plane. The i th component of the electric field with the discontinuity at the boundary can be expressed as

$$E_i = E_i^{(\text{in})} + (E_i^{(\text{out})} - E_i^{(\text{in})})H(z), \quad (6.36)$$

where i can take one of three possible values: x , y and z and $E_i^{(\text{in})}$ and $E_i^{(\text{out})}$ represent the i th component of the electric field inside and outside the medium respectively. The electric field on the left-hand side of the equation is now defined everywhere except at the boundary plane. The other fields, \mathbf{D} and \mathbf{B} are expressed in the same way as the electric field in Eq.(6.36). The derivative of the Heaviside function gives the well-known Dirac delta function,

$$\frac{\partial H(z)}{\partial z} = \delta(z). \quad (6.37)$$

The integration of the product between the Dirac delta function and the Heaviside function is equivalent to the integration of half of the delta function as only the region $z > 0$ that contribute to the integration:

$$\int H(z)\delta(z)dz = \int \frac{\delta(z)}{2} dz. \quad (6.38)$$

As we aim to evaluate the total force and torque, the integration over a volume will take place. We can then replace the product of these two function with half of the delta function without loss of precision at the end of the calculation: $H(z)\delta(z) \rightarrow \delta(z)/2$. From Eq.(6.34) and the boundary condition for the electric displacement, we can express the i th component of the force density as

$$\begin{aligned} f_i &= D_z^{(\text{in})}(E_z^{(\text{out})} - E_z^{(\text{in})})\delta(z)\delta_{iz} - \varepsilon_0 \frac{((E_z^{(\text{out})})^2 - (E_z^{(\text{in})})^2)}{2} \delta(z)\delta_{iz} \\ &+ \partial_l(D_l^{(\text{in})}E_i^{(\text{in})} + \frac{B_l^{(\text{in})}B_i^{(\text{in})}}{\mu_0})H(-z) + \partial_l(D_l^{(\text{out})}E_i^{(\text{out})} + \frac{B_l^{(\text{out})}B_i^{(\text{out})}}{\mu_0})H(z) \\ &- \partial_i \left(\varepsilon_0 \frac{E_l^{(\text{in})}E_l^{(\text{in})}}{2} + \frac{B_l^{(\text{in})}B_l^{(\text{in})}}{2\mu_0} \right) H(-z) - \partial_i \left(\varepsilon_0 \frac{E_l^{(\text{out})}E_l^{(\text{out})}}{2} + \frac{B_l^{(\text{out})}B_l^{(\text{out})}}{2\mu_0} \right) H(z) \\ &- \partial_t(\varepsilon_0 \mathbf{E} \times \mathbf{B})_i, \end{aligned} \quad (6.39)$$

where we have used the fact that $1 - H(z) = H(-z)$. The summation convention is used such that the indices repeated twice imply the summation over x , y and z indices. The derivative operators with respect to the coordinate variables x^i , where x^i is x , y or z , are denoted by ∂_i . The first

and second terms are obtained by using the boundary condition which state that the electric field components parallel to the interface are continuous: $E_j^{(\text{out})}|_{z=0^+} = E_j^{(\text{in})}|_{z=0^-}$ where $j = x, y$, which gives $(E_i^{(\text{out})} - E_i^{(\text{in})})\delta(z) = (E_z^{(\text{out})} - E_z^{(\text{in})})\delta(z)\delta_{iz}$. The boundary conditions of electromagnetic fields given in the previous chapter can be written explicitly for this case as

$$E_j^{(\text{out})}|_{z=0^+} = E_j^{(\text{in})}|_{z=0^-}; \quad j = x, y, \quad (6.40)$$

$$\mathbf{B}^{(\text{out})}|_{z=0^+} = \mathbf{B}^{(\text{in})}|_{z=0^-}, \quad (6.41)$$

$$D_z^{(\text{out})}|_{z=0^+} = D_z^{(\text{in})}|_{z=0^-}. \quad (6.42)$$

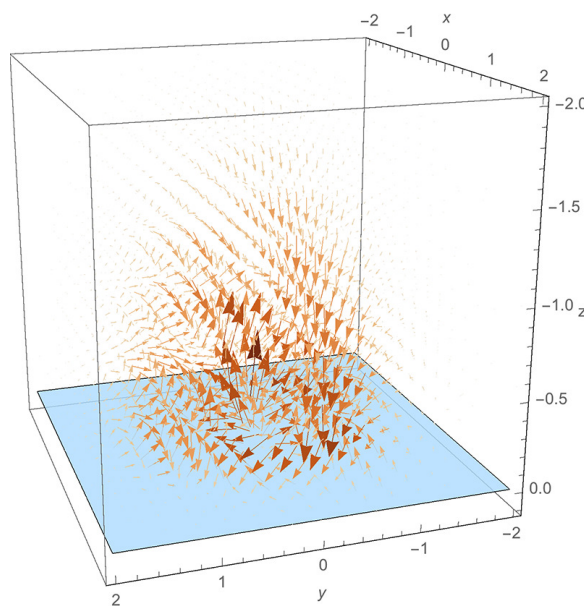


Figure 6.2: The vector field of the dipole-based force density acts on the dielectric medium inside it when the single-photon pulse reaches the interface. The interface plane is at $z = 0$, and the dielectric is in the region $z < 0$. We enhance the azimuthal part of the force density, which is contained only in $\partial_t(\mathbf{P} \times \mathbf{B})$, as it is the part that gives rise the angular momentum transfer from light to the dielectric. The coordinates (x, y, z) in this figure is the interface coordinates (x, y, z) given in figure 6.1 in a different perspective.

The detailed vector field of the force density when the pulse reaches the interface is illustrated in figure 6.2. In the figure, the azimuthal component circulates around the optical axis of the beam. The part of the force density proportional to the delta function is depicted in figure 6.3.

We suppose that the observation begins at the time $t = -T$, at this time the single-photon pulse is far away from the interface. Then, the single-photon pulse reaches the interface around $t = 0$, and we finish our observation at $t = T$. We assign the interval time $2T$ to be very large so that there is no field at the interface at the beginning and the end of the observation. Therefore, in our calculation, we can take the limit of the time T to be infinity. Next, we define a volume V in such

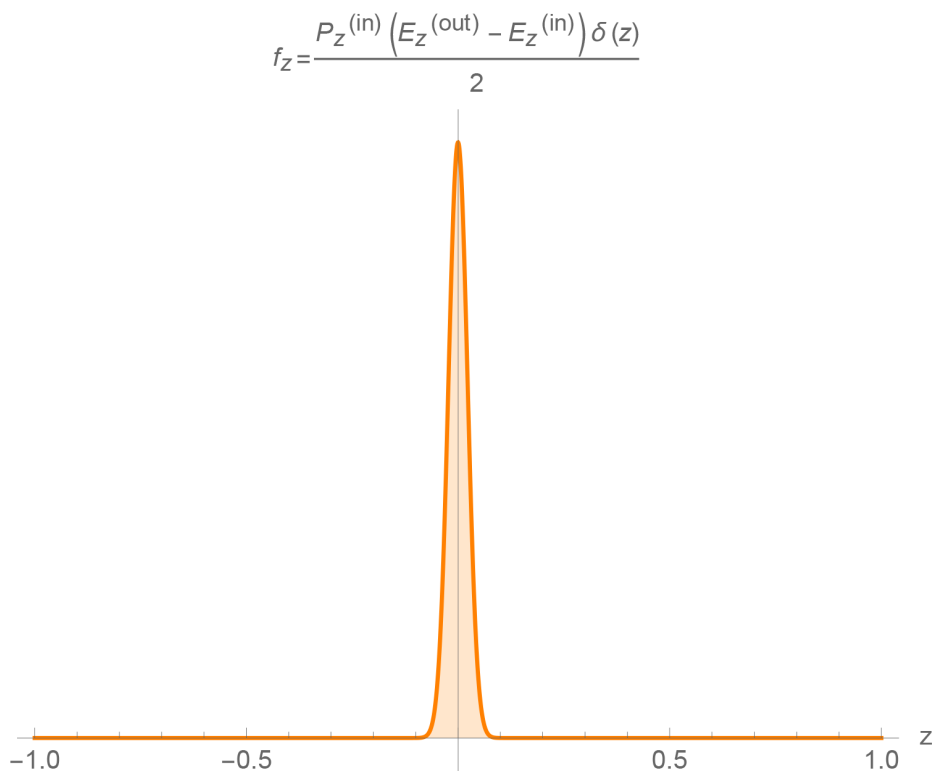


Figure 6.3: The part of the force density that is proportional to the delta function is normal to the interface.

a way that it is very large compared to the volume of the single-photon pulse so that it can contain the single-photon pulse within it during the observation, and there is no field at its surface. Some part of the interface and the region $z > 0$ are included in the volume V . With this definition of the volume V , after we perform the volume integrations of the force and torque densities over the volume, the terms which are in the form of derivatives of x and y in Eq.(6.39) do not contribute as their integrations give the electromagnetic fields at the surface of the volume V . For the other terms, the volume integrations are given as follows. As our integration volume is really large, we can take its limit to be infinity without losing the precision of the calculation. The Heaviside functions in the integrands change the integration limit of integration over z as

$$\begin{aligned} \int_{-\infty}^{\infty} dx \int_{-\infty}^{\infty} dy \int_{-\infty}^{\infty} dz \partial_z f(x, y, z) H(-z) &= \int_{-\infty}^{\infty} dx \int_{-\infty}^{\infty} dy \int_{-\infty}^{0^-} dz \partial_z f(x, y, z) \\ &= \int_{-\infty}^{\infty} dx \int_{-\infty}^{\infty} dy f(x, y, z) \Big|_{z=-\infty}^{z=0^-}, \end{aligned} \quad (6.43)$$

where $f(x, y, z)$ is an arbitrary complex field. Therefore, the volume integration of Eq.(6.39) gives

$$\begin{aligned}
\int_V f_i dV &= \int_{-\infty}^{\infty} \int_{-\infty}^{\infty} dx dy \left\{ D_z^{(\text{in})} (E_z^{(\text{out})} - E_z^{(\text{in})}) \delta_{iz} \Big|_{z=0} - \varepsilon_0 \frac{((E_z^{(\text{out})})^2 - (E_z^{(\text{in})})^2)}{2} \delta_{iz} \Big|_{z=0} \right. \\
&\quad + \left. \left(D_z^{(\text{in})} E_i^{(\text{in})} + \frac{B_z^{(\text{in})} B_i^{(\text{in})}}{\mu_0} \right) \Big|_{z=-\infty}^{z=0^-} + \left(D_z^{(\text{out})} E_i^{(\text{out})} + \frac{B_z^{(\text{out})} B_i^{(\text{out})}}{\mu_0} \right) \Big|_{z=0^+}^{z=\infty} \right. \\
&\quad - \delta_{iz} \left(\varepsilon_0 \frac{E_l^{(\text{in})} E_l^{(\text{in})}}{2} + \frac{B_l^{(\text{in})} B_l^{(\text{in})}}{2\mu_0} \right) \Big|_{z=-\infty}^{z=0^-} \\
&\quad \left. - \delta_{iz} \left(\varepsilon_0 \frac{E_l^{(\text{out})} E_l^{(\text{out})}}{2} + \frac{B_l^{(\text{out})} B_l^{(\text{out})}}{2\mu_0} \right) \Big|_{z=0^+}^{z=\infty} \right\} - \int_V dV \partial_t (\varepsilon_0 \mathbf{E} \times \mathbf{B})_i, \quad (6.44)
\end{aligned}$$

where the terms in the curly bracket have been integrated over z already. These terms in the curly bracket cancel each other perfectly as demonstrated in the following detail. We begin by considering the integration of the third and fourth terms in the curly bracket:

$$\begin{aligned}
\int_V dV \{ f_i^{\text{third}} + f_i^{\text{fourth}} \} &= \int_{-\infty}^{\infty} \int_{-\infty}^{\infty} dx dy \left\{ D_z^{(\text{in})} E_i^{(\text{in})} \Big|_{z=-\infty}^{z=0^-} + D_z^{(\text{out})} E_i^{(\text{out})} \Big|_{z=0^+}^{z=\infty} + \frac{B_z^{(\text{in})} B_i^{(\text{in})}}{\mu_0} \Big|_{z=-\infty}^{z=0^-} \right. \\
&\quad \left. \frac{B_z^{(\text{out})} B_i^{(\text{out})}}{\mu_0} \Big|_{z=0^+}^{z=\infty} \right\} \\
&= \int_{-\infty}^{\infty} \int_{-\infty}^{\infty} dx dy \left\{ D_z^{(\text{in})} (E_i^{(\text{in})} - E_i^{(\text{out})}) \Big|_{z=0} + \frac{B_z^{(\text{in})}}{\mu_0} (B_i^{(\text{in})} - B_i^{(\text{out})}) \Big|_{z=0} \right\} \\
&= \int_{-\infty}^{\infty} \int_{-\infty}^{\infty} dx dy D_z^{(\text{in})} (E_z^{(\text{in})} - E_z^{(\text{out})}) \delta_{iz} \Big|_{z=0}, \quad (6.45)
\end{aligned}$$

where we have used the boundary conditions: Eqs.(6.40) and (6.41), and the fact that there is no field at $|z| = \infty$, the surface of the volume V . This means the integrations of the third and fourth terms perfectly cancel the first term in the curly bracket. The integrations of the fifth and sixth terms, on the other hand, give

$$\begin{aligned}
\int_V dV \{ f_i^{\text{fifth}} + f_i^{\text{sixth}} \} &= \int_{-\infty}^{\infty} \int_{-\infty}^{\infty} dx dy \left\{ -\delta_{iz} \varepsilon_0 \frac{E_l^{(\text{in})} E_l^{(\text{in})}}{2} \Big|_{z=-\infty}^{z=0^-} - \delta_{iz} \varepsilon_0 \frac{E_l^{(\text{out})} E_l^{(\text{out})}}{2} \Big|_{z=0^+}^{z=\infty} \right. \\
&\quad \left. - \delta_{iz} \frac{B_l^{(\text{in})} B_l^{(\text{in})}}{2\mu_0} \Big|_{z=-\infty}^{z=0^-} - \delta_{iz} \frac{B_l^{(\text{out})} B_l^{(\text{out})}}{2\mu_0} \Big|_{z=0^+}^{z=\infty} \right\} \\
&= \int_{-\infty}^{\infty} \int_{-\infty}^{\infty} dx dy \left\{ \delta_{iz} \varepsilon_0 \frac{(E_z^{(\text{out})})^2 - (E_z^{(\text{in})})^2}{2} \Big|_{z=0} \right\}, \quad (6.46)
\end{aligned}$$

where we again have used the boundary conditions, Eqs. (6.40) and (6.41), and only the z -component of electric fields inside and outside the medium that do not perfectly cancel each other in the above equation. Similarly, it means the integrations of the fifth and sixth terms in the curly bracket of Eq.(6.44) cancel the second term perfectly. Therefore, the only term that contributes to the volume

integration of the i th force density is the time derivative of the vector product between electric and magnetic fields, the last term:

$$\int_V \mathbf{f} dV = - \int_V dV \partial_t (\varepsilon_0 \mathbf{E} \times \mathbf{B}) = -\partial_t \int_V dV (\varepsilon_0 \mathbf{E} \times \mathbf{B}). \quad (6.47)$$

This equation is a manifestation of Newton's third law: for every action force, there is an equal and opposite reaction acting on a different object, when the kinetic momentum of light being in its Abraham form: $\mathbf{E} \times \mathbf{H}/c^2$ [155–157] as follows. The left-hand side of the equation is the force that light acting on the dielectric which is equal to the change rate of the dielectric momentum, while the right-hand side is the negative of the change rate of the momentum of the light pulse. This means the force that the photon acting on the dielectric is of the same magnitude as the force that the dielectric acting back to the photon but in the opposite direction. This equation ensures the conservation of momentum. At this point, we can see that, when the physical boundary conditions are applied, the third law of motion is reproduced from the Lorentz force straightforwardly. On the other hand, with this equation, in the case of total internal reflection with a glass-air interface, we can see that the evanescent field also contribute some force to the dielectric, but this interpretation cannot be realised directly from the form of the dipole-based force density because there is no polarisation outside the dielectric, which means no force density outside the medium. However, as the evanescent field is not long-lasting, the effect of this force on the medium cancel itself when time evolves. In other words, it does not have any influence on the momentum transfer.

Using Eq.(6.39) and the chain rule, the i th component of the torque density is expressed by

$$\begin{aligned} \tau_i = & \epsilon_{ijk} x_j D_z^{(\text{in})} (E_z^{(\text{out})} - E_z^{(\text{in})}) \delta(z) \delta_{kz} - \epsilon_{ijk} x_j \varepsilon_0 \frac{((E_z^{(\text{out})})^2 - (E_z^{(\text{in})})^2)}{2} \delta(z) \delta_{kz} \\ & + \partial_l (\epsilon_{ijk} x_j (D_l^{(\text{in})} E_k^{(\text{in})} + \frac{B_l^{(\text{in})} B_k^{(\text{in})}}{\mu_0})) H(-z) + \partial_l (\epsilon_{ijk} x_j (D_l^{(\text{out})} E_k^{(\text{out})} + \frac{B_l^{(\text{out})} B_k^{(\text{out})}}{\mu_0})) H(z) \\ & - \partial_k \left(\epsilon_{ijk} x_j \left(\varepsilon_0 \frac{E_l^{(\text{in})} E_l^{(\text{in})}}{2} + \frac{B_l^{(\text{in})} B_l^{(\text{in})}}{2\mu_0} \right) \right) H(-z) \\ & - \partial_k \left(\epsilon_{ijk} x_j \left(\varepsilon_0 \frac{E_l^{(\text{out})} E_l^{(\text{out})}}{2} + \frac{B_l^{(\text{out})} B_l^{(\text{out})}}{2\mu_0} \right) \right) H(z) - \partial_t (\mathbf{r} \times (\varepsilon_0 \mathbf{E} \times \mathbf{B}))_i, \end{aligned} \quad (6.48)$$

where ϵ_{ijk} is the Levi-Civita symbol. As our medium is linear, homogeneous, isotropic and lossless, the refractive index is a real number. The electric field \mathbf{E} and the electric displacement \mathbf{D} thus are parallel to each other, the vector product of these two fields vanishes: $\mathbf{D} \times \mathbf{E} = \mathbf{0}$, and has been omitted from the right-hand side of the above equation. The volume integration then gives the total torque exerted by the light pulse on the dielectric. Evaluating the volume integration in the same manner as the integration of the force density, the total torque is

$$\mathcal{T} = \int_V \boldsymbol{\tau} dV = -\partial_t \int_V dV (\mathbf{r} \times (\varepsilon_0 \mathbf{E} \times \mathbf{B})). \quad (6.49)$$

The term on the left-hand side of the equation is the total torque acting on the dielectric which is equal to the change rate of the angular momentum. The terms on the right-hand side have the same magnitude as the change rate of the kinetic angular momentum of the photon but in the opposite direction, which is indicated by the minus sign in front of it. This implies the conservation of the

total kinetic angular momentum. The evanescent field provides some torque to the dielectric as well when the pulse hit the interface, but again its effect cancels itself when time evolves.

At this point, one might think that it is not necessary to express the polarisation field \mathbf{P} in terms of the electric displacement \mathbf{D} and the electric field \mathbf{E} and by expressing the polarisation field \mathbf{P} in the same way as Eq.(6.36) the physical force and torque can also be obtained. However, there is no natural boundary condition for this field, and applying the conventional form of the polarisation field, $\mathbf{P} = \varepsilon_0(n^2 - 1)\mathbf{E}$, directly into the dipole-based form before considering the boundary conditions can lead to a paradoxical result. We will discuss this problem later in this chapter.

6.5 Effective torque and angular momentum transfer

As discussed, Eq.(6.49) contains some parts of it that do not contribute to angular momentum transfer, such as the part that is written in terms of the evanescent field. In this section, we try to extract only the parts associated with the angular momentum transfer so that we can understand its mechanism. We call these parts of torque as effective torques. The expectation value of the total torque that a single-photon pulse acting on the dielectric medium can be calculated with the electric and magnetic field operators and the state of a single-photon pulse given in section 6.3 as

$$\langle \mathcal{T} \rangle = -\varepsilon_0 \frac{\partial}{\partial t} \int_V dV \left(\mathbf{r} \times \left(\langle 1 | : \hat{\mathbf{E}}^- \times \hat{\mathbf{B}}^+ + \hat{\mathbf{E}}^+ \times \hat{\mathbf{B}}^- : | 1 \rangle \right) \right), \quad (6.50)$$

where

$$\hat{\mathbf{E}}^- \times \hat{\mathbf{B}}^+ = \left(\hat{\mathbf{E}}_i^- \times \hat{\mathbf{B}}_i^+ + \hat{\mathbf{E}}_r^- \times \hat{\mathbf{B}}_r^+ + \hat{\mathbf{E}}_t^- \times \hat{\mathbf{B}}_t^+ \right) H(-z) + \left(\hat{\mathbf{E}}_t^- \times \hat{\mathbf{B}}_t^+ \right) H(z). \quad (6.51)$$

The spatial and time dependence of these field operators is again omitted for brevity. The subscripts i, r and t are used to indicate the incident, reflected and transmitted fields respectively. We have omitted the terms containing two annihilation and creation operators as their expectation values for the single-photon state vanish. For general photon states that the expectation values of these terms do not vanish, their contributions oscillate at optical frequency, and they, therefore, can be neglected [141]. We use colons to notify that the operators between two colons are in normal order [158]. As the form of the total torque given in Eq.(6.50), its time integration suggests that the terms that only exist shortly when the single-photon pulse reaches the interface do not contribute to angular momentum change of the dielectric, so they are not effective. The examples of the ineffective terms are the contributions from the evanescent field and the following cross terms:

$$\begin{aligned} \langle \mathcal{T}^{\text{ineff}} \rangle = & -\varepsilon_0 \frac{\partial}{\partial t} \int_V dV \mathbf{r} \times \left(\langle 1 | : (\hat{\mathbf{E}}_i^- \times \hat{\mathbf{B}}_r^+ + \hat{\mathbf{E}}_r^- \times \hat{\mathbf{B}}_i^+) H(-z) \right. \\ & \left. + (\hat{\mathbf{E}}_t^- \times \hat{\mathbf{B}}_t^+) H(z) + \text{h.c.} : | 1 \rangle \right), \end{aligned} \quad (6.52)$$

where h.c. denotes the Hermitian conjugate of the preceding terms. After we omit the ineffective part, we then have

$$\begin{aligned} \langle \mathcal{T}^{\text{eff}} \rangle = & -\varepsilon_0 \frac{\partial}{\partial t} \int_V dV \left(\mathbf{r} \times \left(\langle 1 | : \hat{\mathbf{E}}_i^- \times \hat{\mathbf{B}}_i^+ + \hat{\mathbf{E}}_r^- \times \hat{\mathbf{B}}_r^+ + \text{h.c.} : | 1 \rangle \right) \right) H(-z) \\ = & \langle \mathcal{T}_i^{\text{eff}} \rangle + \langle \mathcal{T}_r^{\text{eff}} \rangle, \end{aligned} \quad (6.53)$$

where

$$\langle \mathcal{T}_{i(r)}^{\text{eff}} \rangle = -\varepsilon_0 \frac{\partial}{\partial t} \int_V dV \left(\mathbf{r} \times \left(\langle 1 | : \hat{\mathbf{E}}_{i(r)}^- \times \hat{\mathbf{B}}_{i(r)}^+ + \text{h.c.} : | 1 \rangle \right) \right) H(-z). \quad (6.54)$$

Recall that the electric and magnetic fields of the incident and reflected beams are in the simplest form when they are written in terms of their own coordinate systems. As torques are vectors, or more precisely pseudovectors, and rotations of coordinate systems are passive transformations for vectors. It means only their descriptions that are changed. Therefore, the form in the second line of Eq.(6.53) allows us to calculate the torques from the incident and reflected fields in their own coordinates independently, and add them together later after applying the coordinate transformations to express them in terms of the interface coordinates. With the coordinate transformations given previously, we can write the step function $H(-z)$ in terms of the incident and reflection coordinates as

$$H(-z) = H(x_i \tan \theta - z_i) = H(z_r + x_r \tan \theta). \quad (6.55)$$

the effective torque given by the incident beam is

$$\begin{aligned} \langle \mathcal{T}_i^{\text{eff}} \rangle &= -\varepsilon_0 \frac{\partial}{\partial t} \int_{-\infty}^{\infty} \int_{-\infty}^{\infty} dx_i dy_i \int_{-\infty}^0 dz_i \left(\mathbf{r} \times \left(\langle 1 | : \hat{\mathbf{E}}_i^- \times \hat{\mathbf{B}}_i^+ + \text{h.c.} : | 1 \rangle \right) \right) \\ &\quad - \varepsilon_0 \frac{\partial}{\partial t} \int_{-\infty}^{\infty} \int_{-\infty}^{\infty} dx_i dy_i \int_0^{x_i \tan \theta} dz_i \left(\mathbf{r} \times \left(\langle 1 | : \hat{\mathbf{E}}_i^- \times \hat{\mathbf{B}}_i^+ + \text{h.c.} : | 1 \rangle \right) \right). \end{aligned} \quad (6.56)$$

The integration over the observation time of the last term on the right-hand side of the equation vanishes. This means it does not give any contribution to the net angular momentum transfer. It can be verified easily as there is no incident field in the region between $z_i = 0$ and $z_i = x_i \tan \theta$ at the times when we begin and finish the observation. At the time $t = -T$, the incident pulse does not enter the region yet, while at the time $t = T$ it has left the region already. The same holds for the contribution from the reflected field:

$$\langle \mathcal{T}_r^{\text{eff}} \rangle = -\varepsilon_0 \frac{\partial}{\partial t} \int_{-\infty}^{\infty} \int_{-\infty}^{\infty} dx_r dy_r \int_0^{\infty} dz_r \left(\mathbf{r} \times \left(\langle 1 | : \hat{\mathbf{E}}_r^- \times \hat{\mathbf{B}}_r^+ + \text{h.c.} : | 1 \rangle \right) \right). \quad (6.57)$$

We assume that the refractive index $n(\omega)$ of the medium does not vary significantly with the wave frequency: $n(\omega) \approx n(\omega') = n$. Using the forms of the incident electric and magnetic field operators given in Eqs.(6.27) and (6.28), the normal ordered Poynting vector operator of the incident beam may be written as

$$\begin{aligned} (\varepsilon_0 c^2)^{-1} \hat{\mathbf{S}}_i &= : \hat{\mathbf{E}}_i^- \times \hat{\mathbf{B}}_i^+ + \hat{\mathbf{E}}_i^+ \times \hat{\mathbf{B}}_i^- : \\ &= \frac{\hbar}{4\pi\varepsilon_0 c^2 n} \int_0^{\infty} \int_0^{\infty} d\omega d\omega' \frac{1}{\sqrt{\omega\omega'}} \hat{a}^\dagger(\omega) \hat{a}(\omega') e^{i(\omega-\omega')(t-nz_i/c)} \{ \mathcal{S}_i^x \mathbf{x}_i + \mathcal{S}_i^y \mathbf{y}_i + \mathcal{S}_i^z \mathbf{z}_i \}, \end{aligned} \quad (6.58)$$

with

$$\mathcal{S}_i^x = -i\omega c (u_{k,l}^i)^* \partial_{x_i} u_{k',l}^i + i\omega' c u_{k',l}^i \partial_{x_i} (u_{k,l}^i)^* + c\sigma_i (\omega (u_{k,l}^i)^* \partial_{y_i} u_{k',l}^i + \omega' u_{k',l}^i \partial_{y_i} (u_{k,l}^i)^*), \quad (6.59)$$

$$\mathcal{S}_i^y = -i\omega c (u_{k,l}^i)^* \partial_{y_i} u_{k',l}^i + i\omega' c u_{k',l}^i \partial_{y_i} (u_{k,l}^i)^* - c\sigma_i (\omega (u_{k,l}^i)^* \partial_{x_i} u_{k',l}^i + \omega' u_{k',l}^i \partial_{x_i} (u_{k,l}^i)^*), \quad (6.60)$$

$$\mathcal{S}_i^z = 2n\omega\omega' (u_{k,l}^i)^* u_{k',l}^i, \quad (6.61)$$

where $\sigma_i = i(\alpha\beta^* - \alpha^*\beta)$ is the spin angular momentum quantum number of the incident beam. The expectation value of the Poynting vector can be obtained by replacing annihilation and creation operators with the function $\xi(\omega')$ and its complex conjugate $\xi^*(\omega)$. The narrowband wave packet state of the single-photon pulse allows us to approximately replace the frequencies ω and ω' in the integrand with the central frequency ω_0 , unless they are in the subtraction form: $\omega - \omega'$. Substituting the expectation value of the Poynting vector of the incident beam into Eq.(6.56), the expectation of the effective torque from the incident beam is

$$\begin{aligned} \langle \mathcal{T}_i^{\text{eff}} \rangle &= -\frac{\hbar}{4\pi cn} (2l + 2\sigma_i) \mathbf{z}_i \int_{-\infty}^0 dz_i \int_0^\infty \int_0^\infty d\omega d\omega' \xi^*(\omega) \xi(\omega') i(\omega - \omega') e^{i(\omega - \omega')(t - nz_i/c)} \\ &= \frac{\hbar}{n^2} \left(\frac{c^2}{2\pi L^2} \right)^{1/2} (2l + 2\sigma_i) \mathbf{z}_i e^{-2t^2 c^2 / L^2}. \end{aligned} \quad (6.62)$$

The angular momentum transfer due to this torque becomes

$$\lim_{T \rightarrow \infty} \int_{-T}^T dt \langle \mathcal{T}_i^{\text{eff}} \rangle = \frac{\hbar}{n^2} (l + \sigma_i) \mathbf{z}_i. \quad (6.63)$$

Notice that there is no contribution in x_i - and y_i -directions. This is because these contributions are in the form of $x_i S_i^z$ and $y_i S_i^z$, and, when we apply the narrowband approximation, the z -component of the Poynting vector is symmetric about x_i - and y_i -axes. The integrations over the $x_i y_i$ -plane of these contributions then vanish as they are the integration of odd functions of x_i and y_i .

As we have shown, the forms of the reflected fields are more complicated than that of the incident fields, even in the reflection coordinates. The torque from the reflected fields inarguably contains a lot of terms. However, with the help of the symmetry in the $x_r y_r$ -plane of $|\underline{u}_{k,l}|^2$, some of them do not give contribution to the total torque as their integrations over the $x_r y_r$ -plane vanish. We can then omit these terms. The expectation value of the torque from the reflected field is given as

$$\begin{aligned} \langle \mathcal{T}_r^{\text{eff}} \rangle &= -\frac{\hbar}{4\pi c^2 n} \int_0^\infty dz_r \int_0^\infty \int_0^\infty d\omega d\omega' \xi^*(\omega) \xi(\omega') i(\omega - \omega') e^{i(\omega - \omega')(t - nz_r/c)} \\ &\quad \times \int_{-\infty}^\infty \int_{-\infty}^\infty dx_r dy_r \{ \mathcal{J}_r^x \mathbf{x}_r + \mathcal{J}_r^y \mathbf{y}_r + \mathcal{J}_r^z \mathbf{z}_r \}, \end{aligned} \quad (6.64)$$

with

$$\mathcal{J}_r^x = 2c(\sigma_i + \sigma_r) y_r \cot \theta \partial_{y_r} |\underline{u}_{k_0,l}|^2, \quad (6.65)$$

$$\mathcal{J}_r^y = 2\omega_0 n \left(|\alpha|^2 D^p + |\beta|^2 D^s \right) x_r \partial_{x_r} |\underline{u}_{k_0,l}|^2, \quad (6.66)$$

$$\begin{aligned} \mathcal{J}_r^z &= icx_r (\underline{u}_{k_0,l} \partial_{y_r} \underline{u}_{k_0,l}^* - \underline{u}_{k_0,l}^* \partial_{y_r} \underline{u}_{k_0,l}) - c\sigma_r x_r \partial_{x_r} |\underline{u}_{k_0,l}|^2 \\ &\quad - icy_r (\underline{u}_{k_0,l} \partial_{x_r} \underline{u}_{k_0,l}^* - \underline{u}_{k_0,l}^* \partial_{x_r} \underline{u}_{k_0,l}) + c\sigma_r x_r \partial_{x_r} |\underline{u}_{k_0,l}|^2, \end{aligned} \quad (6.67)$$

where we have defined $\alpha' = \bar{r}^p \alpha$ and $\beta' = \bar{r}^s \beta$ which can be thought of as the polarisation of the reflected beam, and the spin angular momentum quantum number of the reflected beam is defined as $\sigma_r = i(\alpha'\beta'^* - \alpha'^*\beta')$. With the help from the symmetry of $|\underline{u}_{k,l}|^2$, the effective torque of the reflected field is given as,

$$\begin{aligned} \langle \mathcal{T}_r^{\text{eff}} \rangle &= \frac{\hbar}{n^2 c} \left(\frac{c^2}{2\pi L^2} \right)^{1/2} e^{-2t^2 c^2 / L^2} \{ c(2l - 2\sigma_r) \mathbf{z}_r + 2\omega_0 n (|\alpha|^2 D^p + |\beta|^2 D^s) \mathbf{y}_r \\ &\quad + 2c(\sigma_i + \sigma_r) \cot \theta \mathbf{x}_r \}. \end{aligned} \quad (6.68)$$

Notice that for this case there are the components of the effective torque in x_r - and y_r -directions. They originate from the fact that the reflected beam is shifted in both longitudinal and transverse directions. The beam shift will be discussed in more detail in the next section.

With the results from Eqs.(6.62) and (6.68), we then express the effective torques $\langle \mathcal{T}_i^{\text{eff}} \rangle$ and $\langle \mathcal{T}_r^{\text{eff}} \rangle$ in terms of the interface coordinates and add them together to obtain the total effective torque:

$$\begin{aligned} \langle \mathcal{T}^{\text{eff}} \rangle &= \langle \mathcal{T}_i^{\text{eff}} \rangle + \langle \mathcal{T}_r^{\text{eff}} \rangle \\ &= \frac{\hbar}{n^2} \left(\frac{c^2}{2\pi L^2} \right)^{1/2} e^{-2t^2 c^2 / L^2} \left\{ [(4l \sin \theta + 2(\sigma_i - \sigma_r) \sin \theta) \mathbf{x} + 2(\sigma_i + \sigma_r) \cos \theta \mathbf{z}] \right. \\ &\quad \left. + \left(\frac{2\omega_0 n}{c} (|\alpha|^2 D^p + |\beta|^2 D^s) \right) \mathbf{y} - 2(\sigma_i + \sigma_r) \cos \theta \mathbf{z} \right. \\ &\quad \left. - 2(\sigma_i + \sigma_r) \cot \theta \cos \theta \mathbf{x} \right\}. \end{aligned} \quad (6.69)$$

The exponential term indicates that this torque occurs only when the photon pulse hits the interface, and there is no torque elsewhere during the photon pulse propagating inside the dielectric. We decompose the total effective torque into two different parts: the torque that is the result of the beam shift effect and the one that associated with the change of the intrinsic angular momentum (spin and orbital angular momentum) of the photon [24]. The later part is separated from the other by the square bracket in the second line of the equation.

6.6 Beam shift analysis

In this section, we show explicitly that the reflected beam is shifted in both longitudinal and transverse directions, and it is this effect that causes the effective torque in x_r - and y_r -directions. We start by evaluating the centre of gravity of the reflected beam. We use the reflection coordinates to demonstrate this effect. There are two reasons that we use the reflection coordinates: 1. the reflected fields are in the simplest form in this coordinate, 2. the z_r -axis is defined to be the direction of propagation in the geometrical description, so if the centre of gravity of the reflected beam is deviated from the z_r -axis, it means the reflected beam is shifted. The centre of gravity in an $x_r y_r$ -plane is $(\langle x_r \rangle, \langle y_r \rangle)$ such that

$$\langle x_r^j \rangle = \frac{\int_{-\infty}^{\infty} \int_{-\infty}^{\infty} dx_r dy_r x_r^j \langle 1 | : \hat{\mathbf{E}}_r^- \cdot \hat{\mathbf{E}}_r^+ + \hat{\mathbf{E}}_r^+ \cdot \hat{\mathbf{E}}_r^- : | 1 \rangle}{\int_{-\infty}^{\infty} \int_{-\infty}^{\infty} dx_r dy_r \langle 1 | : \hat{\mathbf{E}}_r^- \cdot \hat{\mathbf{E}}_r^+ + \hat{\mathbf{E}}_r^+ \cdot \hat{\mathbf{E}}_r^- : | 1 \rangle}, \quad (6.70)$$

where we have defined x_r^j to be x_r or y_r . The position of the centre of gravity shows that the reflected beam is shifted in both transverse and longitudinal directions:

$$\langle x_r \rangle = (|\alpha|^2 D^p + |\beta|^2 D^s), \quad (6.71)$$

$$\langle y_r \rangle = -\frac{c(\sigma_i + \sigma_r)}{\omega_0 n} \cot \theta, \quad (6.72)$$

as shown in figure 6.4. We note that the sizes of $\langle x_r \rangle$ and $\langle y_r \rangle$ are in the scale of the central wavelength, which are much smaller than the size of the beam waist.

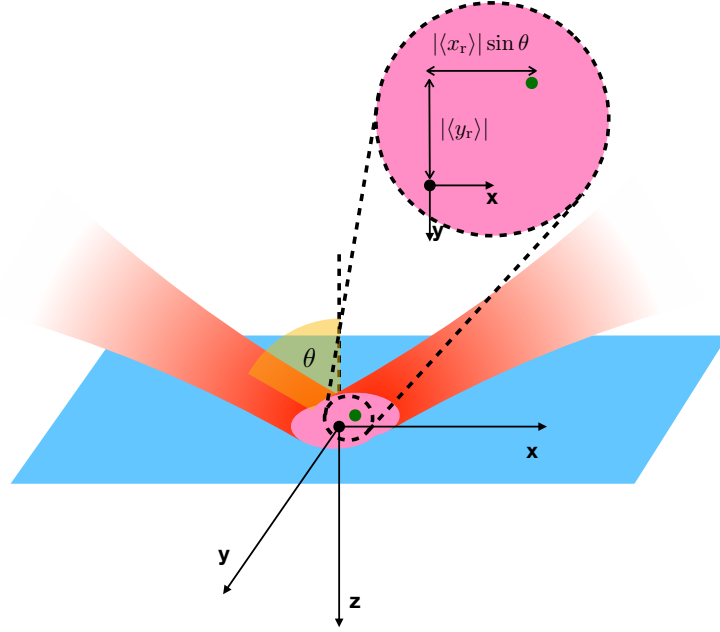


Figure 6.4: The reflected beam is shifted in both transverse and longitudinal directions. The amount of the beam shift depends on the polarisation of the incident beam and the angle of incidence θ . The black and the green points at the centres of the beam waists are the centres of gravity of the incident and reflected beams. The picture around the beam waists of the incident and reflected beams is magnified in the dashed pink circle so that we can see the amount of the beam shift on the interface plane clearly.

To understand this result in more detail, let us consider the following situation. If we assume that the incident beam is linearly polarised such that $|\alpha|^2 = 1$ ($|\beta|^2 = 1$). As the polarisation of the incident beam is linear for this case, the transverse shift given in Eq.(6.72) vanish. We then can see that the reflected beam is shifted only in the longitudinal direction by D^p (D^s). With Eqs.(6.16) and (6.17), both D^s and D^p are negative which implies directly that the beam is shifted in the negative x_r -direction. We recognise this longitudinal shift as the familiar Goos-Hänchen (G-H) shift [159,160]. From the definition of D^s and D^p , they are proportional to \bar{r}'^p and \bar{r}'^s . This means there will be no longitudinal shift if we treat all the plane wave components of the superposition of the incident beam, given in Eq.(6.11), with the same Fresnel reflective coefficients: $\bar{r}'^p = 0 = \bar{r}'^s$. Therefore, we can summarise the longitudinal shift or the G-H shift arises from the fact that each plane wave component experiences a different Fresnel coefficient. On the other hand, this means the transverse shift which is proportional to the summation of the spin angular momentum of the incident and reflected photons is the result of each plane wave component has its own plane of incidence. The transverse shift is known as the Imbert-Fedorov shift [161–163]. These shifts are related to the components of the effective torque in the x_r - and y_r -directions in Eq.(6.68). Let us determine the

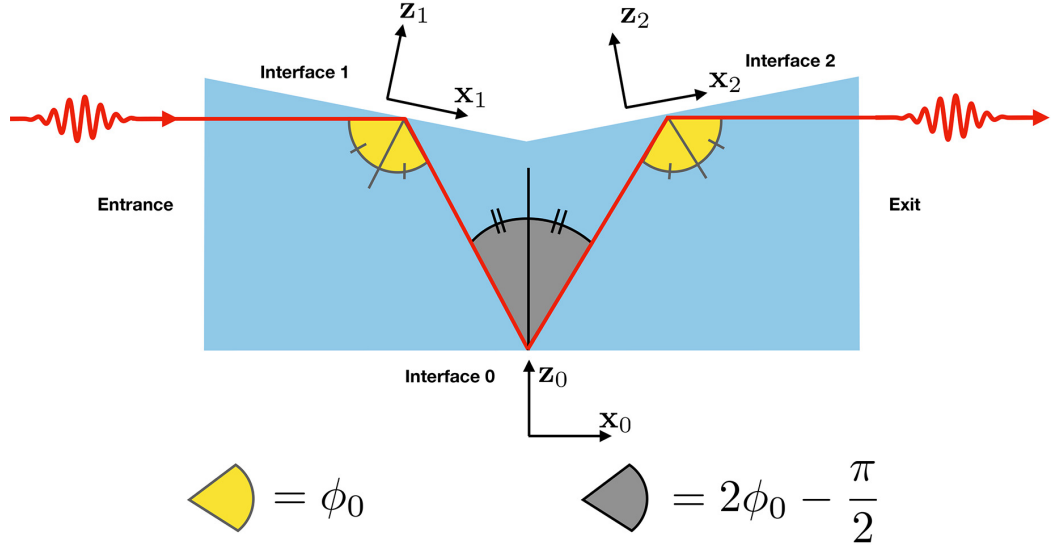


Figure 6.5: The figure shows the propagation path of a single photon when it passing through an M-shaped Dove prism.

Abraham linear momentum of the photon pulse after it has been reflected from the interface:

$$\langle \mathbf{p} \rangle = \int_V dV \langle 1 | : \varepsilon_0 \hat{\mathbf{E}}_{\mathbf{r}} \times \hat{\mathbf{B}}_{\mathbf{r}} : | 1 \rangle \Big|_{t=T} = \frac{\hbar \omega_0}{nc} \mathbf{z}_{\mathbf{r}}. \quad (6.73)$$

The angular momentum of the photon pulse due to the beam shift after reflection with respect to the origin of the reflection coordinates is

$$\begin{aligned} \langle \mathbf{L}_{\text{shift}} \rangle &= \langle \mathbf{p} \rangle \times (\langle x_{\mathbf{r}} \rangle \mathbf{x}_{\mathbf{r}} + \langle y_{\mathbf{r}} \rangle \mathbf{y}_{\mathbf{r}}) \\ &= - \left(\frac{\hbar \omega_0}{nc} (|\alpha|^2 D^{\text{p}} + |\beta|^2 D^{\text{s}}) \right) \mathbf{y}_{\mathbf{r}} - \frac{\hbar (\sigma_{\mathbf{i}} + \sigma_{\mathbf{r}})}{n^2} \cot \theta \mathbf{x}_{\mathbf{r}} \\ &= - \int_{-\infty}^{\infty} dt (\langle \mathcal{T}_{\mathbf{r}}^{\text{eff}} \rangle \cdot \mathbf{y}_{\mathbf{r}}) \mathbf{y}_{\mathbf{r}} + (\langle \mathcal{T}_{\mathbf{r}}^{\text{eff}} \rangle \cdot \mathbf{x}_{\mathbf{r}}) \mathbf{x}_{\mathbf{r}}. \end{aligned} \quad (6.74)$$

Without the beam shift, this part of angular momentum of the photon disappears. With Newton's third law of motion, the torque that produces this angular momentum of the photon has the same magnitude as the corresponding torque that exerts on the dielectric medium but in the opposite direction as shown in the third line of the equation. We can, therefore, conclude that the beam shift gives rise the change of the extrinsic angular momentum of the photon, and this change of angular momentum causes the effective torque in the $x_{\mathbf{r}}$ - and $y_{\mathbf{r}}$ -directions.

6.7 M-shaped Dove prism

This section is devoted to evaluating the angular momentum transfer from the single-photon pulse to an M-shaped Dove prism, as depicted in figure 6.5, on the condition that the photon pulse passes through the Dove prism. First of all, let us recall the effect of this type of Dove prisms on a composite

state of photons. As discussed in chapter 3, M-shaped Dove prisms are designed in order to convert the polarisation of photons in the same manner as a quarter-wave plate [119] and invert the orbital angular momentum of the incident photon as other Dove prisms.

As discussed in the previous section, the shift of the reflected beam causes the contributions of the effective torque in the x_r - and y_r -directions. The effect of the beam shift is depicted in figure 6.6. From the figure, we can see that the beam shifts alter the propagation path of the single photon, which changes the extrinsic angular momentum of the photon in the directions parallel to \mathbf{y}_0 and \mathbf{z}_0 after the single photon leaves the Dove prism. These shifts alter the exit point of the photon from its geometrical expectation. With the conservation of angular momentum, the Dove prism then gains angular momentum with the same amount but in the opposite direction to the photon.

However, in this work, we aim to account for the observation of the intrinsic angular momentum change of the light, $-(2l + \Delta\sigma)\hbar\mathbf{x}_0$, where $\Delta\sigma$ is the change of the spin angular momentum quantum number, when the single photon passing through the Dove prism and the angular momentum transfer according to this change. The definition of intrinsic and extrinsic angular momentum are given in [24]. The intrinsic part includes spin and orbital angular momentum. The effective torque associated with the intrinsic angular momentum exchange is given in the square bracket of Eq.(6.69):

$$\langle \mathcal{T}_{\text{intrinsic}}^{\text{eff}} \rangle = \frac{\hbar}{n^2} \left(\frac{c^2}{2\pi L^2} \right)^{1/2} e^{-2t^2 c^2 / L^2} [(4l \sin \theta + 2(\sigma_i - \sigma_r) \sin \theta)\mathbf{x} + 2(\sigma_i + \sigma_r) \cos \theta \mathbf{z}]. \quad (6.75)$$

The angular momentum change of the dielectric caused by this torque is

$$\langle \Delta \mathbf{L}_{\text{dielectric}} \rangle = \int_{-\infty}^{\infty} dt \langle \mathcal{T}_{\text{intrinsic}}^{\text{eff}} \rangle = \frac{\hbar}{n^2} ((2l \sin \theta + (\sigma_i - \sigma_r) \sin \theta)\mathbf{x} + (\sigma_i + \sigma_r) \cos \theta \mathbf{z}). \quad (6.76)$$

With the geometric shape of the M-shaped Dove prism, in order that the single-photon pulse passes through it, the photon has to encounter three total internal reflections at interface 1, 0 and 2 respectively. According to Loudon's work [134], the photon also exchanges its angular momentum with the dielectric when it enters and leaves the dielectric. Therefore, there are five different positions at which the photon transfers its angular momentum to the M-shaped Dove prism, and all of them are the points where the photon hits the interfaces. We can calculate the total intrinsic angular momentum that transfer to the Dove if the single-photon pulse passes through it as follows. We define three different coordinates as given in figure 6.5. The relations between the unit vectors of these coordinates are given as

$$\mathbf{x}_1 = \mathbf{x}_0 \sin \phi_0 - \mathbf{z}_0 \cos \phi_0, \quad (6.77)$$

$$\mathbf{z}_1 = \mathbf{z}_0 \sin \phi_0 + \mathbf{x}_0 \cos \phi_0, \quad (6.78)$$

$$\mathbf{x}_2 = \mathbf{x}_0 \sin \phi_0 + \mathbf{z}_0 \cos \phi_0, \quad (6.79)$$

$$\mathbf{z}_2 = \mathbf{z}_0 \sin \phi_0 - \mathbf{x}_0 \cos \phi_0. \quad (6.80)$$

We assume that the incoming single photon initially carries spin angular momentum $\hbar\sigma_{\text{in}}$ and orbital angular momentum $\hbar l$ in the positive x_0 -direction. Recall that the direction of the polarisation of a single photon is not changed if the photon normally passes through a dielectric interface. The spin angular momentum quantum number thus is conserved after the single photon passes the entrance

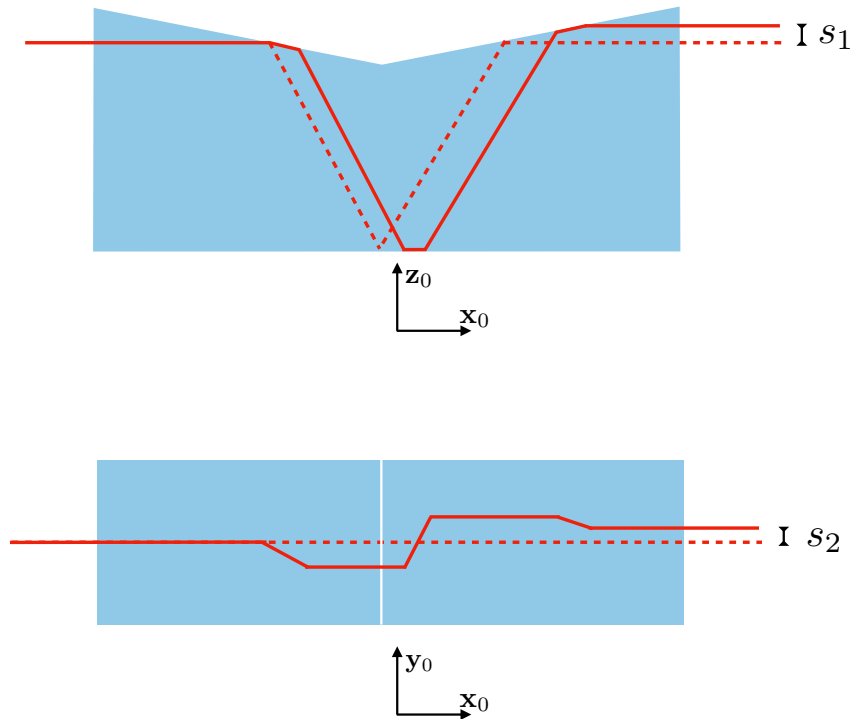


Figure 6.6: In this figure, we compare the difference between the photon paths in the geometrical description and in the actual situation when beam shifts take place. The upper picture is the picture of the Dove prism from the side view, while the lower one is the Dove prism viewed from the upper aspect. The solid lines are the actual propagation path when both longitudinal and transverse shifts occur, while the dashed lines are the geometrical path. These shifts are exaggerated in the picture so that we can see the difference between these two paths. The actual sizes of the beam shifts in Eqs.(6.71) and (6.72) are in the order of the wavelength of the beam, which are much smaller than the beam waist w_0 .

surface. With the given coordinate transformations, the total angular momentum change of the Dove prism acquired from total internal reflections may be written as

$$\begin{aligned}
\langle \Delta \mathbf{L}_{\text{reflections}} \rangle &= \langle \Delta \mathbf{L}_1 \rangle + \langle \Delta \mathbf{L}_0 \rangle + \langle \Delta \mathbf{L}_2 \rangle \\
&= \frac{\hbar}{n^2} \{ (2l \sin \phi_0 + (\sigma_{\text{in}} - \sigma_1) \sin \phi_0) \mathbf{x}_1 + (\sigma_{\text{in}} + \sigma_1) \cos \phi_0 \mathbf{z}_1 \\
&\quad + (-2l \sin(2\phi_0 - \pi/2) + (\sigma_1 - \sigma_2) \sin(2\phi_0 - \pi/2)) \mathbf{x}_0 \\
&\quad - (\sigma_1 + \sigma_2) \cos(2\phi_0 - \pi/2) \mathbf{z}_0 + (2l \sin \phi_0 + (\sigma_2 - \sigma_{\text{out}}) \sin \phi_0) \mathbf{x}_2 \\
&\quad + (\sigma_2 + \sigma_{\text{out}}) \cos \phi_0 \mathbf{z}_2 \} \\
&= \frac{\hbar}{n^2} (2l + (\sigma_{\text{in}} - \sigma_{\text{out}})) \mathbf{x}_0,
\end{aligned} \tag{6.81}$$

where σ_1 , σ_2 and σ_{out} are the spin angular-momentum quantum number of the single-photon pulse after it has reflected from interfaces 1, 0 and 2 respectively. We have denoted the angular momentum change of the Dove prism after the photon has reflected from interface j as $\langle \Delta \mathbf{L}_j \rangle$. As we discussed previously, after each reflection the topological charge of the photon is changed from l to $-l$ or vice versa. The amounts of angular momentum that the Dove prism has gained when the photon passes through the entrance and exit surfaces are given in [134]:

$$\langle \Delta \mathbf{L}_{\text{entrance}} \rangle = \hbar(l_{\text{in}} + \sigma_{\text{in}}) \left(1 - \frac{1}{n^2} \right) \mathbf{x}_0, \tag{6.82}$$

$$\langle \Delta \mathbf{L}_{\text{exit}} \rangle = -\hbar(l_{\text{out}} + \sigma_{\text{out}}) \left(1 - \frac{1}{n^2} \right) \mathbf{x}_0. \tag{6.83}$$

where we denote l_{in} and l_{out} as the topological charges of the incoming and outgoing beams. Recall that we have assumed that the incoming photon carries an orbital angular momentum of $\hbar l_{\text{in}} = \hbar l$, while the orbital angular momentum of the outgoing photon is $\hbar l_{\text{out}} = -\hbar l$, since the Dove prism inverts its topological charge. Combining these angular momentum changes with the ones previously obtained in Eq.(6.81), the angular momentum that the Dove prism obtains when the photon pass through it is

$$\begin{aligned}
\langle \Delta \mathbf{L}_{\text{Dove}} \rangle &= \hbar(l + \sigma_{\text{in}}) \left(1 - \frac{1}{n^2} \right) \mathbf{x}_0 + \frac{\hbar}{n^2} (2l + (\sigma_{\text{in}} - \sigma_{\text{out}})) \mathbf{x}_0 \\
&\quad - \hbar(-l + \sigma_{\text{out}}) \left(1 - \frac{1}{n^2} \right) \mathbf{x}_0, \\
&= \hbar(2l + (\sigma_{\text{in}} - \sigma_{\text{out}})) \mathbf{x}_0.
\end{aligned} \tag{6.84}$$

As we have mentioned, the M-shaped Dove prism is designed to change the polarisation of photons in the same manner as a quarter wave plate [119], if the incoming photon is circularly polarised, $\sigma_{\text{in}} = \pm 1$, the outgoing photon will become linearly polarised, $\sigma_{\text{out}} = 0$. Therefore, the angular momentum that the M-shaped Dove prism gains, if a circularly polarised single-photon pulse passes through it, is

$$\langle \Delta \mathbf{L}_{\text{Dove}} \rangle = (2l \pm 1) \hbar \mathbf{x}_0. \tag{6.85}$$

The angular momentum change of the photon, on the other hand, is $\langle \Delta \mathbf{L}_{\text{photon}} \rangle = -(2l \pm 1) \hbar \mathbf{x}_0$ in the direction of its propagation. The total angular momentum of the system, the single photon and

the Dove prism, is conserved as expected. Figure 6.7 shows the torque exerts on the Dove prism and its angular momentum change, while the force and linear momentum exchange between light and the Dove prism given in figure 6.8. The first picture illustrates the asymmetry of the torque which is not apparent in the longitudinal force in the second picture. The asymmetry of torque arises because of the change of polarisation of light on reflection, which affects the spin angular momentum but not the linear momentum.

6.8 Paradox of conservation of angular momentum

From the given discussion so far in the preceding section, one might think that expressing polarisation \mathbf{P} as electric displacement \mathbf{D} and electric field \mathbf{E} is not necessary and the same physics would be reproduced. However, it can lead us to the paradox of conservation of angular momentum. In this section, we will discuss how this paradox might appear in the calculation, if we evaluate force and torque densities in terms of polarisation \mathbf{P} and apply it conventional form: $\mathbf{P} = \varepsilon_0(n^2 - 1)\mathbf{E}$. In the dipole-based force density form, if we write the polarisation and the other fields in the same way as we did for the electric field in Eq.(6.36), we will find the i th component of the force density is

$$f_i = P_l^{(\text{in})} \partial_i E_l^{(\text{in})} H(-z) + \partial_t (\mathbf{P}^{(\text{in})} \times \mathbf{B}^{(\text{in})})_i H(-z) + \delta_{iz} \delta(z) \frac{P_z^{(\text{in})}}{2} (E_z^{(\text{out})} - E_z^{(\text{in})}), \quad (6.86)$$

where the summation convention is implied for the first term. There is nothing wrong with this equation as we can still recover Eq.(6.39) from this point by writing the polarisation \mathbf{P} in terms of the electric field \mathbf{E} and electric displacement \mathbf{D} .

On the other hand, if we use the conventional form of polarisation of dielectric media, $\mathbf{P} = \varepsilon_0(n^2 - 1)\mathbf{E}$, and directly substitute it into Eq.(6.86), the force and torque densities due to total internal reflection should become

$$f_i = \varepsilon_0(n^2 - 1) \partial_i \left(\frac{E_l^{(\text{in})} E_l^{(\text{in})}}{2} \right) H(-z) + \varepsilon_0(n^2 - 1) \partial_t (\mathbf{E}^{(\text{in})} \times \mathbf{B}^{(\text{in})})_i H(-z) + \delta_{iz} \delta(z) \varepsilon_0(n^2 - 1) \frac{E_z^{(\text{in})}}{2} (E_z^{(\text{out})} - E_z^{(\text{in})}), \quad (6.87)$$

and

$$\tau_i = \varepsilon_0(n^2 - 1) \partial_k \left\{ \epsilon_{ijk} x_j \frac{E_l^{(\text{in})} E_l^{(\text{in})}}{2} \right\} H(-z) + \varepsilon_0(n^2 - 1) \partial_t (\mathbf{r} \times (\mathbf{E}^{(\text{in})} \times \mathbf{B}^{(\text{in})}))_i + \epsilon_{ijk} \delta_{kz} \delta(z) x_j \frac{E_z^{(\text{in})}}{2} (E_z^{(\text{out})} - E_z^{(\text{in})}). \quad (6.88)$$

It is straightforward to show, however, that these two equations may lead to the paradox by considering the following case. The incident beam with the topological charge l is linearly polarised such that its vector potential \mathbf{A} is parallel to the interface, so that $|\alpha|^2 = 0$ and $|\beta|^2 = 1$ in Eqs.(6.27) and (6.28). As we are focusing on the effective torque associated with the transfer of the intrinsic angular momentum of the photon, the term related to the shift of the reflected beam can be ignored. As the cross section of the beam is finite, the area where the beam hits the interface is also finite,

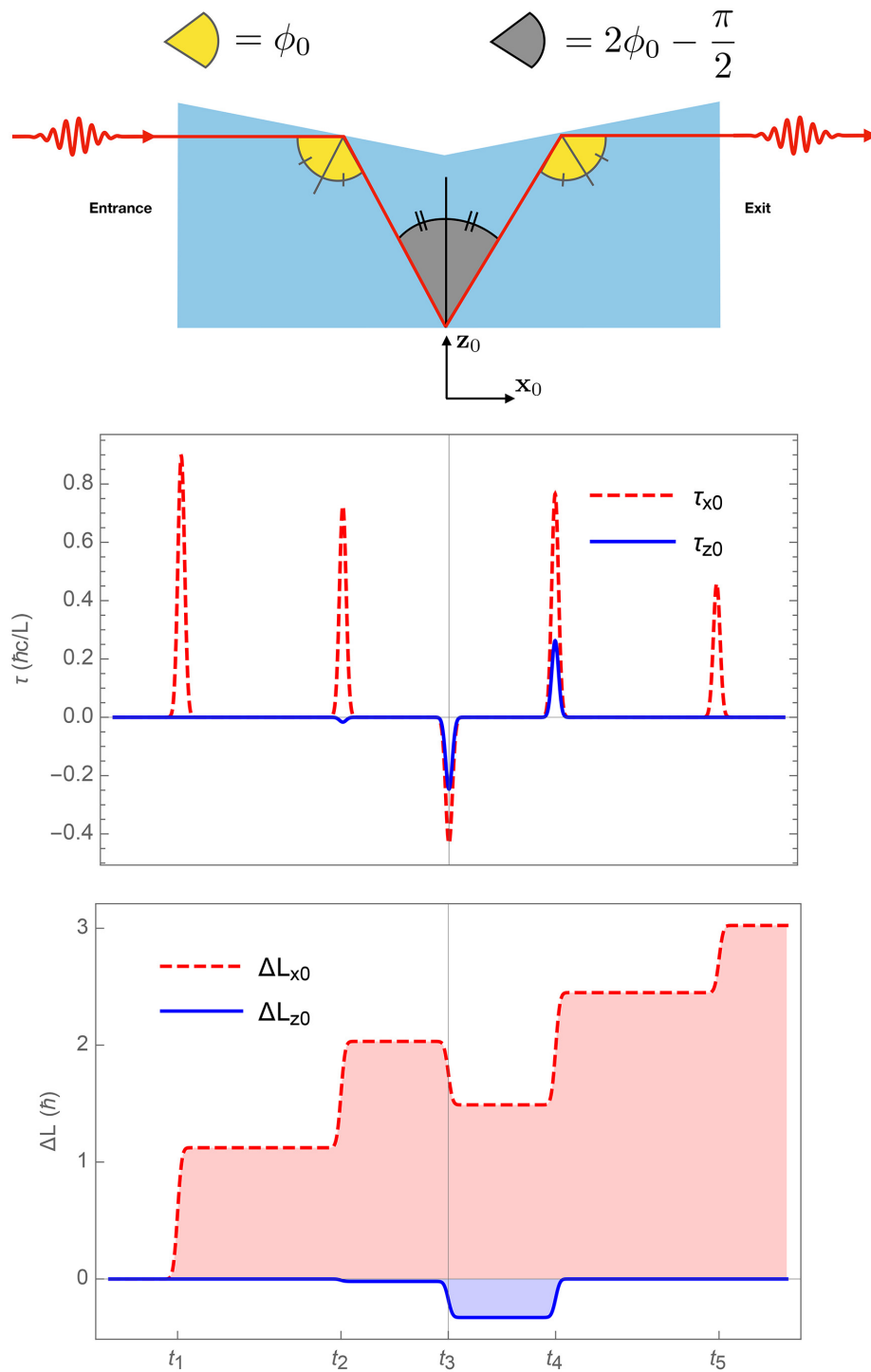


Figure 6.7: The figure shows the torque exerted on the Dove prism by a single-photon pulse that carries orbital angular momentum $l = 1$ and spin angular momentum $\sigma_l = 1$ and the angular momentum change of the Dove prism. We assume that the pulse hit the interfaces of the Dove prism at the times t_1, t_2, t_3, t_4 and t_5 .

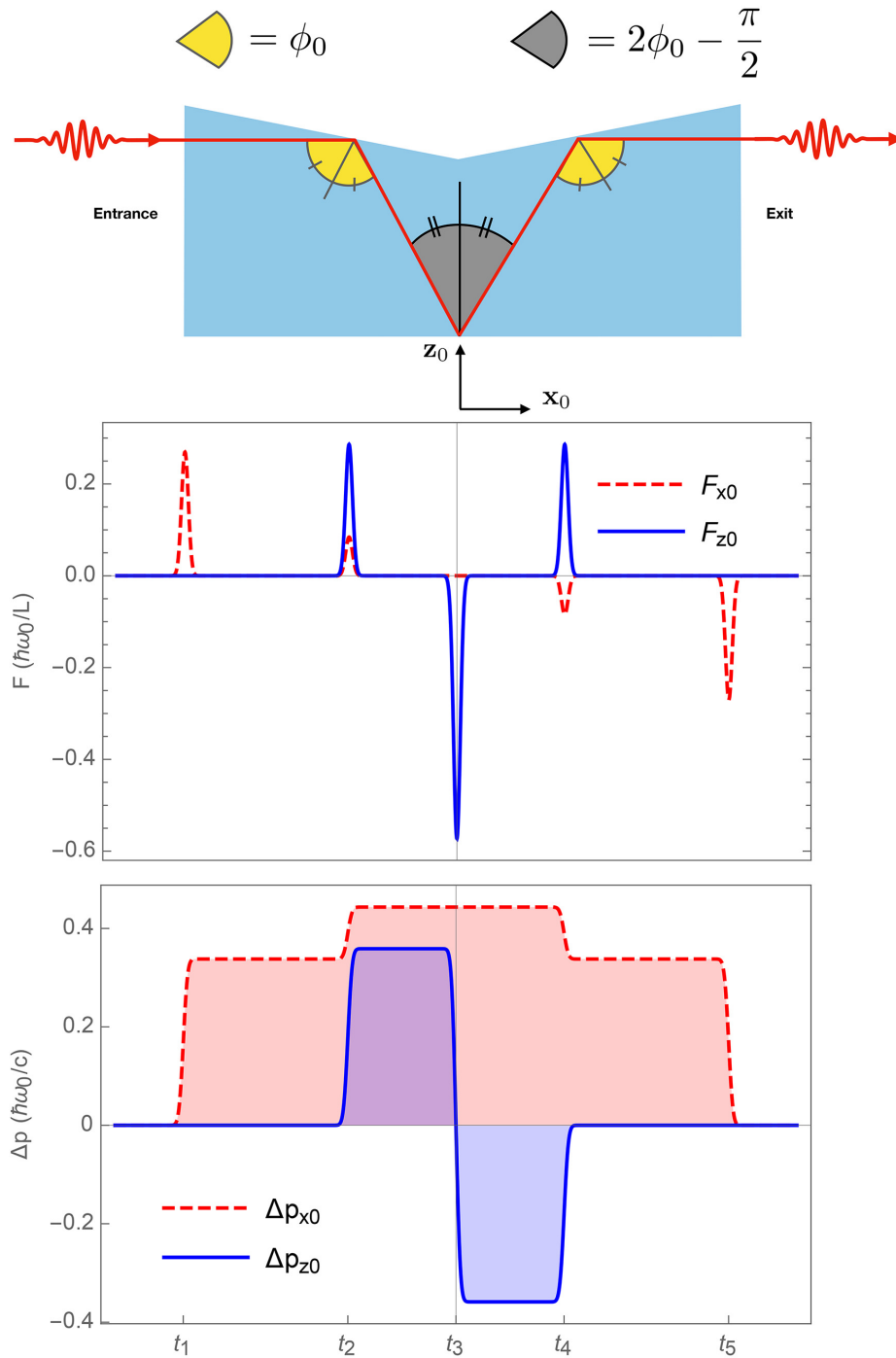


Figure 6.8: The figure shows the force that the single photon pulse exerts on the Dove prism and the linear momentum change at the times t_1 , t_2 , t_3 , t_4 and t_5 .

unless the angle of incidence is $\pi/2$. This implies that after integration over the large volume V , as defined previously, the terms being in the forms of the derivatives with respect to x and y vanish because there is no polarisation field at the surface of the volume V . Within the paraxial regime, the term that is proportional to the delta function in Eq.(6.88) is negligible after integration over the volume. After cutting out the mentioned non-contributing terms, the total torque then becomes

$$\begin{aligned} \mathcal{T}_i = & \epsilon_{ijz}\epsilon_0(n^2 - 1) \int_{-\infty}^{\infty} \int_{-\infty}^{\infty} dx dy x_j \frac{E_l^{(\text{in})} E_l^{(\text{in})}}{2} \Big|_{z=0^-} \\ & + \epsilon_0(n^2 - 1) \int_V dV \partial_t (\mathbf{r} \times (\mathbf{E}^{(\text{in})} \times \mathbf{B}^{(\text{in})}))_i H(-z), \end{aligned} \quad (6.89)$$

where we have used the fact that the step function changes the integration limit as shown in Eq.(6.43). With the coordinate transformation previously given in Eq.(6.10) and (6.21), one can write the incident and reflected electric fields in terms of the interface coordinates (x, y, z) explicitly. At $z = 0^-$, the expectation value of the electric field strength, with paraxial approximation is proportional to the following function:

$$\langle 1 | : \hat{\mathbf{E}}^- \cdot \hat{\mathbf{E}}^+ + \hat{\mathbf{E}}^+ \cdot \hat{\mathbf{E}}^- : | 1 \rangle \Big|_{z=0^-} \propto |u_{k_0,l}(x \cos \theta, y, x \sin \theta)|^2 e^{-2c^2(t-nx \sin \theta/c)^2/L^2}. \quad (6.90)$$

This quantity is finite everywhere and localised in a space-time volume, so according to the Fubini's theorem [164, 165], its integration over space and time then is invariant under switching the order of integration. The angular momentum change of dielectric due to the gradient of intensity, the first term in Eq.(6.89), becomes

$$\begin{aligned} \langle \Delta \mathbf{L}_{\text{gradient}} \rangle = & \epsilon_0(n^2 - 1) \mathbf{x} \int_{-\infty}^{\infty} dt \int_{-\infty}^{\infty} y \frac{\langle 1 | : \hat{\mathbf{E}}^- \cdot \hat{\mathbf{E}}^+ + \hat{\mathbf{E}}^+ \cdot \hat{\mathbf{E}}^- : | 1 \rangle}{2} \Big|_{z=0^-} dx dy \\ & - \epsilon_0(n^2 - 1) \mathbf{y} \int_{-\infty}^{\infty} dt \int_{-\infty}^{\infty} x \frac{\langle 1 | : \hat{\mathbf{E}}^- \cdot \hat{\mathbf{E}}^+ + \hat{\mathbf{E}}^+ \cdot \hat{\mathbf{E}}^- : | 1 \rangle}{2} \Big|_{z=0^-} dx dy \\ \propto & \epsilon_0(n^2 - 1) \mathbf{x} \int_{-\infty}^{\infty} \int_{-\infty}^{\infty} y |u_{k_0,l}(x \cos \theta, y, x \sin \theta)|^2 dx dy \int_{-\infty}^{\infty} dt e^{-2c^2(t-nx \sin \theta/c)^2/L^2} \\ & - \epsilon_0(n^2 - 1) \mathbf{y} \int_{-\infty}^{\infty} \int_{-\infty}^{\infty} x |u_{k_0,l}(x \cos \theta, y, x \sin \theta)|^2 dx dy \int_{-\infty}^{\infty} dt e^{-2c^2(t-nx \sin \theta/c)^2/L^2} \\ = & 0. \end{aligned} \quad (6.91)$$

Because from Eq.(6.4), the strength of the complex function $|u_{k_0,l}(x \cos \theta, y, x \sin \theta)|^2$ is symmetric about the x - and y -axes, this gives rise the result that the gradient intensity does not cause the change of angular momentum of the dielectric. The effective torque due to total internal reflection then becomes

$$\begin{aligned} \langle \mathcal{T} \rangle = & \epsilon_0(n^2 - 1) \int_V dV \partial_t (\mathbf{r} \times (\langle 1 | : \hat{\mathbf{E}}^{(\text{in})} \times \hat{\mathbf{B}}^{(\text{in})} : | 1 \rangle)) H(-z) \\ = & \int_V dV \partial_t (\mathbf{r} \times (\langle 1 | : \hat{\mathbf{P}} \times \hat{\mathbf{B}} : | 1 \rangle)). \end{aligned} \quad (6.92)$$

This is the same form of torque for the normally incident case [134], in which only the cross product of the polarisation and magnetic field contributes to the effective torque. This automatically implies

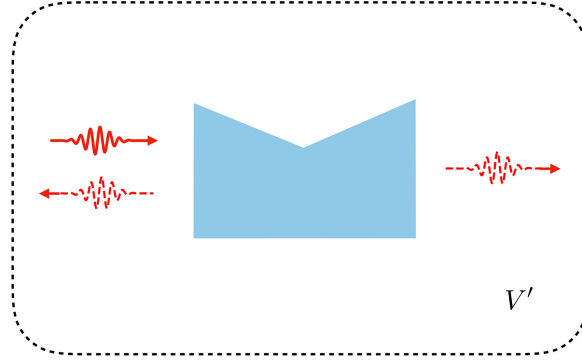


Figure 6.9: The solid wave packet represents the position of the single-photon pulse at the time T_{start} , so there is no field inside the Dove prism yet at that time. The dashed wave packets represent two possibilities that the outgoing photon will appear at the time T_{final} after being reflected back and forth inside the Dove prism, so at that time the electric field already left the Dove prism, and there is no field inside it again. The polarisation of the photon is linear and pointing outward from the paper. The dashed line represents the surface of the integral volume V' which can keep the single photon inside it during the observation time.

that when the polarisation of the beam is parallel to every interface of the M-shaped Dove prism, the total effective torque, after summing over all interfaces involved, is then given by

$$\langle \mathcal{T}_{\text{Dove}} \rangle = \int_{V'} dV \partial_t (\mathbf{r} \times (\langle 1 | : \hat{\mathbf{P}} \times \hat{\mathbf{B}} : | 1 \rangle)) = \partial_t \int_{V'} dV (\mathbf{r} \times (\langle 1 | : \hat{\mathbf{P}} \times \hat{\mathbf{B}} : | 1 \rangle)). \quad (6.93)$$

The integral volume V' with the Dove prism inside is assumed to be extremely large so that every event happens inside it and there is no field at its surface during the observation as illustrated in the figure 6.9. The problem is that Eq.(6.93) implies the angular momentum of the Dove prism in the x_0 -direction is unchanged even though the orbital angular momentum of the photon is inverted from $\hbar l$ to $-\hbar l$, as we will demonstrate it explicitly as follows. Let us suppose that at the beginning of the observation, $t = T_{\text{start}}$, no field has entered the Dove prism yet, and at the end of the observation, $t = T_{\text{final}}$, all of the fields have already left the Dove prism. Therefore, after integrating both sides of Eq.(6.93) over the observation time, the expectation value of the angular momentum change is

$$\begin{aligned} \langle \mathbf{L}_{\text{Dove}} \rangle &= \int_{T_{\text{start}}}^{T_{\text{final}}} dt \partial_t \int_{V'} dV (\mathbf{r} \times (\langle 1 | : \hat{\mathbf{P}} \times \hat{\mathbf{B}} : | 1 \rangle)) \\ &= \int_{V'} dV (\mathbf{r} \times (\langle 1 | : \hat{\mathbf{P}} \times \hat{\mathbf{B}} : | 1 \rangle)) \Big|_{t=T_{\text{final}}} - \int_{V'} dV (\mathbf{r} \times (\langle 1 | : \hat{\mathbf{P}} \times \hat{\mathbf{B}} : | 1 \rangle)) \Big|_{t=T_{\text{start}}} \\ &= 0 - 0 = 0. \end{aligned} \quad (6.94)$$

There is *no angular momentum transfer* to the Dove prism in the x_0 -direction even if there is a significant possibility that the pulse passes through the Dove prism and its orbital angular momentum is changed! This result absolutely conflicts with the conservation of angular momentum, as the intrinsic angular momentum of the photon has changed but has not been transferred to the medium. The reason this paradox appears is because of the subtlety of the order of the calculation given in

this section: we apply the conventional form of polarisation $\mathbf{P} = \varepsilon_0(n^2 - 1)\mathbf{E}$ before considering the physical boundary conditions. As we have shown, once the physical boundary conditions are applied first, the physical results then are straightforwardly obtained. However, according to our knowledge so far, it is only in the case of angular momentum transfer from light to dielectric via total internal reflection that this subtlety appears. For example, in the electrostatic case [131] and the case of linear momentum transfer, both normally incident [137] and total internal reflection cases, the subtlety does not show up, as physically sensible results are still obtained, without any contradiction, even though we use the conventional form of polarisation before we consider the boundary conditions. It is clear, however, that using \mathbf{E} and \mathbf{D} rather than \mathbf{P} produces sensible and physical results. The reason for this is that the boundary conditions on \mathbf{E} and \mathbf{D} are well-defined and fundamental, being consequences of the form of Maxwell's equations, while there is no correspondingly fundamental boundary condition on \mathbf{P} .

6.9 Conclusion

We have shown how to use the angular spectrum method to determine transverse reflected fields. The physical boundary conditions on \mathbf{E} , \mathbf{B} and \mathbf{D} , which are direct consequences of Maxwell's equations, are used in order to evaluate a net optical force acting on a dielectric. The obtained form of the net force is a manifestation of Newton's third law of motion: the force that photons exert on a dielectric is equal and opposite to the force that the dielectric exerts on the photons. The third law ensures the conservation of both linear and angular momentum. The discussion on the torque exerted on the dielectric via total internal reflection has been given, and the result shows that a net torque on the dielectric medium exerted by photons only appears shortly when these photons reach the interface. We then analysed the shifting effect and showed that it also produces an effective torque on the dielectric, but this torque is not related to the transfer of intrinsic angular momentum of light to the dielectric medium. The mechanism of angular momentum transfer to an M-shaped Dove prism has been fully analysed. The paradox of conservation of angular momentum has been demonstrated. We believe this paradox arises because the conventional form of polarisation is applied before the physical boundary conditions are carefully considered,

We also expect the appearance of similar torques in other optical components that are frequently used to transform the angular momentum of light in optical laboratories. For example, astigmatic mode converters have been reported to transform the orbital angular momentum of the light beam propagating through the lenses [30, 166].

Chapter 7

Coherent operation with the Jaynes-Cummings model

In previous chapters, we have mentioned that entanglement is a distinct nonclassical property of quantum mechanics. However, quantum coherence is another feature of quantum mechanics that cannot be satisfactorily described by the classical theory. It is an essential key to describe the difference between a quantum superposition and a statistical mixture. It has been discovered to be closely related to almost all the notable quantum phenomena such as quantum entanglement [167,168] and quantum discord [169,170]. It is also an important resource for various remarkable tasks in several fields such as quantum biology [171–173], quantum thermodynamics [174,175] and quantum transport [176]. It is, of course, essential to understand and have a reliable account of it as a resource. Otherwise, the misunderstanding of it could possibly lead to inaccuracy or even break fundamental laws of physics as shown in [177].

Åberg suggested that quantum coherence is catalytic, or more precisely it is a catalytic resource which can be used repeatedly without degradation in its performance [178]. The idea of catalytic coherence has been extended and applied in several topics [179–181]. Until recently, Vaccaro *et al.* have tested Åberg’s proposal and found that quantum coherence is indeed neither catalytic nor repeatable. They report that coherence is a finite resource and can be exhausted at some point [177]. The sign of degradation can be noticed by considering the correlation between two qubits that interact with the resource. It is also demonstrated explicitly that if coherence were really catalytic it would lead to unphysical state discrimination such that one can discriminate between two non-orthogonal states [177], which is impossible even in principle [182].

The motivation for this work is as follows. In [177], it has been shown that the Åberg model with a resource in a ladder state is very fragile. A single error in transferring of the phase reference to a qubit gives rise to the *complete destruction* of the resource. However, we know that an optical field in a coherent state is robust to environmental decoherence [183]. We then expect that if the resource is in a coherent state then it should be more robust to a single error than if it is in a ladder state.

In this work, we use the Jaynes-Cummings model to describe the interaction between a resource in a coherent state and an atom. We assume that the atom is in an excited state, denoted by $|e\rangle$,

initially. We then let the atom interact with the resource for a specific time such that the atom is more likely to be found in the superposition state:

$$|+\rangle = \frac{1}{\sqrt{2}} (|e\rangle + |g\rangle), \quad (7.1)$$

where $|g\rangle$ is the atomic ground state. We then examine the robustness of the coherence resource.

This chapter is organised as follows. In the first section, we review the work of J. A. Vaccaro *et al.* to understand how quantum coherence transfers from a coherence resource to an atom and induces correlations between two atoms after they have interacted with the resource. These correlations confirm that quantum coherence is not catalytic. We then demonstrate the fragility of a resource in a ladder state of Åberg's model. In section 7.2, we review the Jaynes-Cummings model and show that a resource, a cavity field, that is initially in a coherent state can be used to perform a similar coherent operation. Section 7.3 explicitly demonstrates that two atoms that independently and consecutively interact with the cavity field also become correlated. We analyse the robustness property of a coherent state against failures of coherent operations in section 7.4. The discussion of the evolution of the cavity field is given in section 7.5. In section 7.6, we show that the performance of coherent operations can be improved if we adjust the interaction times in accordance with the expectation of increasing average photon numbers. The quasiprobability distribution of the cavity field is shown in section 7.8. In the last section, we discuss and show that the squeezing of the photon number distribution is also a factor that gives rise to an increase in the success probability if the interaction time is adjusted properly.

7.1 Is coherence catalytic?

7.1.1 Åberg's scheme

We devote this section to review the analysis in [177] and [178] to introduce some background information and the research problem. Åberg's proposal of catalytic coherence is as given follows. There is a resource in the form of a multilevel quantum system, and its state is a coherent superposition of the energy eigenstates:

$$|\eta_{L,l_0}\rangle = \frac{1}{\sqrt{L}} \sum_{l=0}^{L-1} e^{il\theta} |l_0 + l\rangle, \quad (7.2)$$

where $|l_0 + l\rangle$ are energy eigenstates when l is an integer and L is the number of energy eigenstates in the superposition. This state is an eigenstate of the Hermitian optical phase operator [158]. From now on a state in this form will be called a ladder state, and for simplicity, we can set the relative phase of each energy eigenstate in the superposition to be zero, $\theta = 0$, without loss of generality for our main purpose. The main task is to use this resource to prepare repeatedly a coherent superposition of two atomic energy states, corresponding to, at least approximately, the operation

$$\hat{U}|e\rangle = |+\rangle = \frac{1}{\sqrt{2}} (|e\rangle + |g\rangle), \quad (7.3)$$

where we denote $|e\rangle$ and $|g\rangle$ as the excited and ground states of the atom and \hat{U} is a unitary operator. The interaction between the resource and the atom is described by an operator $\hat{V}(\hat{U})$ which can be written as

$$\hat{V}(\hat{U}) = \sum_{|n\rangle, |n'\rangle \in \{|g\rangle, |e\rangle\}} |n\rangle\langle n| \hat{U} |n'\rangle\langle n'| \otimes \hat{\Delta}^{n'-n}, \quad (7.4)$$

where n and n' are the numbers of excitations of the states $|n\rangle$ and $|n'\rangle$ respectively. To be clear, the sum in Eq.(7.4) is run over the atomic energy basis: $|n\rangle, |n'\rangle \in \{|g\rangle, |e\rangle\}$, but n and n' in the exponent of the operator $\hat{\Delta}$ are numbers, and the operator has been defined as

$$\hat{\Delta} = \sum_{j \in \mathbb{Z}} |j+1\rangle\langle j|. \quad (7.5)$$

This is the operator that shifts energy eigenstates up by one energy level, and its inverse is given by

$$\hat{\Delta}^{-1} = \sum_{j \in \mathbb{Z}} |j-1\rangle\langle j|. \quad (7.6)$$

We denote the multiplications of k copies of the operator $\hat{\Delta}$ and its inverse $\hat{\Delta}^{-1}$ as $\hat{\Delta}^k$ and $\hat{\Delta}^{-k}$ respectively. The interaction between the atom and the resource then can be expressed as

$$\hat{V}(\hat{U})|e\rangle \otimes |\eta_{L,t_0}\rangle = \frac{1}{\sqrt{2}} \left(|e\rangle \otimes |\eta_{L,t_0}\rangle + |g\rangle \otimes \hat{\Delta} |\eta_{L,t_0}\rangle \right). \quad (7.7)$$

From this equation, we can see that the total number of excitations after the interaction is preserved. This means the total energy of the atom and the resource is conserved after the interaction. The form on the right-hand side of the equation implies that after the interaction the atom is then entangled with the resource. At this point, we can define the quantum channels for the atom and the resource as

$$\Phi_{\sigma, \hat{U}}(\rho_0) = \text{Tr}_R \left[\hat{V}(\hat{U}) \rho_0 \otimes \sigma \hat{V}(\hat{U})^\dagger \right], \quad (7.8)$$

$$\Lambda_{\rho_0, \hat{U}}(\sigma) = \text{Tr}_A \left[\hat{V}(\hat{U}) \rho_0 \otimes \sigma \hat{V}(\hat{U})^\dagger \right], \quad (7.9)$$

where $\rho_0 = |e\rangle\langle e|$ is the density matrix of the atomic initial state and σ is the state of the resource. The subscripts R and A of the trace operators are used to identify that the Hilbert space of either the resource or that of the atom is traced over. At this point, we can easily see the first key result, that for large L we obtain $\text{Tr}_R \left[\hat{\Delta}^a \sigma \right] \approx 1$ for $-2 \leq a \leq 2$ [177, 178], and Eq.(7.8) gives

$$\begin{aligned} \Phi_{\sigma, \hat{U}}(\rho_0) &= \sum |n\rangle\langle m| U_{n,n'} \langle n'| \rho_0 |m'\rangle U_{m,m'}^* \otimes \text{Tr} \left[\hat{\Delta}^{(n'+m-n-m')} \sigma \right] \\ &\approx \sum |n\rangle\langle m| U_{n,n'} \langle n'| \rho_0 |m'\rangle U_{m,m'}^* \\ &= \hat{U} \rho_0 \hat{U}^\dagger, \end{aligned} \quad (7.10)$$

where $U_{n,n'}$ are matrix elements of the unitary operator \hat{U} : $U_{n,n'} = \langle n| \hat{U} |n'\rangle$, and we note that $|n'+m-n-m'| \leq 2$. Another key point is that the expectation value of the operator $\hat{\Delta}^a$ is invariant under the action of the quantum channel $\Lambda_{\rho_0, \hat{U}}$ [177, 178]:

$$\langle \hat{\Delta}^a \rangle = \text{Tr} \left[\hat{\Delta}^a \sigma \right] = \text{Tr} \left[\hat{\Delta}^a \Lambda_{\rho_0, \hat{U}}(\sigma) \right], \quad (7.11)$$

for every value of a . To see the importance of this key point, let us consider the following scenario. After the interaction, the reduced state of the resource is described by its own quantum channel: $\Lambda_{\rho_0, \hat{U}}(\sigma)$. If we use the same resource to perform the same coherent operation on another atom, the quantum channel for this atom becomes

$$\Phi_{\Lambda(\sigma), U}(\rho_0) = \sum |n\rangle\langle m| U_{n,n'} \langle n'| \rho_0 |m'\rangle U_{m,m'}^* \otimes \text{Tr} \left[\hat{\Delta}^{(n'+m-n-m')} \Lambda_{\rho_0, \hat{U}}(\sigma) \right]. \quad (7.12)$$

This seems to imply that the same quantum channel can be used again to perform the same coherent operation:

$$\Phi_{\Lambda(\sigma), \hat{U}} = \Phi_{\sigma, \hat{U}}. \quad (7.13)$$

It leads to the conclusion that the resource is not degraded after each coherent operation and can be infinitely used.

However, we need to be aware that the state of the resource is changed each time we use it for the operation i.e. $\Lambda_{\rho_0, \hat{U}}(\sigma) \neq \sigma$. This can be noticed easily by looking at Eq.(7.7). The atomic state after the interaction in the basis of $|\pm\rangle = (|e\rangle \pm |g\rangle)/\sqrt{2}$ is

$$\rho_A = (1 - \frac{1}{2L})|+\rangle\langle +| + \frac{1}{2L}|-\rangle\langle -|. \quad (7.14)$$

The state of the resource, on the other hand, becomes

$$\rho_R = \frac{1}{2} (|\eta_{L,l_0}\rangle\langle \eta_{L,l_0}| + \Delta |\eta_{L,l_0}\rangle\langle \eta_{L,l_0}| \Delta^{-1}). \quad (7.15)$$

The fidelity of the state of the resource before and after the interaction is close to unity for large L :

$$\langle \eta_{L,l_0} | \rho_R | \eta_{L,l_0} \rangle = 1 - \frac{1}{L} (1 - \frac{1}{2L}) \approx 1. \quad (7.16)$$

This confirms that the resource state has changed. Even though the change is really small for large values of L , it still indicates that the process is not catalytic, or it will reach the point where we cannot use it as a resource anymore.

In the next subsection, we consider the situation that two atoms independently interact with the resource, and we then note that, if the idea of catalytic coherence were correct, we should not see correlations between these two atoms.

7.1.2 Quantum correlations

The aim of this subsection is to examine the idea of catalytic coherence by considering the correlations between two atomic qubits that independently interact with the coherence resource. We assume that these two atoms are initially in the excited state $|e\rangle$. The interaction between these the two atoms and the coherence resource can be described by [177]

$$V(U) \otimes V(U) |e\rangle|e\rangle|\eta\rangle = \frac{1}{4} [|+\rangle|+\rangle(\mathbb{1} + \Delta)^2|\eta\rangle + (|+\rangle|-\rangle + |-\rangle|+\rangle)(\mathbb{1} - \Delta^2)|\eta\rangle + |-\rangle|-\rangle(\mathbb{1} - \Delta)^2|\eta\rangle], \quad (7.17)$$

where we have written the atomic qubits on the right-hand side in terms of the $|\pm\rangle$ basis. The joint measurement probabilities in this basis are given as

$$P(+, +) = 1 - \frac{3}{4L}, \quad (7.18)$$

$$P(+, -) = \frac{1}{4L} = P(-, +), \quad (7.19)$$

$$P(-, -) = \frac{1}{4L}. \quad (7.20)$$

These joint probabilities demonstrate correlations between the two atomic qubits. They are not equal to the products of the single-qubit probabilities as they would be if quantum coherence were catalytic. The products of the single-qubit probabilities are given as

$$P(+, +) \times P(+, -) = 1 - \frac{1}{L} + \frac{1}{4L^2}, \quad (7.21)$$

$$P(+, +) \times P(-, -) = \frac{1}{2L} - \frac{1}{4L^2} = P(-, -) \times P(+, +), \quad (7.22)$$

$$P(-, -) \times P(-, -) = \frac{1}{4L^2}. \quad (7.23)$$

We do not review the derivation for the case of N qubits here but give some aspects that related to our work. In the N -qubit case, the probability that the outcome is found in a particular tensor product of one qubit in the state $|-\rangle$ and the rest of them in the state $|+\rangle$ is equal to the probability that all N qubits are found in the state $|-\rangle$ [177]:

$$P_{\text{seq}}(N - 1) = P(0). \quad (7.24)$$

This is the result of the fact that, if there is a single qubit found in the state $|-\rangle$, the resource is projected into a state that is devoid of its initial coherence, and the next qubit is equally likely to be found in the state $|+\rangle$ as the state $|-\rangle$ [177]. This means a single error leads to the complete destruction of the initial coherence and the resource can no longer be used to perform a reliable coherent operation. Let us consider the following example. If the first qubit is found to be in the state $|-\rangle$, the unnormalised state of the resource then becomes

$$(\mathbb{1} - \Delta)|\eta\rangle = \frac{1}{\sqrt{L}} (|l_0\rangle - |l_0 + L\rangle), \quad (7.25)$$

from which we can see that the resource has lost almost all of its initial coherence and cannot be a source of coherence anymore.

7.2 Jaynes-Cummings model

At this point let us briefly review the idea of the Jaynes-Cummings model and demonstrate how we can use it to perform a coherent operation. The Jaynes-Cummings model normally describes the interaction between an atomic two-level system and a single-mode field [158]. In this case, we consider the field to be an electromagnetic field in a cavity that is prepared in a coherent state initially. On resonance, the interaction Hamiltonian may be written as

$$\hat{H} = -i\hbar\lambda(\hat{a}\hat{\sigma}^+ - \hat{a}^\dagger\hat{\sigma}^-), \quad (7.26)$$

where \hat{a} and \hat{a}^\dagger are the annihilation and creation operators for the cavity field, $\hat{\sigma}^+ = |e\rangle\langle g|$ and $\hat{\sigma}^- = |g\rangle\langle e|$ are raising and lowering operators respectively, and λ is the coupling strength. The unitary operator for this interaction is given by

$$\hat{U}(t) = \exp\left(-i\frac{\hat{H}t}{\hbar}\right) = \exp[-\lambda t(\hat{a}\hat{\sigma}^+ - \hat{a}^\dagger\hat{\sigma}^-)]. \quad (7.27)$$

An optical coherent state may be expressed as

$$|\alpha\rangle = \sum_{n=0}^{\infty} a_n |n\rangle, \quad (7.28)$$

where $a_n = e^{-|\alpha|^2/2} \alpha^n / \sqrt{n!}$. This coherent state has average photon number $\bar{n} = |\alpha|^2$. We consider the case that α is a real number. Similar to Åberg's model, we assume that the atomic state is initially in the excited state $|e\rangle$, and we aim to prepare the state $|+\rangle$. After the atom interacts with the cavity field for time t the composite system is changed to be

$$\begin{aligned} |\phi(t)\rangle &= \sum_{n=0}^{\infty} a_n \hat{U}(t) |e\rangle |n\rangle = \sum_{n=0}^{\infty} [a_n \cos(\lambda t \sqrt{n+1}) |e\rangle + a_{n-1} \sin(\lambda t \sqrt{n}) |g\rangle] |n\rangle \\ &= \frac{1}{\sqrt{2}} |+\rangle \sum_{n=0}^{\infty} [a_n \cos(\lambda t \sqrt{n+1}) + a_{n-1} \sin(\lambda t \sqrt{n})] |n\rangle \\ &\quad + \frac{1}{\sqrt{2}} |-\rangle \sum_{n=0}^{\infty} [a_n \cos(\lambda t \sqrt{n+1}) - a_{n-1} \sin(\lambda t \sqrt{n})] |n\rangle \end{aligned} \quad (7.29)$$

We call the value of the interaction time t that maximises the probability of getting the state $|+\rangle$ the *optimal time*. In order to obtain the optimal time, we need to perform a projective measurement on the atomic state to evaluate the probability that the state is found in $|+\rangle$, which is a function of the interaction time t , and we then can determine the first and second derivatives of the successful probability with respect to t and find the optimal time. However, we can easily estimate that it should be around τ_0 where $\lambda\tau_0\sqrt{\bar{n}} = \pi/4$. For example, in the case of $\alpha = 10$, the optimal time is numerically found to be τ' such that $\lambda\tau'\sqrt{\bar{n} + 1.5726} = \pi/4$. The value of the optimal time depends on the average photon number of a given coherent state. We, therefore, define $\lambda\tau_\zeta\sqrt{\bar{n} + \zeta} = \pi/4$, where ζ is an arbitrary real number that makes τ_ζ the optimal time and $\zeta \ll \bar{n}$. We note that, for a large average photon number, the optimal time defined above is much less than half of the revival time, $T_{1/2} = T_{\text{revival}}/2 \approx \pi\sqrt{\bar{n}}/\lambda \gg \tau_\zeta$, at which the atomic qubit becomes a particular pure state and disentangled with the cavity state, independent of initial conditions [184].

The probability to find the qubit in the desired state is given by

$$\begin{aligned} P(+) &= \text{Tr}[|+\rangle\langle +| |\phi(\tau_\zeta)\rangle\langle\phi(\tau_\zeta)|] \\ &= \frac{1}{2} \sum_{n=0}^{\infty} |[a_n \cos(\lambda\tau_\zeta\sqrt{n+1}) + a_{n-1} \sin(\lambda\tau_\zeta\sqrt{n})]|^2. \end{aligned} \quad (7.30)$$

This summation, however, is difficult to calculate analytically. We assume that the average photon number is large: $\bar{n} \gg 1$; with this condition, we can approximate the Poisson distribution with a Gaussian as [158]

$$\exp[-\bar{n}] \frac{\bar{n}^n}{n!} \approx \frac{1}{\sqrt{2\pi\bar{n}}} \exp\left[-\frac{(n-\bar{n})^2}{2\bar{n}}\right]. \quad (7.31)$$

The summation in Eq.(7.30) is then replaced by an integration: $\sum_{n=0}^{\infty} \rightarrow \int_0^{\infty} dn$. As the centre of the Gaussian distribution is far away from the point $n = 0$, the integral limit can be extended to be from $-\infty$ to ∞ . The probability that the qubit is found in the desired state can then be approximated as

$$\begin{aligned} P(+) &\approx \int_{-\infty}^{\infty} \frac{dn}{\sqrt{8\pi\bar{n}}} \left| e^{-(\Delta n)^2/4\bar{n}} \cos\left(\frac{\pi}{4} \sqrt{1 + \frac{(\Delta n + 1 - \zeta)}{\bar{n} + \zeta}}\right) + e^{-(\Delta n - 1)^2/4\bar{n}} \sin\left(\frac{\pi}{4} \sqrt{1 + \frac{(\Delta n - \zeta)}{\bar{n} + \zeta}}\right) \right|^2 \\ &= \frac{1}{2} + \frac{e^{-1/8\bar{n}}}{\sqrt{2\pi\bar{n}}} \int_{-\infty}^{\infty} d\mu e^{-\mu^2/2\bar{n}} \cos\left(\frac{\pi}{4} \sqrt{1 + \frac{(\mu - \zeta + 3/2)}{\bar{n} + \zeta}}\right) \sin\left(\frac{\pi}{4} \sqrt{1 + \frac{(\mu - \zeta + 1/2)}{\bar{n} + \zeta}}\right), \end{aligned} \quad (7.32)$$

where we have defined $\Delta n \equiv n - \bar{n}$ and $\mu \equiv n - \bar{n} - 1/2$. We can calculate the second term of the second line in Eq.(7.32) by using the Taylor expansions of the trigonometric functions. After that we can employ the following integration formula to calculate the second term:

$$\int_{-\infty}^{\infty} x^n e^{-\alpha x^2} dx = \frac{(1 + (-1)^n) 1 \cdot 3 \cdot 5 \dots (n-1) \sqrt{\pi}}{2^{n/2} \alpha^{(n+1)/2}}; \quad n > 0. \quad (7.33)$$

The probability of getting the state $|+\rangle$ is approximately given as

$$P(+) \approx 1 - \frac{(\pi + 2)^2}{64\bar{n}} + \frac{\pi^4 - 4(5 - 40\zeta + 16\zeta^2)\pi^2 + 64(1 + 2\zeta)\pi + 16}{4096\bar{n}^2} + \mathcal{O}\left(\frac{1}{\bar{n}^3}\right). \quad (7.34)$$

The probability that the qubit is in the undesired state, the state $|-\rangle$, on the other hand, is directly obtained as

$$P(-) = 1 - P(+) \approx \frac{(\pi + 2)^2}{64\bar{n}} - \frac{\pi^4 - 4(5 - 40\zeta + 16\zeta^2)\pi^2 + 64(1 + 2\zeta)\pi + 16}{4096\bar{n}^2} + \mathcal{O}\left(\frac{1}{\bar{n}^3}\right). \quad (7.35)$$

7.3 Two qubits

In this section, we study the case that two atoms consecutively and independently interact with the cavity field and show the correlations between these two atoms. The scenario is as follows. We let the first atom interact with the cavity field for time τ_ζ , and then after that, we stop the interaction by removing it from the cavity and replace it by the second atom. The second atom then interacts with the cavity for the same amount of time τ_ζ . We then stop the interaction and perform measurements. At this point, we can calculate the joint probabilities of the states of the first and second atoms in the basis $|\pm\rangle$.

As previously discussed, the two atoms are initially prepared in the excited state and the cavity field is in a coherent state. The composite state is then given by

$$|\Psi(t=0)\rangle = |e\rangle_{a_1} |e\rangle_{a_2} \sum_{n=0}^{\infty} a_n |n\rangle, \quad (7.36)$$

where the subscriptions a_1 and a_2 identify the states of the first and second atoms respectively. The interaction of these two atoms and the optical field is described by the evolution operators $\hat{U}_{a_i}(t)$,

which has the same form as the operator given in Eq.(7.27):

$$\hat{U}_{a_i}(t) = \exp \left[-\lambda t (\hat{a} \hat{\sigma}_{a_i}^+ - \hat{a}^\dagger \hat{\sigma}_{a_i}^-) \right]; \quad i = 1, 2. \quad (7.37)$$

The unitary operator $\hat{U}_{a_i}(t)$ operates on the Hilbert spaces of the i th atom and the optical field only. As we have done in the previous section the total state after the first atom has interacted with the optical field is given by

$$\begin{aligned} |\Psi(t = \tau_\zeta)\rangle &= \hat{U}_{a_1}(\tau_\zeta) |\Psi(t = 0)\rangle, \\ &= \frac{1}{\sqrt{2}} |+\rangle_{a_1} |e\rangle_{a_2} \sum_{n=0}^{\infty} (a_n \cos(\lambda\tau_\zeta \sqrt{n+1}) + a_{n-1} \sin(\lambda\tau_\zeta \sqrt{n})) |n\rangle \\ &\quad + \frac{1}{\sqrt{2}} |-\rangle_{a_1} |e\rangle_{a_2} \sum_{n=0}^{\infty} (a_n \cos(\lambda\tau_\zeta \sqrt{n+1}) - a_{n-1} \sin(\lambda\tau_\zeta \sqrt{n})) |n\rangle. \end{aligned} \quad (7.38)$$

We then remove the first atom from the cavity and replace it by the second atom. After the second atom has interacted with the field for the time τ_ζ , the total state becomes

$$\begin{aligned} |\Psi(t = 2\tau_\zeta)\rangle &= \hat{U}_{a_2}(\tau_\zeta) |\Psi(\tau_\zeta)\rangle \\ &= \frac{1}{2} |+\rangle_{a_1} |+\rangle_{a_2} \sum_{n=0}^{\infty} (b_n^+ \cos(\lambda\tau_\zeta \sqrt{n+1}) + b_{n-1}^+ \sin(\lambda\tau_\zeta \sqrt{n})) |n\rangle \\ &\quad + \frac{1}{2} |-\rangle_{a_1} |+\rangle_{a_2} \sum_{n=0}^{\infty} (b_n^- \cos(\lambda\tau_\zeta \sqrt{n+1}) + b_{n-1}^- \sin(\lambda\tau_\zeta \sqrt{n})) |n\rangle \\ &\quad + \frac{1}{2} |+\rangle_{a_1} |-\rangle_{a_2} \sum_{n=0}^{\infty} (b_n^+ \cos(\lambda\tau_\zeta \sqrt{n+1}) - b_{n-1}^+ \sin(\lambda\tau_\zeta \sqrt{n})) |n\rangle \\ &\quad + \frac{1}{2} |-\rangle_{a_1} |-\rangle_{a_2} \sum_{n=0}^{\infty} (b_n^- \cos(\lambda\tau_\zeta \sqrt{n+1}) - b_{n-1}^- \sin(\lambda\tau_\zeta \sqrt{n})) |n\rangle, \end{aligned} \quad (7.39)$$

where we have defined

$$b_n^\pm = a_n \cos(\lambda\tau_\zeta \sqrt{n+1}) \pm a_{n-1} \sin(\lambda\tau_\zeta \sqrt{n}). \quad (7.40)$$

To write Eq.(7.39) in a shorter form, we define the coefficients of energy eigenstates to be

$$C_n^{i,\pm} = b_n^i \cos(\lambda\tau_\zeta \sqrt{n+1}) \pm b_{n-1}^i \sin(\lambda\tau_\zeta \sqrt{n}), \quad (7.41)$$

The form of the equation is reduced to be

$$\begin{aligned} |\Psi(t = 2\tau_\zeta)\rangle &= \frac{1}{2} |+\rangle_{a_1} |+\rangle_{a_2} \sum_{n=0}^{\infty} C_n^{+,+} |n\rangle + \frac{1}{2} |-\rangle_{a_1} |+\rangle_{a_2} \sum_{n=0}^{\infty} C_n^{-,+} |n\rangle \\ &\quad + \frac{1}{2} |+\rangle_{a_1} |-\rangle_{a_2} \sum_{n=0}^{\infty} C_n^{+,-} |n\rangle + \frac{1}{2} |-\rangle_{a_1} |-\rangle_{a_2} \sum_{n=0}^{\infty} C_n^{-,-} |n\rangle. \end{aligned} \quad (7.42)$$

At this point, we can calculate the joint probabilities straightforwardly. For example, the probability that these two atoms end up in the state $|+\rangle$ after measurement are

$$\begin{aligned} P(+ \cap +) &= \text{Tr}_F \left[|_{a_1, a_2} \langle ++ | \Psi(t = 2\tau_\zeta) \rangle|^2 \right] \\ &= \frac{1}{4} \sum_{n=0}^{\infty} |C_n^{+,+}|^2. \end{aligned} \quad (7.43)$$

	Jaynes-Cummings	Åberg's scheme
$P(+)$	$1 - \frac{(\pi+2)^2}{64\bar{n}} + \frac{\pi^4 - 4(5 - 40\zeta + 16\zeta^2)\pi^2 + 64(1+2\zeta)\pi + 16}{4096\bar{n}^2}$	$1 - \frac{1}{2L}$
$P(-)$	$\frac{(\pi+2)^2}{64\bar{n}} - \frac{\pi^4 - 4(5 - 40\zeta + 16\zeta^2)\pi^2 + 64(1+2\zeta)\pi + 16}{4096\bar{n}^2}$	$\frac{1}{2L}$
$P(+)\times P(+)$	$1 - \frac{(\pi+2)^2}{32\bar{n}} + \left(\frac{(\pi+2)^4}{4096} + \frac{\pi^4 - 4(5 - 40\zeta + 16\zeta^2)\pi^2 + 64(1+2\zeta)\pi + 16}{2048} \right) \frac{1}{\bar{n}^2}$	$1 - \frac{1}{L} + \frac{1}{4L^2}$
$P(+)\times P(-)$	$\frac{(\pi+2)^2}{64\bar{n}} - \frac{\pi^4 + 4\pi^3 - (32\zeta^2 - 80\zeta - 2)\pi^2 + 16(4\zeta + 3)\pi + 16}{2048\bar{n}^2}$	$\frac{1}{2L} - \frac{1}{4L^2}$
$P(-)\times P(-)$	$\frac{(\pi+2)^4}{4096\bar{n}^2}$	$\frac{1}{4L^2}$
$P(+\cap+)$	$1 - \frac{(\pi+2)^2}{32\bar{n}} + \frac{5\pi^4 - 64(1 - 6\zeta + 2\zeta^2)\pi^2 + 256(1+\zeta)\pi + 80}{4096\bar{n}^2}$	$1 - \frac{3}{4L}$
$P(-\cap+)$	$\frac{(\pi+2)^2}{64\bar{n}} - \frac{\pi^4 - (11 - 56\zeta + 16\zeta^2)\pi^2 + 16(3+2\zeta)\pi + 16}{1024\bar{n}^2}$	$\frac{1}{4L}$
$P(+\cap-)$	$\frac{(\pi+2)^2}{64\bar{n}} - \frac{\pi^4 + 4\pi^3 + (5 + 40\zeta - 16\zeta^2)\pi^2 + 32(1+\zeta)\pi + 16}{1024\bar{n}^2}$	$\frac{1}{4L}$
$P(-\cap-)$	$\frac{(\pi+2)^2(3\pi^2 + 4\pi + 12)}{4096\bar{n}^2}$	$\frac{1}{4L}$

Table 7.1: The table shows the probabilities and joint probabilities in both models.

We then evaluate the joint probabilities with the approximation method given previously. The joint probabilities are shown in table 7.1.

At this point, we can obviously see that there are correlations between these two atoms. However, the correlations can be noticed in the second order of the approximation while in Åberg's model the correlations can be seen in the order of L^{-1} . Unlike Åberg's model, this model with the cavity field initially being in a coherent state is more robust against failure. Even when the measurement of the first qubit gives the undesired state the probability that the second qubit is found in the desired state is still significantly larger than $1/2$ and almost unity for $\bar{n} \gg 1$. This is because the state of the cavity field still has a significant amount of coherence after a single failure, which will be discussed in the next section.

7.4 Robustness analysis

In this section, we compare the coherent operations in the Jaynes-Cummings model and Åberg's scheme and analyse the reason that makes the first model more robust against failures than the latter. First of all, let us consider the form of the total state of the atoms and the resource after N rounds of interaction. For both models, we can see that the total state is of the form

$$|\Psi\rangle_{\text{total}} = \sum_i \sqrt{P(i)} |S_i^{N-1}\rangle \otimes (|e\rangle_{a_N} |F_e^i\rangle + |g\rangle_{a_N} |F_g^i\rangle), \quad (7.44)$$

where $|S_i^{N-1}\rangle$ is a tensor product state of the previous $N - 1$ qubits, expressed as a sequence of the states $|+\rangle$ and $|-\rangle$:

$$|S_i^{N-1}\rangle = |m_1\rangle_{a_1} \otimes |m_2\rangle_{a_2} \otimes |m_3\rangle_{a_3} \dots |m_j\rangle_{a_j} \dots |m_{N-1}\rangle_{a_{N-1}}; \quad |m_j\rangle_{a_j} \in \{|+\rangle_{a_j}, |-\rangle_{a_j}\},$$

the subscript i is used to identify a string of outcomes associated with the state $|S_i^{N-1}\rangle$:

$$i = (m_1, m_2, m_3, \dots, m_j, \dots, m_{N-1}),$$

$P(i)$ is the probability that the previous $N - 1$ atoms are found in the state $|S_i^{N-1}\rangle$, and $|F_e^i\rangle$ and $|F_g^i\rangle$ are (unnormalised) states of the resource coupled with the atomic excited and ground states of the N th atom. For example, in Eq.(7.7), we have $|F_e^0\rangle = |\eta_{L,l_0}\rangle$ and $|F_g^0\rangle = \Delta|\eta_{L,l_0}\rangle$. The density matrix of the N th atom given that the other $N - 1$ atoms are found in $|S_i\rangle$ is written as

$$\rho_{a_N}^i = \langle F_e^i | F_e^i \rangle |e\rangle\langle e| + \langle F_g^i | F_g^i \rangle |g\rangle\langle g| + \langle F_e^i | F_g^i \rangle |g\rangle\langle e| + \langle F_g^i | F_e^i \rangle |e\rangle\langle g|. \quad (7.45)$$

At this point, we can analyse how the atomic qubit is rotated in the Bloch sphere after interaction. The probability that the N th atom is in the state $|+\rangle$ depends mainly on the inner product $\langle F_e^i | F_g^i \rangle$. We then consider all possible values of this inner product case by case as follows. If the real part of the inner product, $\text{Re}[\langle F_e^i | F_g^i \rangle]$, is a positive number, then there is a component of the qubit in the positive x direction of the Bloch sphere. This means the probability of getting the state $|+\rangle$ is higher than $1/2$. The larger the positive real part, the greater the probability to get the desired state. In the case that the real part of the inner product is negative, $\text{Re}[\langle F_e^i | F_g^i \rangle] < 0$, the qubit is rotated towards the negative x direction. It is more likely to obtain the undesired state, $|-\rangle$, in this case. If the real part of the inner product is zero, $\text{Re}[\langle F_e^i | F_g^i \rangle] = 0$, the qubit is in the $y - z$ plane of the Bloch sphere, and thus the measurement outcome in the $|\pm\rangle$ basis is random. The density matrix of the atom in each case is displayed in the Bloch sphere as shown in figure 7.1.

In both models, the states $|F_e^i\rangle$ and $|F_g^i\rangle$ can be written in terms of superpositions of energy eigenstates as

$$|F^i\rangle = \sum_{n=0}^{\infty} d_n^i |n\rangle. \quad (7.46)$$

The overlap between the states $|F_e^i\rangle$ and $|F_g^i\rangle$ for both models are shown in figure 7.2. We consider only the case that the coefficients, d_n^i , are real numbers in both models.

The first column displays the overlaps of the states $|F_e^i\rangle$ and $|F_g^i\rangle$ for the Jaynes-Cummings model with a resource initially in a coherent state with the average photon number of $\bar{n} = 5$. The second column, on the other hand, shows the overlaps of the states, $|F_e^i\rangle$ and $|F_g^i\rangle$, in Åberg's model using a resource initially in a ladder state with $L = 5$. The first row of the figure, for both columns, shows the overlaps of the resource states $|F_e^0\rangle$ and $|F_g^0\rangle$ after the resource has interacted with the first atom. We can see that the coefficient distributions d_n^0 of the states $|F_e^0\rangle$ and $|F_g^0\rangle$ are almost coincident: $\langle F_e^0 | F_g^0 \rangle \approx 1$. This means in both models after the first-round interaction the first atom is more likely to be found in the desired state $|+\rangle$ with the nearly-unity probability. The second row of the picture shows the graphs of coefficients for both models after the second atom has interacted

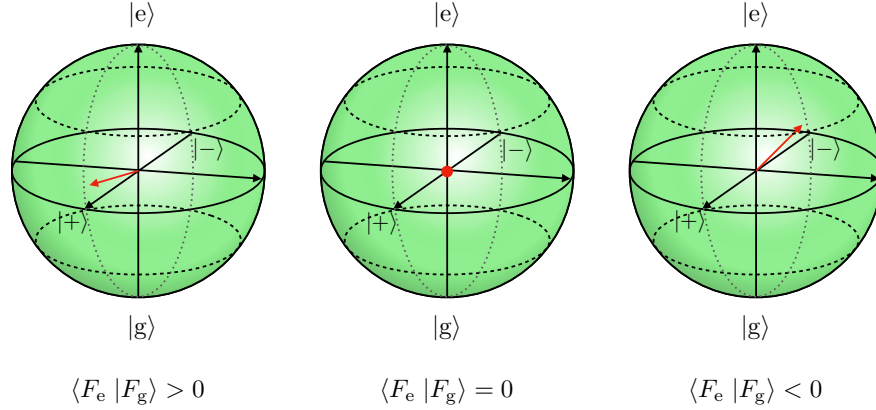


Figure 7.1: The atomic state ρ after the interaction is illustrated by the red arrows and the red dot for three different values of the inner product: $\langle F_e | F_g \rangle$. We consider only the case that the coefficients d_n^i are real.

with the resource given that the first atomic qubit is found in $|-\rangle$. We can see that for the Jaynes-Cummings case the graphs of coefficients are still almost coincident with each other, but there is no overlap between $|F_e^-\rangle$ and $|F_g^-\rangle$ in Åberg's model. This means the resource in the Jaynes-Cummings case can still be used further as a resource after a failure, and the probability of being successful is still very high. However, for Åberg's model, if the first atom is instead found in the undesired state, the second atom is equally likely to be in either $|+\rangle_{a_2}$ or $|-\rangle_{a_2}$. The coefficient distributions of the states $|F_e^{--}\rangle$ and $|F_g^{--}\rangle$ after the third interaction, given that the first two atoms are in the state $|-\rangle_{a_1} \otimes |-\rangle_{a_2}$, are displayed in the third row of the figure. For the Jaynes-Cummings model, it is similar to the previous case: $\langle F_e^{--} | F_g^{--} \rangle \sim 1$. Interestingly, for Åberg's model the inner product of $|F_e^{--}\rangle$ and $|F_g^{--}\rangle$ is negative: $\langle F_e^{--} | F_g^{--} \rangle < 0$. This means in this model if the earlier operations have failed the resource becomes more likely to produce the *undesired* state.

Notice that in both models the shapes of the coefficient distributions of the states $|F_e^i\rangle$ and $|F_g^i\rangle$ are similar but slightly shifted apart from each other. At this point, one may realise the reason that makes a resource initially in a coherent state of the Jaynes-Cummings model is more robust against a single error. This is because no matter how many times we have failed earlier the inner product between the states $|F_e^i\rangle$ and $|F_g^i\rangle$ is still positive, while this is not the case when the resource is in a ladder state in Åberg's model.

7.5 The state of the cavity field

As we can see in section 7.3, the cavity field is changed each time it interacts with an atom. The interaction entangles the states of the field and the atom. The cavity state then becomes a mixed quantum state. For example, in Eq.(7.38), after the first atom interacts with the optical field, the

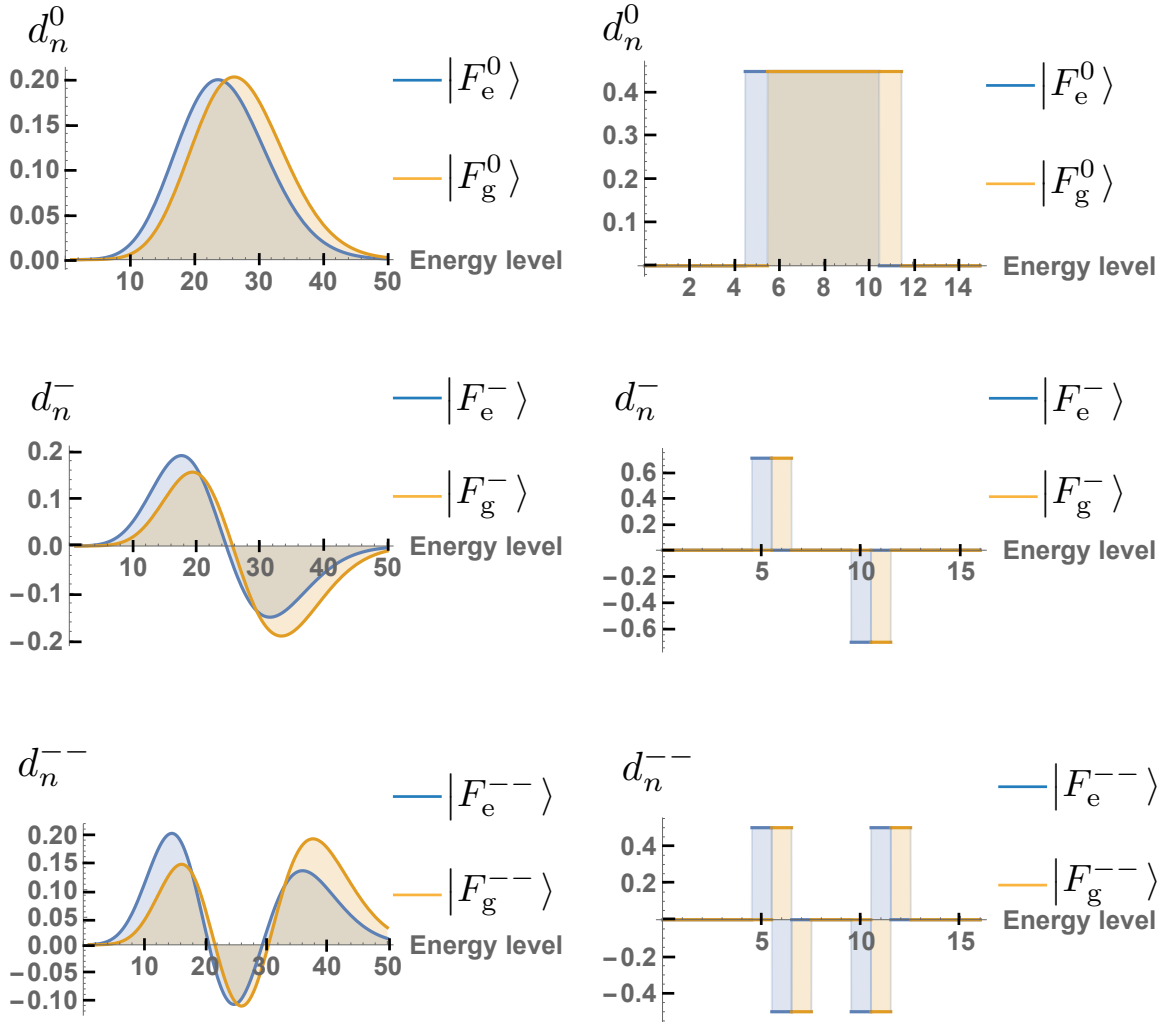


Figure 7.2: This figure shows the overlaps of the states $|F_e^i\rangle$ and $|F_g^i\rangle$. The blue graphs are the coefficient distributions of the state $|F_e^i\rangle$, while the orange ones are that of the state $|F_g^i\rangle$. The first and second columns are given to display the coefficient distributions d_n^i for the Jaynes-Cummings model and Åberg's scheme respectively. The first row of both columns are the coefficient distributions after the first-round interaction. The second row shows that for the second round if the first qubit is found in $|-\rangle$. If the first two operations fail, the coefficient distributions of the states $|F_e^{--}\rangle$ and $|F_g^{--}\rangle$ are shown in the third row.

normalised cavity state associated with the first atom in the state $|+\rangle_{a_1}$ is

$$|\tilde{F}^+\rangle = \frac{1}{\sqrt{2P(+)}} \sum_{n=0}^{\infty} (a_n \cos(\lambda\tau_\zeta\sqrt{n+1}) + a_{n-1} \sin(\lambda\tau_\zeta\sqrt{n})) |n\rangle, \quad (7.47)$$

but, if the atom is in the state $|-\rangle_{a_1}$ instead, its normalised state then becomes

$$|\tilde{F}^-\rangle = \frac{1}{\sqrt{2P(-)}} \sum_{n=0}^{\infty} (a_n \cos(\lambda\tau_\zeta\sqrt{n+1}) - a_{n-1} \sin(\lambda\tau_\zeta\sqrt{n})) |n\rangle. \quad (7.48)$$

Even though these two states of the cavity field look similar, their corresponding photon number distributions are completely different, as displayed in figure 7.3.

At the optimal time τ_ζ , the shape of the photon number distribution of the state $|\tilde{F}^+\rangle$ is almost the same as that of the initial coherent state for a large average photon number $\bar{n} \gg 1$, but their distribution peaks are different. While the peak of the photon number distribution of the coherent state is at $n = \bar{n}$, the peak of the distribution for the state $|\tilde{F}^+\rangle$ is approximately at $n = \bar{n} + 1/2$. This means, after measuring the first atom and obtain the desired result, the average photon number increases approximately by $1/2$. We can confirm this increase in the average photon number numerically. The numerical result shows that for an initial coherent state with average photon number $\bar{n} = 100$, after a successful measurement, the average photon number becomes $\bar{n}_+ = 100.502$.

The photon distribution for the state $|\tilde{F}^-\rangle$, on the other hand, has two distinct peaks. The mean photon number is difficult to evaluate analytically. However, the numerical result shows that it in fact decreases. For an initial coherent state with $\bar{n} = 100$, after a failure, the mean photon number drops slightly to be $\bar{n}_- = 99.812$. At this point, one might think that this could contradict the law of conservation of energy as the total energy of the atom and the optical field decreases after the unsuccessful measurement. However, we need to consider the measurement device and its energy as well. The measurement device can absorb the energy from and as well as release it to the atom and the cavity field.

The state of the cavity field after the first interaction is a mixed state:

$$\rho_F = P(+)|\tilde{F}^+\rangle\langle\tilde{F}^+| + P(-)|\tilde{F}^-\rangle\langle\tilde{F}^-|. \quad (7.49)$$

The photon number distribution of this state is given as

$$\begin{aligned} P_n &= \langle n|\rho_F|n\rangle = P(+)\left|\langle n|\tilde{F}^+\rangle\right|^2 + P(-)\left|\langle n|\tilde{F}^-\rangle\right|^2 \\ &= P(+P_n^+ + P(-)P_n^-, \\ &= \frac{1}{\sqrt{2\pi\bar{n}}}e^{-(n-\bar{n})^2/2\bar{n}}\cos^2\left(\frac{\pi}{4}\sqrt{1+\frac{(n-\bar{n}+1-\zeta)}{\bar{n}+\zeta}}\right) \\ &\quad + \frac{1}{\sqrt{2\pi\bar{n}}}e^{-(n-\bar{n}-1)^2/2\bar{n}}\sin^2\left(\frac{\pi}{4}\sqrt{1+\frac{(n-\bar{n}-\zeta)}{\bar{n}+\zeta}}\right). \end{aligned} \quad (7.50)$$

We have defined P_n^+ (P_n^-) to be the photon number distribution for the state $|\tilde{F}^+\rangle$ ($|\tilde{F}^-\rangle$). For $\bar{n} \gg 1$, this distribution is approximately the same as the distribution of the coherent state with the average photon number of $\bar{n} + 1/2$. The shape of the distribution P_n^- , the dashed black graph shown in figure 7.3, and the second line of the above equation suggest that the distribution P_n^+ may be narrower than that of a coherent state with the same average photon number. The variance of the photon number of the coherent state with $\bar{n} = 100.5$ is $(\Delta n)^2 = \bar{n} = 100.5$, while the variance of P_n^+ , for the initial coherent state with $\alpha = 10$, is $(\Delta n_+)^2 = 100.211$ numerically. This numerical result confirms that at the same average photon number the amplitude uncertainty for the state $|\tilde{F}^+\rangle$ becomes sub-Poissonian. The phase uncertainty, on the other hand, increases and the uncertainty relation of the amplitude and phase numerically becomes $(\Delta n_+)^2(\Delta\phi_+)^2 = \frac{1}{4} \times 1.0050$.

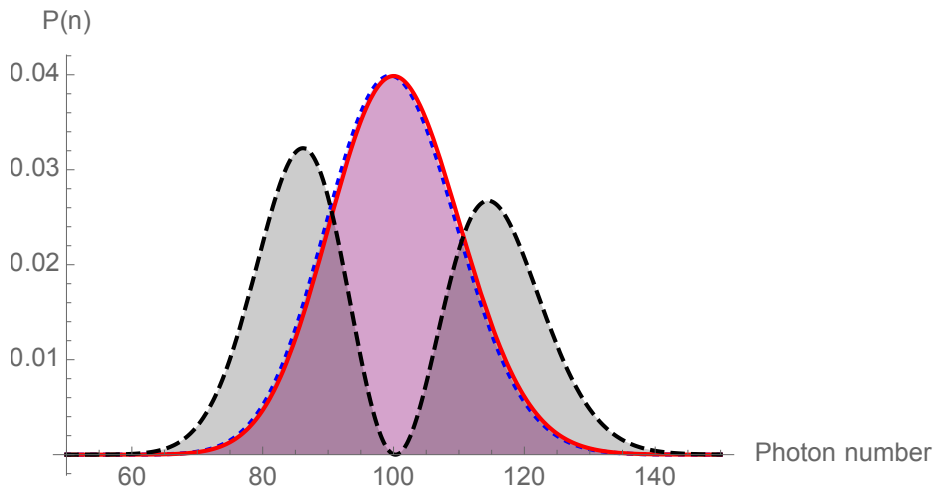


Figure 7.3: The dotted blue, solid red and dashed black graphs are the normalised photon number distributions of the cavity field in a coherent state, the state $|\tilde{F}^+\rangle$ and the state $|\tilde{F}^-\rangle$ respectively. We can see that the shapes of the distributions for the initial coherent state and the state $|\tilde{F}^+\rangle$ almost coincide.

7.6 Multiple uses

Before jumping into the aim and detail of this section let us begin with summarising the aims of the previous section. In the first section, we briefly reviewed [177] and discussed why quantum coherence is not catalytic, and the fragility of the resource in a ladder state. In the second section, we gave a brief review of the Jaynes-Cummings model and showed how it could be used to perform a coherent operation. In the following section, we then derived that the cavity field initially prepared in a coherent state of the Jaynes-Cummings model also produces correlations between two atoms that consecutively and independently interact with the cavity field, and we showed that its coherence is more robust to an error than that of a ladder state in Åberg's scheme. Then, we analysed the robustness property of the cavity field in a coherent state. In section 7.5, we showed that the cavity field is changed after we have performed a coherent operation. As we know that a resource of coherence is finite and the state of the cavity is changed every time we use it, our next question is how we can make the best use of it.

Recall that even though the aim of our coherent operation is to repeatedly prepare atomic qubits in the superposition state $|+\rangle$, after the operations, these atoms are not exactly in the desired state, but their states are really close to it. There is still a possibility that these atoms end up being in the state $|-\rangle$, even though it is very unlikely. We can make a measurement in the $|\pm\rangle$ basis to test the performance of the operation in each round. However, if we aim to use our coherent operations to prepare an ensemble of the state $|+\rangle$ for a quantum computing task instead, the measurement then should be done at the end of the protocol, so that the correct answer of the computation is given by the likely outcome of the measurement. Thus, in this case, as no measurement is performed on the qubit right after each round of interaction, in return, we do not know for certain whether the cavity's

average photon number increases by 1/2 or decreases slightly in each round. It is true that one can determine the average photon number from the reduced density matrix of the cavity field directly. However, it is really difficult to do so, because the number of involved terms in the calculation grows exponentially when the number of rounds increases. For example, as one can notice in Eq.(7.38), in the first round, the reduced density matrix of the cavity field is a mixture of *two* pure states, while in Eq.(7.42), the second round, it becomes a convex combination of *four* pure states. Even though the exact average photon number cannot be obtained easily, its approximation can be calculated more simply. This is because the probability of success is almost unity when $n \gg 1$. The average photon number approximately increases by 1/2 in each round if the number of rounds N is much less than the initial average photon number: $N \ll \bar{n}$. In order to maintain the performance of the operation, in each round of operation, the interaction time needs to be updated in accordance with the new mean photon number of the cavity field.

After the N th round of operations, we can rewrite Eq.(7.44) as

$$|\Psi_{\text{total}}\rangle = \sum_i |S_i^N\rangle |\tilde{F}^i\rangle \quad (7.51)$$

where we once again denote

$$|S_i^N\rangle = |m_1\rangle_{a_1} \otimes |m_2\rangle_{a_2} \otimes |m_3\rangle_{a_3} \dots |m_j\rangle_{a_j} \dots |m_N\rangle_{a_N},$$

with $|m_j\rangle_{a_j} \in \{|+\rangle_{a_j}, |-\rangle_{a_j}\}$, the subscript i represents the outcomes associated with $|S_i^N\rangle$: $i = (m_1, m_2, m_3, \dots, m_j, \dots, m_N)$, and $|\tilde{F}^i\rangle$ is an unnormalised state of the cavity field when all atoms are in the state $|S_i^N\rangle$. We can express the state of the cavity field $|\tilde{F}^i\rangle$ if the string of outcomes i is found as

$$|\tilde{F}^i\rangle = e^{-|\alpha|^2/2} \sum_{n=0}^{\infty} \frac{\alpha^n}{\sqrt{n!}} f_N^i(n), \quad (7.52)$$

with

$$\begin{aligned} f_N^i(n) &= \frac{1}{\sqrt{2}} \left(f_{N-1}^i(n) \cos(\lambda\tau_N\sqrt{n+1}) + m_N f_{N-1}^i(n-1) \frac{\sqrt{n}}{\alpha} \sin(\lambda\tau_N\sqrt{n}) \right), \\ f_j^i(n) &= \frac{1}{\sqrt{2}} \left(f_{j-1}^i(n) \cos(\lambda\tau_j\sqrt{n+1}) + m_j f_{j-1}^i(n-1) \frac{\sqrt{n}}{\alpha} \sin(\lambda\tau_j\sqrt{n}) \right), \\ f_0^i(n) &= 1, \end{aligned}$$

where m_j is the sign associated with the state of the j th atom in the state $|S_i^N\rangle$ such that if it is the state $|+\rangle_{a_j}$ then $m_j = +1$, and $m_j = -1$ for the undesired state $|-\rangle_{a_j}$. The interaction time τ_j needs to be updated in each round of interactions in order to cope with the increasing average photon number. An example of the case of $N = 2$, without adjusting the interaction time, is given in section 7.3. The probability that all atoms are found in the state $|S_i^N\rangle$ is given by

$$P(i) = \langle \tilde{F}^i | \tilde{F}^i \rangle. \quad (7.53)$$

We note that as we do not measure the qubit state each time we perform the operation and do not know the state of the cavity in the previous rounds the interaction time τ_j then is independent

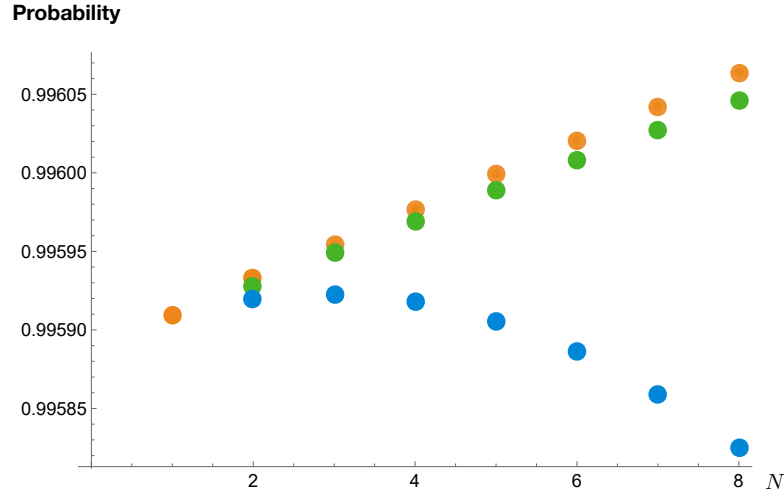


Figure 7.4: The dotted orange graph shows the probability of success for the N th atom if all other atoms are in the desired state with adjusted interaction times. The dotted blue graph represents the probability of success for the N th atom if the desired outcomes have been obtained for the other $N - 1$ atoms, but the interaction time is not updated. The dotted green graph gives the probability of success if a coherent state with $|\alpha|^2 = \bar{n} + N/2$ is the state of the cavity field.

of measuring previous copies. It depends only on how many coherent operations have been done previously.

Figure 7.4 shows the conditional probability that the N th atom is found in the state $|+\rangle_{a_N}$ if all other atoms are in the desired state. We can see that if we do not update the interaction time the conditional probability rises slightly for a few rounds and then continuously drops after the 4th round. For the case that the interaction time is adjusted for each round, the conditional probability then continuously increases. One factor that causes the increase is that each successful operation increases the average photon number of the cavity approximately by $1/2$. However, it is not the only factor here. As shown in the figure, the probability that the qubit is in the desired state when the resource is in a coherent state with an average photon number of $\bar{n} + N/2$ is lower than the conditional probability when the interaction time of each round has been adjusted. The other factor is that the photon number distribution of the cavity field is squeezed when the atoms are in the desired state: it becomes sub-Poissonian. As the complexity of the field state given in Eq.(7.52) grows exponentially when the number of rounds increases, it takes a long time to get the numerical results after the 8th round.

On the other hand, the situation turns around if we update the interaction time for each round of operations, but all $N - 1$ previous qubits are in the undesired state. The conditional probability of success for this case is lower than the case of using the same interaction time, as shown in figure 7.5. This is reasonable because if the previous operations turn out to be failures the average photon then decreases instead, and it means the interaction time has been taken away from the optimal time. As

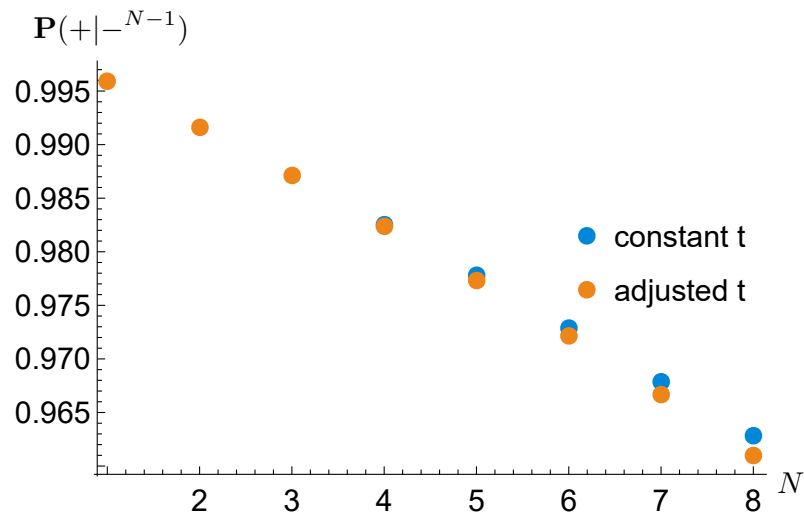


Figure 7.5: The graphs of the conditional probabilities of success for the N th atom if all other $N - 1$ atoms are found in the *undesired* state when all N interaction times are constant (blue dots) and adjusted in accordance with the expectancy of increasing average photon number.

expected, in the graph, the conditional probabilities show that the probability of being successful in the next round decreases if the previous operations have failed. This is because a failure result consumes a larger amount of coherence than a successful one, but multiple errors cannot completely destroy the resource.

7.7 Quasiprobability distribution

In this section, we use the Husimi Q -function to represent the state of the cavity field after interaction with the string of atomic states being measured. The quasiprobability distribution is useful to visualise the change in the cavity state. We then can examine the shift of the mean photon number of the optical field if the operations turn out to be perfectly successful or if all operations fail, that is all qubits are found in the desired or undesired state respectively. The Q -function of a state ρ is defined as

$$Q(\beta) = \frac{1}{\pi} \langle \beta | \rho_{\text{F}} | \beta \rangle.$$

Thus, the Q -function of the normalised state $|\tilde{F}_{\text{norm}}^i\rangle$ of the cavity field when the outcome i is found is given by

$$\begin{aligned} Q_i(\beta) &= \frac{1}{\pi} \left| \langle \beta | \tilde{F}_{\text{norm}}^i \rangle \right|^2 \\ &= \frac{1}{\pi P(i)} \left| e^{-|\beta|^2/2} \sum_{n=0}^{\infty} \frac{\beta^n}{\sqrt{n!}} \langle \tilde{F}^i | n \rangle \right|^2 \\ &= \frac{1}{\pi P(i)} e^{-(|\beta|^2 + |\alpha|^2)} \left| \sum_{n=0}^{\infty} \frac{(\beta\alpha^*)^n}{n!} f_N^i(n) \right|^2. \end{aligned} \quad (7.54)$$

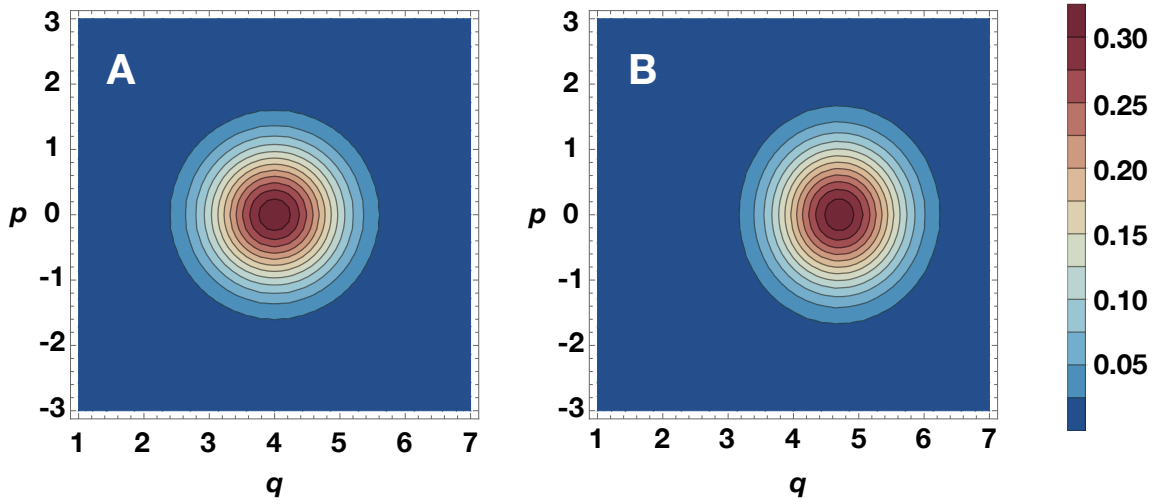


Figure 7.6: The figure compares the Q -functions of the states of the cavity field in phase space. Diagram A illustrates the quasiprobability distribution of an initial coherent state. The Q -function of the cavity field after the 12th round of operations, each of which succeeds, is given in diagram B. The peak of the distribution is squeezed and shifted in the positive q direction.

In figure 7.6, we compare the Q -functions of the initial coherent state and the cavity state after 12 rounds of successful coherent operations. It is clear that the peak of the photon number distribution is shifted, reflecting the increase in the average photon number. The shape of the Q -function shows squeezing in the q direction. The amplitude standard deviation $\sigma_{|\alpha|}$ is also smaller than that of a coherent state. This infers that the photon number distribution of the field is sub-Poissonian as mentioned as [158, 185]

$$\sigma_n^2 \approx 2\bar{n}\sigma_{|\alpha|}^2. \quad (7.55)$$

Figure 7.7 shows the Q -functions of the states after we have completely failed to prepare our two-level atoms in the desired state. We can see that the mean photon number, in this case, decreases if all operations have failed. It moves toward a state resembling the squeezed vacuum state.

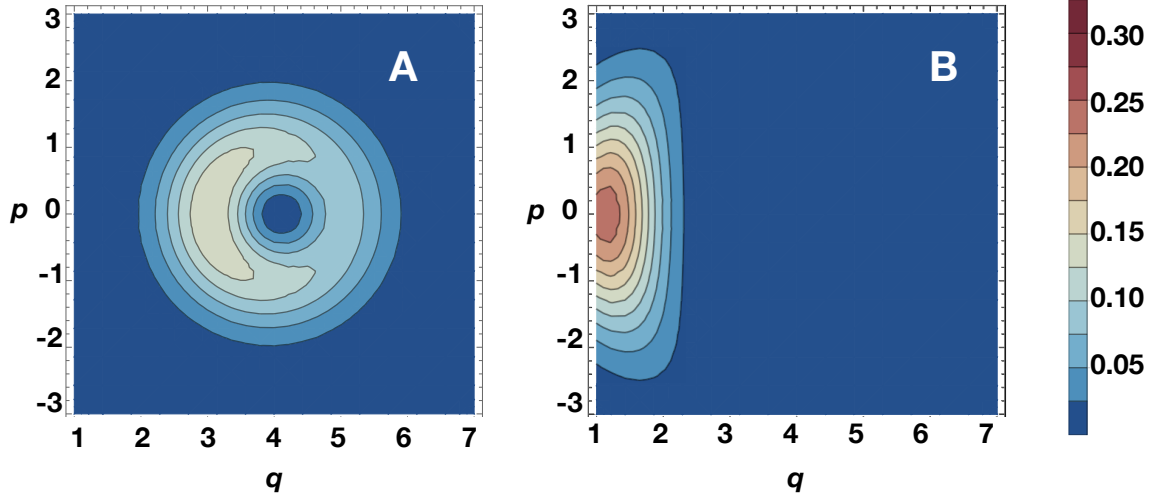


Figure 7.7: The figure shows the quasiprobability distributions of the field states after the first operation turned out to be unsuccessful in diagram A. Diagram B shows the Q -function of the cavity state after the ninth operations given that all nine atoms are found in the undesired state.

7.8 Coherent squeezed states

As we mentioned earlier in section 7.6, the increase of average photon number, if successful coherent operations take place, is not the only reason why the conditional probability in figure 7.4 gets higher when all operations are perfectly successful. The squeezing of the photon number distribution is another factor. In this section, we examine how this factor affects the successful probability by analysing the use of a coherent squeezed state as the initial state of the cavity field. Even though it cannot exactly represent the state of the cavity field following perfectly successful operations, it still helps us to understand why the conditional probability of success in the next operation increases.

A coherent squeezed state is generally defined to be generated by a squeezing operator and a displacement operator acting on the vacuum state consecutively:

$$|\alpha, \gamma\rangle = \hat{D}(\alpha)\hat{S}(\gamma)|0\rangle, \quad (7.56)$$

where

$$\hat{S}(\gamma) = \exp\left(-\frac{\gamma}{2}(\hat{a}^\dagger)^2 + \frac{\gamma^*}{2}\hat{a}^2\right), \quad (7.57)$$

$$\hat{D}(\alpha) = \exp(\alpha\hat{a}^\dagger - \alpha^*\hat{a}), \quad (7.58)$$

are the squeezing and displacement operators respectively, and $\gamma = r \exp(i\phi)$ is an arbitrary complex number with modulus r and argument ϕ . The modulus r is also known as the squeezing parameter. However, this state can be written in terms of a superposition of energy eigenstates as

$$|\alpha, \gamma\rangle = \frac{1}{\cosh r} \exp\left[-\frac{|\alpha|^2}{2} - \frac{(\alpha^*)^2 e^{i\phi} \tanh r}{2}\right] \sum_{n=0}^{\infty} \frac{(e^{i\phi} \tanh r)^{n/2}}{\sqrt{2^n n!}} H_n \left[\chi (e^{i\phi} \sinh(2r))^{-1/2} \right] |n\rangle \quad (7.59)$$

where $\chi = \alpha \cosh r + \alpha^* e^{i\phi} \sinh r$ and $H_n(x)$ is the n th-order Hermite polynomial of the variable x . This form of superposition is really difficult to work with, but we can use the fact that if the squeezing parameter, r , becomes zero, this state will just be the coherent state $|\alpha\rangle$. That means at small r and large $|\alpha|$ its photon number distribution should look like that of the coherent state. We consider an amplitude squeezed state here as its photon number uncertainty is lower than that of a coherent state, which is given by

$$\begin{aligned}\sigma_n^2 &= \langle \hat{n}^2 \rangle - \langle \hat{n} \rangle^2 \\ &= |\alpha|^2 e^{-2r} + 2 \sinh^2 r \cosh^2 r,\end{aligned}\quad (7.60)$$

where $\hat{n} = \hat{a}^\dagger \hat{a}$ is the photon number operator. The average photon number of this state is

$$\bar{n} = \langle \hat{n} \rangle = |\alpha|^2 + \sinh^2 r. \quad (7.61)$$

At this point, we can see that for large $|\alpha|$ and small r , the average photon number and the photon number uncertainty can be approximated as

$$\bar{n} \approx |\alpha|^2, \quad (7.62)$$

$$\sigma_n^2 \approx \bar{n} e^{-2r}. \quad (7.63)$$

At this limit, the photon number distribution of the amplitude squeezed state may be approximated as

$$P_n \approx \frac{1}{\sqrt{2\pi\bar{n}e^{-2r}}} \exp\left[-\frac{(n - \bar{n})^2}{2\bar{n}e^{-2r}}\right]. \quad (7.64)$$

With this distribution, we then redo the derivation given in section 7.2 and find that the probability of success is

$$P(+)=1 - \frac{(e^{-2r}\pi + 2)^2}{64\bar{n}e^{-2r}} + \mathcal{O}(\bar{n}^{-2}), \quad (7.65)$$

which is larger than the probability of success when the resource is in a coherent state having the same average photon number. It will be maximised if $e^{-2r} = 2/\pi$, which gives $P(+)=1 - \pi/(8\bar{n})$. This implies that the squeezing of the photon number distributions is another factor that makes the probability of success increase after being perfectly successful previously: $P(+|+^{N-1}) > P(+|+^{N-2})$. It also suggests that, if the state of the cavity reaches a certain level of squeezing equivalent to $r \approx \ln(\sqrt{\pi/2})$, this effect is then saturated, and it yet contributes an additional increase to the conditional probabilities of success in the next round, but it is smaller than its previous contributions. However, the effect of squeezing then no longer gives any contribution when the squeezing level reaches $r = \ln(\pi/2)$, the intersection point of the two graphs, between $r = 0.4$ and $r = 0.5$, in figure 7.9. After it meets this level, the conditional probability then starts to become lower than the probability of success given by using a coherent state with the same average photon number: the orange dots in figure 7.4 start to go under the green dots.

7.9 Conclusion

We introduced Åberg's scheme and showed how a coherence resource can be used to perform a coherent operation. It appears that there are correlations between atoms that have independently

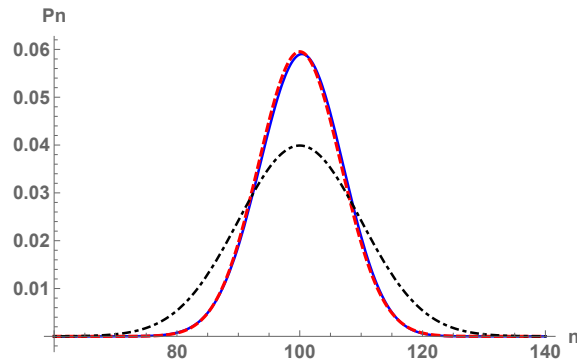


Figure 7.8: In this figure, the solid blue line and dashed red line are the exact and approximated photon number distributions of an amplitude squeezed state with $\alpha = 10$ and $r = 0.4$, respectively. The black dash-dotted line, on the other hand, is the distribution for a coherent state with the same magnitude of α . We can see that the approximated distribution can be used to describe the sub-Poisson distribution of the amplitude squeezed state effectively.

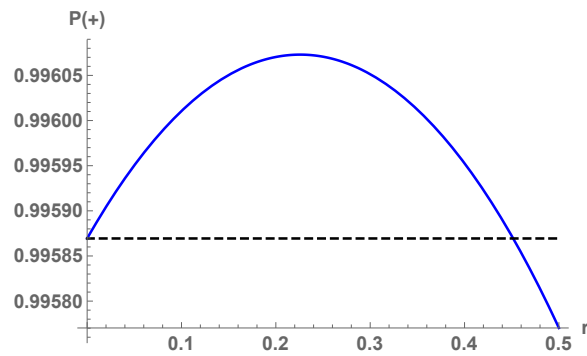


Figure 7.9: The solid blue line represents the relation of the probability of success $P(+)$ and the squeezing parameter r when $\bar{n} = 100$. The dashed black line is the probability of success when a coherent state with the same average photon number is used. In the figure, we can see that, if the squeezing parameter r is non-zero and smaller than 0.4, squeezed states with the squeezing parameter in that range are better than coherent states at the same average photon number.

interacted with the resource. These correlations affirm that quantum coherence is not catalytic. We then showed that with the Jaynes-Cummings model an optical cavity field initialised in a coherent state can also be considered as a coherence resource for a coherent operation, and correlations between atoms that independently and consecutively interact with the cavity field also show up in the second order of the approximation. We analysed the robustness property against failures of coherent operations of the coherent resource for both models. As expected, it turns out that a resource in a coherent state of the Jaynes-Cummings model is more robust against failures, as, no matter what the previous outcomes are, the inner product is still larger than zero: $\langle F_e^i | F_g^i \rangle > 0$, which gives rise to a probability of success larger than 0.5. Its coherence can be repeatedly used for coherent operations. This is in contrast to the case of a coherence resource in a ladder state of Åberg's

model as a single error leads to the complete destruction of the coherence resource. We have studied the change of the cavity state and its corresponding photon distribution after the first operation. This shows that the distribution becomes sub-Poissonian, and the distribution gets more squeezed if the coherent operations are successful in a row. The increase of average photon numbers and the squeezed distribution are the two factors give rise to the increase in the conditional probability.

Bibliography

- [1] A. Ritboon, S. Croke, and S. M. Barnett, "Proposed optical realisation of a two photon, four-qubit entangled χ state," *J. Opt.* **19** 075201 (2017).
- [2] A. Ritboon, S. Croke, and S. M. Barnett, "Optical angular momentum transfer on total internal reflection," *J. Opt. Soc. Am. B* **36** 482 (2019).
- [3] A. Messinger, A. Ritboon, F. Crimin, S. Croke, and S. M. Barnett, "Coherence and catalysis in the Jaynes-Cummings model," *Manuscript in preparation*.
- [4] J. C. Maxwell, *A Treatise on Electricity and Magnetism* (Oxford University Press, Oxford, 1871).
- [5] J. H. Poynting, "On the transfer of energy in the electromagnetic field," *Philos. Trans. R. Soc. Lond.* **175** 343 (1884).
- [6] J. H. Poynting, "The wave motion of a revolving shaft, and a suggestion as to the angular momentum in a beam of circularly polarised light," *Proc. Roy. Soc. A* **82** 560 (1909).
- [7] R. A. Beth, "Mechanical detection and measurement of the angular momentum of light," *Phys. Rev.* **50** 115 (1936).
- [8] L. Allen, M. W. Beijersbergen, R. J. C. Spreeuw, and J. P. Woerdman, "Orbital angular momentum of light and the transformation of Laguerre-Gaussian laser modes," *Phys. Rev. A* **45** 8185 (1992).
- [9] D. Marcuse, *Light transmission optics* (Van Nostrand, New York, 1972).
- [10] S. Franke-Arnold, S. M. Barnett, M. J. Padgett, and L. Allen, "Two-photon entanglement of orbital angular momentum states," *Phys. Rev. A* **65** 033823 (2002).
- [11] M. Born and E. Wolf, *Principle of Optics*, 6th ed. (Pergamon Press, Oxford, 1980).
- [12] L. Landau, "The theory of superfluidity of Helium II," *J. Phys.* **5** 71 (1941).
- [13] I. M. Khalatnikov, *An introduction to the theory of superfluidity* (Perseus Publishing, Cambridge MA, 1989).

- [14] S. M. Barnett, L. Allen, R. P. Cameron, C. R. Gilson, M. J. Padgett, F. C. Speirits, and A. M. Yao, "On the natures of the spin and orbital parts of optical angular momentum," *J. Opt.* **18** 064004 (2016).
- [15] C. G. Darwin, "Notes on the theory of radiation," *Proc. R. Soc. A* **136** 36 (1932).
- [16] H. Helmholtz, "Über Integrale der hydrodynamischen Gleichungen, welche den Wirbelbewegungen entsprechen," *J. Reine Angew. Math.* **55** 25 (1858).
- [17] J. V. Bladel, "A discussion of Helmholtz's theorem," *Electromagnetics* **13** 95 (1993).
- [18] J. D. Jackson, *Classical Electrodynamics*, 3rd ed. (John Wiley & Sons, New York, 1999).
- [19] S. J. van Enk and G. Nienhuis, "Spin and orbital angular momentum of photons," *EPL* **25** 497 (1994).
- [20] S. M. Barnett, "Rotation of electromagnetic fields and the nature of optical angular momentum," *J. Mod. Opt.* **57** 1339 (2010).
- [21] H. He, M. E. J. Friese, N. R. Heckenberg, and H. Rubinstztein-Dunlop, "Direct observation of transfer of angular momentum to absorptive particles from a laser beam with a phase singularity," *Phys. Rev. Lett.* **75** 826 (1995).
- [22] M. E. J. Friese, T. A. Nieminen, N. R. Heckenberg, and H. Rubinsztein-Dunlop, "Optical alignment and spinning of laser-trapped microscopic particles," *Nature* **394** 348 (1998).
- [23] J. Leach, S. Keen, M. J. Padgett, C. Saunter, and G. D. Love, "Direct measurement of the skew angle of the Poynting vector in a helically phase beam," *Opt. Express* **14** 11919 (2006).
- [24] A. T. O'Neil, I. MacVicar, L. Allen, and M. J. Padgett, "Intrinsic and extrinsic nature of the orbital angular momentum of a light beam," *Phys. Rev. Lett.* **88** 053601 (2002).
- [25] V. Garcés-Chávez, D. McGloin, M. J. Padgett, W. Dultz, H. Schmitzer, and K. Dholakia, "Observation of the transfer of the local angular momentum density of a multiringed light beam to an optically trapped particle," *Phys. Rev. Lett.* **91** 093602 (2003).
- [26] E. Noether, "Invariante Variationsprobleme," *Kgl. Ges. d. Wiss. Nachrichten, Math.-phys. Klasse.* 235 (1918).
- [27] M. W. Beijersbergen, R. P. C. Coerwinkel, M. Kristensen, and J. P. Woerdman, "Helical-wavefront laser beams produced with a spiral phaseplate," *Opt. Commun.* **112** 321 (1994).
- [28] G. A. Turnbull, D. A. Robertson, G. M. Smith, L. Allen, and M. J. Padgett, "The generation of free-space Laguerre-Gaussian modes at millimeter-wave frequencies by use of a spiral phaseplate," *Opt. Commun.* **127** 183 (1996).
- [29] N. R. Heckenberg, R. McDuff, C. P. Smith, H. Rubinsztein-Dunlop, and M. J. Wegener, "Laser beams with phase singularities," *OQE* **24** S951 (1992).

- [30] M. W. Beijersbergen, L. Allen, H. E. L. O. van der Veen, and J. P. Woerdman, "Astigmatic laser mode converters and transfer of orbital angular momentum," *Opt. Commun.* **96** 123 (1993).
- [31] D. Garoli, P. Zilio, Y. Gorodetski, F. Tantussi, and F. D. Angelis, "Optical vortex beam generator at nanoscale level," *Sci. Rep.* **6** 29547 (2016).
- [32] Z. Qiao, G. Xie, Y. Wu, P. Yuan, J. Ma, L. Qian, and D. Fan, "Generating high-charge optical vortices directly from laser up to 288th order," *Laser Photonics Rev.* **12** 1800019 (2018).
- [33] J. Jin, J. Luo, X. Zhang, H. Gao, X. Li, M. Pu, P. Gao, Z. Zhao, and X. Luo, "Generation and detection of orbital angular momentum via metasurface," *Sci. Rep.* **6** 24286 (2016).
- [34] C. Maurer, A. Jesacher, S. Fürhapter, S. Bernet, and M. Ritsch-Marte, "Tailoring of arbitrary optical vector beams," *New J. Phys.* **9** 78 (2007).
- [35] J. T. Barreiro, T.-C. Wei, and P. G. Kwiat, "Remote preparation of single photon "hybrid" entangled and vector-polarization state," *Phys. Rev. Lett.* **105** 030407 (2010).
- [36] A. E. Mair, A. Vaziri, G. Weihs, and A. Zeilinger, "Entanglement of the orbital angular momentum states of photons," *Nature* **412** 313 (2001).
- [37] M. I. Kolobov (Ed.), *Quantum Imaging* (Springer, Singapore, 2007).
- [38] J. Leach, M. J. Padgett, S. M. Barnett, S. Franke-Arnold, and J. Courtial, "Measuring the orbital angular momentum of a single photon," *Phys. Rev. Lett.* **88** 257901 (2002).
- [39] G. Ruffato, M. Massari, and F. Romanato, "Diffractive optics for combined spatial-and mode-division demultiplexing of optical vortices: design, fabrication and optical characterization," *Sci. Rep.* **6** 24760 (2016).
- [40] W. Zhang, Q. Qi, J. Zhou, and L. Chen, "Mimicking Faraday rotation to sort the orbital angular momentum of light," *Phys. Rev. Lett.* **112** 153601(2014).
- [41] G. C. G. Berkhout, M. P. J. Lavery, J. Courtial, M.W. Beijersbergen, and M.J. Padgett, "Efficient sorting of orbital angular momentum states of light," *Phys. Rev. Lett.* **105** 153601 (2010).
- [42] G. Ruffato, M. Massari, G. Parisi, and F. Romanato, "Test of mode-division multiplexing and demultiplexing in free-space with diffractive transformation optics," *Opt. Express* **25** 7859 (2017).
- [43] A. Vaziri, G. Weihs, and A. Zeilinger, "Superpositions of the orbital angular momentum for applications in quantum experiments," *J. Opt. B.* **4** S47 (2002).
- [44] J. Courtial, D. A. Robertson, K. Dholakia, L. Allen, and M. J. Padgett, "Rotational frequency shift of a light beam," *Phys. Rev. Lett.* **81** 4828 (1998).
- [45] M. A. Nielsen and I. L. Chuang, *Quantum computation and quantum information* (Cambridge University Press, Cambridge, 2000).

- [46] S. Stenholm and K.-A. Suominen, *Quantum approach to informatics* (Wiley, Hoboken NJ, 2005).
- [47] V. Vedral, *Introduction to quantum information science* (Oxford University Press, Oxford, 2006).
- [48] P. Kaye, R. Laflamme, and M. Mosca, *An introduction to quantum computing* (Oxford University Press, Oxford, 2007).
- [49] S. M. Barnett, *Quantum information* (Oxford University Press, Oxford, 2009).
- [50] C. H. Bennett and S. J. Wiesner, Communication via one- and two-particle operators on Einstein-Podolsky-Rosen states, *Phys. Rev. Lett.* **69** 2881 (1992).
- [51] A. K. Ekert, "Quantum cryptography based on Bell's theorem," *Phys. Rev. Lett.* **67** 661 (1991).
- [52] C. H. Bennett, G. Brassard, C. Crepeau, R. Jozsa, A. Peres, and W. K. Wootters, "Teleporting an unknown quantum state via dual classical and Einstein-Podolsky-Rosen channels," *Phys. Rev. Lett.* **70** 1895 (1993).
- [53] M. J. Padgett and R. W. Boyd, "An introduction to ghost imaging: quantum and classical," *Phil. Trans. R. Soc. A* **375** 20160233 (2017).
- [54] B. Jack, J. Leach, J. Romero, S. Franke-Arnold, M. Ritsch-Marte, S. M. Barnett, and M. J. Padgett, "Holographic ghost imaging and the violation of a bell inequality," *Phys. Rev. Lett.* **103** 083602 (2009).
- [55] T. B. Pittman, Y. H. Shih, D. B. Strelakov, and A. V. Sergienko, "Optical imaging by means of two-photon quantum entanglement," *Phys. Rev. A* **52** R3429 (1995)
- [56] J. G. Rarity, P. R. Tapster, E. Jakeman, T. Larchuk, R. A. Campos, M. C. Teich, and B. E. A. Saleh, "Two-photon interference in a Mach-Zehnder interferometer," *Phys. Rev. Lett.* **65** 1348 (1990).
- [57] Z. Y. Ou, X. Y. Zou, L. J. Wang, and L. Mandel, "Experiment on nonclassical fourth-order interference," *Phys. Rev. A* **42** 2957 (1990).
- [58] P. G. Kwiat, K. Mattle, H. Weinfurter, A. Zeilinger, A. V. Sergienko, and Y. Shih, "New High-Intensity Source of Polarization-Entangled Photon Pairs," *Phys. Rev. Lett.* **75** 4337 (1995).
- [59] Y. H. Shih, A. V. Sergienko, Morton H. Rubin, T. E. Kiess, and C. O. Alley, "Two-photon entanglement in type-II parametric down-conversion," *Phys. Rev. A* **50** 23 (1994).
- [60] A. Mair and A. Zeilinger, *Vienna circle institute yearbook 7/1999*, edited by A. Zeilinger *et al.* (Kluwer, Dordrecht, 1999).
- [61] A. E. Mair, Ph.D. thesis, Leopold Franzens Universität Innsbruck (2000) (in German).
- [62] C. H. Bennett and G. Brassard, "Quantum public key distribution," *IBM Technical Disclosure Bulletin* **28**, 3153 (1985).

- [63] H. Paik, D. I. Schuster, L. S. Bishop, G. Kirchmair, G. Catelani, A. P. Sears, B. R. Johnson, M. J. Reagor, L. Frunzio, L. I. Glazman, S. M. Girvin, M. H. Devoret, and R. J. Schoelkopf, "Observation of high coherence in Josephson junction qubits measured in a three-dimensional circuit QED architecture," *Phys. Rev. Lett.* **107** 240501 (2011).
- [64] R. Hanson, L. P. Kouwenhoven, J. R. Petta, S. Tarucha, and L. M. K. Vandersypen, "Spins in few-electron quantum dots," *Rev. Mod. Phys.* **79** 1217 (2007).
- [65] M. Šašura and V. Bužek, "Tutorial review: cold trapped ions as quantum information processors," *J. Mod. Opt.* **49** 1593 (2002).
- [66] D. Andrews, *Structured light and its applications* (Academic press, New York, 2008).
- [67] H. Bechmann-Pasquinucci and A. Peres, "Quantum cryptography with 3-state systems," *Phys. Rev. Lett.* **85** 3313 (2000).
- [68] S. Gröblacher, T. Jennewein, A. Vaziri, G. Weihs, and A. Zeilinger, "Experimental quantum cryptography with qutrits," *New J. Phys.* **8** 75 (2006).
- [69] D. Collins, N. Gisin, N. Linden, S. Massar, and S. Popescu, "Bell inequalities for arbitrarily high-dimensional systems," *Phys. Rev. Lett.* **88** 040404 (2002).
- [70] D. Kaszlikowski, L. C. Kwek, J.-L. Chen, M. Żukowski, and C. H. Oh, Clauser-Horne inequality for three-state systems, *Phys. Rev. A* **65** 032118 (2002).
- [71] G. Molina-Terriza, A. Vaziri, R. Ursin, and A. Zeilinger, "Experimental quantum coin tossing," *Phys. Rev. Lett.* **94** 040501 (2005).
- [72] A. Ambainis, in *Proceedings of 33rd Annual Symposium on Theory of Computing, 2001* (ACM, New York, 2001).
- [73] R. W. Spekkens and T. Rudolph, "Degrees of concealment and bindingness in quantum bit commitment protocols," *Phys. Rev. A* **65** 012310 (2001).
- [74] F. Verstraete, J. Dehaene, B. D. Moor, and H. Verschelde, "Four qubits can be entangled in nine different ways," *Phys. Rev. A* **65** 052112 (2002).
- [75] A. Higuchi and A. Sudbery, "How entangled can two couples get?," *Phys. Lett A* **273** 213 (2000).
- [76] D. Bruß, "Characterizing entanglement," *J. Math. Phys.* **43** 4237 (2002).
- [77] R. Horodecki, P. Horodecki, M. Horodecki, and K. Horodecki, "Quantum entanglement," *Rev. Mod. Phys.* **81** 865 (2009).
- [78] P. W. Shor, "Scheme for reducing decoherence in quantum computer memory," *Phys. Rev. A* **52** R2493 (1995).
- [79] M. Hillery, V. Bužek, and A. Berthiaume, "Quantum secret sharing," *Phys. Rev. A* **50** 1829 (1999).

- [80] M. Murao, D. Jonathan, M. B. Plenio, and V. Vedral, "Quantum telecloning and multiparticle entanglement," *Phys. Rev. A* **59** 156 (1999).
- [81] X. M. Xiu, H. K. Dong, L. Dong, Y. J. Gao, and F. Chi, "Deterministic secure quantum communication using four-particle genuine entangled state and entanglement swapping," *Opt. Commun.* **282** 2457 (2009).
- [82] W. Dür, G. Vidal, and J. I. Cirac, "Three qubits can be entangled in two inequivalent ways," *Phys. Rev. A* **62** 062314 (2000).
- [83] N. D. Mermin, "Extreme quantum entanglement in a superposition of macroscopically distinct states," *Phys. Rev. Lett.* **65** 1838 (1990).
- [84] J. Batle, C. H. Raymond Ooi, S. Abdalla, and A. Bagdasaryan, "Computing the maximum violation of a Bell inequality is an NP-problem," *Quantum Inf Process* **15** 2649 (2016).
- [85] A. Karlsson and M. Bourennane, "Quantum teleportation using three-particle entanglement," *Phys. Rev. A* **58** 4394 (1998).
- [86] W. Dür, "Multipartite entanglement that is robust against disposal of particles," *Phys. Rev. A* **63** 020303 (2001).
- [87] Y. Yeo and W. K. Chua, "Teleportation and dense coding with genuine multipartite entanglement," *Phys. Rev. Lett* **96** 060502 (2006).
- [88] J. Lee, H. Min, and S. D. Oh, "Multipartite entanglement for entanglement teleportation," *Phys. Rev. A* **66** 052318 (2002).
- [89] M. Enríquez, I. Wintrowicz, and K. Życzkowski, "Maximally entangled multipartite states: a brief survey," *J. Phys. : Conf. Ser.* **698** 012003 (2016).
- [90] S. Brierley and A. Higuchi, "On maximal entanglement between two pair in four-qubit pure states," *J. Phys. A: Math. Theor.* **40** 8455 (2007).
- [91] A. Osterloh and J. Siewert, "Constructing N -qubit entanglement monotones from antilinear operators," *Phys. Rev. A* **72** 012337 (2005).
- [92] C. Wu, Y. Yeo, L. C. Kwek, and C. H. Oh, "Quantum nonlocality of four-qubit entangled states," *Phys. Rev. A* **75** 032332 (2007).
- [93] M. Ardehali, "Bell inequalities with a magnitude of violation that grows exponentially with the number of particles," *Phys. Rev. A* **46** 5375 (1992).
- [94] A. V. Belinskii and D. N. Klyshko, "Interference of light and Bell's theorem," *Phys. Usp.* **36** 653 (1993).
- [95] G. Rigolin, "Quantum teleportation of an arbitrary two-qubit state and its relation to multipartite entanglement," *Phys. Rev. A* **71** 032303 (2005).

- [96] X.-W. Wang, L.-X. Xia, Z.-Y. Wang, and D.-Y. Zhang, "Hierarchical quantum-information splitting," *Opt. Commun.* **283** 1196 (2010).
- [97] M. Zukowski, A. Zeilinger, M. A. Horne, and A. Ekert, "'Event-ready-detector' Bell experiment via entanglement swapping," *Phys. Rev. Lett* **71** 4287 (1993).
- [98] J.-W. Pan, D. Bouwmeester, H. Weinfurter, and A. Zeilinger, "Experimental entanglement swapping: entanglement photons that never interacted," *Phys. Rev. Lett* **80** 3891 (1998).
- [99] Z. Liu, H. Chen, W. Liu, J. Xu, D. Wang, and Z. Li, "Quantum secure direct communication with optimal quantum superdense coding by using general four-qubit states," *Quantum Inf. Process.* **12** 587 (2013)
- [100] G. Gao, "Quantum key distribution by swapping the entanglement of χ -type state," *Phys. Scr.* **81** 65005 (2010).
- [101] S. Chitra and P. Anirban, "Hierarchical quantum-information splitting," *Phys. Lett. A* **377** 1337 (2013).
- [102] X. W. Wang and G. J. Yang, "Generation and discrimination of a type of four-particle entangled state," *Phys. Rev. A* **78** 024301 (2008).
- [103] Y. L. Shi, F. Mei, Y. F. Yu, X. L. Feng, and Z. M. Zhang, "Generation of a genuine four-particle entangled state of trap ions," *Quantum Inf. Process.* **11** 229 (2011).
- [104] X. W. Wang, "Method for generating a new class of multipartite entangled state in cavity quantum electrodynamics," *Opt. Commun.* **282** 1052 (2009).
- [105] H. F. Wang and S. Zhang, "Linear optical generation of multipartite entanglement with conventional photon detectors," *Phys. Rev. A* **79** 042336 (2009).
- [106] G. Y. Liu and L. M. Kuang, "Production of genuine entangled states of four atomic qubits," *J. Phys. B At. Mol. Opt. Phys.* **42** 165505 (2009).
- [107] X. Lin, "Scheme for generating a χ -type four-atom entangled state in cavity QED," *Chin. Phys. Lett.* **27** 044207 (2010).
- [108] L. Dong, X. M. Xiu, Y. J. Gao, and X. X. Yi, "A nearly deterministic scheme for generating χ -type entangled states with weak cross-Kerr nonlinearities," *Quantum Inf. Process* **12** 1787 (2013).
- [109] J. T. Barreiro, N. K. Langford, N. A. Peters, and P. G. Kwiat, "Generation of hyperentangled photon pairs," *Phys. Rev. Lett* **95** 260501 (2005).
- [110] F. M. Miatto, A. M. Yao, and S. M. Barnett, "Full characterization of the quantum spiral bandwidth of entangled photons," *Phys. Rev. A* **83** 033816 (2011).
- [111] A. M. Yao, "Angular momentum decomposition of entangled photons with an arbitrary pump," *New J. Phys.* **13** 053048 (2011).

- [112] J. P. Torres, A. Alexandrescu, and L. Torner, "Quantum spiral bandwidth of entangled two-photon states," *Phys. Rev. A* **68** 050301 (2003)
- [113] G. R. Fowles, *Introduction to Modern Optics*, 2nd ed. (Dover Publications, New York, 1989).
- [114] E. Hecht and A. Zajac, *Optics* (Addison-Wesley, Reading, MA, 1974).
- [115] B. E. A. Saleh and M. C. Teich, *Fundamentals of photonics*, 2nd ed. (John Wiley & Sons, Inc., Hoboken, New Jersey, 2007).
- [116] L.-P. Deng, H. Wang, and K. Wang, "Quantum CNOT gates with orbital angular momentum and polarisation of single-photon quantum logic," *J. Opt. Soc. Am. B* **24** 2517 (2007).
- [117] C. Gao, X. Qi, Y. Liu, J. Xin, and L. Wang, "Sorting and detecting orbital angular momentum states by using a Dove prism embedded Mach-Zehnder interferometer and amplitude gratings," *Opt. Commun.* **284** 48 (2011).
- [118] S. Slussarenko, V. D'Ambrosio, B. Piccirillo, L. Marrucci, and E. Santamato, "The polarizing Sagnac interferometer: a tool for light orbital angular momentum sorting and spin-orbit photon processing," *Opt. Express* **18** 27205 (2010).
- [119] J. M. Bennett, "A critical evaluation of rhomb-type quarterwave retarders," *Appl. Opt.* **9** 2123 (1970).
- [120] H. Wei, X. Xue, J. Leach, M. J. Padgett, S. M. Barnett, S. Franke-Arnold, E. Yao, and J. Courtial, "Simplified measurement of the orbital angular momentum of photons," *Opt. Commun.* **223** 117 (2003).
- [121] J. Leach, J. Courtial, K. Skeldon, S. M. Barnett, S. Franke-Arnold, and M. J. Padgett, "Interferometric methods to measure orbital and spin, or the total angular momentum of a single photon," *Phys. Rev. Lett.* **92** 013601 (2004).
- [122] H. E. Burton, "The optics of Euclid," *J. Opt. Soc. Am.* **35** 357, (1945).
- [123] I. Newton, *Opticks: or, A treatise of the reflexion, refractions, inflexion and colours of light. Also two treatises of the species and magnitude of curvilinear figures* (Printed for S. Smith, and B. Walford, London, 1704).
- [124] J. C. Maxwell, "A dynamical theory of the electromagnetic field," *Phil. Trans.* **166** 459 (1865).
- [125] H. Hertz, *Electric waves*, translated by D. E. Jones, (Macmillan, London, 1893).
- [126] A. Ashkin, "Acceleration and trapping of particles by radiation pressure," *Phys. Rev. Lett.* **24** 156 (1970).
- [127] A. Ashkin and J. M. Dziedzic, "Radiation pressure on a free liquid surface," *Phys. Rev. Lett.* **30** 139 (1973).

- [128] A. Ashkin, J. M. Dziedzic, J. E. Bjorkholm, and Steven Chu, "Observation of a single-beam gradient force optical trap for dielectric particles," *Opt. Lett.* **11** 288 (1986).
- [129] J. P. Gordon, "Radiation forces and momenta in dielectric media," *Phys. Rev. A* **8** 14 (1973).
- [130] M. Mansuripur, "Radiation pressure and the linear momentum of the electromagnetic field," *Opt. Express* **12** 5375 (2004).
- [131] S. M. Barnett and R. Loudon, "On the electromagnetic force on a dielectric medium," *J. Phys. B* **39** S671 (2006).
- [132] R. Loudon and S. M. Barnett, "Theory of the radiation pressure on dielectric slabs, prism and single surfaces," *Opt. Express* **14** 11855 (2006).
- [133] A. R. Zakharian, P. Polynkin, M. Mansuripur, and J. V. Moloney, "Single-beam trapping of micro-beads in polarized light: numerical simulations," *Opt. Express* **14** 3660 (2006).
- [134] R. Loudon, "Theory of the forces exerted by Laguerre-Gaussian light beams on dielectrics," *Phys. Rev. A* **68** 013806 (2003).
- [135] M. J. Padgett, S. M. Barnett, and R. Loudon, "The angular momentum of light inside a dielectric," *J. Mod. Opt.* **50** 1555 (2003).
- [136] R. Loudon, S. M. Barnett, and C. Baxter, "Radiation pressure and momentum transfer in dielectrics: the photon drag effect," *Phys. Rev. A* **71** 063802 (2005).
- [137] R. Loudon, "Theory of the radiation pressure on dielectric surfaces," *J. Mod. Opt.* **49** 821 (2002).
- [138] A. Ashkin, *Optical trapping and manipulation of neutral particles using laser: a reprint volume with commentaries* (World Scientific Publishing Company, Singapore, 2006).
- [139] W. E. Stewart, W. H. Ray, and C. C. Conley, *Dynamics and modelling of reactive systems* (Academic Press, New York, 1980).
- [140] L. Allen, S. M. Barnett, and M. J. Padgett, *Optical angular momentum* (Institute of Physics Publishing, Bristol, 2003).
- [141] R. Loudon, *The quantum theory of light*, 3rd ed. (Oxford University Press, Oxford, 2000).
- [142] G. B. Arfken and H. J. Weber, *Mathematical methods for physicists* (Elsevier, Boston, MA, 2005).
- [143] W. Greiner and J. Reinhardt, *Field quantization* (Springer, Berlin, 1996).
- [144] C. Cohen-Tannoudji, J. Dupont-Roc, and G. Grynberg, *Photons & atoms: introduction to quantum electrodynamics* (Wiley, USA, 1989).
- [145] A. Lipson, S G Lipson, and H. Lipson, *Optics physics*, 4th ed. (Cambridge University Press, New York, 2011).

- [146] M. Lax, "From Maxwell to paraxial wave optics," *Phys. Rev. A* **11** 1365 (1975).
- [147] H. A. Haus, *Waves and fields in optoelectronics* (Prentice-Hall, Englewood Cliffs, NJ, 1984).
- [148] S. M. Barnett and L. Allen, "Orbital angular momentum and nonparaxial light beams," *Opt. Commun.* **110** 670 (1994).
- [149] A. Aiello, C. Marquardt, and G. Leuchs, "Transverse angular momentum of photons," *Phys. Rev. A* **81** 053838 (2010).
- [150] G. F. Calvo, A. Picó, and E. Bagan, "Quantum field theory of photons with orbital angular momentum," *Phys. Rev. A* **73** 013805 (2006).
- [151] L. Allen, M. J. Padgett, and M. Babiker, "IV The orbital angular momentum of light," *Prog. Opt.* **39** 291 (1999).
- [152] L. Allen and M. J. Padgett, "The Poynting vector in Laguerre-Gaussian beams and the interpretation of their angular momentum density," *Opt. Commun.* **184** 67 (2000).
- [153] K. J. Blow, R. Loudon, S. J. D. Phoenix, and T. J. Shepherd, "Continuum fields in quantum optics," *Phys. Rev. A* **42** 4102 (1990).
- [154] D. Griffiths and S. Walborn, "Dirac deltas and discontinuous functions," *Am. J. Phys.* **67** 446 (1999).
- [155] S. M. Barnett, "Resolution of the Abraham-Minkowski dilemma," *Phys. Rev. Lett.* **104** 070401 (2010).
- [156] S. M. Barnett and R. Loudon, "The enigma of optical momentum in a medium," *Phil. Trans. R. Soc. A* **368** 927 (2010).
- [157] M. Abraham, "Zur elektrodynamik bewegter körper," *Rend. Circ. Mat. Palermo* **28** 1 (1909).
- [158] S. M. Barnett and P. M. Radmore, *Methods in theoretical quantum optics* (Oxford University Press, New York, 1997).
- [159] F. Goos and H. Hänchen, "Ein neuer und fundamentaler Versuch zur Totalreflexion," *Ann. Phys., Lpz* **436** 333 (1947).
- [160] J. B. Götte and M. R. Dennis, "Generalized shifts and weak values for polarization components of reflected light beams," *New J. Phys.* **14** 073016 (2012).
- [161] F. I. Fedorov, "To the theory of total reflection," *J. Opt.* **15** 014002 (2013).
- [162] C. Imbert, "Calculation and experimental proof of the transverse shift induced by total internal reflection of a circularly polarized light beam," *Phys. Rev. D* **5** 787 (1972).
- [163] K. Y. Bliokh, F. J. Rodríguez-Fortuño, F. Nori, and A. V. Zayats, "Spin-orbital interactions of light," *Nature Photonics* **9** 796 (2015).

- [164] K. Bichteler and S. J. Lin, "On the stochastic Fubini theorem," *Stoch. Stoch. Rep* **54** 271 (1995).
- [165] E. M. Stein and R. Shakarchi, *Real analysis: measurement theory, integration, and Hilbert space* (Princeton University Press, New Jersey, 2005).
- [166] M. J. Padgett and L. Allen, "Orbital angular momentum exchange in cylindrical-lens mode converters," *J. Opt. B* **4** S17 (2002)
- [167] A. Streltsov, U. Singh, H. S. Dhar, M. N. Bera, and G. Adesso, "Measuring quantum coherence with entanglement," *Phys. Rev. Lett.* **115** 020403 (2015).
- [168] L.-F. Qiao, A. Streltsov, J. Gao, S. Rana, R.-J. Ren, Z.-Q. Jiao, C.-Q. Hu, X.-Y. Xu, C.-Y. Wang, H. Tang, A.-L. Yang, Z.-H. Ma, M. Lewenstein, and X.-M. Jin, "Entanglement activation from quantum coherence and superposition," *Phys. Rev. A* **98** 052351 (2018).
- [169] J. Ma, B. Yadin, D. Girolami, V. Vedral, and M. Gu, "Converting coherence to quantum correlations," *Phys. Rev. Lett.* **116** 160407 (2016).
- [170] K. C. Tan and H. Jeong, "Entanglement as the symmetric portion of correlated coherence," *Phys. Rev. Lett.* **121** 220401 (2018).
- [171] M. B. Plenio and S. F. Huelga, "Dephasing-assisted transport: quantum networks and biomolecules," *New J. Phys.* **10** 113019 (2008).
- [172] S. F. Huelga and M. B. Plenio, "Vibrations, quanta and biology," *Contemp. Phys.* **54** 181 (2013).
- [173] C.-M. Li, N. Lambert, Y.-N. Chen, G.-Y. Chen, and F. Nori, "Witnessing quantum coherence: from solid-state to biological systems," *Sci. Rep.* **2** 885 (2012).
- [174] M. O. Scully, M. S. Zubairy, G. S. Agarwal, and H. Walther, "Extracting work from a single heat bath via vanishing quantum coherence," *Science* **299** 862 (2013).
- [175] J. Roßnagel, O. Abah, F. Schmidt-Kaler, K. Singer, and E. Lutz, "Nanoscale heat engine beyond the Carnot limit," *Phys. Rev. Lett.* **112** 030602 (2014).
- [176] S. W. Kim and M.-S. Choi, "Decoherence-driven quantum transport," *Phys. Rev. Lett.* **95** 226802 (2005).
- [177] J. A. Vaccaro, S. Croke, and S. M. Barnett, "Is coherence catalytic?," *J. Phys. A: Math. Theor.* **51** 414008 (2018).
- [178] J. Åberg, "Catalytic coherence," *Phys. Rev. Lett.* **113** 150402 (2014).
- [179] K. Korzekwa, M. Lostaglio, J. Oppenheim, and D. Jennings, "The extraction of work from quantum coherence," *New J. Phys.* **18** 023045 (2016).

-
- [180] A. S. L. Malabarba, A. J. Short, and P. Kammerlander, "Clock-driven quantum thermal engines," *New J. Phys.* **17** 045027 (2015).
- [181] M. Hayashi and H. Tajima, "Measurement-based formulation of quantum heat engines," *Phys. Rev. A* **95** 032132 (2017).
- [182] S. M. Barnett and S. Croke, "Quantum state discrimination," *Adv. Opt. Photonics* **1** 238 (2009).
- [183] A. Buchleitner and K. Hornberger, *Coherent evolution in noisy environments* (Springer, New York, 2002).
- [184] J. Gea-Banacloche, "Atom- and field-state evolution in the Jaynes-Cummings model for large initial fields", *Phys. Rev. A* **44** 5913 (1991).
- [185] M. C. Teich and B. E. A. Saleh, Squeezed state of light, *Quantum Opt.* **1** 153 (1989).